Dissertation
submitted to the
Combined Faculties for the Natural Sciences and for Mathematics
of the Ruperto-Carola University of Heidelberg, Germany
for the degree of
Doctor of Natural Sciences

presented by Diplom-Physiker Martin Stübig
born in Salzgitter
Oral examination: 04.12.2002

New insights in impact ionization and in time-of-flight mass spectroscopy with micrometeoroid detectors by improved impact simulations in the laboratory

Referees Prof. Dr. Eberhard Grün
Prof. Dr. Immo Appenzeller

Zusammenfassung

Neue Erkenntnisse über Einschlagsionisationsprozesse und über Flugzeitmassenspektroskopie mit Mikrometeoroid-Detektoren durch verbesserte Einschlagssimulation im Labor.

Die vorliegende Dissertation handelt von den Einschlagsionisationsprozessen die bei Höchstgeschwindigkeitseinschlägen von Mikropartikeln auf feste Oberflächen auftreten. Mittels einer neu entwickelten Staubteilchen-Quelle für den Heidelberger Staubbeschleuniger wurden Aluminium-, Kohlenstoff-, Natrium-behandelte Kohlenstoff-, Eisen- und Latex-Projektile auf die Mikrometeoriten-Detektoren CDA und CIDA geschossen. Die Projektilmassen überdecken einen Bereich von 10^{-18} bis 10^{-12} kg, die Projektildichten einen Bereich von 1100 bis 7900 kg/m^3 und die Einschlagsgeschwindigkeiten einen Bereich von 2 bis 70 km/s. Die resultierenden Daten zeigen verschiedene Einschlagsionisationsprozesse in Abhängigkeit von der Impaktgeschwindigkeit: für niedrige Geschwindigkeiten ($v < 6$ km/s) dominiert Oberflächen-Ionisation von Target-Verunreinigungen, für hohe Geschwindigkeiten ($v > 18$ km/s) Volumen-Ionisation des Target- und Projektilmaterials. Aufgrund des Energieverbrauchs durch Schmelz- und Verdampfungsprozesse zeigt die Ladungsausbeute im mittleren Geschwindigkeitsbereich einen reduzierten Anstieg. Flugzeitmassenspektroskopie, die mit beiden Instrumenten durchführbar ist, ermöglicht die Untersuchung der chemischen Bestandteile im Einschlagsplasma in Abhängigkeit von Projektiltyp und Einschlagsgeschwindigkeit. Bei niedrigen Geschwindigkeiten dominieren Alkali-Ionen (Na, K) das Massenspektrum. Bei höheren Geschwindigkeiten erscheinen Targetionen (Rh), Projektilionen und Wasserstoff (H). Die Systematiken charakteristischer atomarer und molekularer Ionenspezies in den Massenspektren hilft bei der Ermittelung der chemischen Natur unbekannter Projektile im Weltraum. Ein verbessertes Model für spezifische Ionenausbeuten konnte angegeben werden. Weiterhin wurden viele Ergebnisse, die für die Instrumentkalibration und für das Verständnis von Flugdaten von Bedeutung sind, wie z.B. Gesamtladungsausbeuten, Anstiegszeiten und Empfindlichkeiten gewonnen. Erste Messungen mit Schüssen auf den inneren Wandbereich des Instruments werden gezeigt.

Abstract

New insights in impact ionization and in time-of-flight mass spectroscopy with micrometeoroid detectors by improved impact simulations in the laboratory

The present thesis deals with the impact ionization processes appearing at hypervelocity impacts of microparticles on solid surfaces. With a newly developed dust particle source, applied to the Heidelberg Dust Accelerator facility, aluminium, carbon, sodium contaminated carbon, iron and latex projectiles were shot on the micrometeorite detectors CDA and CIDA. The projectile masses cover a range of 10^{-18} to 10^{-12} kg, the projectile densities a range of 1100 - 7900 kg/m^3 and the impact speeds a range of 2 - 70 km/s. The resulting data show different impact ionization processes depending on the impact speeds: for low speeds ($v < 6$ km/s) dominates surface ionization of target contaminants, for high speeds ($v > 18$ km/s) volume ionization of the target and projectile material is dominating. The charge yield in the intermediate impact speed regime shows a reduced increase

due to energy consumption by melting and vaporization processes. Time-of-flight mass spectroscopy, provided by both instruments, enabled the investigation of the chemical composition of the impact plasma depending on the projectile type and on the impact speed. Alkaline ions (Na, K) dominate the mass spectra at low impact speeds. For higher impact speeds appear target ions (Rh), projectile material related ions and hydrogen ions (H). The systematics of characteristic atomic and molecular ion species in the mass spectra helps to get clues on the chemical nature of unknown projectiles in space. An improved model on specific ion yields can be given. Furthermore a lot of results which are important for the instrument calibration and the understanding of flight data, like global charge yields, rise times and sensitivities were obtained. First measurements on the inner instrument wall region are provided.

Contents

Chapter 1

Introduction

Denn, indem die um die Sonne in parallelen Zirkeln bewegte Elemente, in nicht gar zu großem Unterschiede des Abstandes von der Sonne genommen, durch die Gleichheit der parallelen Bewegung, beinahe in respektiver Ruhe gegeneinander sein: so tut die Anziehung der daselbst befindlichen Elemente von übertreffender spezifischer Attraktion sogleich hier eine beträchtliche Wirkung, die Sammlung der nächsten Partikeln zur Bildung eines Körpers anzufangen, der, nach dem Maße des Anwuchses seines Klumpens, seine Anziehung weiter ausbreitet, und die Elemente aus weitem Umfange zu seiner Zusammensetzung bewegt.

Immanuel Kant, 1755

It was Descartes (1637), who first proposed a nebular hypothesis for the formation of a planetary system around a central star. Kant (1755) postulated the importance of cosmic dust for the planet formation process in such a nebula. His student Laplace developed the first theoretical models of the nebula (LAPLACE, 1796). Nowadays, dusty discs can be observed around young stars (BECKWITH, S.V.W. et al., 1990). They accompany the star formation process and their role in planet formation is obvious (FAHR, H.J. and WILLERDING, E.A., 1998). Cosmic dust is a general term for the smallest solid bodies in space. They can be defined as grains from 0.02 - 200 μm. The steps from condensation of single particles, the agglomeration to fluffy dust particles and the final accretion to planets are still not reliably understood. Comets count as residuals of the formation of our own solar system (WHIPPLE, 1978). Cometary dust should give hints on the formation and development of our solar system.

As well as the dust discs around stars interstellar dust is of interest. It is responsible for the reddening and weakening of star light proportionally to the stars' distance (extinction). Sources of this interstellar dust might be the cool atmospheres of red giant stars, where sooty material condense ("carbon stars"). These particles might be similar to the presolar material, found in meteoritic material (CHOI, B.-G. et al., 1998). Optical spectra of dust discs around stars show silicate material (JÄGER, C. et al., 1994). The measurement of isotopic abundances may allow clues to the origin of the dust grains.

The dust in our own 4.65 billion years old solar system is of secondary nature: produced by collisions of larger particles, by meteorite impacts on planetary and lunar surfaces, and by volcanism. Small particles, called β-meteorites, move outwards in the solar system, pushed by the solar radiation pressure that exceeds the gravitational force for certain grain sizes. Only the comets, which sublime when they enter the inner solar system, may deposit original material from the time of the solar system formation (WHIPPLE, 1978). This interplanetary dust can be recognized as the zodiacal light,

a faint illumination of the sky in the ecliptic plane - earth's orbital plane (and that of most planets) in space. From observing the optical spectrum, the scattering and the polarization, one finds hints on the physical and chemical parameters of the interplanetary dust: grain sizes, temperature, chemical constitution (WEINBERG, J.L. and SPARROW, J.G., 1978). A topical summary on the results of dust research is given by Grün (GRÜN et al., 2001).

When small particles enter the earth's atmosphere with speeds of several kilometers per second, they glow up, and we can observe meteors. Very small particles, like cosmic dust, will not brake so violently. They might withstand the entry phase into the upper atmosphere and remain stable. When one catches these particles with airplanes in the upper atmosphere, they can be analyzed with mineralogical methods (BROWNLEE, 1985). These particles (and also meteorites, that hit the planet's surface) can be separated in different families (GÜRTLER, J. and DORSCHNER, J., 1993). The largest group are the stony meteorites, made of silicates, in analogy to terrestrial rocks. Furthermore there are carbonaceous chondrites (named by the included glass spheres: chondrules) with contents of organic material. They represent very undifferentiated matter, while iron meteorites, stone meteorites and stony-iron meteorites are differentiated by thermal processes.

Unfortunately the dust particles, which enter the atmosphere, lose their information about their origin and flight direction. They might be also contaminated with terrestrial material. These disadvantages are avoided by observing cosmic dust in situ with instruments onboard spacecraft.

As mentioned above, detectors in space make it possible to observe cosmic dust particles in situ, as well as getting information about their velocities and trajectories. The effects of solar wind, magnetic fields and electric charging processes on the particles can be studied. Particles, produced by volcanism and meteorite impacts on surfaces of larger bodies in our solar system, can be investigated directly at their sources. The first attempts of in situ measurements of cosmic dust have been performed with simple detectors on the Pioneer 8 - 11 spacecraft (BERG and RICHARDSON, 1968; HUMES, 1980), followed by instruments on the Heos and Helios missions (DIETZEL et al., 1973). With improved dust detectors onboard the Ulysses and Galileo spacecraft impact generated dust clouds around the galilean satellites and dust streams in the Jovian system, produced by volcanism on Jupiter's moon Io have been discovered (GRÜN, E. et al., 1996; GRÜN, E. et al., 1997; GRAPS et al., 2000).

The dust detectors PIA onboard the Giotto spacecraft as well as PUMA1 and PUMA2 (Vega1, Vega2), carrying integrated time-of-flight mass spectrometers, encountered comet Halley during its last perihelion 1986, and found silicate and organic material in its coma and tail (KISSEL et al., 1986a; KISSEL et al., 1986b; KISSEL and KRÜGER, 1987). So called CHON-particles consist of light elements (H, C, N, O), or represent the mantle fraction of core-mantle-particles (GREENBERG and HONG, 1974). The element abundances in cometary dust are very similar to the chemical constitution of C1-meteorites, which represent the most undifferentiated matter in our solar system.

At present, the "Cosmic Dust Analyzer" (CDA) onboard the Cassini spacecraft is on the way to Saturn (SRAMA and GRÜN, 1997). CDA combines the advantage of a large detector area, like the dust detectors onboard Galileo and Ulysses, with a simple time-of-flight mass spectrometer. The instrument already performed measurements during the interplanetary cruise. The Jupiter-flyby opened the unique opportunity of combined, simultaneous measurements of the Jovian dust with dust detectors on two spacecraft, Galileo and Cassini (KRÜGER et al., 2001).

Measurements with the dust detector on the Ulysses spacecraft led to the discovery of an interstellar dust stream, that enters our solar system (GRÜN, E. et al., 1994). How can this dust be separated from interplanetary dust by its chemical composition and its grain size distribution? New generation dust instruments with the combination of a large target area and an integrated time-of-flight mass spectrometer (e.g. Cosmic DUNE) with high mass resolution shall help to answer these questions.

Until now, the physical process during a hypervelocity impact (several km/s) of a projectile on a target with supersonic speed is still not fully understood. In this velocity region, the impact speed is faster than the wave propagation inside the target and projectile (MATTMÜLLER, 1994). The impact process is described with a Hugoniot-function (WONDRASCHEK, 1997; REBER, 1997). It is assumed, that a large fraction of the impact energy is used for plastic deformation of the target and projectile. Directly after the contact between projectile and target, a shock wave propagates through the materials, and starts evaporation and ionization processes (DRAPATZ, S. and MICHEL, K.W., 1974). At highest impact speeds ($v > 15$ km/s) volume ionization of the material is the dominating ionization process, while at lower speeds surface ionization dominates. The plasma states are described by non-thermal equilibrium (HORNUNG, K. and KISSEL, J., 1994; HORNUNG, K. et al., 1996; HORNUNG, K. and DRAPATZ, S., 1981).

Dust detectors for in situ detection of micrometeoroids have to be calibrated on ground before they are launched into space. The method of simulating hypervelocity micrometeorite impacts is to accelerate micrometer sized grains to speeds as expected in space and let them impact on the detectors' target areas. Such experiments are performed at the Heidelberg Dust Accelerator facility where electrically charged particles are accelerated by a potential difference of 2 MV up to speeds of 80 km/s.

This thesis deals with the ion formation process during hypervelocity microparticle impacts on solid metal surfaces and with the generation of time-of-fight mass spectra of projectiles that hit a metal target. To obtain data from a large variety of projectile materials a newly developed dust source has been applied to the Heidelberg Dust Accelerator, both described in Chapter 2. Besides iron projectiles aluminium and carbon particles were used. With the electrically conducting latex particles, organic projectiles were successfully accelerated for the first time at the Heidelberg Dust accelerator. In Chapter 3 are explained the two different dust detector instruments, the CDA flight spare unit and the CIDA engineering model, that were used for the measurements. Additionally their setups are described. The presentation of experimental results in Chapter 4 is focussed on the charge yields and the time-of-flight mass spectra. It was found that the charge yields from impact ionization processes are characterized by three impact speed regimes. In the later discussion (Chapter 5) this behavior is successfully compared with related studies of the impact ionization process. It turns out that the global charge yields in different impact speed regimes are consistent with present theories of the impact ionization. The results are summarized in Chapter 6. Additionally, an outlook to possible future aspects of hypervelocity impact experiments is given. The large appendix of this work is dedicated to the successfully application of the new dust source at the Heidelberg Dust Accelerator (Appendix A) and the importance of the results for the calibration of the CDA instrument (Appendix D). Appendix B and C give a detailed overview of the instrument setups, the data processing and the measurements. The most important physical constants that are used in this work are summarized in Appendix E.

The results in this work are a further chapter to complete the understanding of the physical processes that appear at hypervelocity impacts. The opportunity of achieving time-of-flight mass spectra from the impact plasma allows the determination of chemical constituents in the plasma depending on the projectile composition and on the impact speed. The observations of alkali elements at low impact speeds and projectile as well as target material related ions at high impact speeds confirm and extend earlier studies and better characterize impact ionization models. New ion yield functions have been developed. The observation of characteristic molecular ion signatures in the time-of-flight mass spectra depending on the projectile material give us a rough clue on the chemical nature of any projectile that hit the Cosmic Dust Analyzer with impact speeds between 2 and several 10 km/s.

Chapter 2

The Heidelberg Dust Accelerator facility

This chapter gives an overview of the Heidelberg Dust Accelerator facility. The working principle of the electrostatic accelerator and the newly developed dust source are explained in the following section (Section 2.1). The new dust source allows the use of various projectile materials which were used for impact experiments in this thesis. The different materials are described in Section 2.2 in detail, including their physical properties and their possible astrophysical relevance in space. Since this is the first work which uses the new dust source, empirical operation parameters (voltage settings, speed and mass ranges of projectiles) and a detailed evaluation of the dust source performance is given in Appendix A.

2.1 The Heidelberg Dust Accelerator

The development of the Heidelberg Dust Accelerator was done by Friichtenicht (1962). A Van-de-Graaf belt generator produces an acceleration voltage of 2 MV. This potential drops to ground (0 V) over a cascade of equipotential rings. This causes an electric field gradient along the accelerators' beam line. To avoid sparkling, the voltage generation proceeds in a pressure tank, filled with protection gas ($SF_6 + N_2$, 16 bar). This setup is shown in Figure 2.1. The beam line itself is evacuated to a vacuum of $10^{-4} - 10^{-5}$ Pa ($10^{-6} - 10^{-7}$ mbar) with turbo molecular pumps, cryo-pumps and one ion-getter-pump. This system makes it possible to have a "clean" vacuum without residuals of oil vapor, like for example from oil diffusion pumps. A clean vacuum is necessary for a reliable mass spectroscopy. Otherwise, these residuals might be seen as organic molecules in the mass spectra. Mass spectra, obtained from organic projectile materials, like the latex samples in this work, would be disturbed by the oil contamination and are not reliable anymore.

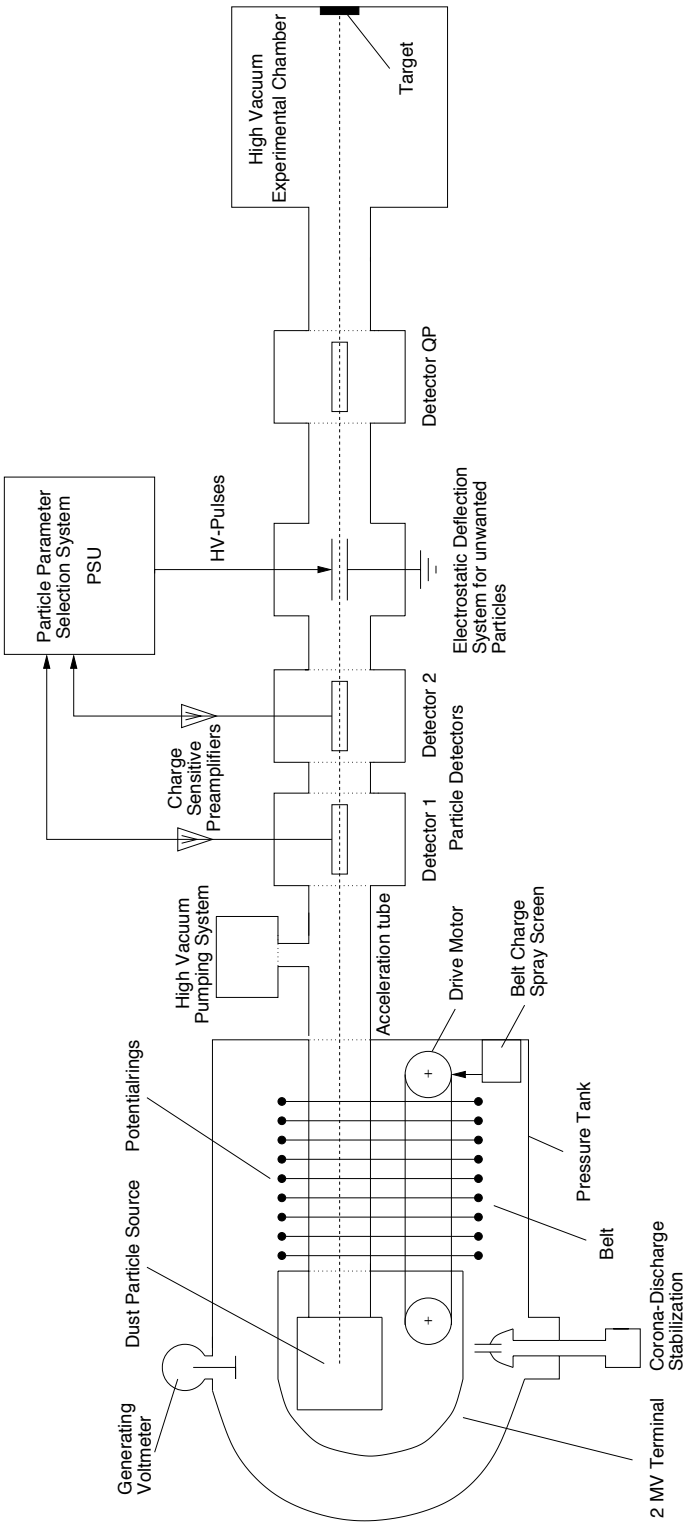

Figure 2.1: Sketch of the 2 MV dust accelerator with particle selection unit and experiment chamber.

2.1.1 The new dust particle source

The heart of the accelerator is the dust particle source, invented by Shelton (1960). The dust source is directly connected to the beam line tube at the 2 MV terminal of the accelerator. All measurements in this work were performed with a newly developed dust source (except for iron projectiles, where the former dust source was used) (STÜBIG et al., 2001). A powder of electrically conducting particles resides in a cylindrical reservoir of 10 mm diameter and 25 mm length in vacuum (cf. Figure 2.2). In the reservoirs' cylinder axis is located a 1 mm thick tungsten needle, sharpened to a few micrometer at its tip. Both the reservoir and the needle are connected to high voltage potential of 15 - 25 kV (with respect to the 2 MV of the Van-de-Graaf generator voltage). While the potential of the needle remains fix, the potential of the reservoir is frequently reduced with amplitudes of 10 - 15 kV (10 ms rectangular pulses at 25 Hz repetition rate, both values are adjustable). The time varying electric field inside the reservoir induces a charge on the dust particles. Due to Coulomb repulsion force, the particles start to swirl around. If a particle hits the thin tip of the tungsten needle, it will be charged by a field emission current from the tip to the particle. Now the particle has a surface potential between 100 and 1000 V, and a surface field strength of $10^8 - 10^9 \mathrm{V/m}$. The dust source has an extraction hole in 3 mm distance from the tip of the needle. Outside the reservoir is located a grounded (ground means the 2 MV of the accelerators' high voltage terminal) extraction plate. The field between this plate and the needle potential extract the particle out of the reservoir. Collimation plates and focussing electrodes lead the particle into the 2 MV acceleration section. More details of operational parameters and speed mass distributions of projectiles, accelerated with the new dust source can be found in Appendix A.

2.1.2 Particle selection

Unique at the Heidelberg Dust Accelerator is the so called Particle Selection Unit (PSU, cf. Figure 2.1). It allows the experimenter to select ranges for the particle speed and the particle charge manually or via personal computer (cf. (RUDOLPH, 1966)). The final speed v of the particle is given by energy conservation:

$$\begin{aligned} \frac{1}{2}mv^2 &= qU_B \\ \Longrightarrow \qquad v &= \sqrt{\frac{2qU_B}{m}}\,, \end{aligned} \tag{2.1}$$

where q is the particles' charge and m its mass. U_B is the acceleration voltage of 2 MV (in the most experiments). In this way, a certain combination of charge and speed ranges allows also a mass selection of the particles.

If a particle left the dust source and passed the acceleration section, its speed and charge are measured with influence tube detectors, connected to charge sensitive amplifiers. The q- and v- values are passed to the PSU electronics, which compares the measured values with the range settings. If the values match the settings, a 4 kV-voltage on a deflection capacitor, which usually deflects all particles from the straight beam line, is switched to ground potential and the particle can pass the whole beam line to the experiment chamber. The PSU allows to shoot particles in a continuous mode as well as in a single particle mode.

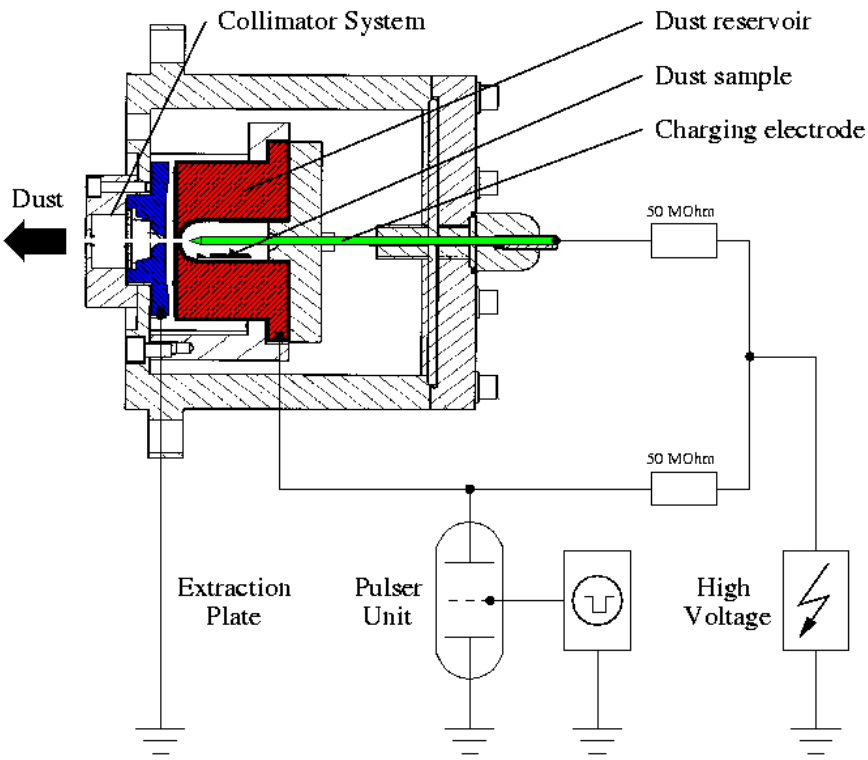

Figure 2.2: Function principle of the dust source. This vertical Section shows how the dust sample (black) resides inside the reservoir (red). A time varying voltage swirls the particles up, a charging needle(green) gives the final charge to the particles. A grounded extraction plate (blue) pulls the charged particles out of the reservoir.

2.2 Projectile materials

The new dust particle source at the Heidelberg Dust Accelerator allows an efficient use of different projectile materials. But the restriction on particles, that are electrically conducting still remains. The final speed after acceleration is proportional to the square root of the charge/mass-ratio $\frac{q}{m}$ (cf. Eq. 2.1). The maximum grain size, that can be extracted from the dust source, is empirically measured to 3μm for aluminium projectiles. In the following subsections the projectile materials, that have been used in this work, are listed in alphabetical order. Additionally to the chemical and physical properties of the materials, the mineralogical background, why this specific material has been used, is given.

2.2.1 Aluminium, Al

Aluminium is an easily deformable metal with a low density of 2700 $\mathrm{kg/m^3}$. Since it can easily be charged, high charge/mass-ratios $\frac{q}{m}$ can be achieved, leading to high projectile speeds. Despite the fact that metallic aluminium is not expected in meteoritic material, it belongs to the most abundant elements in the solarsystem and was found in many meteorites (BEATTY, J.K. et al., 1999a). Aluminium is also an important contributor to feldspar minerals that appear in planetary crusts (60

Vol.%) (MATTHES, 1996). The exceptionally low ionization potentials of aluminium (cf. Table 2.1) might allow to obtain multiple ionized ions, and therefore to get a deeper insight into the ionization process from the hypervelocity impact. The aluminium samples used in this work were obtained by Dr. Groebl and Dr. Besold 1976 from Eckart-Werke, Fürth, Germany. A picture of the sample and it's grain size distribution is given in Figure 2.3. It appears an obvious large discrepancy between the grain size distribution of the sample and the size distribution of the accelerated particles. For all other samples in this work the output of the dust source reflects very well the grain size distributions that were obtained by electron microscopic analysis. A new grain size analysis of the sample by Thomas Stephan, Universität Münster, confirmed the discrepancy. The sample was filled into a glass container in 1977 by Pailer together with Argon as protection gas.

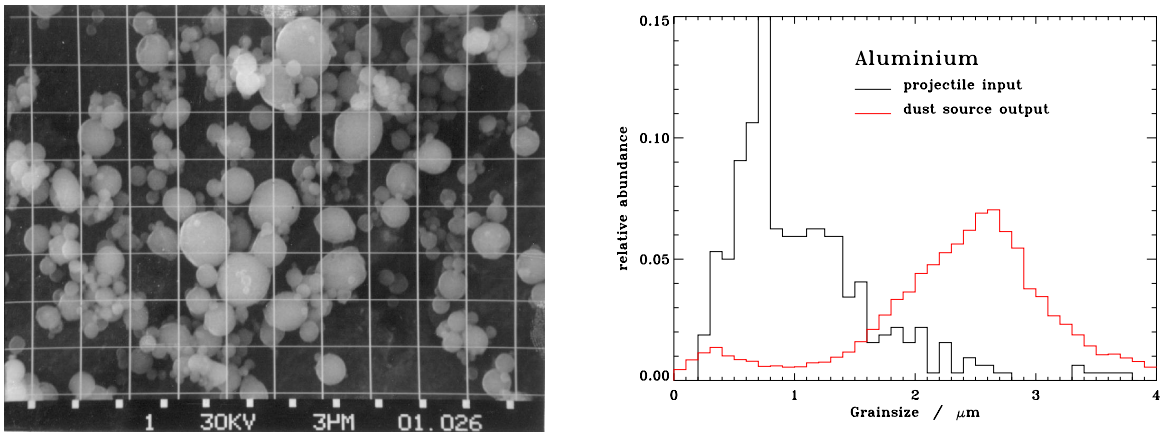

Figure 2.3: The left figure shows a SEM-picture of the used aluminium particles (sample Al76.027.006). The right figure reflects the grain size distribution of 320 particles on the picture (black histogram). The red histogram shows the grain size distribution of 20000 aluminium projectiles, measured from the PSU at the Heidelberg Dust Accelerator.

2.2.2 Carbon, C

Apart from hydrogen and helium, carbon is one of the most abundant elements in the universe (ANDERS, E. and GREVESSE, N., 1989). It is the main part of organic molecules detected in molecular hydrogen clouds (HII-regions) in the interstellar medium (cf. (UNSÖLD, A. and BASCHEK, B., 1991)). Carbonaceous chondrites and comets (their dark surfaces and optical spectra allow clues to their high carbon content) are regarded as residuals of the primordial matter, from which our own solar system formed (BEATTY, J.K. et al., 1999b). Furthermore carbon is produced as soot in the cool atmospheres of giant red stars, so carbon/graphite should be expected in interstellar meteoroids (FRENKLACH et al., 1989). On planetary surfaces, carbonate rocks indicate the (former) occurrence of liquid water (BEATTY, J.K. et al., 1999c; BEATTY, J.K. et al., 1999a). Volcanic activity may enrich planetary atmospheres with carbon oxides, and carbonatite lava may cover large areas on planetary surfaces (HOFFMAN, 1999; NORTON and PINKERTON, 1992; FEGLEY and ZOLOTOV, 2000). Carbon has a density of 2200 kg/m^3 and high ionization potentials, given in Table 2.1. For this work samples of the lot 70.012.002 were taken. They were acquired in 1970 from an unknown producer. Figure 2.4 gives an impression of the mostly sub-micrometer sized particles. The particles were preserved in a

glass container under Argon atmosphere since 1977 thanks to Pailer.

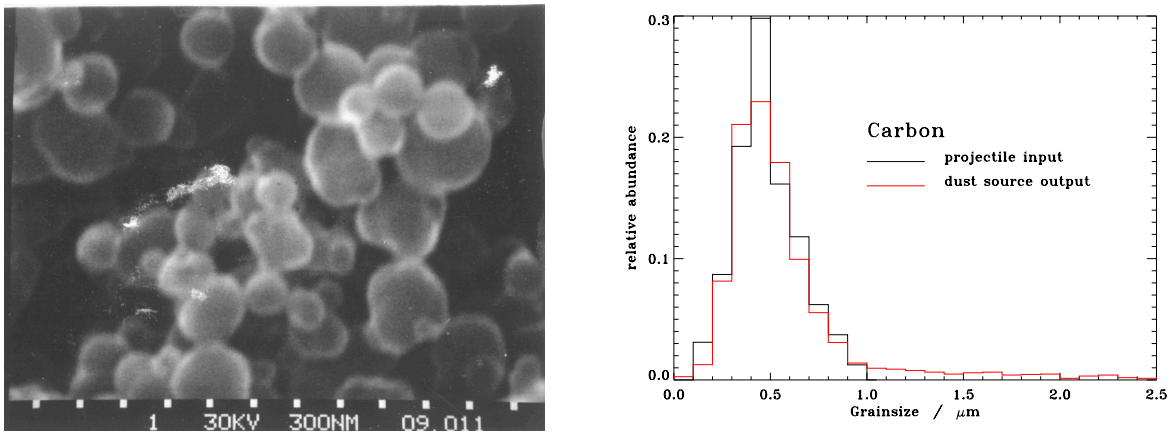

Figure 2.4: The left figure shows a SEM-picture of the used carbon particles (sample C70.012.002). The right figure reflects the grain size distribution of 161 carbon particles on another picture (black histogram). The red histogram shows the grain size distribution of 3960 carbon projectiles, measured from the PSU at the Heidelberg Dust Accelerator.

2.2.3 Sodium contaminated carbon, C-Na

Sodium, as well as potassium, is well known as contaminant on the target surface of impact ionization dust detectors. Due to their chemical nature, alkaline elements (Alk) like sodium and potassium have very low ionization potentials for the Alk^{+}-ion (cf. Table 2.1). Thus, alkaline elements usually produce prominent signatures in time-of-flight mass spectra (DALMANN et al., 1977). Io, the innermost of Jupiter's Galilean satellites, is surrounded by a sodium cloud that might contaminate the dust particles, which are ejected from Io's volcanic activity (TRAFTON et al., 1974). To see, if the time-of-flight mass spectra from sodium-contaminated projectiles can be distinguished from uncontaminated projectiles, a sample of "sodium coated" carbon particles was produced. For this, a sample of the above mentioned carbon particles and a cube of pure sodium were put together in a closed glass container and kept two weeks at room temperature ($\approx 20\,^{\circ}$C). The vapor pressure of sodium at room temperature is in the order of 10^{-8} Pa (10^{-10} mbar) (GMELIN-INSTITUT FÜR ANORGANISCHE CHEMIE, 1965). This should prevent a coating but lead to a contamination of the carbon powder. Unfortunately, an estimation of the amount of adsorbed sodium on the surfaces of the carbon particles is not possible. The grain size distribution of the accelerated particles is equal to that of Figure 2.4.

2.2.4 Iron, Fe

Iron is the easiest material to shoot with at the dust accelerator. Since it works also well with the former dust source, it has been used as reference material for the calibration of all previous dust detectors. Thus, iron has also been used in this study, and is additionally used as reference material for the wall shots. With 7900 kg/m^3, iron is the projectile material with the highest density from the given selection. Due to its high conductivity, iron is easy to charge, and despite the high density, good charge/mass-ratios are achievable. The most important ionization potentials of iron are 7.87 eV for

Fe^{+} and 16.18 eV for Fe^{2+} (cf. Table 2.1). The iron sample is a mixture of 67 Vol.% iron particles *F*e 70.056.714 produced 1970 by BASF, Ludwigshafen, and of 33 Vol.% iron powder consisting of 20 nm small spheres produced by Goodfellow, Bad Nauheim. Due to the achievable high charge/mass-ratio, the latter particles should provide very fast projectiles with impact speeds of several ten km/s. The BASF particles were filled in glass containers with Argon atmosphere by Pailer in 1977, the Goodfellow sample still remains in its original tin. The samples were produced as carbonyl-iron ($Fe(CO)_5$) with a purity > 99 %. Figure 2.5 shows a picture of the BASF iron sample and its grain size distribution. The Goodfellow sample (not shown here) consists of 20 nm monospherical particles that tend to form clusters with sizes up to 100 nm. From the mineralogical point of view, the iron projectiles represent the class of iron-nickel-meteorites. The material of these highly differentiated meteorites must have undergone thermal processes in the interior of large planet-like bodies, before it was released into space by a deep impact event on the parent body. For example, iron-nickel-alloys are expected in the earth's core. When corroding iron-nickel-meteorites with acid, they show the so called Widmanstätten figures, pattern from a long-term recrystallization process, which manifest their extraterrestrial origin.

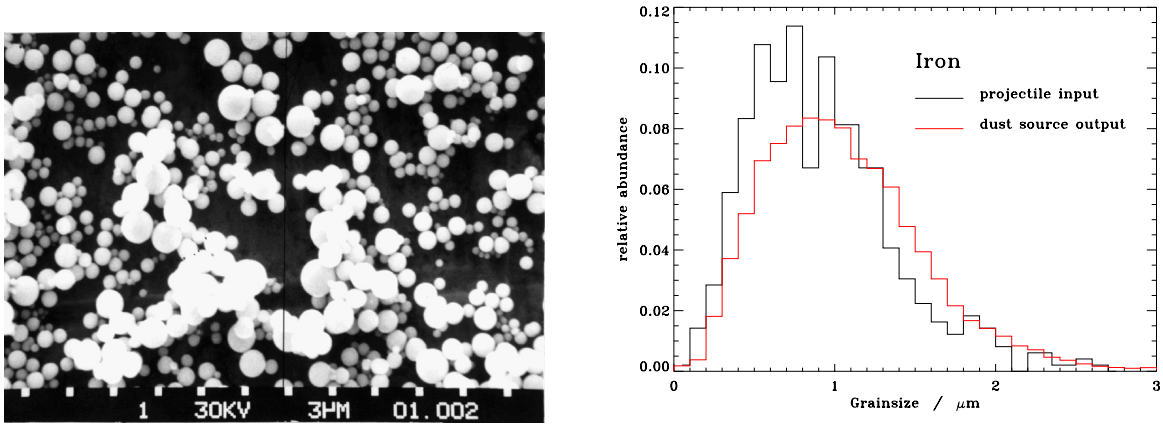

Figure 2.5: The left figure shows a SEM-picture of the used BASF iron particles (sample Fe70.056.714). The right figure reflects the grain size distribution of 492 iron particles on the picture (black histogram). The red histogram shows the grain size distribution of 20080 iron projectiles, including the Goodfellow-sample. These latter data was measured from the PSU at the Heidelberg Dust Accelerator.

2.2.5 Polyaniline coated polystyrene latex, PANi-PS-latex

As mentioned in the introduction and in Section 2.2.2, organic matter can be found in cometary and meteoritic material as well as in the interstellar medium. In this work for the first time, organic projectiles have been used for the calibration of impact ionization dust detectors. The latex particles are a kind of core-shell-particles, produced by S. Armes and his group at the University of Sussex. Electrically non-conductive polystyrene cores have been coated with thin layers of conductive polyaniline by polymerization in an aqueous solution (BARTHET, CHR. et al., 1998a; BARTHET, CHR. et al., 1998b). To obtain a regular layer thickness, a nearly mono-disperse sample of particles (shown in Figure 2.7) have been used for coating. Polystyrene latex is a chain of aromatic molecules, con-

sisting of benzol-rings C_6H_6 with one H replaced by a C_2H_3-group as shown in Figure 2.6 a). The polyaniline-coating are chains of C_6H_3-groups, connected via NH-bridges as drawn in Figure 2.6 b).

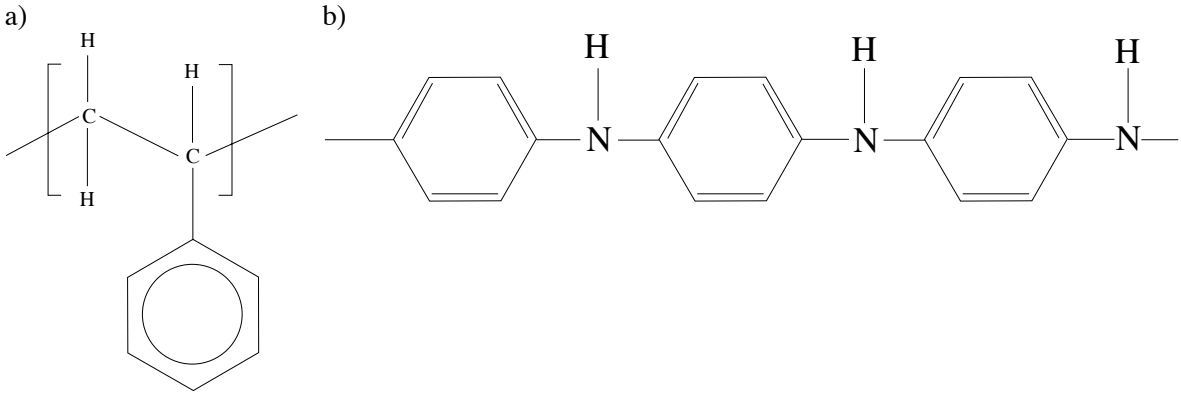

Figure 2.6: The left hand figure a) shows the chemical structure of polystyrene, which is the core material in all latex samples. The sketch b) on the right shows a chain of polyaniline molecules, used as coating material.

The sample in this study was kindly provided by M. Burchell, who first reported successful acceleration of latex at Canterbury, UK with a particle accelerator, similar to that at Heidelberg (BURCHELL, M.J. et al., 1999). The particles have $0.75 \pm 0.04\,\mu$m diameter, including 10 nm polyaniline coating. The mean density of the particles is 1100 kg/m^3, and therefore the lowest density of all projectile materials in the present study. Thus, latex projectiles represent the density of water ice (1000 kg/m^3), which is very abundant in space. For "fluffy" particles, loose conglomerates of small grains, densities even below this value are expected (BROWNLEE, 1985). The core-shell structure (cf. Figure 2.8 b)) may additionally represent the core-mantle particle type as postulated by Greenberg (1974) for interstellar dust: a mineral core, surrounded by organic molecules and ices.

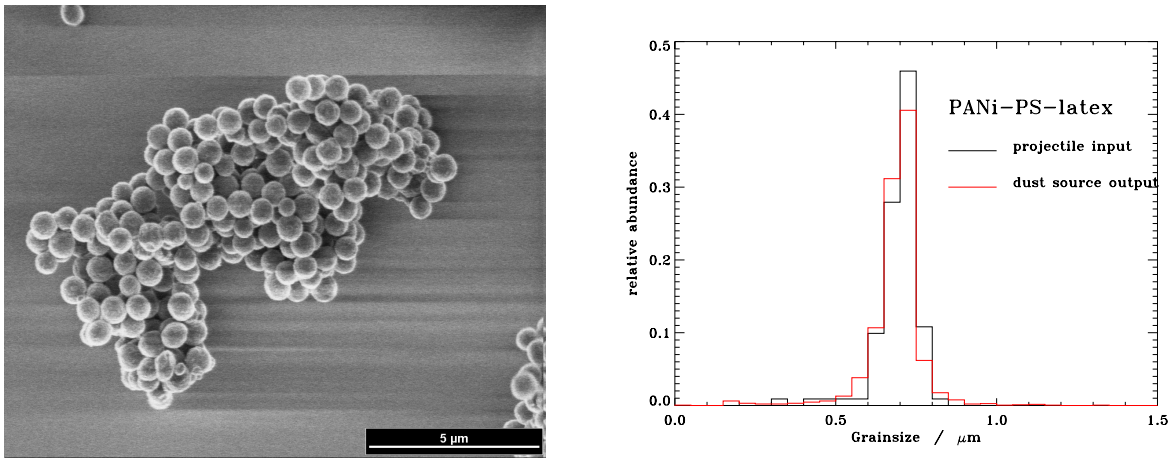

Figure 2.7: The left figure shows a SEM-picture of the used PANi-PS-latex particles. The right figure reflects the grain size distribution of 111 particles on the picture (black histogram). The red histogram shows the grain size distribution of 2670 projectiles, measured from the PSU at the Heidelberg Dust Accelerator.

2.2.6 Polypyrrole coated polystyrene latex, PPY-PS-latex

Like the polyaniline coated polystyrene latex, this sample is also produced by S. Armes, and provided by M. Burchell. The material density is again $1100\mathrm{kg/m^3}$. The grain size distribution is also monodisperse, but larger in size: $1.58 \pm 0.13\mu$m. The grain size distribution in Figure 2.9 shows a small portion of particles with grain sizes even below 1 μm. The particles are coated with a 14 nm layer of polypyrrole (LASCELLES, S.F and ARMES, S.P., 1997; LASCELLES, S.F et al., 1997). The polypyrrole molecule is shown in Figure 2.8 a). Figure 2.8 b) shows the core-shell structure of a coated particle. The structure of the coating is like a golf ball surface as can be seen in Figure 2.9.

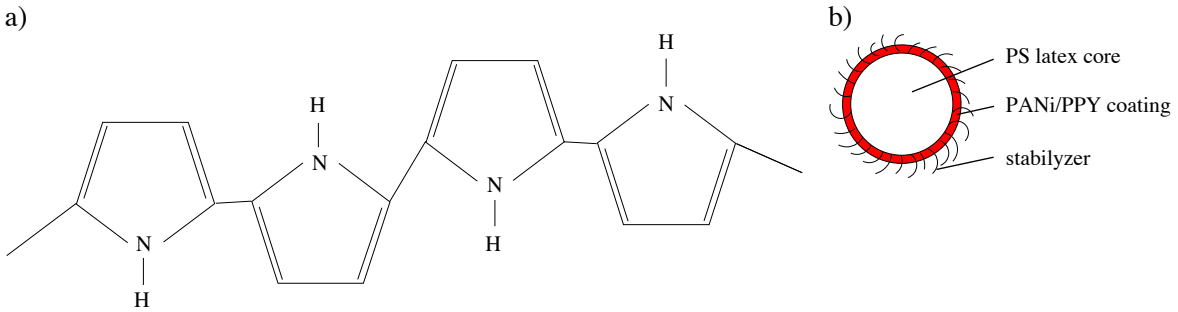

Figure 2.8: Figure a) shows the molecular structure of polypyrrole. The general core-shell character of the coated polystyrene latexes is shown in the figure b) on the right hand.

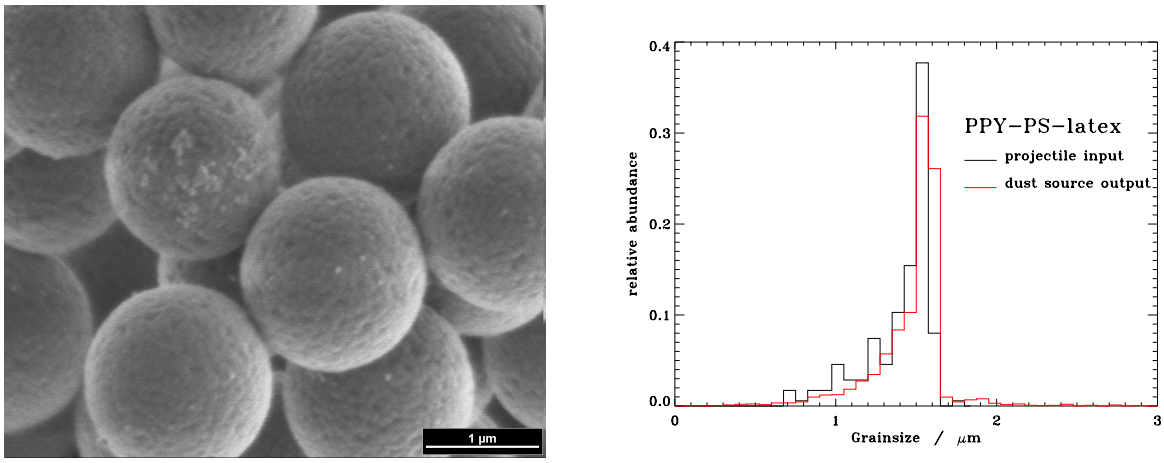

Figure 2.9: The left figure shows a SEM-picture of the used PPY-PS-latex particles. The right figure reflects the grain size distribution of 175 particles on another picture (black histogram). The red histogram shows the grain size distribution of 3310 projectiles, measured from the PSU at the Heidelberg Dust Accelerator.

2.2.7 Other materials

The projectile materials mentioned above cover a wide range of astrophysically relevant minerals. Nevertheless, a very important group is missing: silicates. In an earlier study by Göller and Grün (1989) was reported the acceleration of zinc coated silicon-dioxide particles (SiO_2). Unfortunately,

the acceleration of gold coated SiO_2-spheres, provided by B. Clark, USA in the 1970s failed at the dust accelerator with both the new dust source and the previous dust source. Own coating techniques, tested at silicon-dioxide spheres (SiO_2) and natural silicates, couldn't handle the problem of particle agglomeration: the micrometer- and submicrometer-sized particles clump together and form agglomerates of several ten micrometers (STÜBIG, 1999). Kuhn (2002b) succeeded to get silicon signatures in the time-of-flight mass spectra from accelerating polypyrrole particles with 80 Vol.% silicon (Si) incorporated into the matrix.

Material			Ionization potentials / eV			electron configuration
			X^+	X^{2+}	X^{3+}	
1	H	Hydrogen	13.60	-	-	$1s^1$
12	C	Carbon	11.26	24.38	47.89	(He)$2s^2 2p^2$
14	N	Nitrogen	14.53	29.61	47.45	(He)$2s^2 2p^3$
16	O	Oxygen	13.62	35.12	54.93	(He)$2s^2 2p^4$
23	Na	Sodium	5.14	47.29	71.64	(Ne)$3s^1$
27	Al	Aluminium	5.99	18.83	28.45	(Ne)$3s^2 3p^1$
28	Si	Silicon	8.15	16.35	33.49	(Ne)$3s^2 3p^2$
39	K	Potassium	4.34	31.63	45.72	(Ar)$4s^1$
56	Fe	Iron	7.87	16.18	30.65	(Ar)$3d^6 4s^2$
103	Rh	Rhodium	7.46	18.08	31.06	(Kr)$4d^8 5s^1$
	C_xH_y	Hydrocarbons	8 - 12			

Table 2.1: Overview of the ionization potentials of different projectile-, contamination- and target-materials. Additionally are given the electron shell configurations of all materials. The data were taken from Stöcker (1994).

Chapter 3

Experimental setups

The following Section 3.1 explains the function principle and technical properties of the Cosmic Dust Analyzer instrument (CDA) including a very brief overview of the Cassini-Huygens mission to Saturn. Section 3.2 is dedicated to the time-of-flight mass spectrometer Cometary and Interstellar Dust Analyzer (CIDA). CIDA has a smaller target area than CDA. But since CIDA has a reflector unit for the ions in its drift tube, the obtained time-of-flight mass spectra have a first order energy correction, and therefore a much higher mass resolution. Section 3.3 of this chapter describes roughly the setups for the experiments that have been performed at the Heidelberg Dust Accelerator facility for this thesis. More details on the general instrument settings, the vacuum pumping process, the impact locations and on data acquisition and evaluation are given in Appendix B.

3.1 The micrometeoroid detector CDA

The Cosmic Dust Analyzer (CDA) was developed for the investigation of dust in the vicinity of Saturn (SRAMA and GRÜN, 1997; SRAMA et al., 2002). During the 7 year long cruise to Saturn, CDA is used for the measurement of interplanetary and interstellar dust particles and streams. The dimensions of CDA are 0.7 x 0.45 x 0.8 m^3, the total weight is 17.2 kg. CDA can be rotated on a turntable within an angle of 270 °. The internal operating voltage is 30 V, the maximum power consumption 12 W. CDA is designed to withstand a radiation energy dose of 1000 Gy (100 krad). A detailed instrument description and first instrument calibration is given by Srama (2000).

The function principle of CDA is shown in Figure 3.1. Due to solar wind and solar UV interactions (photo effect), it is expected that dust particles in space carry surface charges (DRAINE, B.T. and SALPETER, E.E., 1979). For the solar system equilibrium potentials of several Volts are assumed, depending on local conditions. This surface charge can be detected with a pair of inclined grids, connected to a charge sensitive amplifier (channel QP). To avoid noise and disturbances, the grids are shielded by grounded grids. Each grid has a transmission of 95 %. To influence a measurable signal on the grids, a minimum charge of 10^{-15}C is necessary. The particles' charges, impact speeds and entrance angles can be acquired from the rise times and amplitudes of the trapezoid-like charge signals. This allows to detect dust streams in the solar system.

After passing the grids, the particle, depending on its trajectory, will hit a central rhodium target of 160 mm diameter (Field of View: 28 °), a surrounding gold target of 410 mm diameter (Field of View: 45 °) or the instrument wall. In the central region of the instrument, 230 mm in front of the rhodium target, resides a secondary electron multiplier and three grids (the two outer grids as shielding), which measure the charge signal of the ejected ions from the impact plasma. A bias voltage of -350 V on the

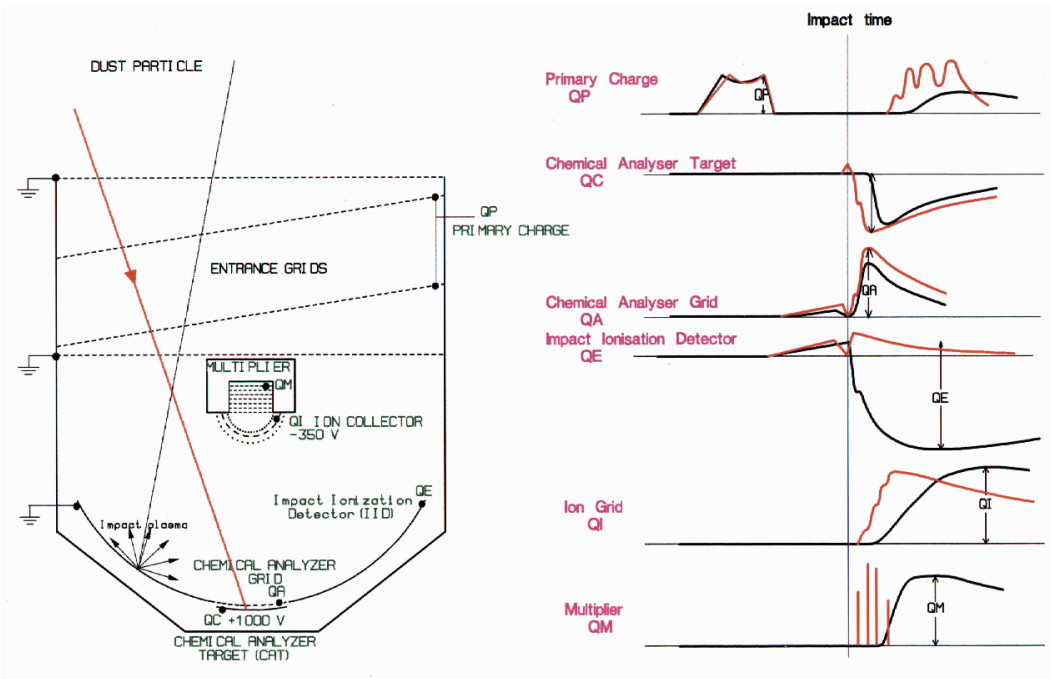

Figure 3.1: Schematic view of CDA. The trajectories of dust particles, that hit the Chemical Analyzer Target (red) and the Impact Ionization Detector (black), are shown. The right hand figure shows the corresponding signals on the sensitive channels of CDA.

grids is focussing the ions towards the multiplier.

The grounded gold target is a simple impact ionization detector (IID). The -350 V of the ion grids separate the impact plasma. The IID measures the remaining electron charge and the rise time of the charge signal (channel QT, QE). Laboratory calibrations of the impact signals allow clues on the impact speed and the mass of the projectile.

The rhodium target functions as target of a simple time-of-flight mass spectrometer ("Chemical Analyzer Target", CAT). The CAT is biased with +1000 V. 3 mm in front of the CAT is located a grounded grid (68 % transmission). This strong electric field ($\approx$ 330 kV/m) divides the plasma nearly totally in electrons and positive ions. The ions are accelerated towards the multiplier, while the electron charge signal and it's rise time are measured at the CAT (channel QC). The -350 V of the ion grids in front of the multiplier focus the ions. The total ion charge, that reaches the multiplier, is measured at the middle grid (channel QI). Ions, that hit the first dynode of the multiplier, release electrons from the dynode surface. A cascade of in total 10 dynodes, and a total potential difference of $\approx$ 3 kV between the first and the last dynode, lead to secondary electron emission. The output signal of the multiplier (channel QM) depends on the arrival time of the ions, while the signal amplification depends on the dynode voltage. The differences of the ion arrival times at the multiplier are related to their charge and mass. The energy conservation in Eq. 3.1 describes the correlation between the ion mass m_{ion}, ion charge q_{ion} (usually $q_{ion} = 1.6 \cdot 10^{-19}$ C), and the flight time t. Note, that this equation is simplified for acceleration directly at the target (which is nearly realized by the grounded grid in 3 mm distance from the CAT).

$$
\begin{aligned}
q_{ion} \cdot U &= \frac{1}{2} m_{Ion} v_{ion}^2 \\
\Longrightarrow \; m_{ion} &= \frac{2 q_{ion} U}{d^2} \cdot t^2. \qquad (3.1)
\end{aligned}
$$

The parameters U and d are the biased target voltage and the distance between the target and the multiplier. This correlation gives the instrument the name time-of-flight mass spectrometer.

The instrument has a dead-time of 1 s. Event rates higher than 1 particle/s can be measured with the High Rate Detector (HRD), that is placed below the entrance grids of CDA. Fast particles penetrate a system of thin foils. The foils form a simple plate capacitor. The damage caused by the penetrating particle leads to a measurable change of the capacity. In this way, event rates up to 10^4 particles/s can be detected.

Further information on the CDA instrument and on recent results can be found in (SRAMA et al., 2002) and on the web at *http://www.mpi-hd.mpg.de/dustgroup/*. A detailed description of the Cassini-Huygens mission is given at *http://www.jpl.nasa.gov/cassini/*.

3.2 The micrometeoroid detector CIDA

The Cometary and Interstellar Dust Analyzer (CIDA) is a dust particle detector for in situ measurements, that makes it possible to achieve high resolution time-of-flight mass spectra from micrometeorite impacts. CIDA has only a silver target of 100 mm diameter, separated in several sections. In analogy to the Chemical Analyzer Target of CDA (cf. Section 3.1), the target, a bias voltage on the target itself and a grounded grid 3 mm in front of the target, form the acceleration section of a time-of-flight mass spectrometer. In contrast to CDA, the target voltage of CIDA can be switched to negative polarity. This allows the measurement of electrons and negatively charged ions.

CIDAs' ion drift zone is more complicated than that of CDA. A reflector unit with an electric counter-field brakes the ions, which were accelerated at the target, and reflects them like a mirror. This configuration is shown in Figure 3.2. Fast ions will penetrate deeper into the counter-field than slow ions. In this way, the energy distribution of the plasma ions is corrected in first order. The reflected ions are registered at a microchannel plate, which is more sensitive than a multiplier as used for CDA.

Since CIDA has no further detector area like CDAs' IID, the disadvantage of CIDA, compared to CDA, is the small target area of 80 cm^2.

CIDA has been developed for the investigation of cometary and interstellar dust (BROWNLEE et al., 1997; BROWNLEE et al., 2000). The instrument is part of the Stardust spacecraft, on a cometary nucleus flyby at comet Wild 2. Additional information on the Stardust mission, the spacecraft and CIDA itself are available at *http://stardust/jpl.nasa.gov/*.

3.3 Instrument setup

For the experiments, the CDA flight spare and the CIDA engineering model were installed in a large vacuum chamber at the end of the dust accelerator's beam line (1.4 m free diameter due to the cooling and heating systems inside the chamber), approximately 8 m behind the 2 MV terminal (cf. Figure 2.1). A movable table inside the chamber allows the movement of experiments, perpendicular to the

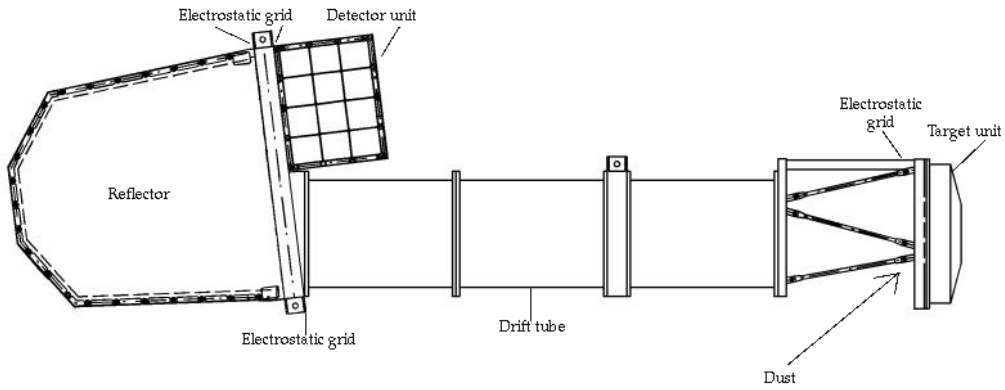

Figure 3.2: Cut through the CIDA instrument. The target area is on the right hand, the reflector unit for energy correction is shown on the left.

beam line in y-direction with a total range of 300 - 400 mm. The table can be moved manually by external steerers. Additional steerers allow movements in other degrees of freedom, e.g. z-direction or rotation. The chamber itself is fitted with electric heating coils and a cooling system (liquid nitrogen). Thus, the inner temperature of the chamber can be regulated between +80 and -100°C.

3.3.1 Mounting of CDA

Figure 3.3 shows the instrument inside the vacuum chamber, mounted on a turntable for shots on the central CAT-target. For shots on the outer CAT region, the IID-target and the instrument wall has been build an extra fixture that allows movement in y-direction. The setup and the various shoot positions are explained in detail in Appendix B.1.

3.3.2 Mounting of CIDA

The large dimensions of CIDA don't allow large movements with the table inside the chamber. For the measurements in this work, CIDA was installed on a self-made fixture in such a way, that the particle beam hit the central Section of the silver target as shown in Figure 3.4. The inclination angle of the beam was nearly 0 ° in y- and z-direction.

For the further measurements with the instruments, the experiment chamber has to be evacuated to high vacuum. The pumping process is explained in Appendix B.1.4.

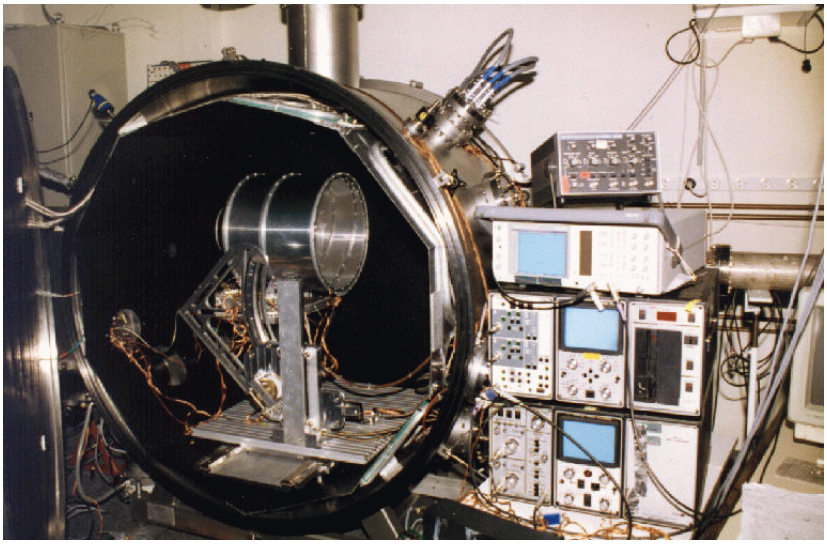

Figure 3.3: Vacuum chamber with CDA (here shown: engineering model), mounted on a turntable for shots on the central CAT section. Accelerated projectiles enter the vacuum chamber from the right side. At the far right side of the figure the vacuum tube from the accelerator beam line is visible.

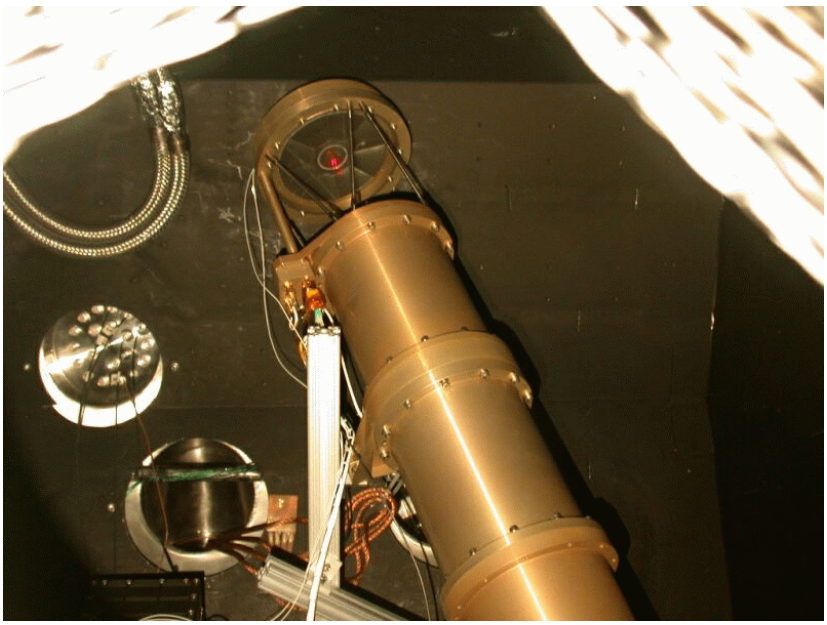

Figure 3.4: The CIDA engineering model, mounted in the vacuum chamber for shots on the central target section. The red spot from a laser indicates the position of the dust particle beam focus.

Chapter 4

Experimental results

Most experiments have been performed with the dust detector instrument CDA. A brief overview of the used projectiles, target regions and impact speed ranges is given in the following section. A more detailed listing of the experiments can be found in Appendix C. The most important results of this work are the impact charge yields and time-of-flight mass spectra of different projectile materials. Section 4.2 describes the observation of charge yield functions for impacts on the CAT- and the IID-target that show characteristic variations depending on the impact speed. As shown in Section 4.3, time-of-flight mass spectra of all used projectile materials could be obtained. The results show characteristic changes of the impact plasma composition depending on the impact speed. The data sets allowed the determination of absolute charge yields for different ion species. Mass spectra from different projectile materials can be distinguished by specific atomic and molecular ions. For the carbon and latex samples have been observed molecular clusters and hydrocarbons with atomic weights up to 200 amu. The unique opportunity of measuring with the CIDA engineering model arised. This allowed to obtain time-of-flight mass spectra of the organic PANi-PS-latex sample with a three to four times higher mass resolution (Section 4.4).

4.1 Measurements with CDA

Experiments for CDA were performed with the six different projectile materials that are mentioned in Section 2.2 on page 8 ff. From the full range of projectile speeds small impact speed intervals [v_0-0.5 km/s, v_0+0.5 km/s] with even v_0 values (except for iron and PPY-PS-Latex) were taken in steps of 2 km/s. The setting of narrow speed ranges should prevent a selection effect: a huge majority of the non-monospheric projectiles released from the dust source are "big" ($d > 1.0$ μm) and slow ($v < 8$ km/s) particles. The additional setting of mass intervals (via the setting of charge intervals for the projectiles) was not possible, since the charge measurement of the particle selection unit (PSU) often failed. This work is also the first work that tries to give an estimation of the distribution of the impact charge and the implications for the actual instrument sensitivity of CDA. Therefore the number of projectiles that definitely reached the CDA instrument (controlled via the last charge detector QD in the beam line directly in front of the vacuum chamber) was compared with the number of projectiles that were actually registered by the instrument, whether the instrument internal classification classifies the event as noise or as a proper impact event.

Table 4.1 gives an overview of the data set with registered events for all projectile materials and target sections. The abbreviations of the target sections are explained in detail in Section 3.3. The 2656 events were taken from 5230 shots in total. Additionally, signals from 1924 events that Srama

(2000) measured with iron projectiles, shot on the CAT and the IID, were used. A detailed overview of the measurements in each speed range and a comparison of the amount of shots with the number of events that were registered are given in Tables C.3 to C.8 respectively in histogram form in Figures C.1- C.5 in Appendix C. Additionally, three examples of raw data from shots with PANi-PS-latex on the CAT, the IID and the inner instrument wall (Figures C.6 - C.8 are given in Appendix C.

Material	cCAT		oCAT		cIID		oIID		cWALL		oWALL		
	n	v [km/s]	n	v [km/s]	n	v [km/s]	n	v [km/s]	n	v [km/s]	n	v [km/s]	total
Aluminium	332	2 - 50											332
Carbon	158	2 - 18	246	2 - 25	24	4 - 16	18	4 - 16	14	4 - 18			460
Carbon + Na	135	4 - 28											135
Iron			127	2 - 50	152	2 - 40	120	2 - 40	110	2 - 40	130	2 - 40	639
PANi-PS-latex	264	4 - 22	174	4 - 19	100	4 - 19	100	4 - 19	83	4 - 19	85	4 - 19	806
PPY-PS-latex			102	2 - 8	47	2 - 8	49	2 - 8	42	2 - 8	44	2 - 8	284
total	889		649		323		287		249		259		2656

Table 4.1: Summary of all events that were registered by the CDA FS by shooting projectiles on the different target sections (cCAT = central CAT target, oCAT = outer CAT target, cIID = central IID target, oIID = outer IID target, cWALL = central instrument wall, oWALL = outer instrument wall. The exact geometric shoot positions are described in Section B.1).

4.2 Charge yields

This section deals with the electron and ion charge that is produced by hypervelocity impacts. The first subsection 4.2.1 is dedicated to shots on the Chemical Analyzer Target. The next subsection gives the results from shots on the Impact Ionization Target (IID).

Figure 4.1 shows, how the total ion charge from impacts on the CAT-target scatters around in the instrument. Not all ions that are produced at the impact site QC will reach the multiplier. Due to a limited transmission of the grids (the acceleration grid has only 68 % transmission, the three ion grids in front of the multiplier 90 %, 50 % and 90 %) only 27.5 % of the ions can reach the first multiplier dynode. Further losses will appear due to poor focussing of the ions, which have an intrinsic energy and angular distribution from the impact. Figure 4.1 shows, that the ion grid detects only 15 % of the total charge at QC. With rising impact speed a rising portion of the total charge gets out of the instrument through the entrance grids. Additionally a few percent of the ions hit the IID target at very low impact angles (QE/QC-ratio). Although it cannot be measured, it is obvious, that a similar ion portion that hits the IID target or leaves through the entrance grids will also hit the instrument wall. The movement of ions and electrons inside the instrument was also simulated with the ion-optic software tool SIMION (GRÜN, E. et al., 2002).

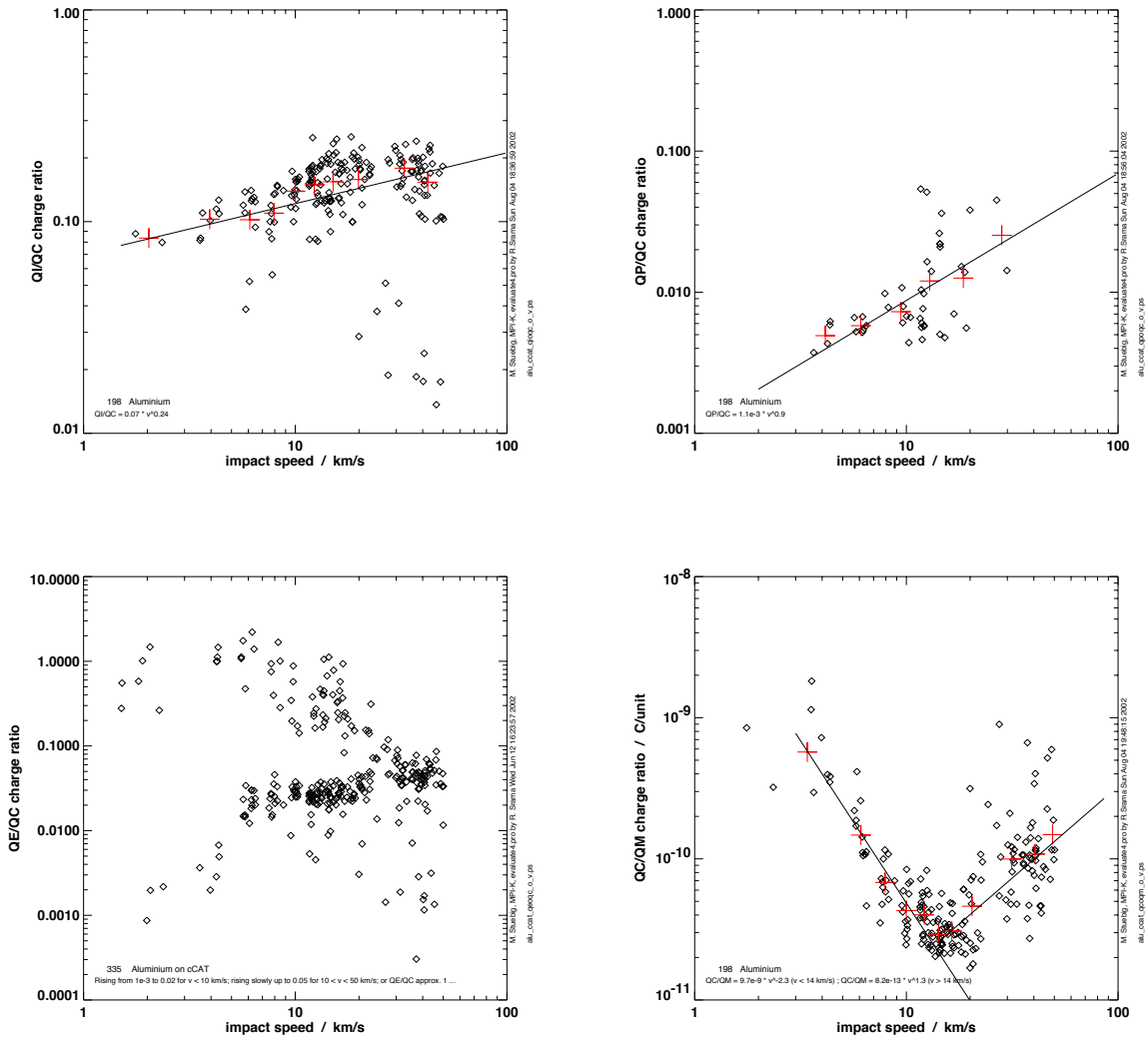

Figure 4.1: Charge ratios of the channels QI/QC (upper left diagram), QP/QC (upper right diagram) for aluminium projectiles and QE/QC (lower left diagram). The lower right diagram shows the ratio of the total charge of the CAT channel QC against the multiplier integral QM.

4.2.1 Charge yields at the Chemical Analyzer Target

The CAT consists of rhodium and is the best suitable target of the CDA instrument to receive reliable information on the total charge from hypervelocity impacts. The +1000 V bias voltage on the target and the grounded grid 3 mm in front of the target provide a strong electric field of 333 kV/m. This field penetrates the impact plasma and separates it into electrons and negative ions and into positive ions. The electrons and negative ions remain at the positively charged target area, while the positive ions are accelerated away from the target towards the multiplier. The results of the charge yield measurements depending on the impact speeds are shown in Figures D.4 to D.6 in Appendix D.2. Earlier works ((DIETZEL et al., 1973; GÖLLER and GRÜN, 1989; RATCLIFF, P.R. et al., 1997)) already tried to describe the charge yield with power laws of the type

$$q = c \cdot m^{\alpha} v^{\beta}. \tag{4.1}$$

All authors report the mass coefficient α in Eq. 4.1 to be 1.0. Ion formation models from Kissel and Krüger (1987) predict values for α below 1.0. The polyaniline-coated polystyrene latex sample in this work has a very narrow grain size distribution. This provides projectiles of a well defined mass. The left diagram in Figure 4.2 shows the mass distribution of 213 PANi-PS-latex particles that hit the CAT of the CDA instrument and generated a time-of-flight mass spectrum. For impact speeds between 6 and 16 km/s the projectile mass varies only by a factor of 2 from the nominal mass m_0 of $2.4 \cdot 10^{-16}$ kg. Aluminium and iron projectiles show a mass variation of more than two decades in the same velocity range. If q is not proportional to m ($\alpha = 1.0$), the projectile grain size may have influence on the impact plasma and falsify the results for the charge yield. The right diagram in Figure 4.2 shows the absolute charge yield as function of the impact speed for the 213 latex projectiles, which generated mass spectra. For particles with masses between $1.6 - 3.2 \cdot 10^{-16}$ kg ($m = (1.00 \pm 0.33) m_0$), a least square fit of the form

$$q = c^* \cdot v^{\beta} \tag{4.2}$$

gives values of $6.9 \cdot 10^{-16}$ for c^* and 2.6 for β.

A least square fit in the form of Eq. 4.1, assuming α to be 1.0 results into values of 1.0 for c and 3.0 for β (cf. Figure 4.2). Plotting only the mass distribution depending on the impact speed for all particles with $m_0 \pm$ 30 % (not shown here) one derives $m \propto m_0 \cdot v^{-0.4}$ which exactly explains the deviation in the impact speed power. The results allow the assumption that the mass coefficient α is 1.0 for all measurements.

The impact charge distribution of the projectiles in Figure 4.2 shows a scatter of the data within a factor of 3. As shown in Table 4.2, the standard deviation of the produced impact charge is about 30 % of the mean value at constant projectile impact speed ($\frac{\Delta v}{v} < 0.07$) and mass ($\frac{\Delta m}{m} < 0.3$).

Figure 4.3 shows an example of the charge yield determination for iron projectiles. The power law for the charge production depends on the impact speed regime. For iron projectiles, as shown here, and three regimes with different charge yield functions appear. The same behavior has been observed for carbon projectiles, while aluminium projectiles show only two impact speed regimes, latex only one. The error of the power coefficient is approximately 10 %. Regarding Table 4.3, it turns out that the power laws change in a characteristic manner: high v-powers at low impact speeds ($v < 10 \pm 2$ km/s), lower v-powers at medium impact speeds ($10 < v < 20$ km/s) and again high powers at high impact speeds ($v > 20$ km/s). Events that show no spectra (black diamonds in Figure 4.3) show a larger

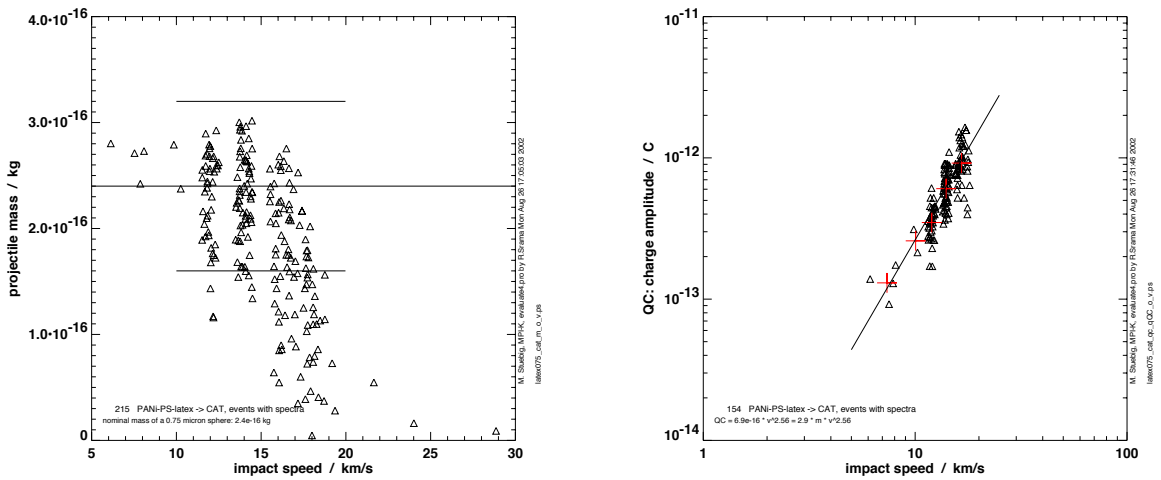

Figure 4.2: Left hand diagram: projectile mass distribution vs. impact speed for 213 PANi-PS-latex projectiles, that generated a time-of-flight mass spectrum after an impact onto the CAT of CDA. Right hand diagram: absolute charge yield depending on the impact speed for the same projectiles.

Impact speed [km/s]	Impact charge [C]	rel. deviation
8	$(1.3 \pm 0.4) \cdot 10^{-13}$	0.31
10	$(2.6 \pm 0.5) \cdot 10^{-13}$	0.19
12	$(3.6 \pm 0.9) \cdot 10^{-13}$	0.25
14	$(6.2 \pm 1.8) \cdot 10^{-13}$	0.29
16	$(9.5 \pm 2.5) \cdot 10^{-13}$	0.26
18	$(10.0 \pm 4.2) \cdot 10^{-13}$	0.42

Table 4.2: Impact charge distribution of PANi-PS-latex projectiles at a constant mass ($(2.4 \pm 0.8) \cdot 10^{-16}$ kg) depending on the impact speed. The error of the impact speed is $\Delta v = \pm$ 0.5 km/s. The relative deviation of the impact charge is 30 %.

scatter of the charge yield. This prohibits reliable power law fits to certain impact speed intervals. Nevertheless, the charge yield seems to be lower than for events with spectra for small impact speeds and seems to be similar to events with spectra for high impact speeds. The received power law fits for events with and without spectra are listed in Table 4.3. Additionally the charge ratios $\frac{\mathrm{QI}}{\mathrm{QE+QC}}$, which measure how much of the impact charge reaches the ion grid, are given. It turns out that the CAT and IID target together measure 5 - 50 times more charge than is registered by the ion grid in front of the multiplier, meaning only 2 - 20 % of all produced ions at the impact site reach the ion grid detector. This is much less than the 61 % transmission of the acceleration grid and the first ion grid. It is important to mention that the $\frac{\mathrm{QI}}{\mathrm{QE+QC}}$-ratio rises with increasing impact speed. This contradicts the results that were obtained from simulations (GRÜN, E. et al., 2002). Averaging over the complete impact speed range, the charge yields and $\frac{\mathrm{QI}}{\mathrm{QE+QC}}$-ratios show no big differences whether the projectile hits the CAT properly and generates a mass spectrum or whether the projectile hits the acceleration grid. Taking into account 45 % total transmission of the middle and the last ion grids (SRAMA, 2000),

it results that a time-of-flight mass spectrum is generated by only 1 - 9 % of the total impact charge produced by a hypervelocity impact of a micrometer sized body.

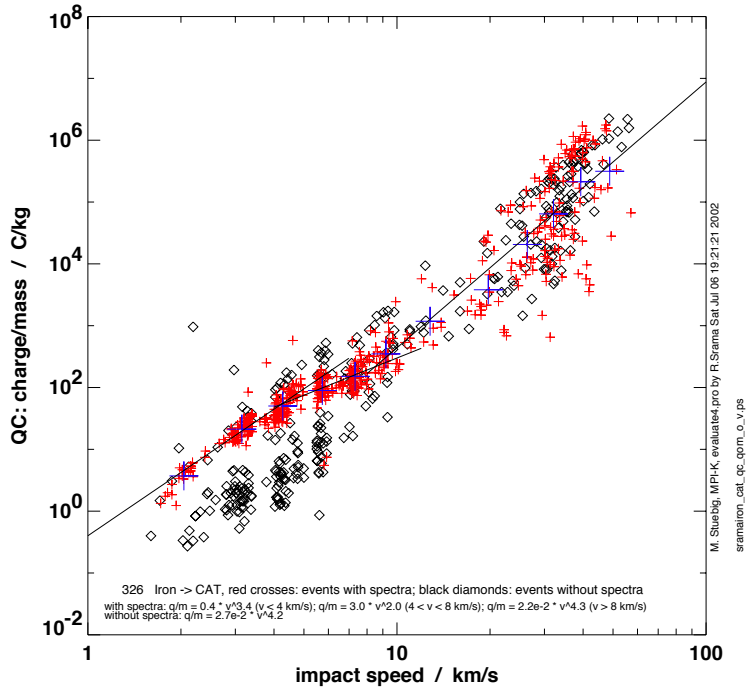

Figure 4.3: The ion charge yield per mass unit for shots with iron projectiles onto the CAT depending on the impact speed. Black diamonds show impacts without a TOF mass spectrum, red crosses show impacts with a TOF mass spectrum with at least two mass lines.

Material	QC: charge yields				charge ratios	
	Events with spectra charge/mass / C/kg			Events without spectra charge/mass / C/kg	with spectra $\frac{QI}{QE+QC}$	without spectra $\frac{QI}{QE+QC}$
	$v < 10$ km/s	$10 < v < 18$ km/s	$v > 18$ km/s			
Aluminium	$5.3 \cdot v^{2.5}$	$5.3 \cdot v^{2.5}$	$0.0016 \cdot v^{5.3}$	$0.1 \cdot v^{3.8}$	$1.3 \cdot 10^{-3} \cdot v^{1.3}$	0.03 - 0.14
Carbon	$0.088 \cdot v^{4.3}$	$44 \cdot v^{1.6}$	$0.45 \cdot v^{3.3}$	$6.7 \cdot v^{2.0}$	$1.1 \cdot 10^{-3} \cdot v^{1.4}$	0.03 - 0.11
Carbon + Na	$0.33 \cdot v^{3.7}$	$115 \cdot v^{1.3}$	$0.088 \cdot v^{3.8}$	$2.4 \cdot v^{2.4}$	$1.2 \cdot 10^{-3} \cdot v^{1.5}$	0.02 - 0.11
Iron	$0.4 \cdot v^{3.4}$	$3.0 \cdot v^{2.0}$	$0.022 \cdot v^{4.3}$	$0.027 \cdot v^{4.2}$	0.08 - 0.25	0.02 - 0.20
PANi-PS-latex	$1.0 \cdot v^{3.0}$	$1.0 \cdot v^{3.0}$	-	$0.022 \cdot v^{4.9}$	0.02 - 0.20	0.02 - 0.20
				500 ($v > 8$ km/s)		
PPY-PS-Latex	$0.21 \cdot v^{5.0}$	-	-	$0.37 \cdot v^{3.0}$	0.03 - 0.20	0.04 - 0.20

Table 4.3: Least square power law fits of the total charge per mass yield of projectiles impacting on the CAT for specific speed ranges. The impact speed is in units of km/s. The charge is measured at the QC channel. Additionally $\frac{QI}{QE+QC}$-charge ratios are given. They are a measure of the ion focussing inside the instrument, which fraction of the total impact charge reaches the ion collector grid QI.

For a better comparison of the charge yields, absolute values for all materials and specific impact speeds are listed in Table 4.4. The values are calculated with the yield functions of Table 4.3, valid in the respective velocity range. Additionally the yield functions for all materials are plotted in Figure 4.4. The figure shows that the yields for carbon and sodium contaminated carbon are nearly the same over the complete accessible impact speed range (6 - 28 km/s for carbon projectiles).

Material	QC: charge/mass-yield / C/kg					
	5 km/s	10 km/s	15 km/s	20 km/s	30 km/s	50 km/s
Iron	95	300	675	8600	$50 \cdot 10^3$	$440 \cdot 10^3$
Aluminium	225	2000	4600	10000	$107 \cdot 10^3$	$1620 \cdot 10^3$
Carbon	90	1750	3350	8800	$[33 \cdot 10^3]$	$[180 \cdot 10^3]$
Carbon + Na	130	2000	3890	6200	$[36 \cdot 10^3]$	$[250 \cdot 10^3]$
PANi-PS-latex	125	1000	3380	[8000]	$[27 \cdot 10^3]$	$[125 \cdot 10^3]$
PPY-PS-Latex	655	$[21 \cdot 10^3]$				

Table 4.4: Overview of the charge yields for specific impact speeds, as calculated from the yield functions in Table 4.3. The values in brackets are extrapolated.

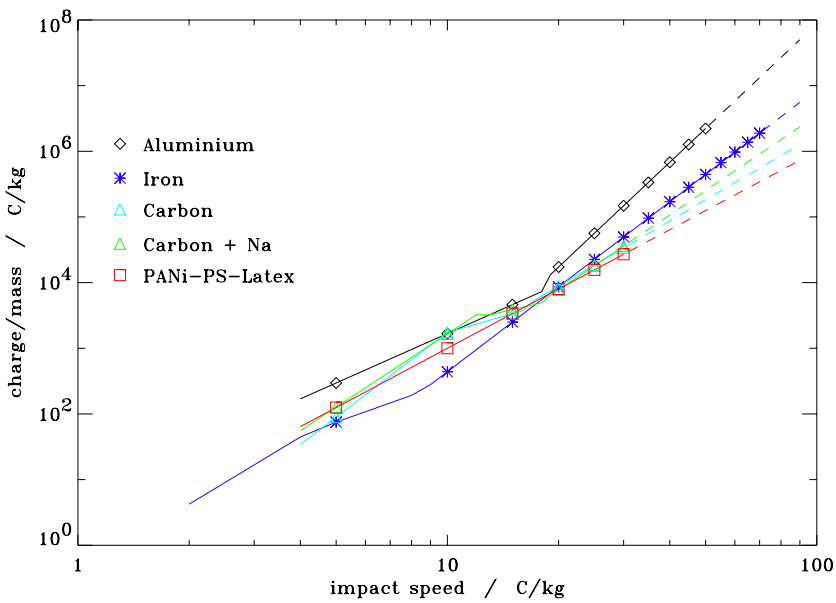

Figure 4.4: Comparison of the yield functions for all materials used in this work. The symbols and colours are explained in the legend. The symbols are in 5 km/s - steps and cover the measured velocity regimes for each material. The dashed lines represent extrapolated data.

4.2.2 Charge yields at the IID-Target

Shots on the impact ionization detector Section (IID) should generate a similar amount of ions like shots on the CAT. There are no grids, which would provide a strong electric field for a better separation of the positive and negative plasma constituents directly above the target area. Only a weak field between the grounded target (+ 0 V) and the focus voltage of -350 V on the ion collector grid in front of the multiplier can accelerate the ions away from the impact site. The resulting electric field strength is in the order of 1 kV/m and therefore a factor of 300 weaker than the field between the CAT-target and the acceleration grid. It is expected that the measurable charge yield should be somewhat lower than at the CAT. The lower electric field strength at the impact site is responsible for a worse charge separation - ions and electrons may recombine. The charge yields differ from the results of shots on the CAT. Only for iron (Figure 4.5) could be obtained a proper fit to the data. In the case of carbon and for the latex samples the results vary, and the least square power law fits show a strange behavior, that is not consistent with the results from shots on the CAT. The evaluated charge yields are summarized in Table 4.5. All corresponding figures are shown in in Figures D.7 and D.8 in Appendix D.2.

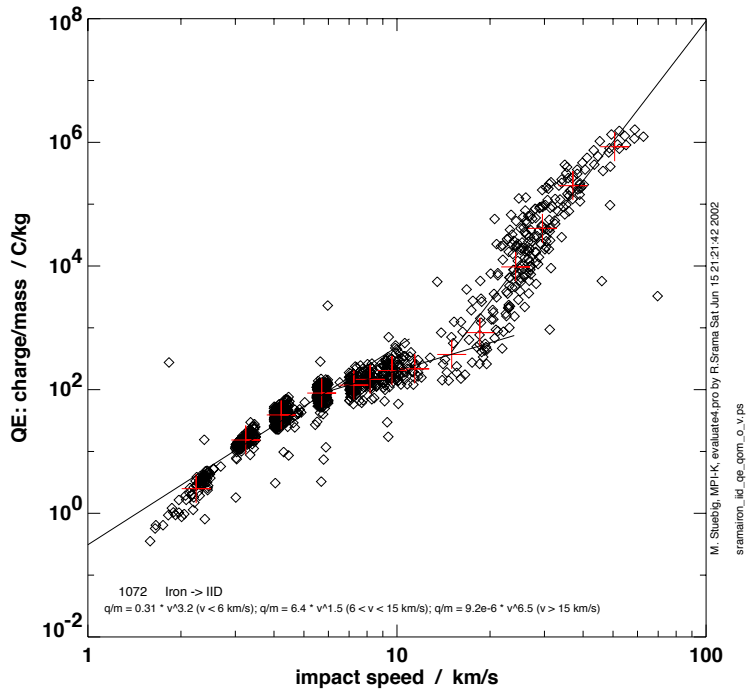

Figure 4.5: The ion charge yield per mass unit depending on the impact speed for shots with iron projectiles onto the IID-target.

For shots with iron projectiles one can see a similar development of the charge yield function as for shots in the CAT: three impact speed regions, where the speed-exponent β in the charge yield formula 4.1 is changing. A comparison of the data from Srama (2000) and additional shots for this thesis shows that the data are roughly reproducible. Only few carbon projectiles, that were shot on the

Material	QE: charge/mass / C/kg		
	$v < 6 \pm 2$ km/s	$6 < v < 12$ km/s	$v > 12 \pm 2$ km/s
Iron (Srama)	$0.3 \cdot v^{3.2}$	$6.4 \cdot v^{1.5}$	$9.2 \cdot 10^{-6} \cdot v^{6.5}$
Iron (Stübig)	$0.2 \cdot v^{3.8}$	$6.1 \cdot v^{1.4}$	$1.8 \cdot 10^{-3} \cdot v^{5.0}$
Carbon		$4.1 \cdot v^{1.2}$	
PANi-PS-latex	171	171	16.1
PPY-PS-Latex	$35.8 \cdot v^{-0.7}$	$0.0035 \cdot v^{5.4}$	

Table 4.5: Least square power law fits of the charge yield per mass unit QE/m at the IID-target for different projectiles impacting on the IID within specific speed ranges.

IID, were registered as impact events (cf. lower diagram in Figure D.7 on page 151). The data won't allow reliable statements on the ion charge yield over a larger impact speed range. The charge yield function of the PANi-PS-latex particles finally shows an unexpected drop for impact speeds above 12 km/s. The function for PPY-PS-Latex projectiles shows a drop between an impact speed of 2.5 and 4.5 km/s and then a very steep increase with a β of 5.4 for impact speeds above 4.5 km/s. There had been no experiments with aluminium projectiles and sodium contaminated carbon particles until now. The ions that are produced at the impact site will scatter around inside the instrument. Taking this into account, one has to sum up the registered ion charge at the IID target (QE) and the ion charge at the CAT target (QC). The corresponding charge yields are summarized in Table 4.6. As for impacts on the CAT (section 4.2.1) the charge yield ratios $\frac{\mathrm{QI}}{\mathrm{QE+QC}}$ are given. These ratios are now scattering between values of 0.1 and 0.3. This is larger than the measured ratios for shots on the CAT (0.03 - 0.20, cf. Table 4.3) and means that a larger fraction of all ions will reach the ion grids than for shots on the CAT. This contradicts again the theoretical simulations (GRÜN, E. et al., 2002).

Material	(QE+QC): charge/mass / C/kg			$\frac{\mathrm{QI}}{\mathrm{QE+QC}}$
	$v < 6$ km/s	$6 < v < 12$ km/s	$v > 12$ km/s	
Iron (Srama)	$1.0 \cdot v^{2.8}$	$5.5 \cdot v^{1.8}$	$2.4 \cdot 10^{-4} \cdot v^{5.5}$	0.10 - 0.20
Iron (Stübig)	$0.4 \cdot v^{3.4}$	$2.8 \cdot v^{2.0}$	$5.0 \cdot 10^{-3} \cdot v^{4.9}$	0.11 - 0.33
Carbon		$4.8 \cdot v^{2.1}$		0.03 - 0.13
PANi-PS-latex		$12.5 \cdot v^{1.5}$		$0.7 \cdot v^{-0.7}$
PPY-PS-Latex		$1.8 \cdot v^{5.9}$		0.18 - 0.33

Table 4.6: Least square power law fits of the sum charge per mass yield of the QE- and QC-target from projectiles that impact onto the IID-target. Again the charge yield functions are separated in different specific speed ranges.

4.3 Time-of-flight mass spectroscopy

This Section describes the generation of time-of-flight mass spectra 4.3.1 and gives an overview of the ion composition of the impact plasma 4.3.3 as measured in this work.

4.3.1 Time-of-flight mass spectra

Projectiles, that hit any targets with hypervelocity impact speeds, generate an impact plasma. With strong electric fields (like at the CAT of CDA) the plasma can be separated into a negative and a positive component. The negative component consists of electrons and negatively charged ions. The positive plasma component consists of positive charged ions. In this work, positively charged ions, that are generated by impacts on the CAT, are accelerated away from the impact site with a voltage of +1000 V to a grounded acceleration grid (0 V), 3 mm in front of the impact site. The speed of the ions is determined by energy conservation. The acceleration grid has a transmission of 68 % and the ions, that pass the grid, enter a 226.4 mm long drift region. Only a weak electric field helps to focus the ions towards a multiplier. Before reaching the multiplier, the ions will pass an ion grid that measures their total charge again. Ions that impact on the multiplier will release secondary electrons. The electron current is amplified by 10 dynodes inside the multiplier.

From Eq. 3.1 one derives the ion flight time t for singly charged ions as follows:

$$t = a \cdot \sqrt{m_{ion}} + b, \tag{4.3}$$

where a, b are constants and m_{ion} is the ion mass. The factor a is the stretching parameter of the mass scale and depends on the applied acceleration voltages. The time offset b depends on the trigger-time of the instrument and therefore also on the trigger thresholds. The time-to-mass conversion allows to convert a time-of-flight spectrum into a mass spectrum. Multiply charged ions will appear at a mass position $m^* = \frac{m}{q}$, where q is the ion charge in units of the elementary charge e. For example Al^{2+}-ions will appear at $m^* = 13.5$ and Al^{3+}-ions at $m^* = 9$.

The identification of the mass of a peak itself is complicated, since the starting time of sampling the mass spectrum with a very high sampling rate is depending on the trigger time of the CDA instrument. Thus, events that generate only a small amount of charge (low projectile mass and speed), may trigger the instrument late and even cut off the first part of the mass spectrum. The assignment of the mass lines was done by adapting a "theoretical spectrum" to the measured line spectrum. This theoretical spectrum was obtained from flight time calculations, using Eq. 4.3 with an empirical stretching parameter a. Although, due to a varying b, the absolute flight times are not appropriate for a reliable mass line identification, the relative flight time distances should be. A subjective assumption is made by an "expected" spectrum. Already former works showed, that Na and K will appear as dominant mass lines in spectra from low impact speeds (HANSEN, 1968; DALMANN et al., 1977). For higher speeds also ions from the projectile and target material are expected. This knowledge helps to get a convenient mass line identification. In this work only time-of-flight mass spectra containing at least 2 mass lines are taken as valid spectra. For low impact speeds these lines were in general the Na- and K-mass line, for higher impact speeds were taken the H- and Rh-mass line as reference, in some cases also the projectile material mass line. An example of a time-of-flight spectrum and the corresponding mass spectrum is shown in Figure 4.6. Approximately 60 % of all particles that were shot on the CAT-target show time-of-flight mass spectra. As already shown in Section D.3, this value is an upper limit due to the grid transmission of the entrance grids and the acceleration grid in front of the target. More TOF mass spectra examples of all projectile materials for various impact speeds are shown in

Figures D.33 to D.38 (Appendix D.7, page 193ff). It has to be noted here, that all flight time spectra show an artefact at 0.12μs after starting the spectrum. This artefact is related to the starting of the 100 MHz (5 x 20 MHz, interleaved) sampling rate of the multiplier. Since the time position of the artefact is constant, it may appear in the mass spectra at lower or higher masses than the hydrogen line at 1 amu. Since only a dozen of the PPY-PS-latex projectiles showed a time-of-flight mass spectrum, and since these spectra are very noisy they won't be treated in detail in this section. Nevertheless, a few spectra showed very broad peaks in the flight time spectrum. But since these lines are not understood, an appropriate mass scaling was not possible.

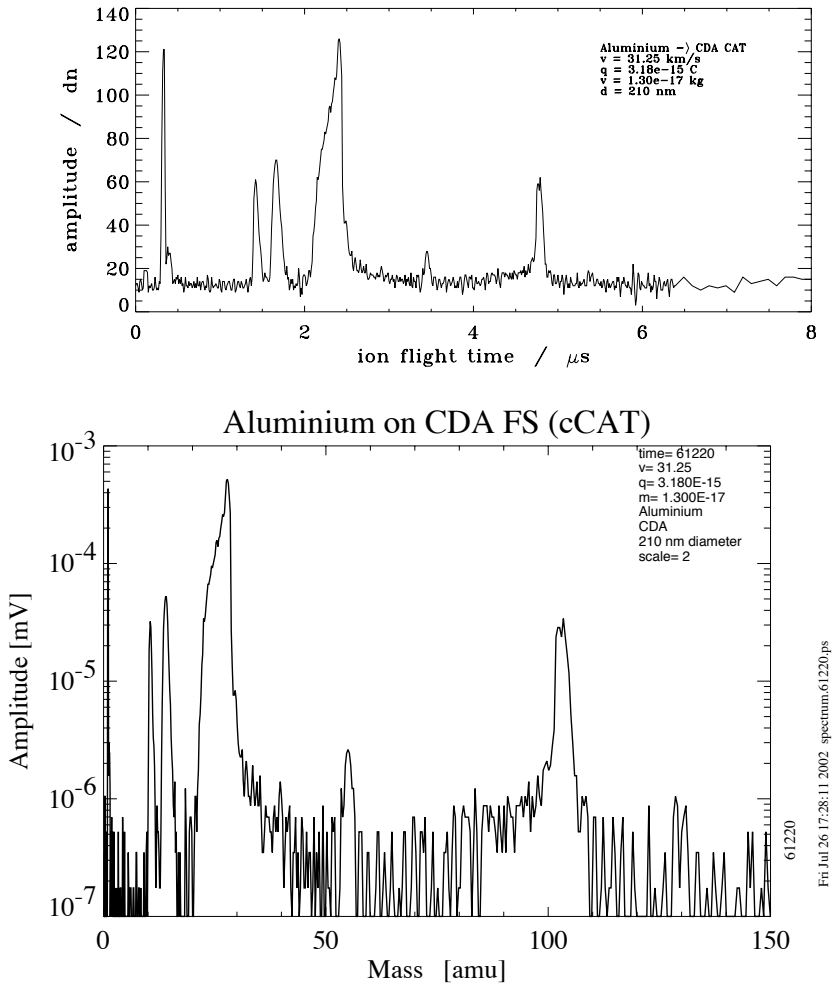

Figure 4.6: Example of a time-of-flight raw spectrum (upper figure) that has been converted to a mass spectrum (lower figure). The spectrum was generated by an impact of a 210 nm diameter aluminium projectile with 31 km/s onto the CAT.

4.3.2 Mass resolution

The mass resolution $\frac{m}{\Delta m}$ is defined as the position m of the mass line divided by its half maximum full width (Δm). The mass resolution is determined by the instrument properties (acceleration voltage, length of the drift tube) and by the energy and angular distribution of the plasma ions. The theoretical mass resolution of a time-of-flight mass spectrometer is given in Eq. 4.4 (STEPHAN, 2001):

$$\frac{m}{\Delta m} = \left(\frac{1}{R_{An}}^{2} + 2\frac{\Delta t_{reg}^2 + \Delta t_p^2}{t^2} \right)^{-\frac{1}{2}}, \tag{4.4}$$

where R_{An} is the instrument related mass resolution, t_{reg} the time resolution of the electronics and t_p the duration of the ionizing event. From Eq. 3.1 follows a correlation between flight time t and ion mass m: $t^2 = c \cdot m$.

In the case of CDA, t_{reg} is the sampling frequency of the multiplier (10^{-8} s) and for t_p should be taken as duration of the impact event. The following extremes were observed: 3000 nm projectile with 1.5 km/s and 100 nm projectile with 50 km/s. With a reduced impact speed between $u = v_0 \cdot \frac{\rho_P}{\rho_T} \approx 0.09\, v_0$ for latex $\rightarrow$ Rh and $0.64\, v_0$ for Fe $\rightarrow$ Rh (HORNUNG, K. and KISSEL, J., 1994), the following "impact durations" can be found: $2 \cdot 10^{-8} < t_p < 2 \cdot 10^{-11}$ s. The absolute flight time t of the ions is $t \approx \sqrt{2.2 \cdot 10^{-13} \cdot m}$ s for 1000 V acceleration voltage. Using these values, Eq. 4.4 can be rewritten as follows (Eq. 4.5), assuming the "worst case":

$$\frac{m}{\Delta m} = \left(\frac{1}{R_{An}}^{2} + \frac{2.3 \cdot 10^{-3}}{m} \right)^{-\frac{1}{2}}. \tag{4.5}$$

As shown in Figure 4.7, the actual mass resolution shows a large scattering and it seems appropriate to approximate instead of square-root functions simple linear functions of the type

$$\frac{m}{\Delta m} = c \cdot m + d \tag{4.6}$$

The results of fitting linear functions to the data sets at various impact speed ranges are listed in Table 4.7. It is obvious that the mass resolution rises for higher ion masses. Although for different impact speed ranges different functions were applied, a further investigation how the mass resolution depends directly on the impact speed (not shown here) pointed out, that the mass resolution is independent of the impact speed within the accessible speed range of 2 - 60 km/s. This can also be taken from an overview of the absolute mass resolution values as shown in Appendix D.7, calculated with the resolution functions in Table 4.7. A comparison of the mass resolutions from impacts on the central CAT region and impacts on the outer CAT region showed no differences. This means that the mass resolution of a TOF mass spectrum is independent of the exact impact location on the CAT. The mass resolution rises from $\frac{m}{\Delta m} \approx 10$ for 1 amu (hydrogen) to $\frac{m}{\Delta m} \approx 30$ for 100 amu (rhodium) and 60 amu for 200 amu (molecular/cluster ions). This low mass resolution makes it difficult to distinguish between isotopes of element mass lines e.g. for iron $^{54}_{26}$Fe and $^{56}_{26}$Fe. In addition it is not possible to distinguish between molecular and elemental ions or hydrocarbon ions. For such measurements mass resolutions of $\frac{m}{\Delta m} > 3000$ are required (STEPHAN, 2001).

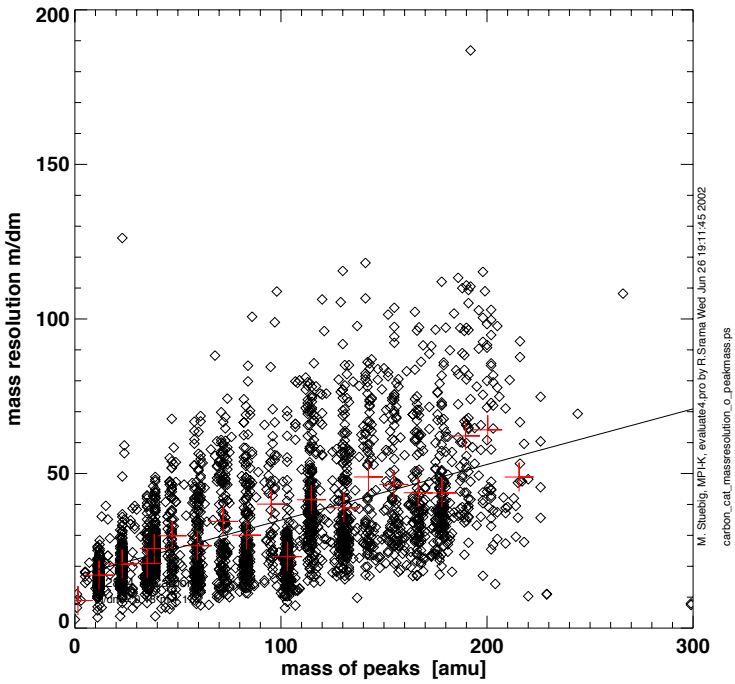

Figure 4.7: Mass resolution of mass spectra generated from carbon projectiles.

4.3.3 Ion plasma composition

The characteristics of the time-of-flight mass spectra from a named projectile material are changing with the impact speed. The Figures 4.8 to 4.10 show how different ion species contribute to the total spectrum. The relative contribution $\frac{\text{mass line integral}}{\text{mass spectrum integral}}$ is plotted against the impact speed. The diagrams show only target ions (Rh^+ in all cases, black diamonds), projectile ions (e.g. Al^+ for aluminium projectiles, blue asterisks) and contaminant ions (Na^+ and K^+, added together, green triangles; H^+, light blue squares). Additionally target-projectile cluster ions that appear in the mass spectrum at the position of $m_{P+T} = m_P + m_T$ with m_P and m_T as ion masses of the projectile and target material are shown. Further cluster ions or multiply ionized ions are not shown here. Table 4.8 points out, at which impact speeds certain ion types will first appear in the mass spectra. The contaminant ions Na and K are the first to appear at impact speeds between 2 and 7 km/s. The target material Rh is usually the next ion type that appears at impact speeds between 4 and 12 km/s, depending on the projectile material. Ions from the projectile material itself appear only at higher impact speeds between 5 and 12 km/s. The only exception is aluminium, where projectile ions first appear at 4 km/s but the target ions at 12 km/s. It is remarkable that target-projectile cluster ions appear at similar impact speeds as the target material. Thus, projectile material appears in molecular ions in the mass spectra before it appears in atomic ions. Hydrogen ions appear only at high impact speeds (10 - 20 km/s, material depending), except for a few observations of hydrogen ions in low speed time-of-flight mass spectra from iron projectiles. The ion occurrence depending on the impact speed

Material	Mass resolution $\frac{m}{\Delta m}$		
Aluminium	0.34 m + 17.5 (2 - 8 km/s)	0.38 m + 14.4 (15 - 25 km/s)	0.31 m + 10.7 (30 - 50 km/s)
Carbon	0.17 m + 19.0 (2 - 8 km/s)	0.21 m + 15.5 (12 - 18 km/s)	0.24 m + 17.5 (20 - 28 km/s)
Carbon + Na	0.14 m + 29.2 (2 - 8 km/s)	0.21 m + 18.3 (12 - 18 km/s)	0.25 m + 17.8 (20 - 28 km/s)
Iron (Srama) Iron (Stübig)	0.09 m + 25.6 0.04 m + 23.7 (2 - 10 km/s)	0.12 m + 24.6 0.07 m + 22.2 (15 - 25 km/s)	0.22 m + 18.5 - (30 - 70 km/s)
PANi-PS-latex	0.09 m + 16.8 (6 - 10 km/s)	0.21 m + 16.3 (12 - 16 km/s)	0.30 m + 10.3 (18 - 28 km/s)

Table 4.7: Mass resolution for different materials and different impact speeds.

is also responsible for contribution of specific ion types to the complete mass spectrum at different impact speeds. For all projectile materials, contamination ions with low ionization potential (Na + K) dominate the time-of-flight mass spectra in the low impact speed regime. In a mid impact speed regime the target ions will then dominate the spectra up to impact speeds of 22 - 25 km/s. For even higher speeds, the projectile ions will dominate. This behavior is common to all materials except for aluminium (cf. 4.9), where the projectile ions dominate the mass spectra from 3 km/s on up to the highest achievable impact speeds of 50 km/s.

Projectile Material	Na + K	H	Rh	Projectile ions	Rh-Projectile cluster
Aluminium	2	10	12	4	12
Carbon	4	10	6	10	6
Carbon + Na	6	20	6	12	8
Iron	4	4 (20)	4	5	2
PANi-PS-latex	7	14	12	12	12

Table 4.8: Minimum impact speeds (in km/s) at which specific ion types appear regularly in the time-of-flight mass spectra.

Projectile Material	Contamination ions	Target ions	Projectile ions
Aluminium	< 3		> 3
Carbon	< 12	12 - 22	> 22
Carbon + Na	< 18	18 - 22	> 22
Iron	< 8	8 - 25	> 25
PANi-PS-latex	< 18	18 - 22	> 22

Table 4.9: Impact speed ranges (in km/s), where specific ion types are dominating the time-of-flight mass spectra for impact speeds up to 50 km/s.

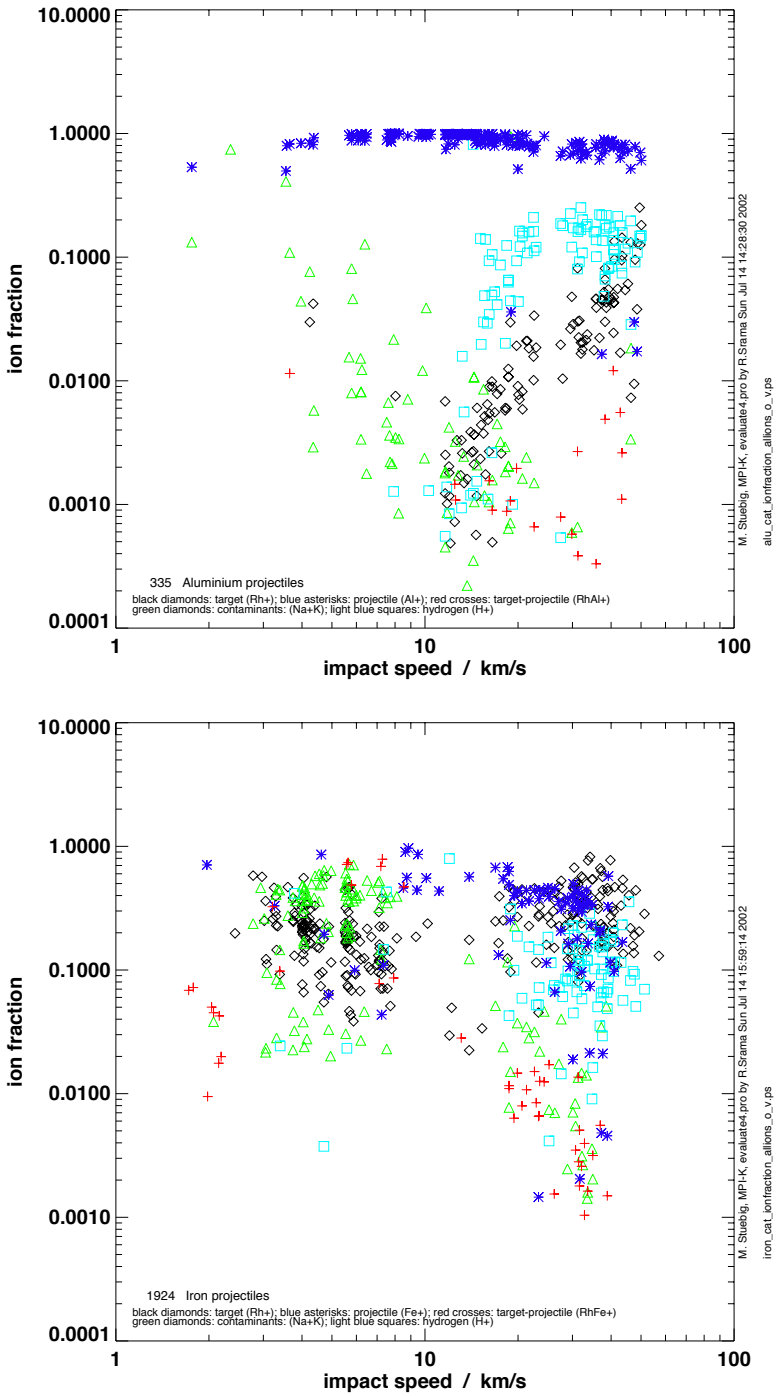

Figure 4.8: The positive ion plasma composition depending on the projectile impact speed in the time-of-flight mass spectra. The upper figure shows the results for aluminium projectiles, the lower figure for iron projectiles. Black diamonds represent the target material (Rh^+), blue asterisks the projectile material (Al^+, respectively Fe^+), red crosses represent target-projectile clusters ($RhAl^+$, $RhFe^+$), green triangles are surface contaminants (sum of Na^+ and K^+) and light blue squares represent hydrogen (H^+).

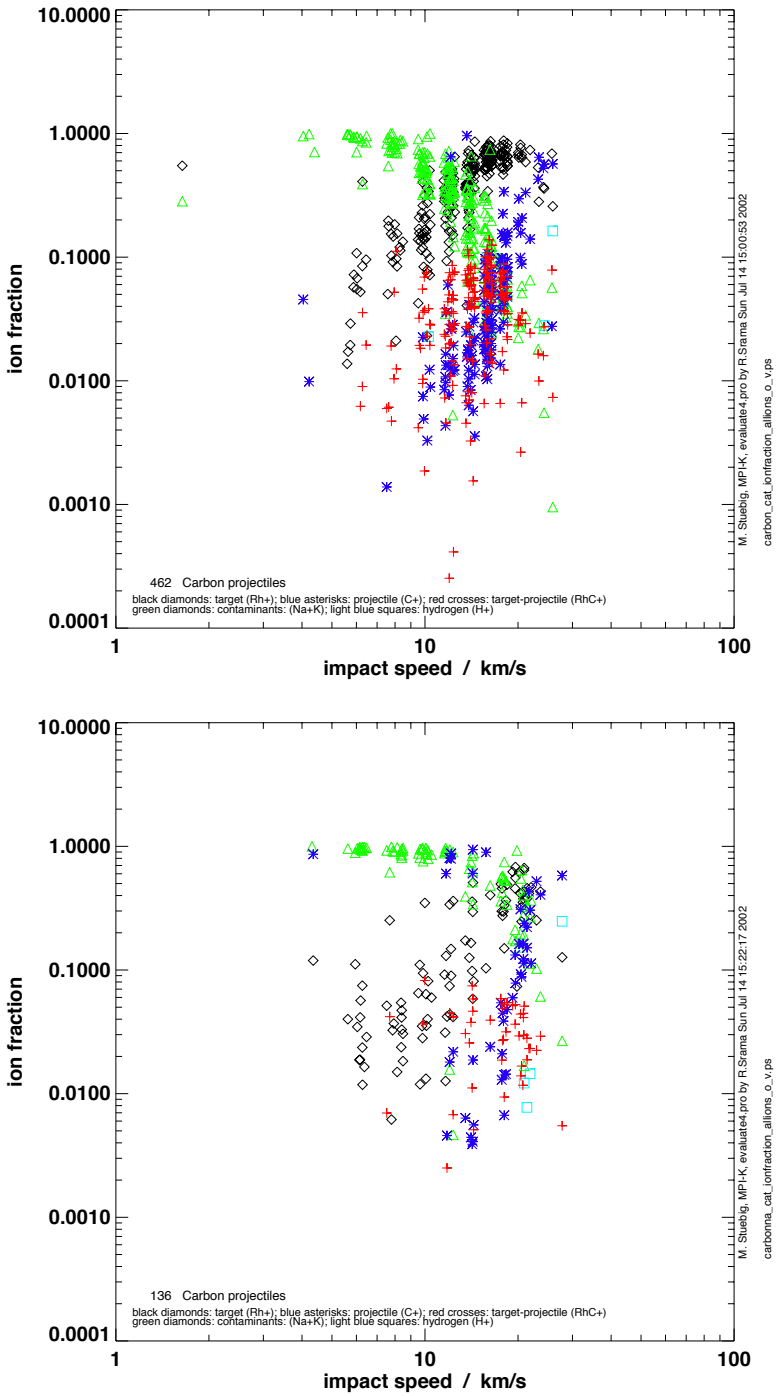

Figure 4.9: The positive ion plasma composition depending on the projectile impact speed in the time-of-flight mass spectra. The upper figure shows the results for carbon projectiles, the lower figure for sodium contaminated carbon projectiles. Black diamonds represent the target material (Rh^+), blue asterisks the projectile material (C^+ in both cases), red crosses represent target-projectile clusters (RhC^+ in both cases), green triangles are surface contaminants (sum of Na^+ and K^+) and light blue squares represent hydrogen (H^+).

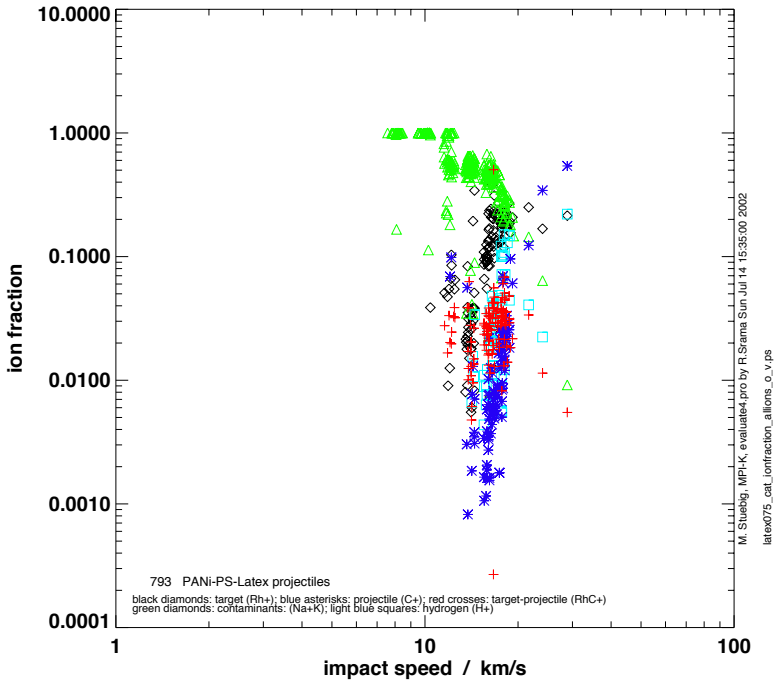

Figure 4.10: The positive ion plasma composition depending on the projectile impact speed in the time-of-flight mass spectra of PANi-PS-latex projectiles. Black diamonds represent the target material (Rh^+), blue asterisks the projectile material (C^+), red crosses represent target-projectile clusters (RhC^+), green triangles are surface contamainants (sum of Na^+ and K^+) and light blue squares represent hydrogen (H^+).

4.3.4 Absolute ion yields

Additionally to the determination of the ionic plasma composition, the time-of-flight mass spectroscopy in this work allows an empirical determination of the absolute ion yields of the different ion types. Therefore it has to be assumed that the measured ion plasma at the multiplier position is representative for the ion plasma that is formed at the impact site (here: the CAT target). In this case, the easiest way to obtain absolut charge production rates for specific ion types will be a direct comparison between the QC charge signal from the CAT and the linearized QM integral from the time-of-flight mass spectrum as measured by the multiplier. This ratio is additionally shown in the lower right diagram of Figure 4.1. The yield Y_i of specific ions i is calculated as follows:

$$Y_i = \frac{I_i}{I_{total}} \cdot \frac{q_{QC}}{m_p}, \tag{4.7}$$

where I_i and I_{total} are the integrals of the mass line from element i in respect to the total mass spectrum. The absolute charge q_{QC} represents the charge, which is generated by an impact of a projectile of mass m_p. The absolute yields of different ion types for various projectile materials are listed in Table 4.10. For a better comparison, the absolute charge yields of different ion types are compared directly in diagrams, shown e.g. in Figure 4.11 for projectile related atomic ions. Similar diagrams are shown in Figures D.39 and D.40 in Appendix D.7 (p. 193f) for atomic H-, Na-, K- and Rh-ions. It turns out that the absolute charge yield for the target material Rh rises roughly with a proportionality of v^5 and lies within one order of magnitude for all projectile materials. A similar behavior appears for hydrogen ions: the absolute charge yield rises $\propto v^{5\pm1}$ and is comparable within one order of magnitude for all projectile materials and impact speeds up to 60 km/s. As will be shown below, the absolut yield of hydrogen ions has to be corrected with a factor of 2.5. The specific ion yields of the projectile related ions (e.g. Al-ions for aluminium projectiles), which show also a rough v^5-proportionality, differ in orders of magnitude. A very steep increase of the absolute ion yields for carbon and latex projectiles $\propto v^{11}$ can be explained by the break-up of cluster ions, which are preferred ions at lower impact speeds (cf. Section 4.3.5 later in this work). Taking this effect into account, the yield for the total amount of carbon is $\propto v^7$. The ion yield for the contaminants Na and K is rising for impact speeds up to 15 km/s. For even higher speeds the absolute ion yield is stable or even decreasing. An interesting point is the appearance of target-projectile clusters. Their ion yield is proportional to v^2 - v^3. This is much less steeper than the projectile or target yield. An explanation might be a rising plasma temperature with rising impact speed. The higher temperature corresponds to the fact a higher degree of molecular dissociation of the clusters.

Correction of the hydrogen ion yield

From measurements with the CDA engineering model it turned out that the hydrogen ions appear underrepresented (REBER, 1997). This can be figured out by comparing the ratio of the hydrogen mass line integral QM(H) in the mass spectrum and the corresponding ion charge that passed the ion grid QI(H) with the charge ratios of other mass lines. Reber observed that the $\frac{\mathrm{QM(H)}}{\mathrm{QI(H)}}$-ratios are about a factor of 3 lower than the ratios for other mass lines. His explanation was that slow electronic devices cannot follow the very steep rise of the hydrogen ion peak in the mass spectrum, whereas the QI-signal yields an integrated ion signal and thus it should be more reliable. The full width half mean-values (FWHM) of the hydrogen mass line scatters between 10 and 60 ns with a mean value of 30 ns (aluminium and rhodium mass lines have FWHM-values of 70 ns). This time period corresponds to 2 - 7 samples of the mass line. Especially for the very narrow FWHM-values it is possible that the

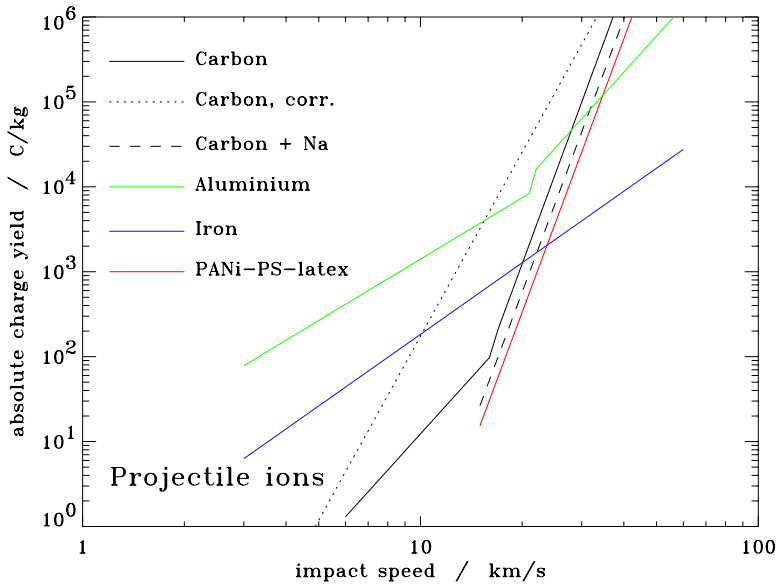

Figure 4.11: Absolute charge/mass yields of projectile ions depending on the impact speed. The different line colors and styles indicate different projectile materials, explained in the legend. The dotted black line is a theoretically calculated charge yield that takes into account the formation of cluster ions.

maximum of the mass line will not be sampled and the hydrogen line appears lower than it actually is. For aluminium, carbon and iron projectiles the $\frac{\mathrm{QM(H)}}{\mathrm{QI(H)}}$-ratio was compared to the corresponding ratio of the projectile material related mass line and the rhodium-mass line. Figure 4.12 shows that the ratio for hydrogen ions scatters between 0.05 and 1.0 times the ratio for rhodium ions. Comparison to all other mentioned ratios, a rough mean value of 0.4 ± 0.2 turned out. The large error might be explained with the difficulties to correlate a mass line to a peak in the differentiated QI-signal, and with the lower time resolution of the QI channel (170 ns, cf. table D.13). However, the measured absolute charge yield has to be multiplied with a factor of $2.5^{+2.5}_{-1.0}$ (Eq. 4.8). This correction factor confirms the results of Reber.

$$Y_{\mathrm{H},corr.} = 2.5^{+2.5}_{-1.0} \cdot Y_{\mathrm{H},meas.} \tag{4.8}$$

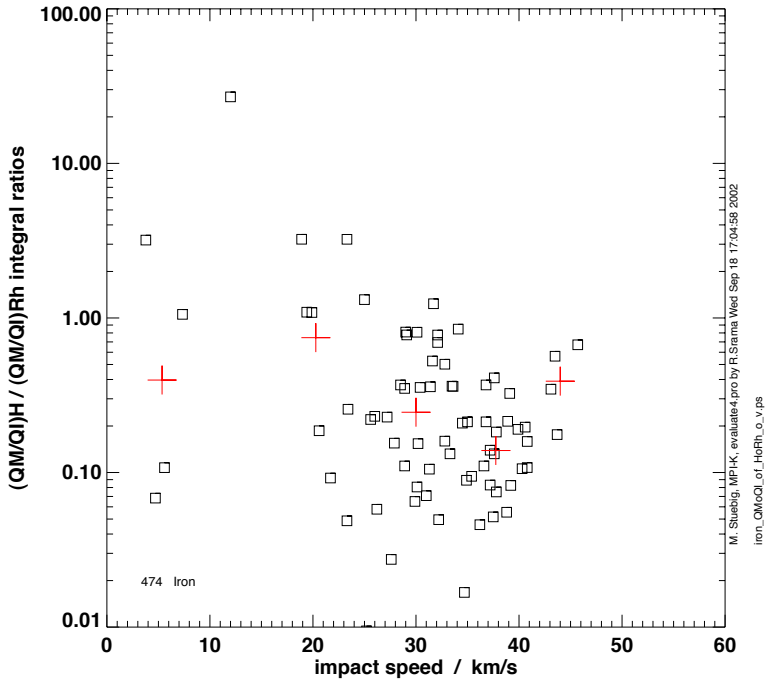

Figure 4.12: The $\frac{\mathrm{QM(H)}}{\mathrm{QI(H)}}$-ratio in comparison to the $\frac{\mathrm{QM(Rh)}}{\mathrm{QI(Rh)}}$-ratio depending on the impact speed.

Projectile material	Absolute charge yield / C/kg	
projectile ions		
Iron		$0.29 \cdot v^{2.8}$ (2 - 50 km/s)
Aluminium	$5.6 \cdot v^{2.4}$ (2 - 20 km/s)	$0.02 \cdot v^{4.4}$ (20 - 50 km/s)
Carbon	$4.9 \cdot 10^{-4} \cdot v^{4.4}$ (5 - 16 km/s)	$1.1 \cdot 10^{-11} \cdot v^{10.8}$ (16 - 25 km/s)
Carbon + Na		$6.9 \cdot 10^{-12} \cdot v^{10.7}$ (14 - 25 km/s)
PANi-PS-latex		$4.0 \cdot 10^{-12} \cdot v^{10.7}$ (14 - 25 km/s)
rhodium ions		
Iron	$0.53 \cdot v^{1.9}$ (3 - 13 km/s)	$1.7 \cdot 10^{-4} \cdot v^{5.2}$ (13 - 50 km/s)
Aluminium		$2.3 \cdot 10^{-8} \cdot v^{7.4}$ (12 - 50 km/s)
Carbon	$1.3 \cdot 10^{-4} \cdot v^{6.3}$ (6 - 12 km/s)	$1.2 \cdot v^{2.7}$ (12 - 25 km/s)
Carbon + Na	$1.0 \cdot 10^{-3} \cdot v^{5.0}$ (6 - 20 km/s)	
PANi-PS-latex		$6.6 \cdot 10^{-4} \cdot v^{4.8}$ (12 - 25 km/s)
projectile-target-cluster ions		
Iron	$9.8 \cdot 10^{-3} \cdot v^{3.9}$ (3 - 7 km/s)	$2.3 \cdot v^{1.1}$ (7 - 35 km/s)
Aluminium	$6.4 \cdot 10^{-4} \cdot v^{3.2}$ (12 - 30 km/s)	$1.0 \cdot 10^{-15} \cdot v^{11.1}$ (30 - 50 km/s)
Carbon	$5.9 \cdot 10^{-4} \cdot v^{4.7}$ (6 - 12 km/s)	$1.0 \cdot v^{1.8}$ (12 - 25 km/s)
Carbon + Na	$0.058 \cdot v^{2.7}$ (8 - 22 km/s)	
PANi-PS-latex		$0.31 \cdot v^{2.0}$ (12 - 25 km/s)
hydrogen ions, values have to be multiplied with factor 2.5		
Iron	$0.023 \cdot v^{3.8}$ (4 - 60 km/s)	
Aluminium	$7.0 \cdot 10^{-12} \cdot v^{11}$ (10 - 20 km/s)	$1.0 \cdot 10^{-4} \cdot v^{5.5}$ (20 - 50 km/s)
Carbon		$5.8 \cdot 10^{-4} \cdot v^{4.8}$ (10 - 30 km/s)
Carbon + Na		no data
PANi-PS-latex		$4.8 \cdot 10^{-7} \cdot v^{6.8}$ (14 - 25 km/s)
sodium ions		
Iron	$0.087 \cdot v^{3.5}$ (3 - 6 km/s)	$13.2 \cdot v^{0.6}$ (6 - 40 km/s)
Aluminium	$0.19 \cdot v^{1.4}$ (4 - 20 km/s)	
Carbon	$6.3 \cdot v^{1.1}$ (5 - 25 km/s)	
Carbon + Na	$0.078 \cdot v^{4.2}$ (4 - 12 km/s)	1880 (12 - 25 km/s)
PANi-PS-latex	$0.53 \cdot v^{2.9}$ (8 - 16 km/s)	$1.9 \cdot 10^{6} \cdot v^{-2.5}$ (16 - 25 km/s)
potassium ions		
Iron	$9.6 \cdot 10^{-3} \cdot v^{4.7}$ (2 - 7 km/s)	$32 \cdot v^{0.3}$ (7 - 40 km/s)
Aluminium	$8.3 \cdot v^{-0.2}$ (2 - 30 km/s)	
Carbon	$2.8 \cdot v^{2.3}$ (6 - 12 km/s)	$1.0 \cdot 10^{7} \cdot v^{-3.8}$ (12 - 25 km/s)
Carbon + Na	$40 \cdot v^{0.7}$ (6 - 12 km/s)	$1.1 \cdot 10^{4} \cdot v^{-1.6}$ (12 - 25 km/s)
PANi-PS-latex	$1.1 \cdot 10^{4} \cdot v^{-1.9}$ (8 - 18 km/s)	

Table 4.10: Absolute charge per mass ion yields depending on the impact speed for different ion species and projectile materials. The errors of the impact speed exponents are approximately 10 %. The unit of the impact speed is km/s.

4.3.5 Formation of molecular ions and cluster ions

This section describes the observation of molecular and mono-atomic cluster ions in the time of flight mass spectra. It is divided into three parts. The first part deals with the formation of molecular cluster ions. The second part summarizes the observations of projectile-target cluster ions. Since the carbon and latex projectiles showed a large amount of clusters, appearing at regular mass distances, the last part is dedicated only to the carbon cluster observation.

Molecular cluster ions

Previous works already reported the formation of molecular cluster ions (KNABE, W. and KRÜGER, F.R., 1982; KNABE, 1983; KISSEL, J. and KRÜGER, F.R., 1987). Cluster ions can be formed from the different constituents in the impact plasma, containing ions from the projectile, the target and from surface contaminations. Target-target cluster Rh_2^+, which should appear in the mass spectra at 206 amu could not be observed in this work. Molecular projectile-projectile cluster ions could be observed for all materials, except for iron. As shown in Figure 4.13 next to the atomic aluminium mass line at 27 amu appear cluster ions of Al_2^+ and Al_3^+ at 54 respectively 81 amu. Target-projectile clusters, like the $RhAl^+$ mass line at 130 amu, were observed for all projectile materials. The results are summarized in the following paragraph.

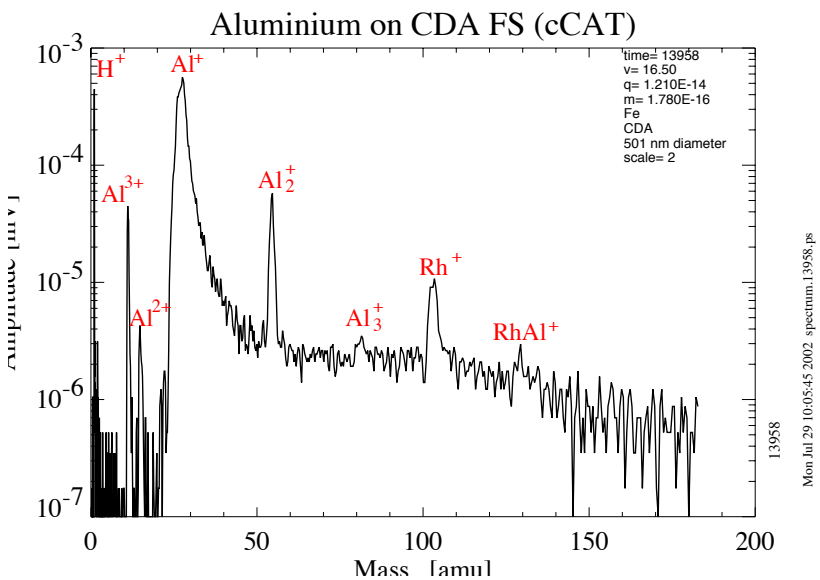

Figure 4.13: Time-of-flight mass spectrum of a 500 nm aluminium projectile, which hits the CAT target with a speed of 16.5 km/s. The spectrum shows mass lines of multiply ionized aluminium atoms and also clusters of projectile atoms and target-projectile ions.

The relative amount of the molecular aluminium cluster to the atomic line is displayed in Figure 4.14. Al_2^+ ions could be observed for the complete impact speed range. The $\frac{Al_2^+}{Al^+}$ ratio remains stable at 1.2 % with a large scattering within a factor of six. Al_3^+ ions were only observed in mass spectra from impact speeds between 15 and 20 km/s. The $\frac{Al_3^+}{Al^+}$ ratio is only 0.1 %, approximately stable in the observed impact speed range. Since the carbon and latex projectiles show a vast zoo of molec-

ular carbon (C_m) cluster or hydrocarbons (C_mH_n), the cluster ion formation from these projectiles is described in an own paragraph.

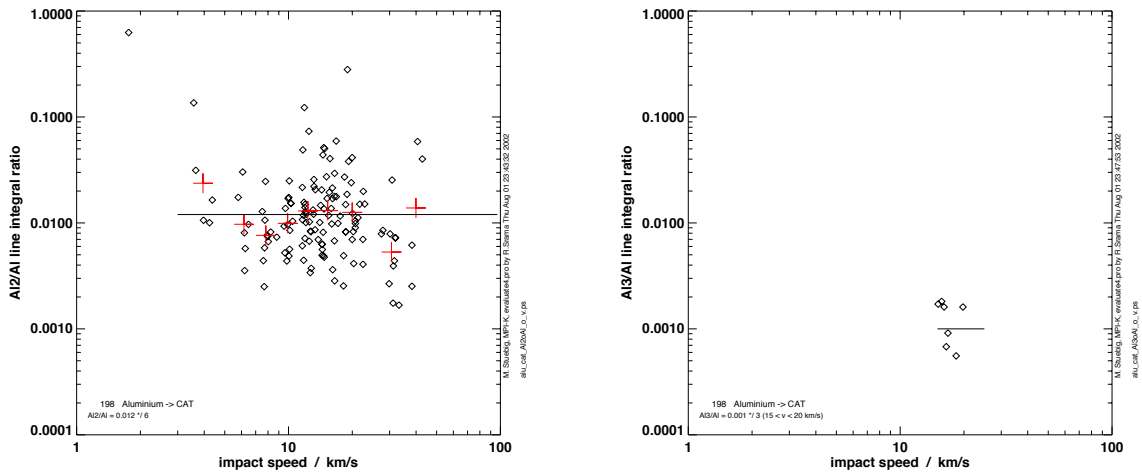

Figure 4.14: Relative ratio of Al_2^+ to Al^+ (left) and Al_3^+ to Al^+ (right).

Clusters with contaminant ions like Na or K could not be identified within the mass spectra. While hydrogen ions (H^+) were found in the time-of-flight mass spectra of all projectile materials at impact speeds higher than 15 - 20 km/s, molecular hydrogen was only observed in the spectra from the PANi-PS-latex sample. Their relative abundances to hydrogen are shown in Figure 4.15. The $\frac{H_2^+}{H^+}$ and $\frac{H_3^+}{H^+}$ ratios for impact speeds about 15 km/s are of the order of 30 %. The ratios show a decrease with increasing impact speed.

Many mass spectra from iron projectiles show ions appearing at 12 and 16 amu. This can be C^+- and O^+-residua ions from the carbonyl-iron production ($Fe(CO)_5$). In a lot of mass spectra appears additionally a mass line at 27 - 28 amu. Examples of these features can be found in Figure D.36 on page 201. This 27/28 amu mass line has already been discussed in earlier studies and was assigned to Al^+- or $C_2H_3^+$ ions (cf. (POSNER, 1995)). Since the accelerator works with a clean vacuum (cf. Section B.1.4), $C_2H_3^+$ as contamination molecule can be excluded in this work. Elsewhere, the 27/28 amu feature is only present in TOF mass spectra from aluminium and PANi-PS-latex projectiles. Aluminium as projectile constituent in the iron particles could be excluded. Posner (1995) investigated the volume contribution of aluminium with the PIXE-analysis method[1] and found an upper limit of 0.03 Vol. % Al in the iron sample, with an error of 100 %. In this work the mass line is assigned to 28 amu, representing CO^+, as residua from the carbonyl-iron production, or Fe^{2+}. The presence of CO-molecules would fit well with the appearance of C^+- and O^+-ions in the mass spectra. Figure 4.16 shows that the $\frac{C^+}{28amu^+}$ ratio is decreasing from values of over 100 at impact speeds of 4 km/s to values below 1 for impact speeds higher than 40 km/s. The $\frac{O^+}{28amu^+}$ ratio remains stable at values of 3 for impact speeds faster than 4 km/s. It is worth annotating that both diagrams show a large scattering in the ratios for single events. The correlation between the C- and O-mass line is well defined as Figure 4.16 can be seen. A correlation between the 28 amu-mass line and iron itself is not given.

[1] PIXE = Proton Induced X-ray Emission

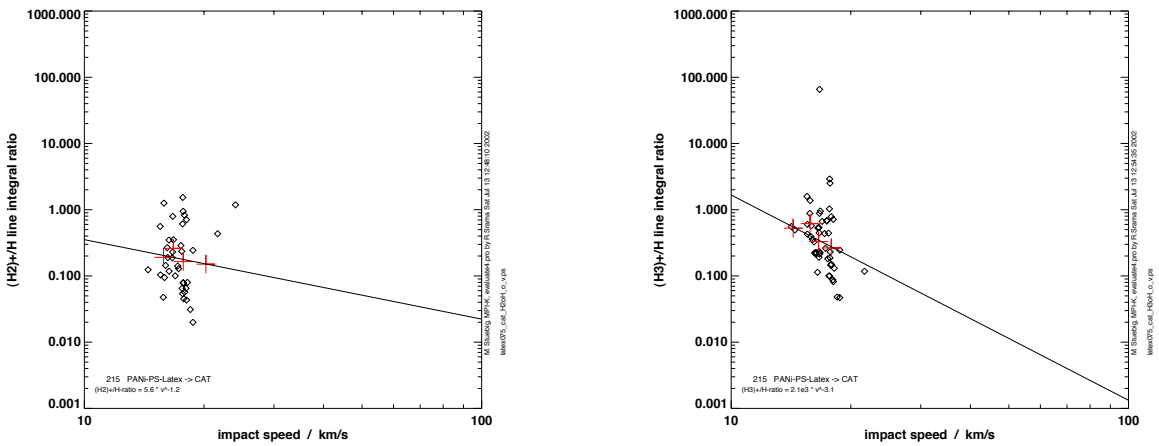

Figure 4.15: Relative ratio of H_2^+ to H^+ and H_3^+ to H^+, as observed in the spectra of PANi-PS-latex projectiles.

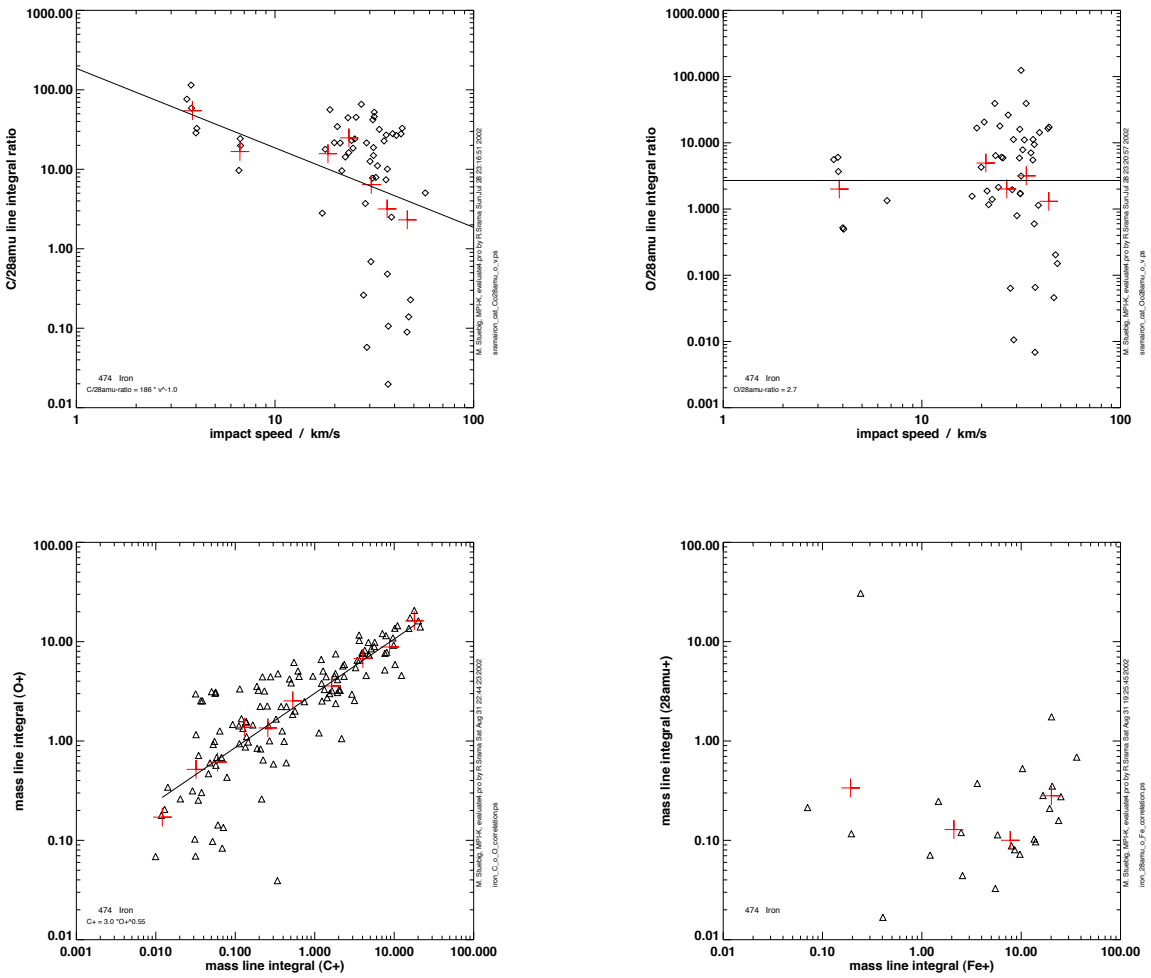

Figure 4.16: The upper diagrams show the relative ratios of C^+ to $28amu^+$ (left) and O^+ to $28amu^+$ (right). The Figures below show how the appearance of C^+ correlates with the appearance of O^+ (left) and $28amu^+$ to Fe^+.

Target-Projectile cluster

Many TOF-mass spectra show peaks at a mass which is the sum of the mass of projectile and target ions, e.g. 115 amu for Rh(103) + C(12) with carbon projectiles or 130 amu for Rh(103) + Al(30) with aluminium projectiles. Figure 4.17 shows the relative ratio of such cluster ions with respect to the Rh-ions from the target material. As mentioned above, target-projectile cluster ions appear in the time-of-flight mass spectra at lower impact speeds than atomic projectile ions (except for aluminium projectiles, cf. Figure 4.8 - 4.10). At impact speeds of about 10 km/s, the amount of target-projectile cluster ions relative to target ions is approximately 0.1, except for the PANi-PS-latex sample, where this ratio is 1.0. It turns out that the relative abundance of target-projectile clusters is decreasing with increasing impact speed. The decrease depends on the projectile material and is highest for iron ($\propto v^{-2.5}$) and lowest for carbon ($\propto v^{-0.9}$). The decrease of the relative cluster abundance for the latex sample is similar to the iron sample, but the relative cluster portion is 10 times higher than for iron at all impact speeds.

Even when the atomic projectile ions appear first in the mass spectra, the target-projectile cluster ions are more abundant than the atomic ions. Only for high impact speeds the atomic projectile ions will dominate the cluster ions in the mass spectra. The following Table 4.11 gives an overview of the impact speeds where the abundance of target-projectile cluster ions exceeds the abundance of the atomic projectile ions.

Projectile Material	Impact speeds, where $\frac{n_{P-T\,cluster\,ions}}{n_{P\,atomic\,ions}} > 1$
Aluminium	-
Carbon	6 - 14
Carbon + Na	7 - 16
Iron	4 - 8
PANi-PS-latex	12 - 18

Table 4.11: Impact speed ranges (in km/s), where target-projectile cluster ions are more abundant than the corresponding atomic projectile ions.

Carbon cluster ions and hydrocarbons

Knabe (1983) already reported the observation of complex cluster molecules containing up to 13 C-atoms. While he got his results from shooting iron projectiles onto a carbon target, in this work carbon was used as projectile material. The time-of-flight mass spectra from carbon and latex projectiles in this work often show a dozen of equidistant mass lines. It should be mentioned here that approximately 10 % of the mass spectra obtained from both types of latex-projectiles (PANi-PS, PPY-PS) show features that consist of 4 - 6 broad bulges which cannot be identified as known mass lines. Good examples are the "normal" mass spectra in Figure 4.18 and in Figures D.34, D.35 and D.37 in Appendix D.7. The 10 % other spectra are discussed later in Section 5.2.4. Since it is not possible to distinguish a priori between clusters of pure carbon atoms and hydrocarbons, all clusters which appear in the mass scale at a multiple of 12 are assigned as carbon clusters. The relative abundances of the clusters in the total mass spectrum for different impact speeds are shown in Figure 4.19. It is obvious, that the clusters with odd numbers of C-atoms are more abundant than clusters with even numbers of C-atoms. The abundance of clusters with more than 9 C-atoms (except for 11 C-atoms) in the latex spectra are strongly decreasing with rising impact speed. Table 4.12 shows how much the

cluster ions contribute to the total spectrum in the accessible impact speed range. For carbon projectiles, the clusters ions contribute approximately 30 % of the mass spectrum. For the latex projectiles this contribution is even higher: 40 - 50 %. The amount of carbon atoms that are bound in cluster ions relative to the amount of atomic carbon ions is calculated as follows:

$$\frac{\text{atoms in clusters}}{\text{C} - \text{atom}} = \frac{\sum_n \cdot I_{C_n}}{I_C}, \tag{4.9}$$

where I_{C_n} is the mass line integral of cluster ions that contain n carbon ions and I_C the mass line integral of atomic C-ions. From Table 4.12 one sees that the $\frac{\text{atoms in clusters}}{\text{C}-\text{atom}}$-ratios for carbon and latex projectiles strongly decrease with rising impact speed, due to the formation of less complex clusters at high impact speeds or the thermal destruction of complex clusters in hot plasma. It has to be noted, that it was not possible to distinguish between Na^+ and C_2^+ ions, so that we have no reliable data for the C_2^+ abundances. Since for the latex sample it is not clear whether the clusters origin from pure carbon or hydrocarbons, only a power law depending on the impact speed for the carbon projectiles was calculated and plotted for the $\frac{\text{atoms in clusters}}{\text{C}-\text{atom}}$-ratio (cf. Figure 4.20 and Eq. 4.10).

$$\text{C} - \text{atoms in clusters} = 1.0 \cdot 10^6 v^{-3.6} \cdot n(\text{C}^+ - \text{ions}) \tag{4.10}$$

A direct comparison of the cluster abundances for carbon and latex, as shown in Figure 4.21 for a 15 km/s projectile impact speed, shows that cluster ions with up to 8 C-atoms are relatively more abundant in the spectra from latex projectiles while cluster ions with more than 8 C-atoms are relatively more abundant in the spectra from carbon projectiles.

Impact speed [km/s]	Carbon		PANi-PS-latex	
	ion contribution	$\frac{\text{atoms in clusters}}{\text{C}-\text{atom}}$	ion contribution	$\frac{\text{atoms in clusters}}{\text{C}-\text{atom}}$
10	0.26	209	0.48	27100
15	0.30	88	0.38	606
20	0.30	23	0.40	51
25	0.32	8	0.48	9

Table 4.12: Relative abundances of cluster ions to the total amount of ions (ion contibution) depending on the impact speed in the time-of-flight mass spectra from carbon and PANi-PS-latex. Additionally the total number of C-atoms that are bound in clusters per single C-ion in the spectra are given.

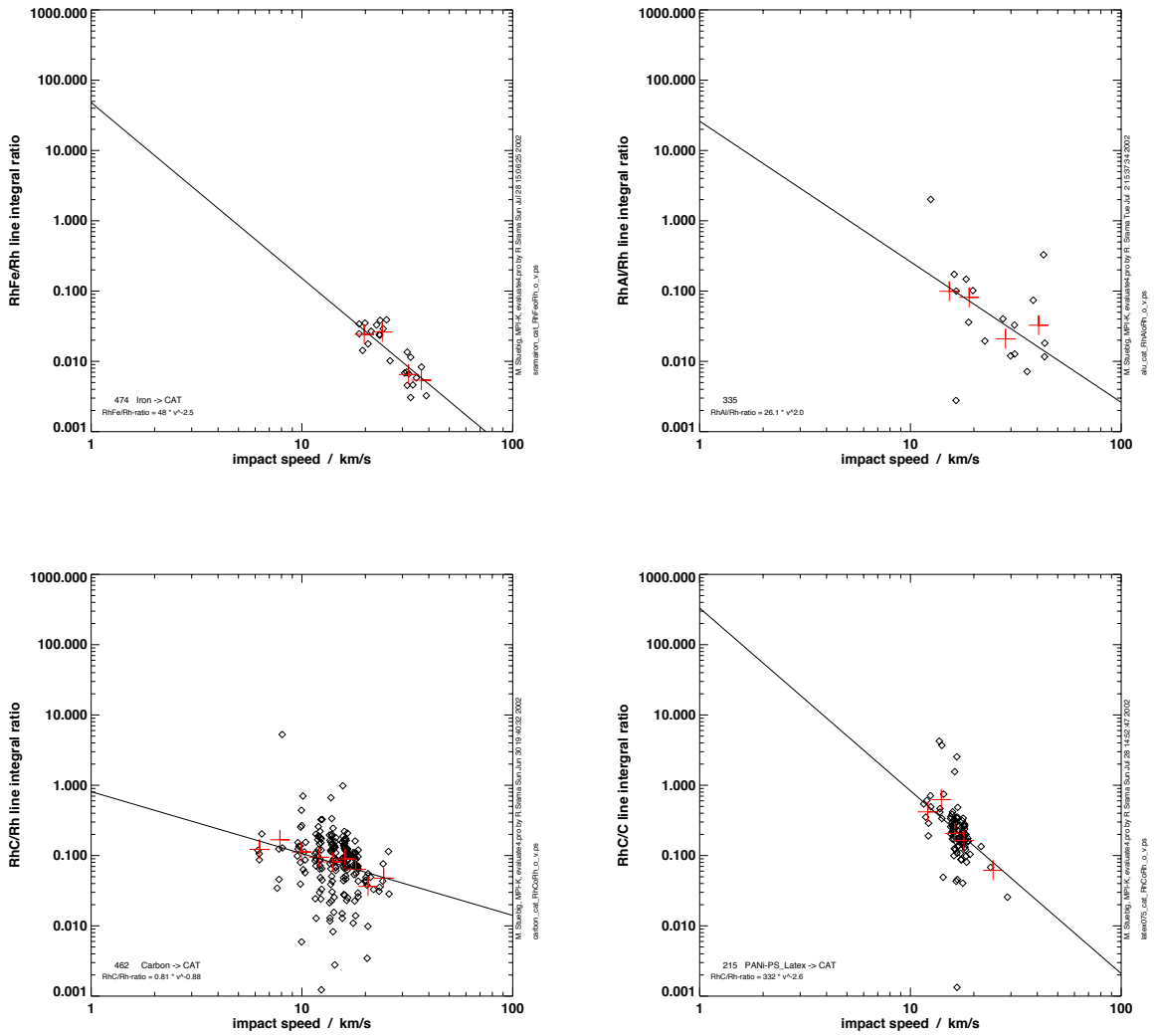

Figure 4.17: Overview of the relative abundances of target-projectile cluster ions compared to the amount of target ions. The diagrams show the results for iron (top left), aluminium (top right), carbon (bottom left) and PANi-PS-latex projectiles (bottom right).

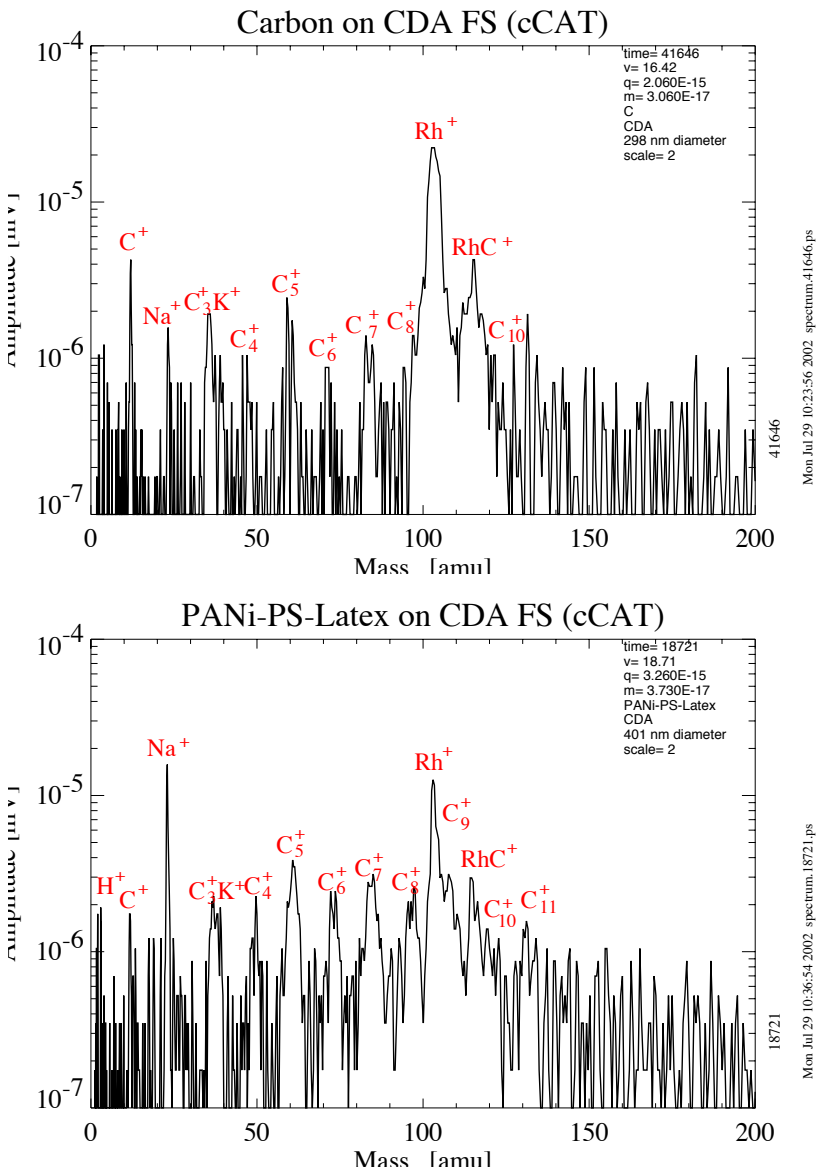

Figure 4.18: Time-of-flight mass spectra from a carbon (upper figure, 300 nm diam., 16.4 km/s) and a latex projectile (lower figure, 400 nm diam., 18.7 km/s).

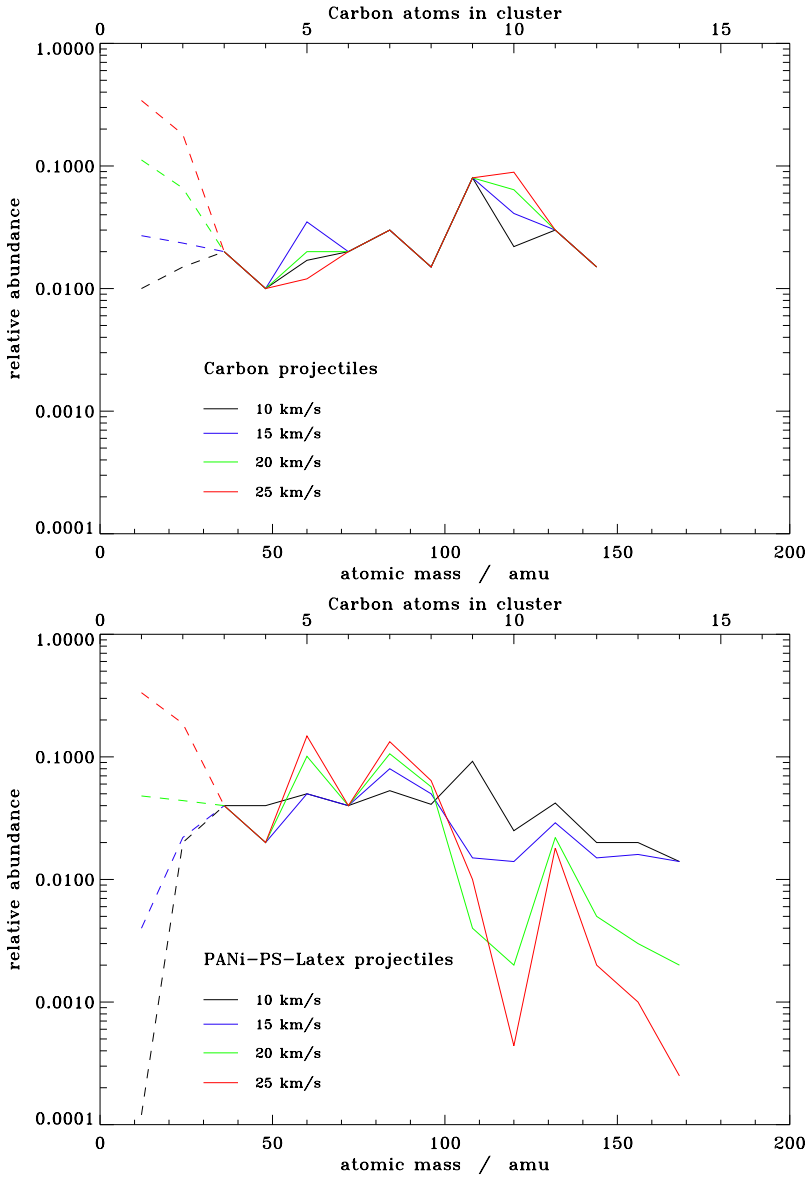

Figure 4.19: Carbon cluster abundances in the time-of-flight mass spectra for carbon projectiles (upper diagram) and latex projectiles (lower diagram). The relative abundances are given for impact speeds between 5 and 25 km/s. Dashed lines: no data for C_2^+-ions.

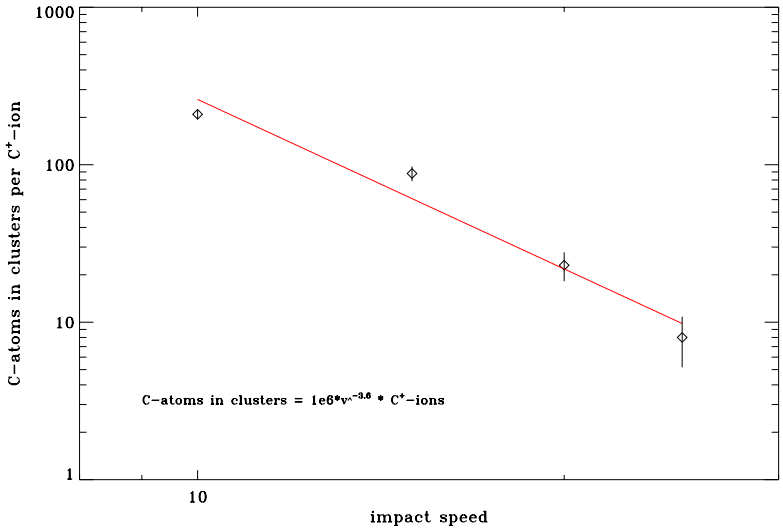

Figure 4.20: Number of carbon atoms bound in clusters for each single C^+-ion depending on the impact speed.

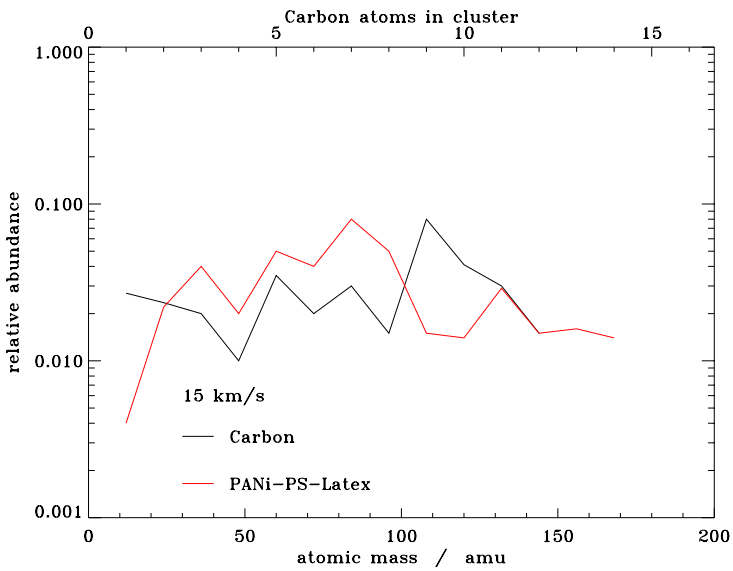

Figure 4.21: The relative abundances of carbon clusters in the mass spectra compared for carbon (black line) and latex (red line) projectiles at 15 km/s impact speed.

4.3.6 Possibly multiply ionized atoms

In the TOF mass spectra of fast aluminium projectiles often appeared mass lines at positions around 10 and 14 amu which could not easily be assigned to C^+- and O^+-ions as appearing in TOF mass spectra from iron projectiles (Figure 4.22). Otherwise this would mean that the two mass lines are shifted about 2 amu against all other mass lines. An assignment of theses lines with masses of 9 and 13.5 amu would correspond with the positions of Al^{2+}- respectively Al^{3+}-ions in the time-of-flight mass spectra. Figure 4.22 shows that the mass lines Al^{2+} and Al^{3+} shift towards their nominal ion mass position with rising impact speed. The mass line position can described as follows:

$$\begin{aligned} Al^{2+} &: \quad m(\text{amu}) = 15.4 - 0.046 \cdot v \\ Al^{3+} &: \quad m(\text{amu}) = 11.9 - 0.041 \cdot v \end{aligned}$$

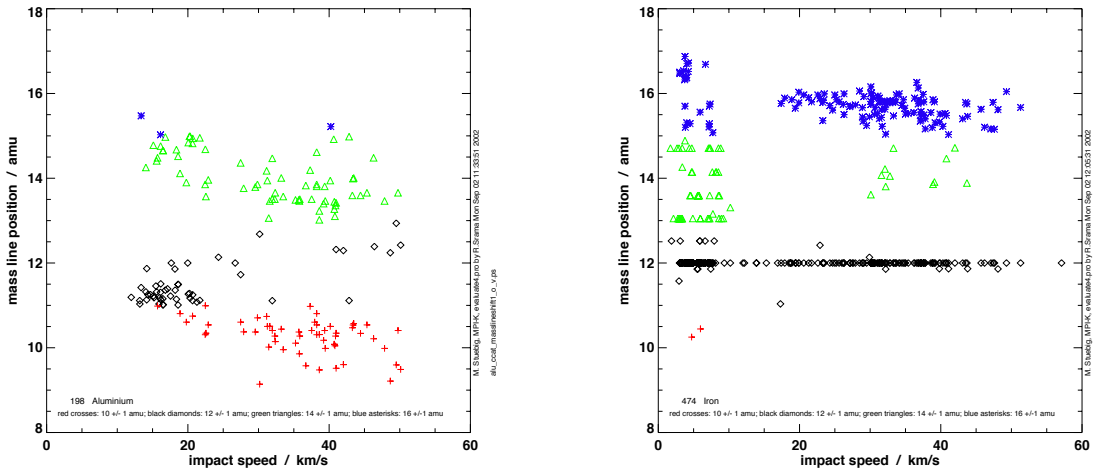

Figure 4.22: The diagram on the left side shows the positions of the possibly Al^{2+}- and Al^{3+}-mass lines in the time-of-flight mass spectra of aluminium projectiles, depending on the impact speed. For comparison, in the right diagram are shown the positions of the C^+- and O^+-mass lines in the mass spectra of iron projectiles, depending on the impact speed.

Comparing the mass spectra at various impact speeds (cf. Figure D.33 on page 198), it appears that the relative contribution of the multiply ionized Al-atoms to the mass spectrum rises with increasing impact speeds. A detailed analysis of the specific contribution to the impact plasma (upper diagram in Figure 4.23) shows, that the detectable contribution of Al^{2+} starts at impact speeds of 15 km/s and reaches a maximum of 10 % at about 30 km/s and decreases slightly for even higher impact speeds. The contribution of Al^{3+} starts above 20 km/s and rises slightly to a values between 1 and 10 % for impact speeds up to 50 km/s. The lower diagrams in Figure 4.23 show the relative contribution of Al^{2+} and Al^{3+} to singly charged Al^+. Since the Al^+ mass line is absolutely dominating the TOF mass spectra within the accessible impact speed range (cf. upper diagram in Figure 4.8 on page 38), the relative contributions of the multiply ionized Al-atoms to Al are similar to their contribution to the

total spectrum.

These results are encouraging to look into the time of flight spectra of iron projectiles. In Section 4.3.5 the appearance of a peak at 28 amu in the mass spectra has already been mentioned. Unclear is, whether the peak is produced by CO^+ molecular ions (as residua from the carbonyl-iron production process) or whether the peak represents doubly ionized Fe^{2+}-ions. Also a combination of both is imaginable. Additionally a peak at the position of 51 to 52 amu appears frequently in the TOF mass spectra. With respect to the possibility of multiple ionization, this peak might be identified as doubly ionized Rh^{2+}-ions from the target. The spectrum in Figure 4.24 represents an impact of a 30-40 km/s, 200 nm iron particle. Characteristic mass peaks at 28, 51.5, 56 and 103 amu appear as projectile and target ions and their doubly ionized states. The ratios of 28 amu-ions to Fe^+-ions and 51.5 amu-ions to Rh^+-ions are increasing depending on the impact speed proportional to $v^{2.0}$ for rhodium and $v^{3.5}$ for iron.

A comparison of the appearance of specific mass lines in the TOF-spectra from aluminium and iron projectiles (Figure 4.25) shows that the integrals of Al^{2+} and Al^{3+} in the spectra of aluminium projectiles are correlated as well as the integrals of C and O in the spectra of iron projectiles. This means a nearly constant line integral ratio of the correlated mass peaks in the spectra. Nevertheless, the correlation functions for both cases are different: $Al^{3+} = 0.8 \cdot {Al^{2+}}^{0.71}$ vs. $C^+ = 3.0 \cdot {O^+}^{0.55}$. The integrals of Al^{2+} to Al respectively 28 amu to Fe seem not to be correlated. This might be due to the fact that a strong atomic mass line can be produced by both a large projectile or a high impact speed. Due to their high ionization potential, C^+- and O^+-ions or multiply ionized atoms like Al^{2+} and Al^{3+} will only appear at high impact speeds, which were only derived with small particles.

For the carbon or latex projectiles no specific doubly ionized atoms (e.g. for C or Rh) could be found in the mass spectra. This might be due to low impact speeds ($v < 20$ km/s) or low projectile densities.

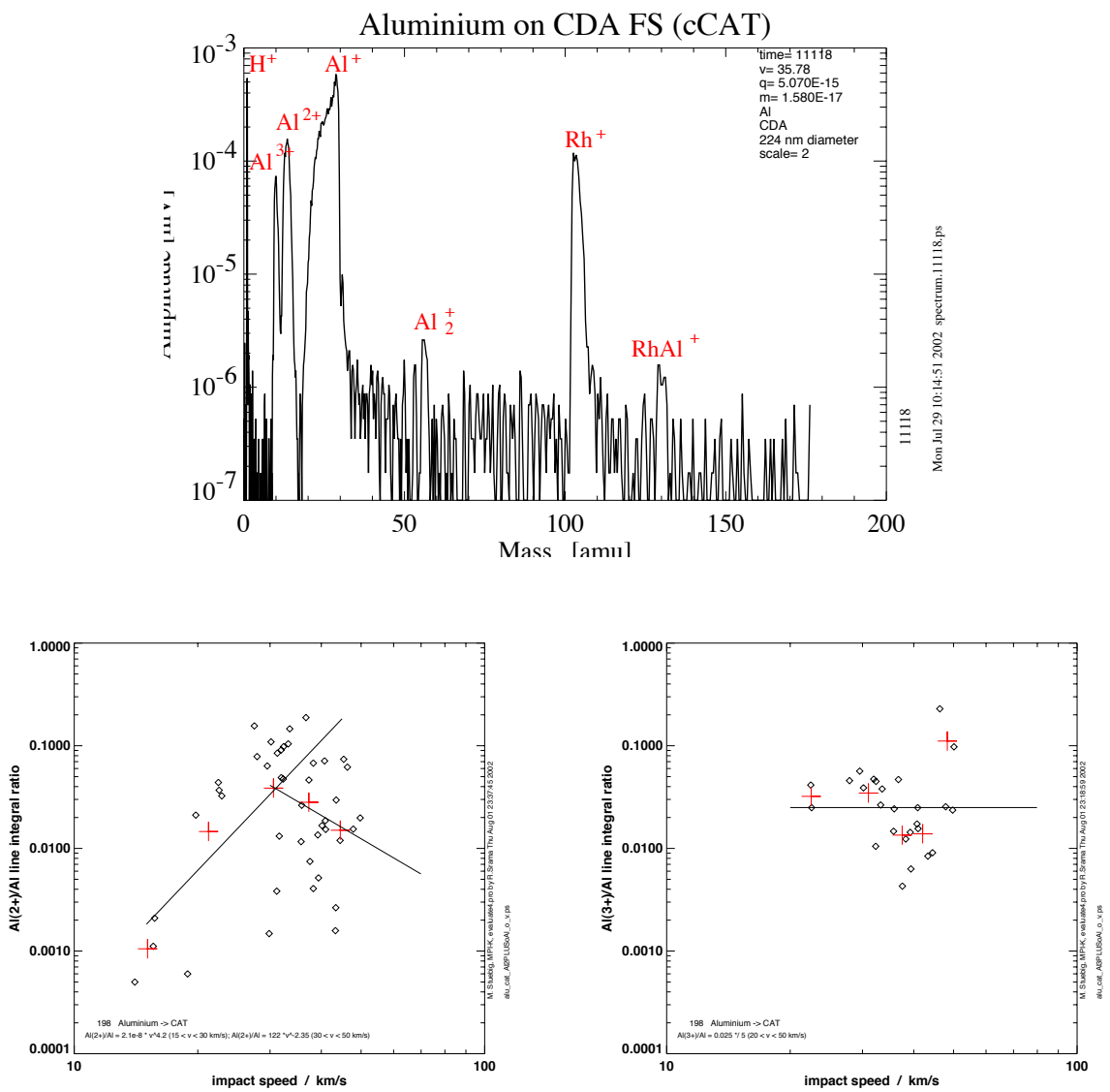

Figure 4.23: Upper figure: Time-of-flight mass spectrum of a 220 nm aluminium projectile that hits the CAT target with a speed of 35.8 km/s. The spectrum shows strong mass lines of multiply ionized aluminium atoms and also some clusters of projectile atoms and target-projectile ions. Lower figures: Relative contribution of Al^{2+}-ions (left) and Al^{3+}-ions (right) with respect to the amount of Al^{+}-ions

.

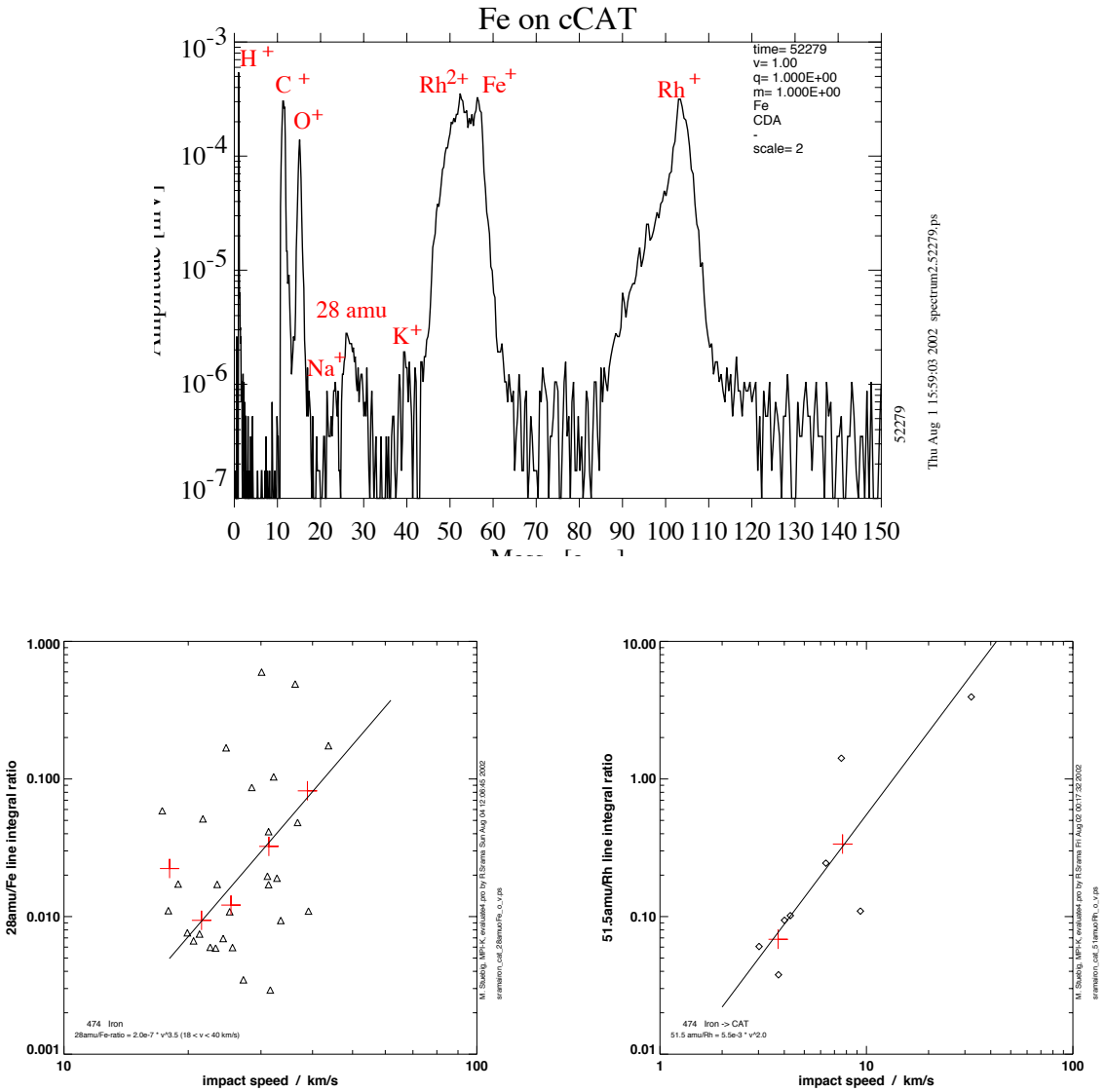

Figure 4.24: Upper figure: TOF mass spectrum of an iron projectile impacting on the CAT of CDA with 30-40 km/s (ca. 200 nm diameter). The spectrum shows mass line signatures at 1, 12, 16, 23, 28, 39, 51.5, 56 and 103 amu. Relative contribution of 28 amu-ions to Fe^{+}-ions (lower left diagram) and 51.5 amu-ions to Rh^{+}-ions (lower right diagram).

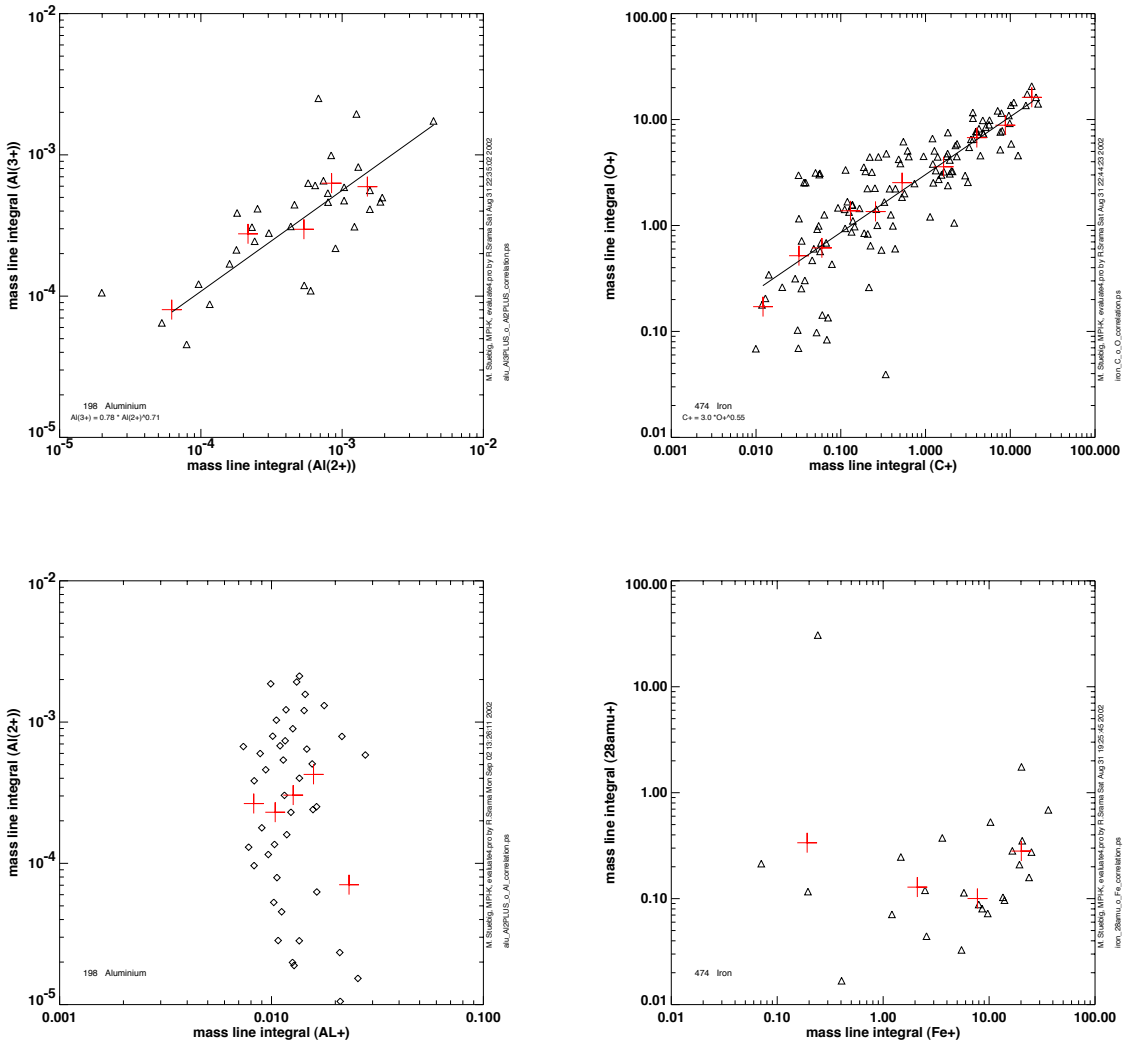

Figure 4.25: Correlations between the appearance of specific mass lines in the time of flight spectra for aluminium projectiles (left column) and iron projectiles (right column). The diagrams in the upper row show the correlations between the integrals of the Al^{3+}- and Al^{2+}-mass line (upper left diagram) respectively between the C- and O-mass line (upper right figure, this diagram has been already shown before and is added again for better comparison). The diagrams in the bottom row show the correlations between Al^{2+} and Al^{+} (lower left diagram) respectively the 28 amu mass line and the iron signature.

4.3.7 Contaminated projectiles

In this work one carbon sample was contaminated with sodium by keeping the carbon powder two weeks in a closed tin together with a block of pure sodium. The low melting and vaporizing temperatures of sodium should lead to a degassing of sodium and a not negligible sodium vapor pressure inside the tin. The sodium molecules may react with the carbon particles and contaminate their surface. Indeed, Figure 4.9 on page 39 shows that sodium ions will dominate the time-of-flight mass spectra for much higher impact speeds than for pure carbon projectiles. Comparing the relative amount of sodium to rhodium (Figure 4.26), the sodium contaminated carbon sample shows ten times higher $\frac{\mathrm{Na}}{\mathrm{Rh}}$ ratios than the pure carbon sample for all impact speeds between 8 and 20 km/s. Although this crude contamination method doesn't allow a reliable estimation of the sodium amount on the particle surface, the results show that a fine surface contamination of the particles may have a large impact on the chemical composition of their impact plasma.

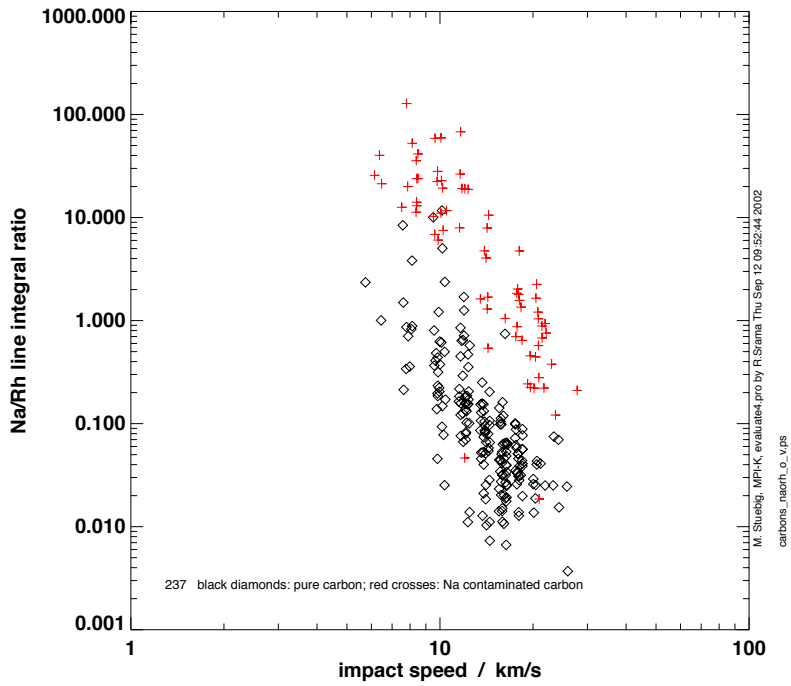

Figure 4.26: Na/Rh-ion ratio for sodium contaminated carbon projectiles (red crosses) and pure carbon projectiles (black diamonds).

4.3.8 Line shape

Regarding the line shape of the aluminium peak at 27 amu in the mass spectra, an obvious change with varying impact speed can be seen (Figure 4.27).

For low impact speeds ($v < 10$ km/s) the mass line shows a broad tail towards higher masses. With rising impact speed this tail is more and more reduced till the line appears nearly symmetric at medium impact speeds ($15 < v < 20$ km/s). For high impact speeds ($v > 25$ km/s) the tail towards higher masses has completely disappeared, but a shift of the left flank of the aluminium mass line to lower masses begins and proceeds for higher speeds. The change of the line asymmetry should be visible in the ratio of the width of the left to the right part of the full width half mean-value with respect to the position of the peak maximum: $\frac{t_{left}}{t_{right}}$ (cf. Figure 4.28). This ratio should be smaller than 1 for low impact speed spectra and larger than 1 for high speed spectra. From Eq. 4.3 follows that a varying time length Δt of any flank corresponds directly to a varying $\Delta\sqrt{m}$ broadness of the line.

Unfortunately the change of the line asymmetry has only been evaluated for the flank width at the half maximum level. At this peak-height the Al- and C- mass line from aluminium respectively carbon projectiles show a mean value of $\frac{t_{left}}{t_{right}} = 1.0$ for the flank width ratio, although Figure 4.27 shows an obvious change of the line profile. A similar evaluation of the flank width ratios for the H^+- and the Rh^+-mass line in the TOF mass spectra from aluminium, carbon and iron projectiles yields impact speed independent ratios of 1.0 for H and 0.7 for Rh. Nevertheless the Rh-mass line is known to have a tail towards lower masses. A new evaluation of the flank width ratios at e.g. quarter maximum peak heights should yield more reliable values.

Broad aluminium peak

The time-of-flight mass spectra from aluminium projectiles at low impact speeds show a broad bulge to higher masses behind the Al-mass line at 27 amu (cf. Figure D.33). This bulge is vanishing with increasing impact speed. One possible explanation might be a contamination of the aluminium sample with hydrocarbons starting with C_2H3 at 27 amu (STEPHAN, 2002). A similar bulge can be observed in the mass spectra of the PANi-PS-latex sample. Another explanation might be the duration of the ion release. If large aluminium ions hit the target, on the front end aluminium ions are generated while the back end is still "cold". Since the aluminium sample provides the largest projectiles in the present data set (grain diameters up to 3 μm), the duration of the impact process can play a role. But the calculations in Section 4.3.1 yield impact times in the order of 10^{-8} s, what is in good agreement with the time-resolution of the flight-time spectrum. A last possibility is Debye-shielding. The charged particles inside a dense plasma cloud are shielded against the external acceleration potential. This will be discussed later (cf. Section 5.1.3).

Mass line shifting

It is remarkable to note that the maximum position of the aluminium mass line in the mass spectra of aluminium projectiles is shifting from 27 amu for low impact speeds at about 5 km/s to 28 amu for high impact speeds up to 50 km/s (left diagram in Figure 4.29). It has to be noted that this shift is measured for impact events where the aluminium line peak was not used as reference mass peak for the mass scaling. How this shifting corresponds to the change of the line shape could not be figured out, since the line asymmetry has to be evaluated for smaller heights than the half peak maximum. In Section 4.3.6 already a shifting of the Al^{2+}- and the Al^{3+}-mass line has been reported. This shifting is in the opposite direction than for the Al^+-mass line itself. If the mass line shifting for multiply

ionized atom lines is related to plasma effects (time of ion formation, shielding effects) is unclear.

If the Al^{2+}- and Al^{3+}-mass lines would be assigned to C and O, and if these were described as surface contaminations, the mass line shifting might be explained by their different energy distribution. Then also the Na- and K-mass lines, especially in the case of sodium contaminated carbon projectiles, should show shifting effects. But both mass line positions show only a scattering within the uncertainty of the mass determination, which is $\Delta m \approx 1$ amu for Na and K. However, the scattering of the sodium peak position is between 23 and 24 amu in the mass spectra of iron projectiles and between 22 and 23 amu in the mass spectra of aluminium projectile. This general effect might be related to the choice of the reference mass lines.

The projectile mass lines for other projectile materials, like carbon or iron show no shifting effects at all (cf. right diagram in Figure 4.29). Also the H- and Rh-mass line maximum positions show no shifting depending on the impact speed in the mass spectra of aluminium, carbon and iron.

The results from the pure and the contaminated carbon samples contradict the statement of Krüger and Kissel (1987), that in the case of core-mantle particles, ions from the mantle material will be generally ”earlier” in the time-of-flight spectra than ions from the core material due to their earlier formation and due to higher ion energies up to 150 eV, compared to 50 eV of the bulk material . But there are two open questions: Can the sodium contaminated carbon projectiles be considered as core-mantle particles? And is the mass resolution of the CDA instrument to low, to register this effect?

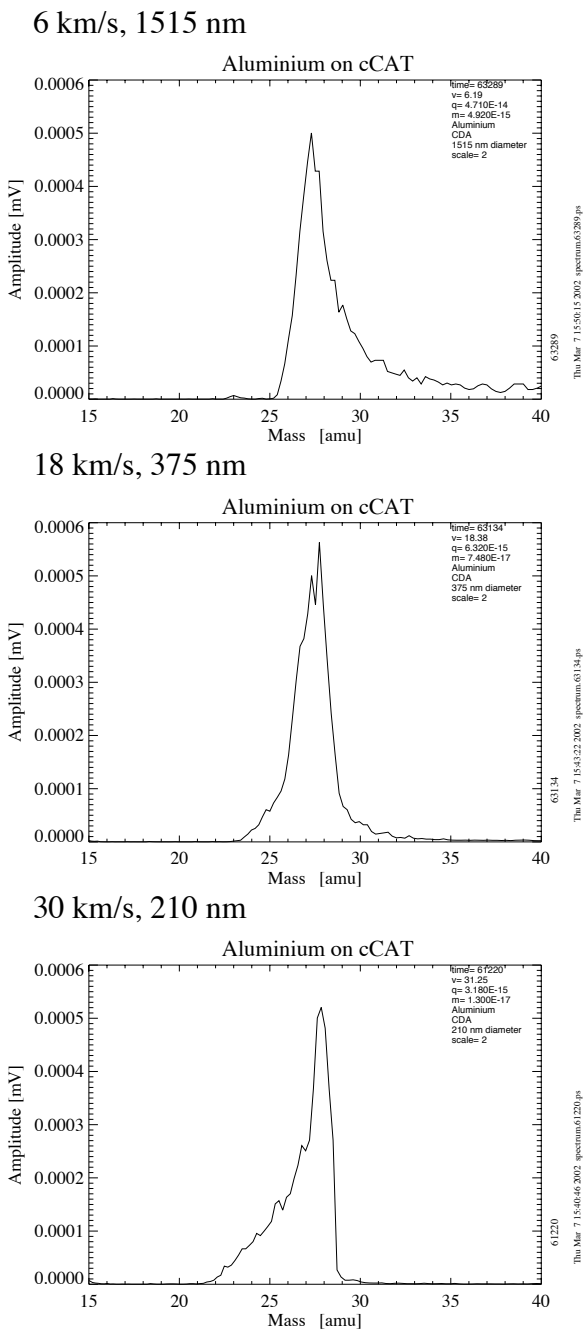

Figure 4.27: Line profile of the Al^+ mass line from impact spectra of pure aluminium projectiles depending on the impact speed.

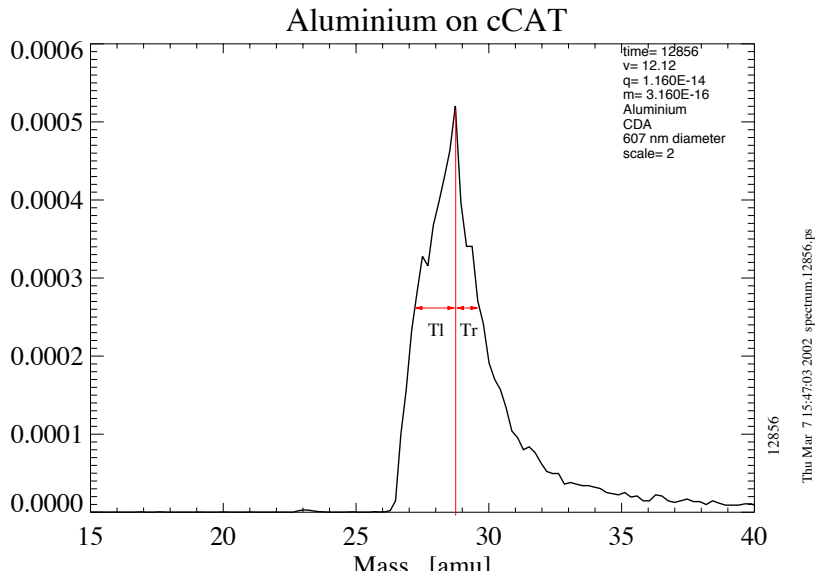

Figure 4.28: Definition of the left flank width t_{left} and the right flank width t_{right} with respect to the peak maximum position.

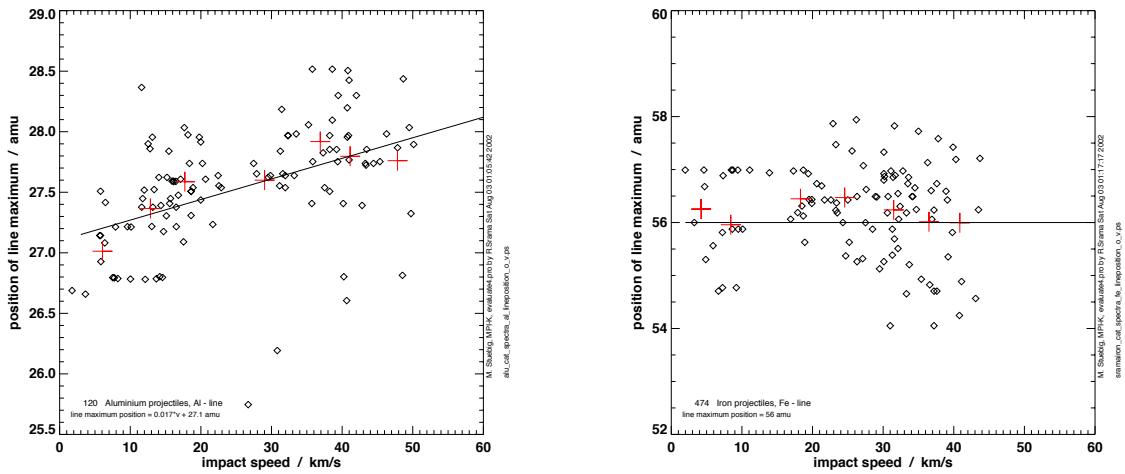

Figure 4.29: Position of projectile material mass line maximum depending on the projectile impact speed in the time-of-flight mass spectra. Left diagram: 27 amu mass line (Al^+) for aluminium projectiles, right diagram: 56 amu mass line (Fe^+) for iron projectiles.

4.4 Shots on the target of CIDA

To get a deeper insight into the broad peaks from the carbon and latex TOF-mass spectra, projectiles from the PANi-PS-latex sample were shot on the target of the CIDA engineering model. For impact speeds between 6.0 ± 0.5 and 18.0 ± 0.5, 15 time-of-flight mass spectra at each impact speed interval have been obtained. The impact speed interval was raised in steps of 2 km/s. The CIDASPEC3-software tool allows a common readout of three signals: target-signal (to measure the impact charge), multiplier-signal (contains the TOF-mass spectrum), anode-signal (linear signal of the TOF mass spectrum). The 15 flight-time spectra in each impact speed interval were converted into mass spectra by using the starting point of the target-signal amplitude as zero time $t_0 = 0$. The mass scale was applied by empirical evaluated a and b values for the flight-time to mass conversion in formula 4.3. Afterwards the amplitudes of the multiplier signals were linearized and added up to a sum spectrum. Regarding the resulting spectra, for high impact speeds one can clearly see the two isotopic mass lines from the silver target at 107 and 109 amu. The mass resolution is in the order of $\frac{m}{\Delta m} \approx 100$ and therefore 3 to 5 times better than for CDA. Since the polarity of the CIDA target voltage can be changed, the instrument allows the investigation of positive ions as well as negative ions. The results from shooting PANi-PS-latex projectiles will be shown in the following subsections.

4.4.1 Positive Ions

A mean spectrum of 13 PANi-PS-latex projectile impacts is shown in Figure 4.30. The silver-isotopes can be seen as well as H-, C, Na and K-ions. Next to these ions appear broad groups with mass peaks at (49-51 amu), (63, 65 and 67 amu), (70 and 72), (84 and 86 amu), 98 amu, (120 and 122), 134, 141 amu and at (147-148 amu). Values in parentheses describe the peaks that belong to a group of lines.

Three mass spectra of a data set with 18 km/s projectile impact speed showed a completely different time of flight mass spectrum, as shown in Figure 4.31. These spectra are dominated by a broad peak at 78 amu. Additionally appear groups of mass lines at (29 and 31 amu), (42, 44, 46 and 48 amu) and (58, 60 and 62 amu). Similar group triplets but without resolution of single mass lines can be found around 122, 138 and 152 amu as well as around 198, 212 and 228 amu and 258, 272 and 290 amu. The group with the highest mass appears at 334 amu. None of the contamination ions (H, Na and K) are visible, also no silver ions appear in the spectra.

4.4.2 Negative ions

The time-of-flight mass spectra of negative ions show a complete different behavior. Very regularly appear groups of mass lines at equidistant mass positions. The peak heights within the group are altering from group to group but show a general trend of decreasing intensity with increasing mass. Figure 4.32 shows a mean spectrum of 14 PANi-PS-latex projectiles that hit the silver target with 16 km/s. The groups with higher maxima are (26-30 amu), (49 and 50 amu), (72 and 73 amu), (96, 97 and 98 amu), (120, 121 and 122 amu) and (144 and 146 amu). Groups of mass lines with lower maxima are (around 36 amu), (60 and 61 amu), (84 and 85 amu), (around 108 amu) and (around 132 amu). Such groups can be identified up to masses of 200 amu.

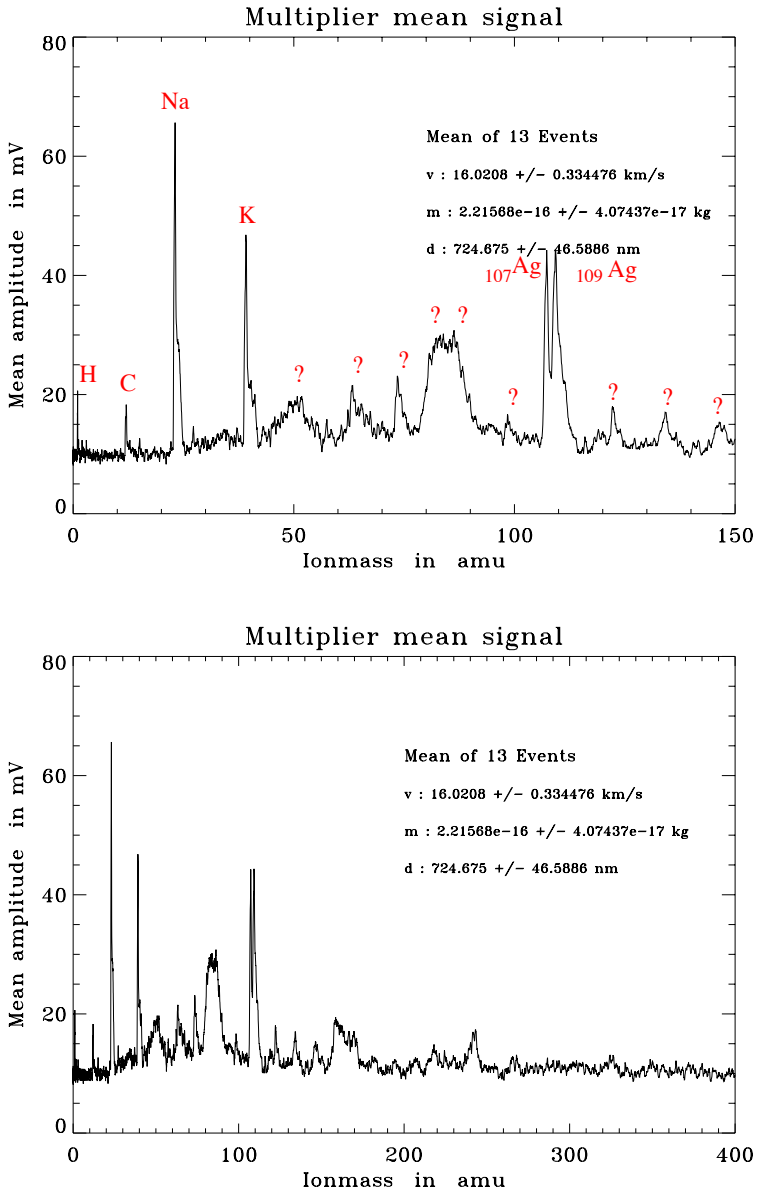

Figure 4.30: Mean mass spectrum of positive ions from 13 PANi-PS-latex projectiles that hit the target of CIDA with impact speeds of 16 km/s.

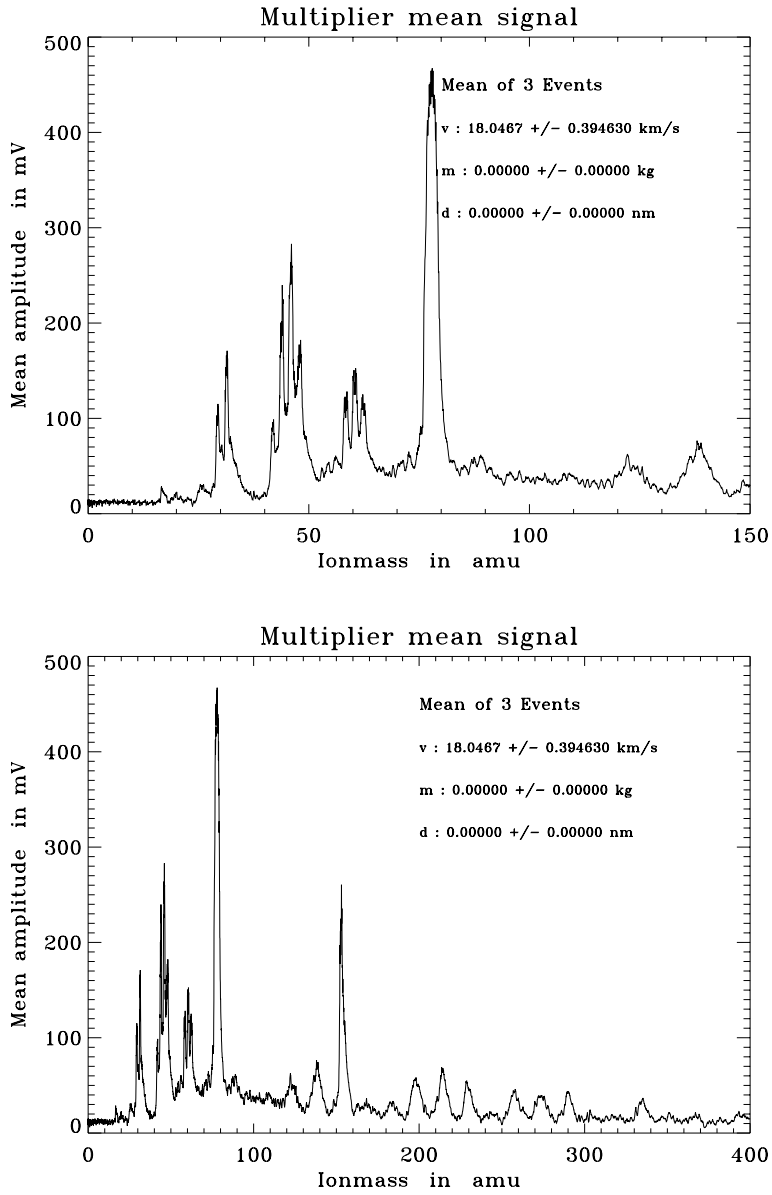

Figure 4.31: Mean mass spectrum of positive ions from 3 PANi-PS-latex projectiles that hit the target of CIDA with impact speeds of 18 km/s.

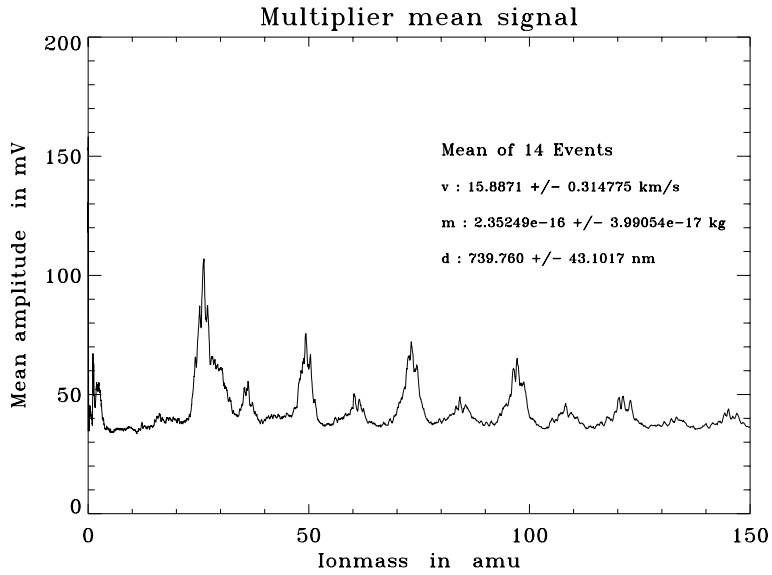

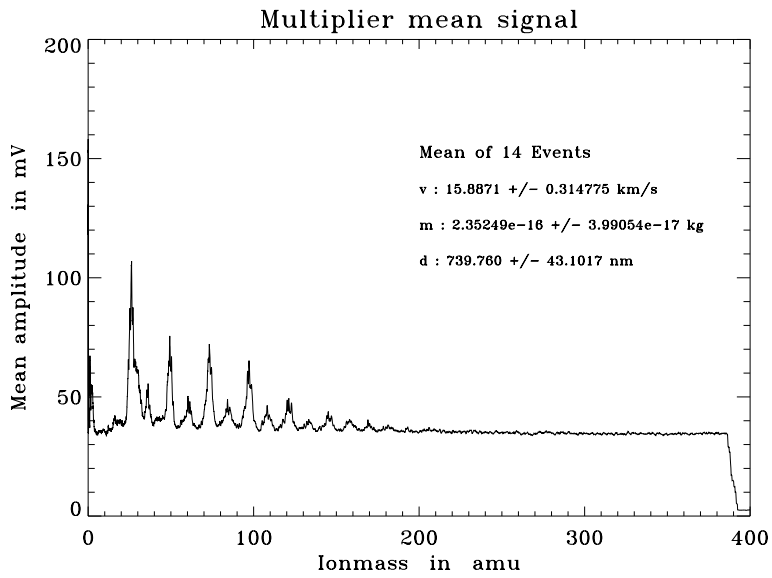

Figure 4.32: Mean spectrum of negative ions from 14 PANi-PS-latex projectiles that hit the target of CIDA with impact speeds of 16 km/s.

mass [amu]	possible molecules
27	CHN, C_2H_3
29	CH_3N, C_2H_5
31	CH_5N, H_3N_2
36	C_3
42	CH_2N_2, C_2H_4N, C_3H_6, N_3
44	CH_4N_2, C_2H_6N, C_3H_8, H_2N_3
46	CH_6N_2, H_4N_3
48	C_4
58	CH_4N_3, $C_2H_6N_2$, C_3H_8N, C_4H_{10}, H_2N_4
60	CH_6N_3, $C_2H_8N_2$, C_5
62	C_4N, C_5H_2, H_6N_4
63	C_4HN, C_5H_3
65	C_3HN_2, C_4H_3N, C_5H_5
67	C_2HN_3, $C_3H_3N_2$, C_4H_5N, C_5H_7
122	$C_5H_6N_4$, $C_6H_8N_3$, $C_7H_{10}N_2$, $C_8H_{12}N$, C_9H_{14}, C_9N, $C_{10}H_2$

Table 4.13: Possibly contributions to the mass spectra that were generated by hypervelocity impacts of organic polyaniline-coated polystyrene latex.

4.4.3 Mass line identification

Since the polystyrene and polyaniline material contains only, C, H and N-atoms, the mass lines in the TOF spectra can be identified with compounds of these elements. Possibly molecules for selected mass lines are summarized in Table 4.13. More molecules for other and higher mass positions can be found in (SILVERSTEIN, R.M. et al., 1981) and are shown in Figure 4.33. Since the molecular groups appear with mass distances of Δm = 14 respectively 16 amu, these differences will be caused by adding or splitting off CH_2- respectively NH_2-fragments to the existing molecules. The lines within each group are separated by a mass difference of Δm = 2 amu. This can be achieved by adding 2 H-atoms or replacing one C- by one N-atom and vice versa. However, ”incomplete” hydrocarbons like C_3H_5 tend to form positive ions much easier than ”complete” hydrocarbons like C_3H_6, where all possible bonding electrons are saturated (STEPHAN, 2002). The line groups for negative ions are separated by Δm = 12 amu (24 amu for group with high maxima respectively for groups with low maxima). This is a hint on adding/splitting off C-atoms to the existing molecules.

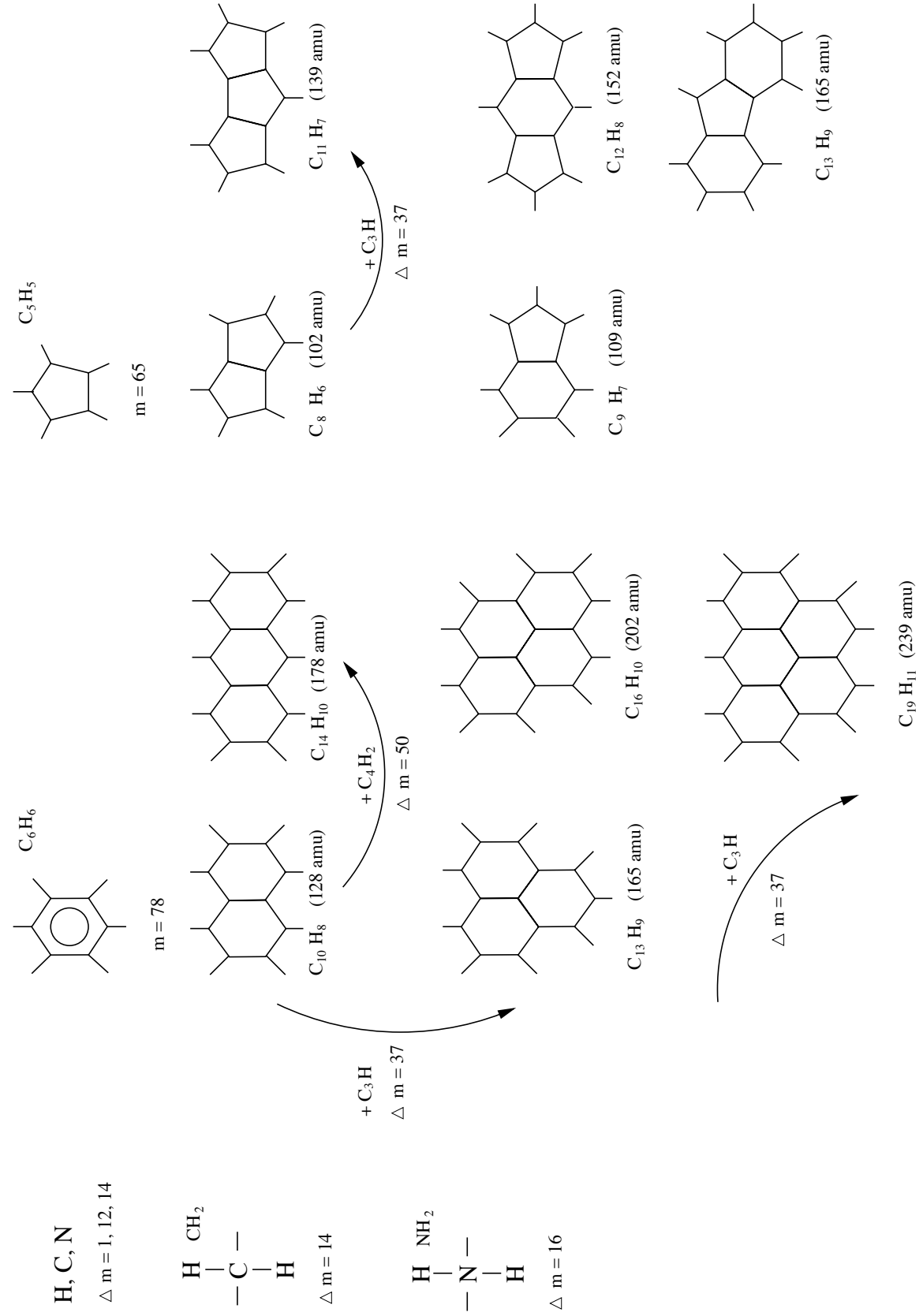

Figure 4.33: Possibly organic compounds that may form at the impact site. Cyclic carbon molecules can build complex molecules with high masses → Polycyclic Aromatic Hydrocarbons (PAHs).

4.4.4 Isotopic effects

In Table 4.14 are summarized the most important isotopes of chemical elements that appear in the mass spectra as projectile or target material or as contaminants. If the mass resolution is sufficient and if the signal to noise ratio of the mass line that represents the main isotope of an element is in the order of 100, isotopes which contribute more than 1 % to the isotopic composition should be detectable. Regarding Table 4.14 isotopes of the following elements should be detectable (in the order of the largest signatures): Ag, K, Fe and C. In this work, silver is only present in the target material of CIDA. In the mean spectrum in Figure 4.30 the two silver peaks with very similar peak amplitudes at mass positions of 107 and 109 amu can easily be seen. However, the signal amplitudes of individual spectra can vary significantly. The ratio of the peak amplitudes reflects well the actual isotopic abundances. Potassium, well known as contaminant material, shows a broad flank towards mass 40 and 41. Due to the high noise level, a final distinction whether the peak appears broadened by the $^{41}_{19}$K-isotope or by the energy- and angular-distribution of the ions respectively Debye-shielding (cf. Section 5.1.3 in the Discussion) cannot be given here. Regarding some single spectra, also a contamination with calcium $^{40}_{20}$Ca or hydrocarbons with 40 amu mass cannot be excluded. Iron as projectile material was only used for experiments with CDA. The mass resolution $\frac{m}{\Delta m} \approx 30$ at 56 amu (cf. Table D.19) would allow a distinction of both elements. Nevertheless, in none of he mass spectra a mass peak of $^{54}_{26}$Fe could be clearly figured out.

A special view should be given to carbon. Although the carbon isotope $^{13}_{6}$C contributes only 1.1 % to the total carbon, this isotope is important when considering the effect of cluster molecules which appear in the mass spectra of carbon and latex projectiles. If m is the atomic mass in amu of any carbon containing molecule, the heights of the mass peaks at $m+1$ and $m+2$ correlate as follows to the number n_C of carbon atoms inside the molecule (SILVERSTEIN, R.M. et al., 1981):

$$\frac{m+1}{m} \cdot 100 = 1.1\, n_C + 0.36\, n_N \tag{4.11}$$

$$\frac{m+2}{m} \cdot 100 = \frac{(1.1\, n_C)^2}{200} + 0.2\, n_O. \tag{4.12}$$

The numbers n_N and n_O consider the presence of oxygen respectively nitrogen within the molecule. From Eqs. 4.11 and 4.12 follows that next to the mass line of a C_5-cluster molecule at 60 amu will appear mass lines at 61 and 62 amu with peak amplitudes that are 5.5 % respectively 0.2 % of the 60 amu peak. For a low mass resolution as for CDA, the peaks would smear together and form a broader peak. If the signal to noise ratio is not to low, the 61 amu peak should appear in the spectrum. For a C_{11}-cluster molecule at 132 amu this effect is even more dramatic: at 133 respectively 134 amu the relative amplitudes are 12.1 % respectively 0.7 % of the 132 amu amplitude. Unfortunately these high absolute masses cannot be resolved even by CIDA. However the mass peaks will appear broader.

Element	Isotope	Abundance [%]	Mass [amu]
Hydrogen	${}^{1}_{1}$H	100.0	1
Carbon	${}^{12}_{6}$C	98.9	12
	${}^{13}_{6}$C	1.1	13
Nitrogen	${}^{14}_{7}$N	99.6	14
Oxygen	${}^{16}_{8}$O	99.8	16
Sodium	${}^{23}_{11}$Na	100.0	23
Aluminium	${}^{27}_{13}$Al	100.0	27
Potassium	${}^{39}_{19}$K	93.3	39
	${}^{41}_{19}$K	6.7	41
Iron	${}^{54}_{26}$Fe	5.8	54
	${}^{56}_{26}$Fe	91.7	56
	${}^{57}_{26}$Fe	2.2	57
Rhodium	${}^{103}_{43}$Rh	100.0	103
Silver	${}^{107}_{47}$Ag	51.8	107
	${}^{109}_{47}$Ag	48.2	109

Table 4.14: Terrestrial isotopic abundances of selected elements. Only isotopes with abundances > 1 % are listed.

Chapter 5

Discussion

One aim of this work is the improvement of the knowledge of the impact process (Section 5.1). The results for the measured charge yields are compared with former calibration work of the Galileo Dust detector and with the observations of the light flash that appears at hypervelocity impacts. Important similarities that lead to an improved understanding of the observed impact phenomena, especially for high impact speeds, were found. Broadened mass lines appearing at high impact speeds indicate high kinetic energies of the plasma ions. Taking the experimentally derived data of this thesis together with theoretically considerations a more complete understanding of different impact ionization regimes can be presented. The signatures in the time-of-flight mass spectra that were obtained in this thesis give hints on the chemical nature of the projectile that hit the CAT (Section 5.2). The investigation of single mass lines allows the verification of the present model that describes the relative target to projectile ion yield. It turns out that the present data fits the model only for iron projectiles. A further investigation of the specific ion yields allows to set up a new model for the ion yields that considers also the formation of contaminant ions and target-projectile cluster ions. The determination of absolute charge yields allows also to calculate the ionization degree of the projectile depending on the impact speed. The identification of specific molecular ions, depending on the projectile material makes possible to give rough classification attributes. This allows to classify unknown projectiles detected in space by their time-of-flight mass spectra. In Section 5.3 is discussed the possibility for multiply ionized atoms to appear in the mass spectra. Last but not least the impact ionization of microparticles is compared to laser induced ionization (Section 5.4).

5.1 Physical implications for the impact ionization process

The observation of the charge yield function depending on the impact speed is compared to former results. A reevaluation of the Galileo calibration data (Section 5.1.1) and a comparison with light flash observations at hypervelocity impacts (Section 5.1.2) are consistent with the observation of the charge yields in this thesis. The shape of the mass lines depending on the impact speed is a hint on the high ion energies of several 10 eV that appear at high impact speeds of several 10 km/s (Section 5.1.3). A general overview of present impact ionization models is given in Section 5.1.4. Section 5.1.5 summarizes the now known impact ionization regimes for microparticles depending on the impact speed.

Material	impact speed range [km/s]	charge/mass $\frac{q}{m}$[C/kg]	
		Göller & Grün	this work
Iron	$v < 6$	$0.1 \cdot v^{2.9}$	$0.07 \cdot v^{3.4}$
	$6 < v < 12$	$1.1 \cdot v^{1.5}$	$1.9 \cdot v^{1.4}$
	$12 < v < 60$	$1.5 \cdot 10^{-4} \cdot v^{5.2}$	$2.5 \cdot 10^{-4} \cdot v^{5.0}$
Carbon	$v < 12$	$0.08 \cdot v^{3.1}$	
	$12 < v < 20$	$2.3 \cdot v^{1.8}$	$0.5 \cdot v^{1.9}$
	$v > 20$	$6.0e-5 \cdot v^{5.3}$	
Silicate	$v < 6$	$3.3 \cdot 10^{-2} \cdot v^{4.6}$	
	$6 < v < 15$	$5.5 \cdot v^{1.7}$	
	$v > 15$	$5.1 \cdot 10^{-3} \cdot v^{4.2}$	

Table 5.1: Charge yields functions from different projectile materials. The values of this work are compared with values derived from Göller and Grün (1989).

5.1.1 Comparison with the Galileo Dust Detector System DDS

In Section 4.2.2 the charge yields from different projectile materials shot on the Impact Ionization Detector (IID) of the CDA-flight spare unit are shown. The yield functions show a proportionality to the projectile mass and the impact speed. The power law exponent for the impact speed is changing in certain impact speed regions. This behavior has already been reported by Göller and Grün (1989) from experiments with the Galileo Dust Detector System (DDS). Nevertheless, the authors gave only a mean value of 3.5 for the impact speed exponent β in the charge yield formula Eq. 4.1. A recalculation of the charge yields for specific impact speed ranges (where the exponent β is nearly constant) has been done here to compare the former data with the new data in this work. The obtained charge yields for carbon, iron and silicates are listed in Table 5.1 and compared to the measured charge yields at the ion grid from impacts onto the IID-target. Figure 5.1 shows a graphical comparison for the carbon and iron charge yields. It turns out, that the measured charge yield data from iron projectiles are well reproducible. In the case of carbon, this work provides only a lower impact speed range, in which the measured charge yields are one order of magnitude below the data of Göller and Grün (1989). Since both targets have a gold coated surface and a similar construction, the charge yields should be very similar. Why this is not the case for carbon is somewhat unclear. The impact site may play a certain role. The central region of the CDA detector area is fitted with the CAT, consisting of rhodium. Shots on this target have not been considered here. Shots on the central region of the Galileo DDS may yield better values for the carbon charge yield.

Göller and Grün explained the "lack" in the charge yield for medium impact speeds as follows: for low impact speeds, the charge yield should be dominated by the production of secondary ions from ejecta, mainly surface contaminants with low ionization potentials (sodium and potassium). From a later point on, the secondary ion production is not rising any longer and the primary ions from the impact site will dominate the total ion yield. Since here ions are produced from a volume (projectile volume, impact crater volume), this yield function should be steeper than the yield function from ionizing surface contaminants. This theory is corroborated by new results from Ratcliff et al. (1997). Their experimental setup allowed the measurement of both, the primary and the secondary ions. The yield functions show dominating secondary ions with an impact speed exponent $\beta = 3$ for low impact speeds and an exponent $\beta = 5$ from dominating primary ions for high impact speeds. Ratcliff et al. didn't observe an intermediate region as shown by Göller and Grün (1989) and in this work. Göller

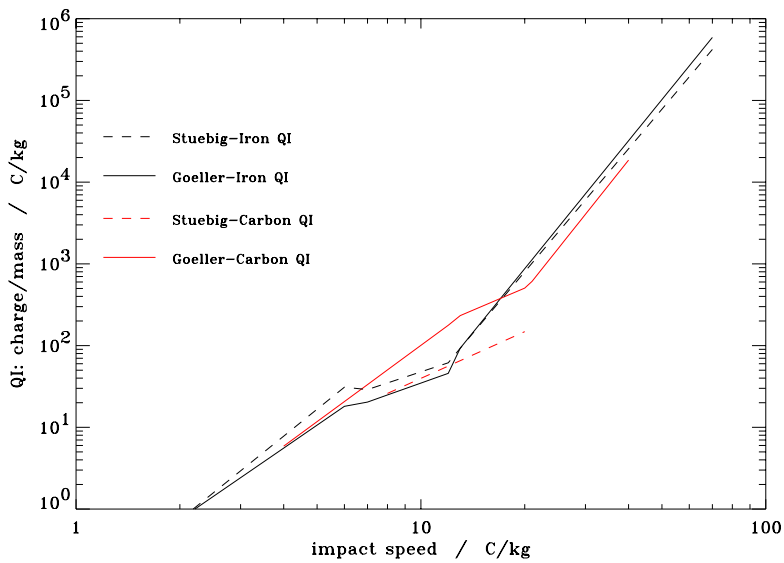

Figure 5.1: Comparison of the charge yields as measured at the ion grids from impacts of carbon (red curves) and iron projectiles (black curves) on the Galileo Dust Detector System (Göller and Grün, 1989, solid lines) and on the CDA IID-target (this work, dashed lines).

and Grün explained the intermediate region, characterized by very low β-values ($\beta < 2$) with melting and vaporizing processes: the impact energy is needed to heat, melt and vaporize the target material before ionizing it. Thus the energy cannot be provided for ion formation. The "melting-effect" is also observed from measurements of the light emission due to hypervelocity impacts (EICHHORN, 1972) as it will be discussed in the following subsection.

5.1.2 Comparison with light flash observations

Eichhorn (1976) observed the light flash that appears during the impact of hypervelocity projectiles. The total light energy from Al, Fe and W-projectiles shows a similar behavior as seen for the case of iron in Figure 5.2: A relative steep increase, followed by a flatter increase within an impact speed range of 4 - 10 km/s, followed again by a steep light energy increase. Only the impact speed depending light flash energy from carbon projectiles showed a different behavior. Comparing the energy curves with those of the total charge yield as measured from impacts at the CAT and the IID (cf. subsections 4.2.1 and 4.2.2), one may find a similar course for both, the light energy function and the charge yield function.

Eichhorn (1976) discussed the flattening of the functions with the approach of the impact energy to the melting temperature. Further investigations of the vaporization process (EICHHORN, 1978a) yielded degrees of vaporization between a few percent up to 70 % for impact speeds between 4 and 13 km/s, depending on the target material. A rough calculation, using the heat capacity c_p and the melting and vaporization heat (e.g. from (STÖCKER, 1994)), shows that at impact speed between 4 km/s (iron) and 5 km/s (aluminium) enough kinetic energy is present for a complete vaporization of the projectile. Taking into account, that a large fraction of the kinetic energy will be displaced to the target ($\propto \sqrt{\frac{\rho_P}{\rho_T}}$, (HORNUNG, K. and DRAPATZ, S., 1981)) and that other energy consuming processes are present (e.g. partial ionization), total vaporization will appear at much higher impact

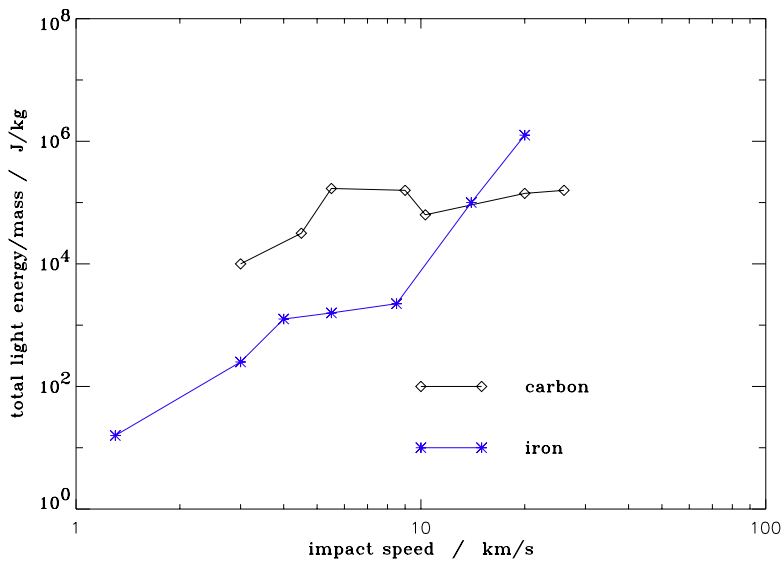

Figure 5.2: Total light energy of the impact flash from hypervelocity carbon and iron projectiles (data taken from Eichhorn, 1976).

speeds. This is similar to the development of the degree of ionization: at low impact speeds only a very low fraction of the total kinetic energy is used for projectile ionization. This fraction rises to a few percent for increasing impact speeds.

5.1.3 Characteristics of mass lines

First of all it has to be noted, that CDA has only a poor mass resolution of $\frac{m}{\Delta m} = 20 - 50$. This makes it difficult to distinguish between mass lines that are divided by a Δm of only 1 amu for nominal masses $m > 20$ amu. The mass lines appear broadened due to the energy and angular distribution of the generated ions at the impact site.

Energy and angular distribution

It is well known, that the ions will have an initial starting energy and angular distribution. Measurements with classical SIMS-methods yielded a rough cosine angular distribution (Eq. 5.1) (BENNINGHOVEN, A. et al., 1987). A more detailed analysis of the angular distribution by Krüger (1982) and Reber (1997) improved the angular distribution for the case of hypervelocity projectile impacts (Eq. 5.2). The angle ϑ in the angular-distributions is given relative to the target normal vector. The target normal has to be considered as symmetric axis.

In his Dissertation, Reber (1997) reported a Maxwell-Boltzmann-like exponential energy distribution function given in Eq. 5.3. Posner (1995) reported the appearance of Gaussian energy distributions (Eq. 5.4). However, the observed ion energies can reach values of several ten eV up to 150 eV for impact speeds of several 10 km/s. With Eq. 5.6 this corresponds to kinetic ion temperatures of $10^5 - 10^6$ K. Such values are in good agreement with the results from light flash observations (EICHHORN, 1976) at similar impact speeds. This is consistent with the results from Grün (2002) and Lavila

(2002a; 2002b), who approximated a Maxwell-Boltzmann distribution to the shape of the aluminium and rhodium mass line.

Øren (ØREN, 2000) found a combined energy and angular distribution given by Eq. 5.5.

$$n(\vartheta) = n_0 \cdot \cos(\vartheta) \tag{5.1}$$

$$n(\vartheta) = n_0 \cdot \cos(\vartheta) \cdot e^{\left(1-\frac{1}{\cos(\vartheta)}\right)^r} \tag{5.2}$$

$$n(E) = a\left(\frac{1}{k_B T}\right)^{\frac{3}{2}} \cdot E \cdot e^{-\frac{E}{k_B T}} \tag{5.3}$$

$$n(E) = \frac{1}{\sigma\sqrt{2\pi}} e^{-\frac{(E-E_0)^2}{2\sigma^2}} \tag{5.4}$$

$$n(\vartheta, E) = n_0 \cdot \cos(\vartheta)\cos(E) \tag{5.5}$$

$$E = k_B T = \frac{1}{2} m_{ion} v_{ion}^2 \tag{5.6}$$

From SIMS-experiments it is additionally known, that molecular ions show a fast drop of the distribution towards high energies, while atomic ions are known to have a much broader energy distribution (SHIMIZU, 1978).

Regarding the mass spectra in this work, the mass line of the target material Rh appears asymmetric with a broad tail towards lower masses. Since for projectile materials like aluminium or iron interferences with other mass lines can be excluded, this means that the target material ions have an initial energy distribution. Already Reber (1997) approximated successfully Maxwell-Boltzmann energy distributions to the Rh mass line. At high impact speeds ($v > 20$ km/s), the mass lines of the projectile materials aluminium and iron show a similar asymmetric shape. The impact speeds of the carbon and latex projectiles might have been too low to see this effect. The mass lines of hydrogen, sodium and potassium appear nearly symmetric at all impact speeds. Due to their nature as contamination material ions, they might be characterized by a Gaussian energy distribution (cf. (POSNER, 1995)).

Another hint on an initial energy distribution of the ions is the observed increase of the mass scale stretch parameter a for higher impact speeds in the correlation of the ion flight time to the ion mass (Eq. 4.3). This effect has been investigated in Appendix D.7.2.

An attempt to derive information on the energy distribution of the plasma ions from the relative Na/K-ion yield failed due to inconsistent data that shows additionally a large scattering. The idea was that Na and K are distributed well-balanced on the target surface. Due to their different ionization degrees the fraction of sodium ions relative to potassium ions should increase with rising impact speed till the energy distribution is such high that ion formation of both materials happens in a similar manner.

Debye-shielding

Debye-shielding is the effect that charged particles inside a dense plasma cloud are shielded against external electric fields by the surrounding charged particles. This can be expressed with a reduced

Coulomb-potential (Eq. 5.7), where λ_D is the characteristic Debye-length where the potential is reduced to $1/e$ (Eq. 5.8). The electron number density n_e is given in $1/\mathrm{cm}^3$.

$$V(r) = \frac{1}{4\pi\varepsilon_0}\frac{e}{r}\cdot e^{-r/\lambda_D} \tag{5.7}$$

$$\lambda_D = \sqrt{\frac{\varepsilon_0 k_B T}{2e^2 n_e}} \tag{5.8}$$

To make clear if Debye-shielding can be responsible for the broad ion bulge in the mass spectra of slow aluminium projectiles, at first the plasma density should be estimated. The total charge produced at the impact site by a 6 km/s, 1 μm aluminium projectile on the Chemical Analyzer Target is in the order of 10^{-12} C corresponding to 10^7 electrons. This charge may be distributed within a radius of 2μm what is approximately the double projectile radius (as found in impact crater studies at low impact speeds (NEUKUM, 1971)). With these values follows for $n_e = 2.4\cdot 10^{18}\,\mathrm{cm}^{-3}$. The plasma temperature at low impact speeds is assumed to be of the order 10^5 K. Then follows for the Debye-length $\lambda_D = 10\mu$m. This is 5 times larger than the size of the plasma cloud. Regarding the Debye-lengths for various impact charges depending on the size of the plasma cloud, it appears that Debye-shielding will play a minor role on the ion acceleration process even for an impact charge of 10^{-11} C within a volume of 1 μm diameter. Debye shielding might be responsible for the line asymmetry as observed for aluminium (cf. Section 4.3.8). But the influence of Debye-shielding should not be as large to explain the ion bulge in the mass spectra from aluminium projectiles.

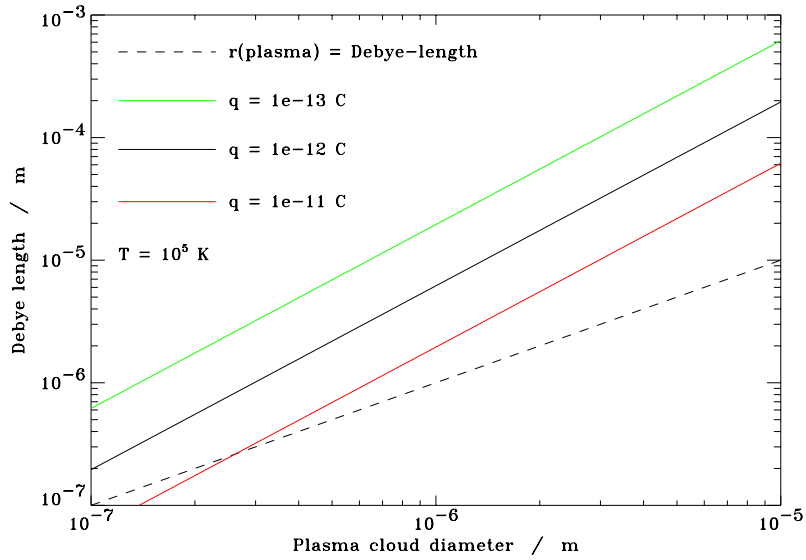

Figure 5.3: Debye-length λ for impact charges of 10^{-11}, 10^{-12} and 10^{-13C} depending on the size of the plasma cloud. The dashed line indicates where the Debye length is equal to the size of the plasma cloud.

5.1.4 A model of the impact ionization process

The impact process of a hypervelocity projectile onto a solid target has been studied experimentally as well as theoretically. The equation-of-state of the shocked matter has been successfully described using Rankine-Hugoniot calculations (ARTMANN, 1966; HORNUNG, K. and MICHEL, K.W., 1972; DRAPATZ, S. and MICHEL, K.W., 1974). The impact plasma is assumed to be in local thermodynamic equilibrium (LTE). The LTE-model allows the calculation of particle densities (neutrals and ions) from total plasma densities and temperature (DRAWIN, H.-W. and FELENBOK, P., 1965). Requirements for the LTE are a Maxwell-velocity distribution of the plasma constituents, a Boltzmann-distribution of the exited states, validity of the mass action law do describe the distribution of molecules and their dissociation products (important for the proportions of molecular ions in the impact plasma) and a Planck-distribution of the electromagnetic radiation. Spectroscopic investigations of the light flash that is generated at hypervelocity impacts confirmed black-body radiation with element specific emission lines (GÖTTING, 1977). The partition of ions relative to neutrals is mathematically described by the Saha-Eggert-equation (Eq. 5.9):

$$\frac{n_+ n_{e^-}}{n_0} = \frac{2Z^+(T)}{Z^0(T)} \cdot \left(\frac{2\pi m_e k_B T}{h^2}\right)^{3/2} \cdot e^{-\frac{\chi_\varepsilon - \Delta E}{k_B T}}. \tag{5.9}$$

In Eq. 5.9 n_+ and n_{e^-} are the volume densities of the positive charged ions and the electrons, n_0 is the volume density of neutral atoms. The electron concentration correlates with the plasma temperature T as follows: $\log n_{e^-} \approx 25.1 - \frac{43200}{T}$. The functions $Z^+(T)$ and $Z^0(T)$ describe the internal partition functions between neutral and singly ionized atoms depending in on the plasma temperature T. The value of the phase space element ΔE is $\Delta E = e^3 \left(\frac{8\pi n_e}{k_B T}\right)^{1/2}$. For a 50 nm iron projectile on tungsten calculations by Drapatz and Michel (1974) yield residual ionization between 10 % for impact speeds of 20 km/s and 60 % for impact speeds of 50 km/s. For particles with larger grain size the lower the ionization degree at similar impact speeds. The observed ionization degrees in this work (Section 5.2.3) are more than one order of magnitude lower than the predicted values. One effect that causes the differences might be the varying projectile size. Another deviation might be due the energy transfer from the projectile to the target (Eq. 5.10, (DRAPATZ, S. and MICHEL, K.W., 1974)):

$$\Delta E = \frac{1}{2} m \left(\frac{v}{\sqrt{\rho_P/\rho_T} + 1}\right)^2 \tag{5.10}$$

For iron impacting on tungsten 30 % of the projectile's kinetic energy will be transferred to the target, for iron impacting onto rhodium the transfer rate is 37 %. In the latter case, less energy can be used for projectile vaporizing and ionizing.

Recent modelings by Hornung and Drapatz (1981) and Hornung et al. (1996) yield ionization degrees that fit better to the experimental results given in Section 5.2.3.

Limits of the LTE-model

The LTE-model describes the formation of ions at hypervelocity impacts. The ionization process is often divided into two impact speed regimes. The low impact speed regime is characterized by so called *surface ionization*: only ionization of the projectile's surface and, due to impact ejecta, the ionization of alkali contaminants with low ionization potentials on the target surface appear. In the high impact speed regime *volume ionization* of the projectile and target material is dominating. The

speed regime	speed range [km/s]	charge yield function	dominating physical process
low	$2 < v < 6 \pm 2$	$\propto v^{3.5} - v^{4.5}$	secondary ions from ejecta (Na, K)
middle	$6 \pm 2 < v < 15 \pm 5$	$\propto v^{1.5} - v^{2.5}$	vaporization processes
high	$15 \pm 5 < v \leq 60$	$\propto v^{3.0} - v^{5.5}$	target and projectile ionization
very high	$v > 100$	$\propto v^{3.0} - v^{5.5}$?	target ionization
	$v > 500$	$\propto v^{2.0}$	ionization limited by kinetic energy

Table 5.2: Charge yield functions and the dominating physical processes in the observed impact speed regimes.

impact speed where volume ionization starts to dominate the ionization process might be given by the last bent in the charge yield functions appears (cf. Section 4.2). This is the case for impact speeds between 15 and 20 km/s.

For very small projectiles of only 10 nm grain size ($m \approx 10^{-19}$ kg), the shock heating and expansion timescales are smaller than the relaxation time of the plasma (HORNUNG, K. and KISSEL, J., 1994). A thermal state cannot be established in this case. Since these projectiles are not accessible in the laboratory[1], no experimental results are known so far. Nevertheless, it should be mentioned here, that the LTE-model has been also successfully applied to standard SIMS technology to explain phenomenologically the ion formation (BENNINGHOVEN, A. et al., 1987). In SIMS, the projectiles are ions which are even smaller than 10 nm.

In practice the knowledge of the ionization processes of such small particles is important for the understanding of the time-of-flight mass spectra that were generated by fast and small particles of the Jovian dust streams (SRAMA, R. et al., 2002).

5.1.5 Impact ionization regimes

The comparison with similar investigations, like done in the subsections above, lead to a more complete understanding of the impact phenomenology than before. Additionally Eichhorn (1978b) investigated the generation of ejecta by hypervelocity impacts. Since these ejecta reach velocities faster than the impact speed of the main projectile, they can contribute to the surface ionization of the target. This effect is dominating the ion formation at low impact speeds, where time-of-flight mass spectra are characterized by prominent sodium and potassium ion signatures. Within the in the laboratory accessible impact speed range, one can divide the ion charge production in three main impact speed regimes (Table 5.2).

In Table 5.3 are compared the impact speed exponents β with the ionization potential of the corresponding projectile materials. It seems, that the β-values increase with decreasing projectile density and decreasing ionization potentials. Since aluminium has the highest charge yield exponent but only a low density, the high charge yield should be caused by the low ionization potential. A roughly linear relation between X^+ and β could be found (Eq. 5.11):

$$\beta(v > 20km/s) = (7.2 \pm 1.3) - (0.37 \pm 0.14) \cdot X^+ \tag{5.11}$$

[1]Even for a maximum theoretical surface field strength of $3 \cdot 10^{10}$ V/m, the absolute charge on the surface of a 10 nm particles is only $8 \cdot 10^{-17}$ C and thus too low for present charge detectors at the Heidelberg Dust Accelerator. With new generation charge sensitive detectors these small charges might be detectable (HO, 2000).

Material	ρ [kg/m^3]	X^+ [eV]	β
Aluminium	2700	6.0	5.3
Carbon	2200	11.3	3.5
Hydrocarbons	1100	8 - 12	3.0
Iron	7900	7.9	4.0
Rhodium	12400	7.5	

Table 5.3: Comparison of the projectile density ρ and the ionization potential X^+ with the charge yield exponent β in $\frac{q}{m} \propto v^{\beta}$ at high impact speeds above 20 km/s.

5.2 Determination of the impacting projectile type

The possibility of measuring time-of-flight mass spectra should bring more information on the chemical nature of micrometeoroids in space. Up to now, this thesis is the most detailed investigation of time-of-flight mass spectra from hypervelocity impacts. Never before have been used so many different projectile types for similar measurements. The time-of-flight mass spectra show a large variety of signatures that should help to get a clue on the chemical nature of the projectile. A hint on the nature of the impactor's mass, speed and density might be given by the ratio of projectile related ions to target ions. The data of this work were adapted to a model, given in earlier works (Section 5.2.1). It turns out the model cannot explain the large varieties due to the different types of projectile materials. Thus, in Section 5.2.2 is developed a new model for the charge yields of specific ions (target, projectile, contaminants, cluster). The measured absolute ion yields of the projectile material allowed the calculation of the projectile's ionization degree (Section 5.3. In Section 5.2.4 are described characteristic features of molecular ions depending on the projectile type. Taking this knowledge it seems possible to give a rough classification of the projectile's chemical nature (Section 5.2.5).

5.2.1 Projectile and target ion yield ratios

Measurements from Knabe (1983) and Krüger (cf. (KISSEL, J. and KRÜGER, F.R., 1987)) tried to find empirical and theoretical yield-ratios for the projectile and the target material ions. They found the following absolute ion yields Y_P and Y_T for projectile and target ions (KRÜGER, F.R. and KISSEL, J., 1984; KRÜGER, 1996):

$$Y_P = 10^7 m_P^{\frac{5}{6}} \cdot \left(\frac{\rho_T}{\rho_P}\right)^2 \cdot F_1(V) \tag{5.12}$$

$$Y_T = 3.16 \cdot 10^7 m_P^{\frac{1}{2}} \cdot F_2(V) \tag{5.13}$$

$$F_1(V) = 0.43 \ln V - 0.24 \tag{5.14}$$

$$F_2(V) = 0.47 \cdot e^{0.054V} \tag{5.15}$$

$$V = \left(\frac{\rho_P}{\rho_T}\right)^{\frac{1}{2}} \cdot v \tag{5.16}$$

The functions $F_1(V)$ and $F_2(V)$ (Eqs. 5.14 and 5.15) have been empirically derived and can be found in the literature mentioned above. The velocity V in Eq. 5.16 is the reduced impact speed that describes the shock front propagation at the impact site. The impact speed v is given in km/s, the projectile mass m_P in 10^{-15} kg.

In Figure 5.4 are plotted the, in this work experimentally derived, $\frac{Y_P}{YT}$-ratios depending on the impact speed. The solid lines represent the theoretical yield-ratios for certain projectile sizes, calculated with the yield-formulae in Eqs. (5.12) and (5.13). The density-values for the projectiles ρ_P can be found in Section 2.2, the density of the target material rhodium is 12400 kg/m^3. Since most particles have grain sizes between 0.1 and 1.0 μm, the yield functions that correspond to these grain sizes are colored red. It can be seen that the measured yield ratios for iron projectiles fit well with the predicted values. This is not the case for aluminium projectiles. For impact speeds below 20 km/s the measured projectile to target ion yield ratios exceed the predicted values by up to two orders of magnitudes. For impact speeds up to 50 km/s the yield ratios correspond to the predicted ratios for particles with grain sizes between 1 and 5 μm. The actual grain size of the projectiles that could be accelerated to such high impact sizes are one order of magnitude smaller. Since Kissel, Knabe and Krüger derived their yield formulae from experiments with carbon, iron and metallized glass projectiles, it was expected that the measured yield ratios for carbon fit the predicted yields. However, the measured values are too low (middle-left diagram in Figure 5.4). Kissel and Krüger (1984) explained such discrepancies with the possible formation of negative ions. Considering the formation of cluster ions as described in Section 4.3.5, the total yield of carbon was corrected with Eq. 4.10. The corrected yield ratios fit nearly perfectly the predicted ratios for projectiles of 0.1 - 1.0 μm grain size (middle-right diagram in Figure 5.4). The yield ratios for the PANi-PS-latex data were corrected in the same way. Nevertheless, the ratios appear to low for 0.75 μm sized particles. Finally it should be mentioned that Kissel and Krüger didn't look at the ionization potentials of the target and projectile material. The very low ionization potential for aluminium might be responsible for the high projectile to target ion ratios which are 50 - 100 times higher than for iron projectiles, although both material samples contain particles of similar grainsizes and the density varies by a factor of 3. The influence of the ionization potentials on the projectile to target ion yields appears to be more important than it was assumed before.

Additional power law functions for the yield-ratios that depend directly on the impact speed could be derived. The large scatter of the data allowed only to give power laws for high impact speeds for aluminium and iron projectiles. The functions are summarized in Table 5.4. The yield-ratios show a rough v^{-3}-proportionality for impact speeds above 15 km/s. The steep decrease of the ratio for high impact speeds also correlates to the fact that the projectiles of several 10 km/s impact speed show already ionization degrees of some 10 % (cf. Section 5.2.3).

Projectile Material	Projectile to Target yield ratio Y_P/Y_T
Aluminium	$1.8 \cdot 10^6 \cdot v^{-3.3}$ $(12 < v < 50 km/s)$
Iron	$3100 \cdot v^{-2.6}$ $(16 < v < 40 km/s)$

Table 5.4: Projectile to target ion yield ratios for aluminium and iron.

The estimation of absolute ion yields and elemental composition with SIMS methods is very problematic (BENNINGHOVEN, A. et al., 1987). The measured ion yields depend not only on the projectile type and the impact energy but also on the incidence angle of the impact, on the energy and angular distribution of plasma ions and finally on the target itself: its composition and its crystallographic structure. This allows only to give rough empirical yield data for a single experiment which cannot be applied to other experiment configurations. Thus, the empirical values derived by Kissel and Krüger might differ from the results in this thesis, derived with the CDA flight spare.

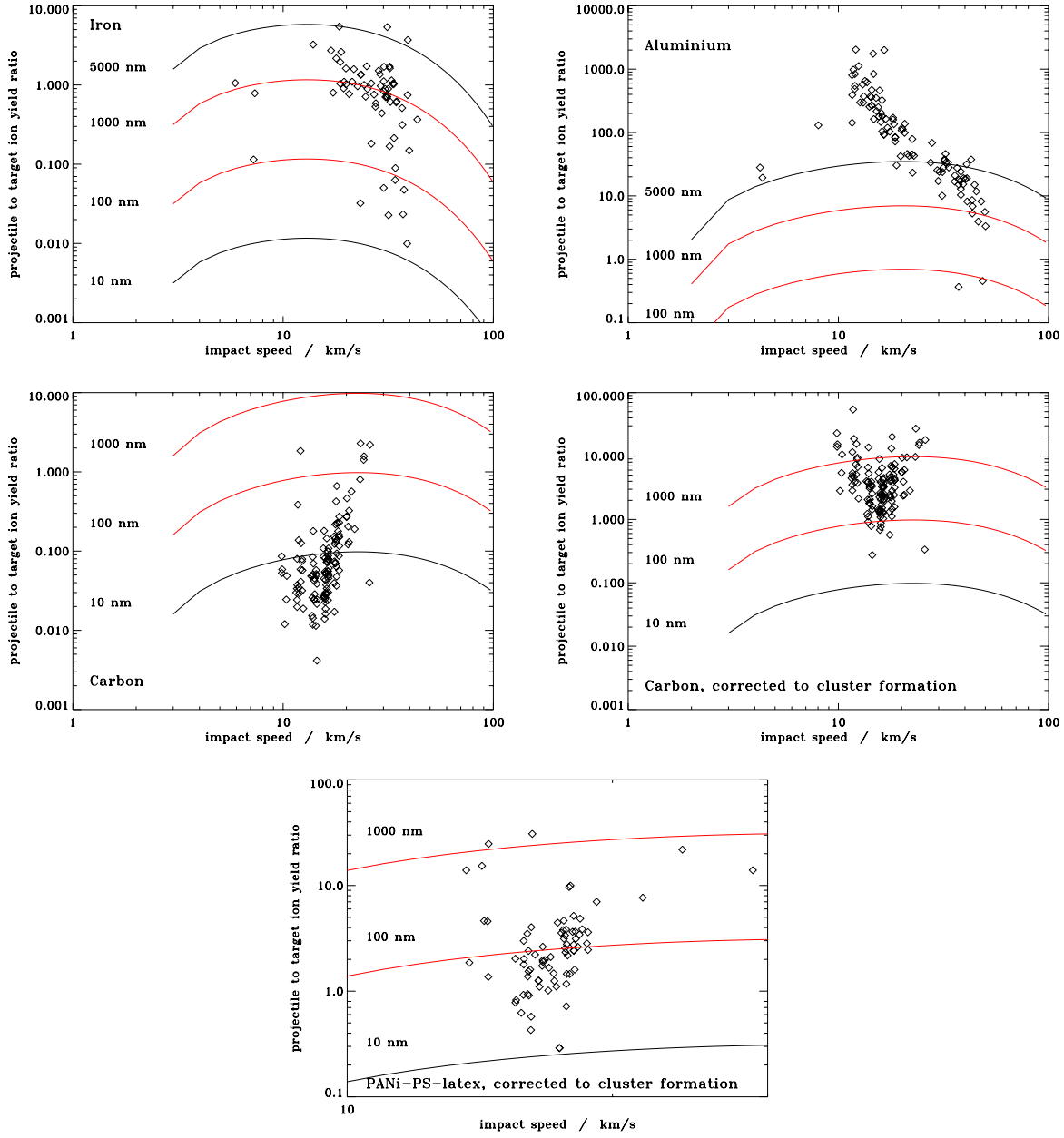

Figure 5.4: Projectile to Target ion yield ratios depending on the impact speed for the following projectiles: iron (top left), aluminium (top right), carbon (middle left), carbon with corrected yields (middle right) and PANi-PS-latex with corrected yields (bottom). The black and red lines represent the calculated $\frac{Y_P}{Y_T}$-ratios with the formula by Kissel and Krüger as given in the text.

The mass exponent α

In Section 4.2 was assumed that the mass exponent α in the global charge yield function Eq. 4.1 (page 26) is equal to 1. This was experimentally confirmed by the measurements with mono-sized latex spheres in this thesis and by measurements with aluminium, carbon and iron by Göller and Grün (1989). With additional experiments of more massive particles at a light gas gun, Falk (1983) found a mass exponent of 0.7. In his diploma thesis Knabe (1980) used an iterative method that is equivalent to standard χ^2-fitting routines and obtained values of $\alpha = 1.0$ for positive ions and $\alpha = 0.6$ for electrons. However, the values for the positive ions scatter between 0.7 and 1.0.

With the ionization models in Section 5.1.4 Knabe (1983) discussed the different yields for projectile and target ions. Accordingly the projectile yield Y_P depends on the impact speed and is proportional to $m^{2/3}$ (surface ionization at low impact speeds) respectively m^1 (volume ionization at high impact speeds). In analogy the yield of target ions Y_T is proportional to $m^{1/3}$ (concentric ring around the impact site at low speeds) respectively $m^{2/3}$ (concentric area around the impact site). These correlations led Krüger (1996) to the different mass exponents for the projectile ion formation $\propto m^{5/6}$ and the target ion yield $\propto m^{1/2}$. Then the functions $F_1(V)$ and $F_2(V)$ are the impact speed corrections of the mass exponents.

The evaluation of the mass spectra in this work offers the possibility to obtain the mass exponents for specific ions. Therefore the ion charge of a specific mass line was plotted against the projectile mass for mass spectra that were obtained within a narrow impact speed range ($v \pm 0.5$ km/s, v $<$ 20 km/s; $v \pm 2.5$ km/s, v $>$ 20 km/s). The approximated power law to the data then directly yields the mass exponent α. The results are somewhat problematic, since mass lines like hydrogen appear only at certain impact speeds and sometimes only few data points were obtained. If more data points are obtained, they often show a large scattering around their mean value, e.g. as shown in Figure 5.5. However, the α-values show a large scatter and seem to be independent of the impact speed within a range of 3 and 40 km/s. The mean values of α are listed in Table 5.5. It appears that the mass exponents in the ion yield of the target material Rh are all consistent with $\alpha = 1$. These results contradict the statements of Knabe and Krüger that mass exponent of the target material cannot exceed 2/3. An the other hand the charge yield of the projectile material is described with values of $\alpha < 1$. The charge yields of the contaminants Na and K are consistent with $\alpha = 2/3$ which is really a hint that both elements belong to surface contamination whether of the target or the projectile. Then also a value of 1 for α for target and projectile material seems reasonable, since while forming an impact crater, both the target and the projectile suffer a volume vaporization/ionization. The behavior that similar material types (like K and Na as contaminants) show a similar development of the charge yield has already been mentioned by Knabe and Krüger (1982).

The global charge yield QC is proportional to $m^{\alpha<1}$. Since the data show large errors, a value of 1 for α cannot be excluded. Here the data of Göller and Grün (1989) appear more reliable.

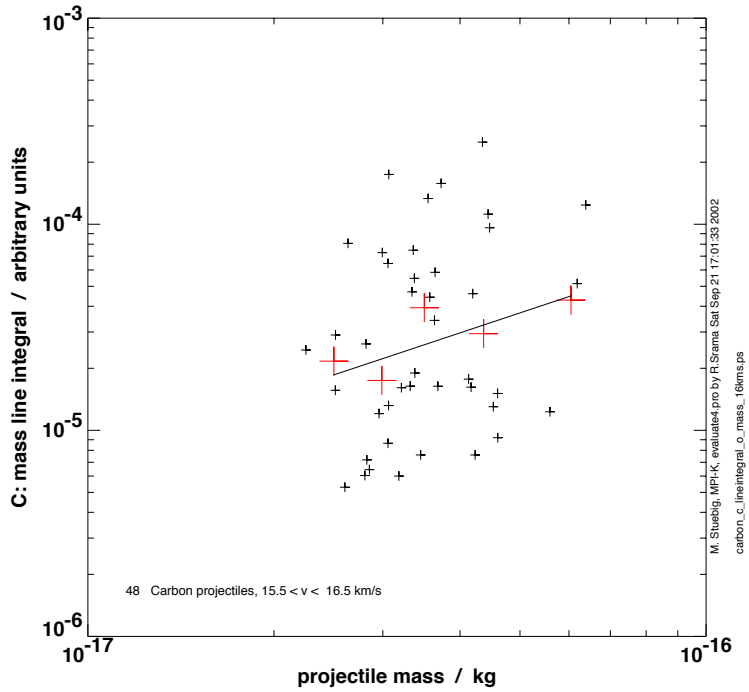

Figure 5.5: Ion yield of carbon ions depending on the projectile mass from carbon projectiles impacting with 16 km/s on the CAT-target.

	Mass exponent α					
Projectile material	H	Na	K	Rh	projectile	QC
Aluminium	(-0.3 ± 0.5)	(1.2 ± 0.6)	(0.6 ± 0.3)	1.1 ± 0.2	0.5 ± 0.3	0.7 ± 0.3
Carbon	-	0.4 ± 0.6	0.7 ± 0.8	0.9 ± 0.5	1.0 ± 1.0	0.2 ± 0.4
Carbon + Na		0.5 ± 0.8				
Iron	(0.2 ± 0.4)	-	(0.4 ± 0.8)	1.0 ± 0.3	(0.2 ± 0.4)	0.9 ± 0.4

Table 5.5: Mean values of the mass exponent α in the charge yield functions for specific mass lines and various projectile materials. The global mass exponent at the CAT-Target (QC) is additionally given. Values in brackets are very uncertain or only taken from 5 or less data sets.

5.2.2 A new model for specific ion yields

Taking the results of the projectile mass dependence together with the results of the absolute ion yields given in Section 4.3.4 gives improved empirical yields for the following specific ion types: projectile ions (Y_P), target ions (Y_T), projectile-target-clusters (Y_{P-T}) and surface contaminants (Y_C):

$$Y_P = c_P \cdot m^{1.0\pm0.2} v^{5.0\pm2.0} \tag{5.17}$$

$$Y_T = c_T \cdot m^{1.0\pm0.3} v^{5.0\pm1.0} \tag{5.18}$$

$$Y_C = c_C \cdot m^{0.7\pm0.1} v^{2.5\pm0.5} \tag{5.19}$$

$$Y_{P-T} = c_{P-T} \cdot m^{1.0\pm0.3} v^{2.8\pm0.3} \tag{5.20}$$

The constants c_I are material constants that depend on the ionization potentials and the electron affinity (neutralization, negative ions). An idea of such yields can be taken from (KRÜGER, 1996). The mass exponent α for projectile-target cluster ions has not been investigated and is assumed to be 1.0. The yield of hydrogen ions is still not good understood. As can be seen in Section 4.3.3, hydrogen ions appear late but with a very steep increase and then stay constant at a certain fraction of the total plasma ions. The steep increase might be an artefact since the fast sampling of time-of-flight mass spectrum has to be triggered before hydrogen appears. As shown in Section 4.3.1, the time offset (b) of the trigger time corresponds to the appearance of hydrogen. This means that the ion fraction of hydrogen is the sufficient to trigger the fast sampling while other charges are to small.

It should be mentioned that the impact speed exponent β in the high impact speed regime (20 - 60 km/s) is given by the relation $\beta(v > 20km/s) = 7.23 - 0.37 \cdot X^+$ (Eq. 5.11, cf. Section 5.1.5).

Projectiles of arbitrary composition

All projectiles used at the Heidelberg Dust Accelerator are mono-elemental, except the latex projectiles that consist of organic molecules. In space are expected projectiles with a more or less complicate chemical composition, e.g. olivine-silicates $(\mathrm{Mg,Fe})_2\mathrm{SiO_4}$. As the investigation of the impact plasma in Section 4.3.3 shows, the ion composition depends strongly on the impact speed and the ionization potential. For an arbitrary projectile composition the ionization processes for the different constituents has to be considered. Krüger (1996) proposed a total projectile ion yield that is the yield sum of the different constituents given by Eq. 5.21:

$$Y_P = \sum_{j=1}^{m} Y_{P_j} = \sum_{j=1}^{m} n_j S_j \cdot c_P^* \cdot m^{1.0\pm0.2} v^{5.0\pm2.0} \tag{5.21}$$

with the mole fraction n_j of element j, S_j as element specific constant and c_P^* as a normalized constant in the yield formula Eq. 5.17.

Following the relative ion yields in classical SIMS-methods, Krüger (1996) calculated relative ion yields for micrometeorite impacts. The most important contributors are listed in Table 5.6. More yields can be found in the literature. Except for hydrogen, the relative yields S_j rise rapidly with increasing ionization potential χ_j. Excluding hydrogen, the following correlation between S_j and χ_j, given in eV, could be figured out:

$$S_j = 220000^{+200000}_{-100000} \cdot \chi^{-(4.4\pm0.3)}. \tag{5.22}$$

Mass [amu]	1	12	14	16	23	24	27	28	32	39	56	59
Element	H	C	N	O	Na	Mg	Al	Si	S	K	Fe	Ni
χ_j	13.6	11.3	14.5	13.6	5.0	7.6	6.0	8.2	10.1	4.3	7.9	7.6
S_j	40	5	2	3	310	49	58	16	8	390	17	17

Table 5.6: Relative ion yields S_j for different elements. In addition is given the ionization potential χ_j of the corresponding element.

Using these corrections, the above mentioned olivine-mineral $(Mg_1Fe_1)Si_1O_4$ will appear in the mass spectra as $(Mg_4Fe_1)Si_1O_1$. Magnesium will appear overabundant by a factor of four relative to silicon, oxygen will appear reduced to only a quarter of its true value.

5.2.3 Ionization degree of the projectile

From standard SIMS-technology it is known that approximately 99 % of the material that is released by ion/projectile impacts are neutrals (STEPHAN, 2002), it turns out that the projectile material itself may be highly ionized. In this subsection method to estimate the ionization degree of the projectile will be developed. Assuming that the chemical constitution of the ions at the multiplier is representative for the impact plasma at the impact site, one can calculate how much of the projectile material is ionized. The following rough estimation neglects the presence of cluster ions that contain projectile material and also the presence of multiply ionized projectile ions. That these assumptions are possible, can be taken from the relative abundances of clusters and multiply ionized atoms to the abundance of singly ionized projectile ions. Except for carbon and latex, the cluster ions and multiply ionized ions contribute less than a few percent of the singly ionized projectile ions to the plasma ions. Eq. 5.23 gives the total amount of ionized projectile material Ψ_ε. The ratio $\frac{I_\varepsilon}{I_{total}}$ is the relative abundance of singly ionized projectile ions I_ε to the full amount of ions I_{total} in the time-of-flight mass spectra. The charge yield function $(\frac{q}{m})_{Target}$ depends on the impact speed is described in Section 4.2.

The ion charge ($\Psi_{max}(\varepsilon)$ in Eq. 5.24) describes the possible maximum charge, given by the molar charge $N_A e$ (equal to the Faraday constant F) times the number of atoms in the projectile $\frac{m}{M_\varepsilon}$. M_ε is the molar mass of the projectile material ε, m the projectile mass itself. Then $\frac{\Psi_\varepsilon}{\Psi_{\varepsilon max}}$ yields the ionization degree $\Gamma_\varepsilon(v)$ of the projectile (Eq. 5.25).

$$\Psi_\varepsilon = \frac{I_\varepsilon}{I_{total}} \cdot \left(\frac{q}{m}\right)_{Target} \cdot m \tag{5.23}$$

$$\Psi_{max}(\varepsilon) = \frac{N_A e}{M_\varepsilon} \cdot m \tag{5.24}$$

$$\Gamma_\varepsilon(v) = \frac{\Psi_\varepsilon}{\Psi_{max}(\varepsilon)} = \frac{I_\varepsilon}{I_{total}} \cdot \left(\frac{q}{m}\right)_{Target} \cdot \frac{M_\varepsilon}{N_A e} \tag{5.25}$$

These calculations have been done for selected projectile materials (with pure elemental composition) and are shown in Figures 5.6 and 5.7. The data could be fitted with power law functions as listed in Table 5.7. For aluminium and carbon sharp bends in the ionization degree functions at 20 km/s respectively 14 km/s impact speed appear. At these points, the power law exponents are roughly doubled from 4.0 to 8.3 for aluminium and from 2.5 to 4.7 for aluminium. The data for iron doesn't show such a distinction. The power exponents seem to increase with decreasing projectile density.

projectile material	ionization degree $\Gamma_\varepsilon(v)$	
Aluminium	$1.6 \cdot 10^{-6} \cdot v^{2.5}$ (4 - 20 km/s)	$2.2 \cdot 10^{-9} \cdot v^{4.7}$ (20 - 50 km/s)
Carbon	$1.6 \cdot 10^{-10} \cdot v^{4.0}$ (4 - 14 km/s)	$2.4 \cdot 10^{-15} \cdot v^{8.3}$ (14 - 25 km/s)
Iron	$1.2 \cdot 10^{-7} \cdot v^{3.0}$ (2 - 50 km/s)	
Carbon (corr.)		$2.4 \cdot 10^{-9} \cdot v^{4.7}$ (14 - 25 km/s)

Table 5.7: Power law functions to describe how the ionization degree depends on the impact speed for pure aluminium, carbon and iron projectiles. The "Carbon (corr.)" row gives a yield that considers the formation for molecular carbon clusters.

A possible explanation for the high exponent for carbon might be the formation of complex carbon cluster ions at lower impact speeds. For higher impact speeds it was observed, that these clusters were less complex and relatively less abundant in the mass spectra than for lower speeds (cf. 4.3.5). In this case, the cluster-breakup leads to an artificial rise of the power law exponent. Formula 4.10 on page 49 yields the total amount of carbon that is bound in clusters for each single carbon ion in the time-of-flight mass spectra. Multiplying this function with the number of single ions, used for calculating the ionization degree, results to the true amount of carbon that is set free from the projectile. The new "ionization degree function" is also listed in Table 5.7. This function fits very well with the power laws for aluminium and iron for high impact speeds.

However, the projectile ionization can be limited by two factors:

1. the projectile is fully ionized
2. projectile ionization needs more energy than can be provided by the impact energy

To get a deeper insight into this problem, in Figure 5.8 comparisons of the total energy E_{total} (Eq. 5.27 with the specific ionization potential χ_ε), necessary for a complete projectile ionization, and the energy portion E_{part} (Eq. 5.28, 5.29) that is actually used for ionization of projectile material are shown. Both energies are shown relatively to the kinetic energy E_{kin} (Eq. 5.26) of the projectile, given by equations 5.30 respectively 5.31. The factor 10^6 in Eq. 5.26 results from the fact that all charge yields and ionization degrees are calculated with v given in km/s.

$$E_{kin} = 0.5 \cdot 10^6 m v^2 \tag{5.26}$$

$$E_{total} = \frac{N_A m}{M_\varepsilon} \cdot \chi_\varepsilon e \tag{5.27}$$

$$E_{part} = \Gamma_\varepsilon \cdot E_{total} \tag{5.28}$$

$$= \frac{\left(\frac{q}{m}\right)_\varepsilon}{e} \cdot m \cdot \chi_\varepsilon e = \left(\frac{q}{m}\right)_\varepsilon \cdot m \cdot \chi_\varepsilon \tag{5.29}$$

$$\Rightarrow \frac{E_{total}}{E_{kin}} = \frac{N_A \chi_\varepsilon e}{5 \cdot 10^5 M_\varepsilon v^2} \tag{5.30}$$

$$\Rightarrow \frac{E_{part}}{E_{kin}} = \Gamma_\varepsilon \cdot \frac{E_{total}}{E_{kin}} \tag{5.31}$$

$$= 2 \cdot 10^{-6} \frac{\left(\frac{q}{m}\right)_\varepsilon \cdot \chi_\varepsilon}{v^2} \tag{5.32}$$

The energy portion E_{part} can be calculated in two ways, first directly from the total energy E_{tot} needed for complete projectile ionization times the ionization degree Γ as done in Eq. 5.28. The

Projectile material	$\Gamma = 1$	$\left(\frac{q}{m}\right)_\varepsilon = \frac{N_A e}{M_\varepsilon}$	Mean	$\frac{v_{CI}}{\rho}$
Aluminium	70 ± 35	75 ± 31	73 ± 4	0.027 ± 0.001
Carbon	58 ± 25	45 ± 20	52 ± 9	0.024 ± 0.004
Iron	203 ± 120	262 ± 180	233 ± 42	0.029 ± 0.005

Table 5.8: Required impact speeds v_{CI} in km/s to achieve a complete projectile ionization. The impact speeds were calculated with two methods, described in the text. Additionally values for v_{CI} divided by the projectile density ρ are given.

second way is using the absolute charge yields $(\frac{q}{m})_\varepsilon$ from Table 4.10 (Eq. 5.29). Both ways are theoretically the same, but practically they show slight deviations within the errors of the impact speed exponents of the charge yield function respectively the ionization degree function. Complete projectile ionization is only possible, where $\frac{E_{total}}{E_{kin}} < 1$. An ionization degree of 100 % is reached where $\Gamma = 1$ or $E_{part} = E_{total} \Leftrightarrow (\frac{q}{m})_\varepsilon = \frac{N_A e}{M_\varepsilon}$. χ_ε and M_ε are the element specific ionization potentials as listed in Table 2.1 on page 14 and the specific molar mass, respectively. The results of calculating the required impact speed v_{CI} for a complete projectile ionization with both methods are summarized in Table 5.8. The above mentioned projectile density dependency for the ionization degree power laws (cf. Table 5.7) are also expressed in the impact speeds v_{CI}, necessary for a complete ionization. In Table 5.8 additional values for $\frac{v_{CI}}{\rho}$ are shown. Thus the following correlation between v_{CI} and ρ is got for rhodium targets:

$$v_{CI} = (0.027 \pm 0.003) \cdot \rho_P \qquad (\mathrm{Rh-target}). \tag{5.33}$$

Regarding the relative abundance of projectile ions in the TOF-spectra (Figures 4.8 - 4.10), it appears that Rh-ions may dominate the TOF-mass spectra for even lower speeds than given by v_{CI}. For carbon projectiles, rhodium is the most abundant material for impact speeds between 12 and 20 km/s. Since carbon has a much higher ionization potential than rhodium, carbon ions may dominate over rhodium for higher impact speeds than accessible in the laboratory at present. The steep rise of the relative carbon abundance in the diagrams of Figure 4.9 on page 39 supports this assumption. For further considerations, like in Section D.4.1, it is assumed that the total charge yields, as described in Section 4.2, are valid for impact speeds up to v_{CI}.

Theoretical calculations from Hornung and Drapatz (1981) showed that the degree of ionization depends on the ratio of the square root of the projectile and target densities[2]. For a 100 nm iron projectile, impacting with 57 km/s on a tungsten target ($\sqrt{\rho_P/\rho_T} \approx 0.6$), they obtained an ionization degree of nearly 100 %. In the experimental work here, only for aluminium and iron projectiles could be accelerated to similar speeds. The projectile sizes at these impact speeds fit well with a grain size of 100 nm (cf. Appendix A.1). The target in the present case is rhodium and the $\sqrt{\rho_P/\rho_T}$-values are 0.5 for aluminium projectiles respectively 0.8 for iron projectiles. The empirical ionization degrees can be taken from Figure 5.6 and are a few 10 % for aluminium and a few percent for iron.

[2]This ratio is essential for the energy transfer from the projectile to the target.

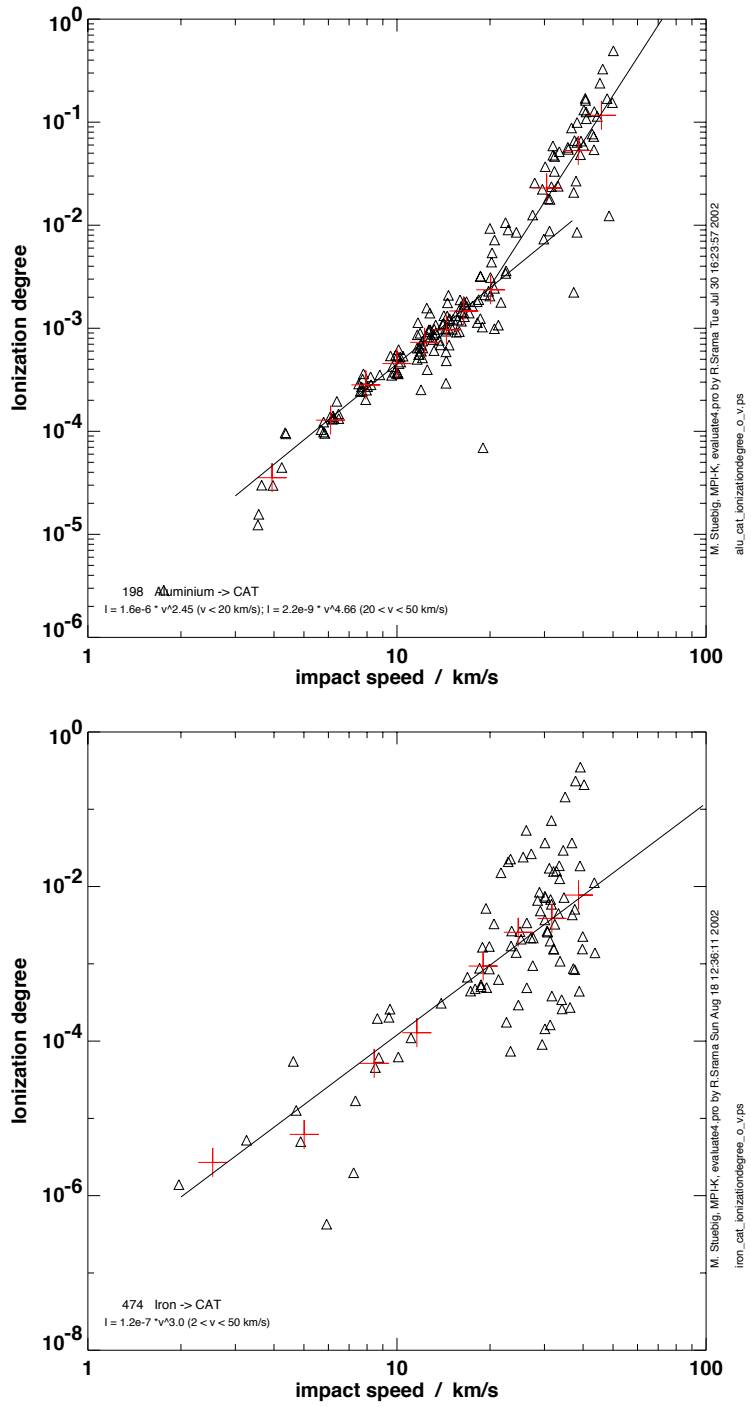

Figure 5.6: The ionization degree depending on the impact speed for aluminium (top) and iron (bottom). The estimated error of the power law exponent is 10 %.

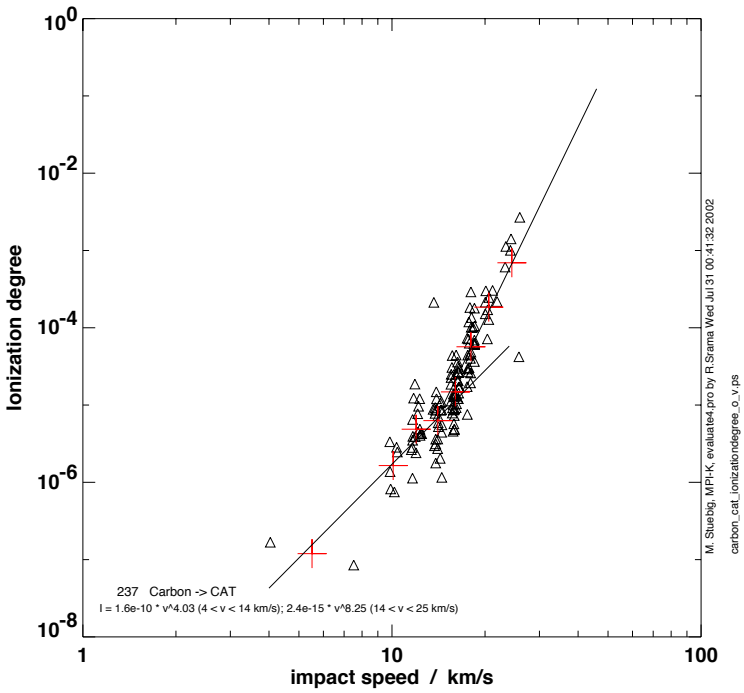

Figure 5.7: The ionization degree depending on the impact speed for carbon projectiles.

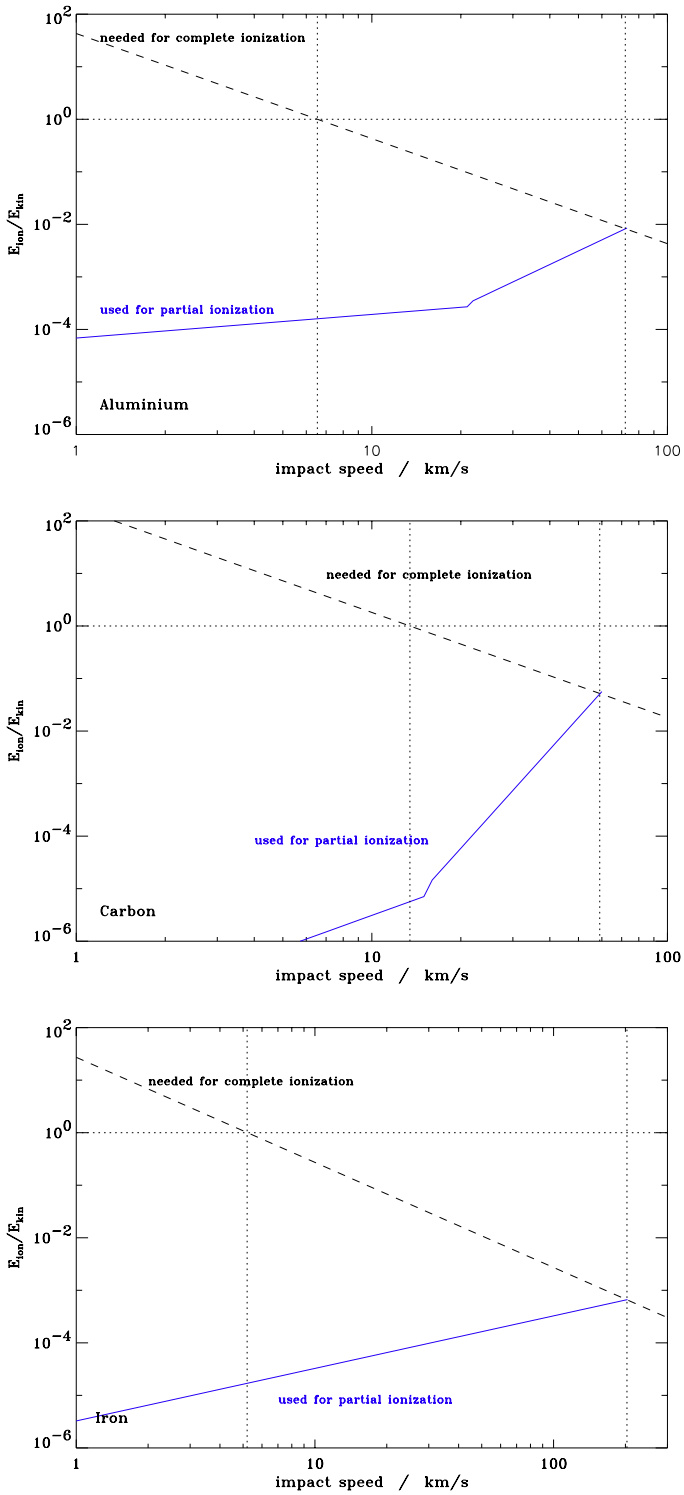

Figure 5.8: Comparison between the energy, necessary for a complete projectile ionization, and the actually used energy for the projectile ionization with respect to the kinetic energy of the impacting projectile. The energy used for projectile ionization has been calculated with the Γ-function for the ionization degree. The left vertical dotted lines give the minimum impact speed that is required for a full projectile ionization, if all kinetic energy is used for projectile ion formation. The right vertical dotted lines mark the impact speed v_{CI}, where complete ionization appears.

5.2.4 Identification of molecular ions and comparison with CIDA data

The observation of cluster ions is described in Section 4.3.5. These cluster ions can be used to characterize the impacting projectile. In SIMS-technology the appearance of cluster ions (especially with silver, that forms cluster ions very easily) is used to identify material ions, which otherwise may have interfering mass lines at their nominal mass position (e.g. hydrocarbons: Al and C_2H3) (STEPHAN, 2002). In the mass spectra of all used projectile materials (except the PPY-PS-latex sample) could be observed target-projectile cluster ions. For projectile materials with high ionization potentials like carbon, the target-projectile cluster ions appear at even lower impact speeds than atomic projectile ions themselves. Molecular clusters of the projectile material itself in equidistant masses (e.g. Al^+, Al_2^+ and Al_3^+ at 27, 54 and 81 amu) will additionally help to identify the projectile material. Nevertheless, an accurate investigation of molecular mass lines can only be performed if the mass scaling of time-of-flight spectrum is also performed by using molecular mass lines. Due to their different energy distributions (SHIMIZU, 1978), a mass scaling with atomic ions may yield wrong molecular mass positions (STEPHAN, 2002). Especially for simple TOF mass spectrometers like CDA, which have no energy correction, this effect might be critical.

General differences between CDA and CIDA

Due to its ion reflector unit, CIDA performs a first order energy correction of the ion's energy distribution. Thus the mass lines appear more narrow and the mass resolution is higher than for CDA. Before comparing the time-of-flight mass spectra of both instruments CDA and CIDA should be mentioned that the different construction principles may cause "artefact lines" in the spectra. It is known that complex metastable molecular ions may fragment into two or more pieces during the flight from the target to the multiplier (STEPHAN, 2002). Some of these products can be electrically neutral. If the fragmentation happens before the molecular ion reaches the reflector unit, only the charged fragments will be repelled und focussed towards CIDA's microchannel plate. Since CDA has no reflector unit, all fragments including the neutral ones reach the multiplier. Neutral ions that hit the backside of the CIDA's reflector unit can generate an impact plasma and release further ions. These "tertiary" ions will be accelerated by the electric field inside the reflector towards the microchannel plate and cause the appearance of additional lines in the time-of-flight mass spectra.

In both cases, the ion fragmentation during the flight and the generation of "tertiary" ions, the correlation between ion mass and flight time gets lost.

Comparison of the latex mass spectra from CDA and CIDA

The time-of-flight mass spectra from carbon and latex projectiles show a vast amount of carbon-clusters or hydrocarbons. Although the time-of-flight mass spectra from CIDA should help to understand the broad peaks in the CDA mass spectra of PANi-PS-latex projectiles, the results are a little bit confusing. As well as CDA, CIDA shows two types of spectra: the first type shows projectile and target material (C, Ag) and contaminants (H, Na, K). Next to these relatively sharp mass lines appear broad peaks at equidistant mass positions of $\Delta m = 12$ amu. This behavior is similar to the broad peaks that were observed in the latex mass spectra from CDA. However, these peak centers of the broad peaks in the CIDA mass spectra seemed to be shifted relative to the positions of the peak centers of the CDA mass spectra. The peaks in the CIDA mass spectra appear at mass positions which are approximately $\Delta m = 3 - 4$ amu higher than the peak positions in the CDA mass spectra. The strong

feature in the CIDA spectra at 80 - 90 amu might be explained by a benzene-ring or a cyclopentadiene molecule (C_6H_6 at 78 amu respectively C_5H_5 at 65 amu) with an additional C-atom at one edge and a varying number of H-atoms on the other edges. Nevertheless, other polycyclic aromatic hydrocarbons (PAHs, Figure 4.33) could not be identified in these mass spectra.

The second type of CIDA-spectra appeared at impact speeds of 18 km/s. Only 3 of 20 spectra where of this type. They show groups of lines but no target or contamination ion related mass lines as described in Section 4.4. From 252 mass spectra, produced by PANi-PS-latex projectiles, 27 show similar features at the same mass positions without any target or contamination related ions. But due to the lower mass resolution the mass lines groups with line distances of $\Delta m = 2$ amu smear to a broad peak. A correct mass assignment of the features in the CDA mass spectra was only possible with the help of the CIDA mass spectra. Even some mass spectra of the PPY-PS-Latex projectiles show similar features. All these spectra are characterized by a broad and dominant mass line at 78 amu (Figure 5.9). This mass line can be related to C_6H_6-benzene rings. Due to the many possibilities of composing hydrocarbons of nearly equal mass, the other features are still not understood. For an appropriate distinction between molecules like H_2CN and C_2H_4, mass resolutions of $\frac{m}{\Delta m} \approx 3000$ are necessary (STEPHAN, 2002; STEPHAN, 2001).

Comparison with data from similar experiments

From similar experiments like those in this thesis performed at a dust accelerator facility in Canterbury, Goldsworthy et al. (2002) reported the successfully reception of time-of-flight mass spectra from polypyrrole and PEDOT coated polystyrene latexes with grain sizes between 0.5 and 1.8 μm diameter shot on the CDA laboratory model. Mass spectra could be already obtained for impact speeds at about 3 km/s, whereas reliable mass spectra in this work have been found only for impact speeds $v \leq 6$ km/s. While the mass spectra at 6 km/s in this work show only alkali-ions with low ionization potentials, Goldsworthy et al. reported the observation of molecular ions from the projectile even at the lowest impact speeds. Similar features in the mass spectra of the present work could be observed only for impact speeds above 6 km/s (PPY-PS-latex) respectively 12 km/s (PANi-PS-latex) with both instruments CDA flight spare and CIDA laboratory model. A pronounced mass line at 91 amu was observed, especially at low impact speeds $v < 8$ km/s, by Goldsworthy et al. (2002) was assigned to a tropylium cation species of the polystyrene molecule (projectile core material) (SILVERSTEIN, R.M. et al., 1981). This feature was observed in only eight mass spectra from PANi-PS-latex projectiles at impact speeds between 8 and 25 km/s. The mean spectra of the same projectiles shot on the target of CIDA show a smart peak at 91 amu which develops with increasing impact speed to a broad feature towards lower masses. This has been already reported by Kissel and Krüger[3] (2001) who analyzed the same mass spectra of CIDA.

It is worth to note that Goldsworthy et al. didn't report the observation of the "benzene"-spectra with a prominent mass peak at 78 amu. These spectra were observed for ≈ 10 % of all mass spectra from latex projectile impacts.

[3] In their publication, Kissel and Krüger named the PANi-PS-latex sample by mistake "PEDOT-coated polystyrene latex".

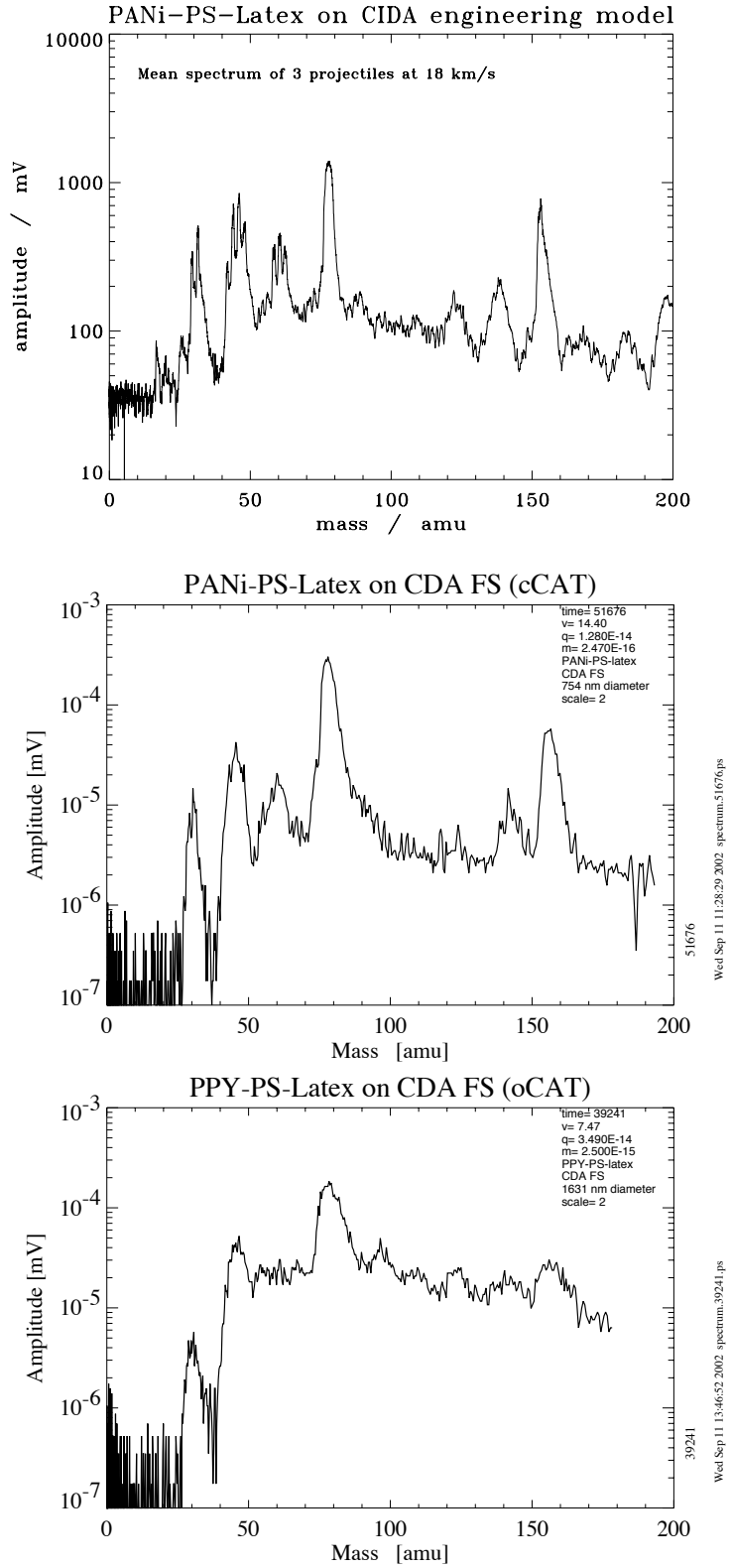

Figure 5.9: Comparison of time-of-flight mass spectra from PANi-PS- and PPY-PS-latex projectiles. The upper spectrum is a sum spectrum of 3 PANi-PS projectiles at 18 km/s measured with CIDA. The spectrum in the middle is measured by CDA (PANi-PS-latex, 14 km/s). The spectrum at the bottom was generated by the impact of a 7.5 km/s fast PPY-PS-latex spectrum and was also measured by CDA. All spectra are characterized by a dominant peak at 78 amu (benzene) and broad peaks at characteristic mass positions.

5.2.5 Classification of the impacting projectile

The different projectiles in the present work generate mass spectra that show characteristic molecular lines. Although the chemical nature of a mass line is not always clear, especially for hydrocarbons, some basic features appear in the spectra that should help to classify the projectile-type. The results are summarized in Table 5.9. Although it is impossible to work with icy particles as projectiles for electrostatic acceleration, ice is mentioned as projectile class, since it is the most important material type in the Saturn rings (SHOWALTER, MARK R. et al., 1991).

Projectile origin	Characteristics of the mass spectra
metallic	- molecular clusters of Me_n^+ and $RhMe^+$ - atomic mass line shows pronounced Maxwell-Boltzmann energy distribution for impact speeds above 30 km/s.
carbonaceous	- molecular clusters of C_n^+ - molecular C_n^+ contributes 30 % to the total ion charge - molecular RhC^+ (115 amu) appears at lower impact speeds than atomic C^+ (12 amu) - average complexity of C_n^+-molecules decreases with increasing impact speed
organic	- molecular clusters of $C_mH_n^+$, possibly mixed with N- and O-contributions (broad peaks) - molecular $C_mH_n^+$ contributes 40 - 50 % to the total ion charge - average complexity of C_n^+-molecules decreases with increasing impact speed - molecular RhC^+ (115 amu) appears at lower impact speeds than atomic C^+ (12 amu) - molecular hydrogen H_2^+ and H_3^+ at 2 respectively 3 amu
rocky	- silicon Si^+ and Si_2^+ at 28 respectively 54 amu - Possibly magnesium contribution should generate a large and broad peak at 24 amu due to a medium ionization potential (7.7 eV) and isotopes at 25 amu (10 %) and 26 amu (11 %)
ice	?
surface contamination	- Unusual high mass lines related to the contamination, especially at lower impact speeds

Table 5.9: Characteristics of the mass spectra from different projectile types for impact speeds up to ca. 100 km/s. Between impact speeds of 20 and 100 km/s, the mass spectra are dominated by mass lines that correspond to the target and the projectile material. For impact speeds above 100 km/s it is expected that the target material will be absolutely dominant. The characteristics for metallic, carbonaceous and organic material were taken from the results of this work. The silicate characteristics of rocky material have been taken from the mass spectra of silicon doped polypyrrole particles (Kuhn, 2002)

5.3 Appearance of higher ionization stages

In Section 4.3.6 is described the possibly observation of multiply ionized aluminium (Al^{2+}, Al^{3+}) and iron (Fe^{2+}). These ionization stages appear in the most mass spectra for impact speeds above 15-20 km/s. The plasma temperature at such impact speeds is in the order of $10^5 - 10^6$ K. Assuming a Maxwell-Boltzmann energy distribution as shown in Figure 5.10 (cf. Eq. 5.3) and comparing it to the ionization potentials that are given in Table 2.1, it turns out that for plasma temperatures of 10^6 K enough ion energy for the second ionization state of C, N and K and even the third ionization stage of Al, Fe and Rh will be provided. From this consideration, multiply ionized atoms are expected to appear in the time-of-flight mass spectra of projectiles that hit the target with impact speeds of several 10 km/s. Especially for aluminium, multiply ionized atoms is frequently observed with classical SIMS-methods (STEPHAN, 2002; STEPHAN, 2001). Spectroscopic investigation by Götting (1977) of the light flash produced at hypervelocity impacts gave also evidence of multiply ionized atoms.

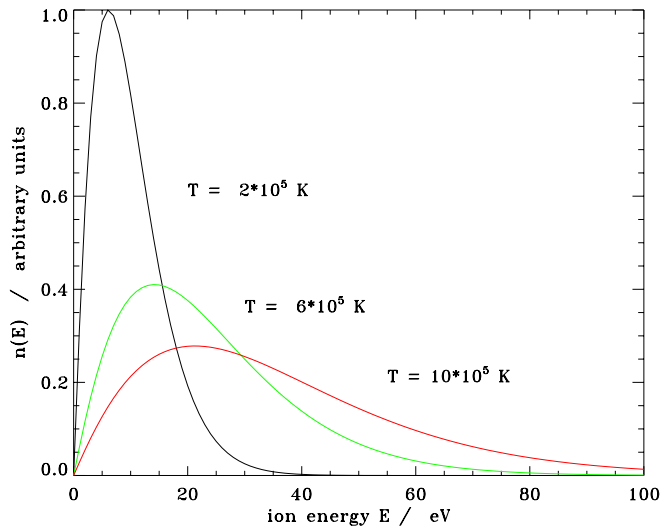

Figure 5.10: Maxwell-Boltzmann energy distributions for plasma temperatures of $2 \cdot 10^5$ K (black curve), $6 \cdot 10^5$ K (green curve) and $10 \cdot 10^5$ K (red curve).

However, in the case of aluminium remains the problem of the line shifting of the Al^{2+}- and Al^{3+}-mass line positions from 16 to 13.5 amu, respectively from 12 to 9 amu (cf. Section 4.3.6). As mentioned in Section 5.1.3, atomic and molecular ions have different energy distributions. If carbon and oxygen are present as surface contamination on the rhodium target, their ions may have a completely different energy distribution than the projectile and target ions. But then this effect should also be observed for the sodium and potassium ions, which are also related to the surface contamination. Both mass lines show no shifting effects any way. Unfortunately, for the mass spectra from iron projectiles, the carbon mass line was very often used as reference mass at 12.00 amu. In this case, a line shifting is impossible to see. In some of the mass spectra the Al^{3+}-peak has an amplitude that is one order of magnitude higher than the amplitude of the Al^{2+}-peak. This effect is not consistent with the present energy distributions and would only appear in very hot plasma, where nearly the complete aluminium atoms are already doubly ionized.

Also problematic is the mass peak at 28 amu in the mass spectra of iron projectiles. Since carbon and oxygen are known as contaminant material in standard SIMS-methods (STEPHAN, 2002), carbon-monoxide (CO) may be present as component in the residual gas atmosphere. A vacuum of 10^{-6} mbar is a "very bad" vacuum compared to typical vacua of $2 \cdot 10^{-10}$ mbar in SIMS technology (STEPHAN, 2002). However CO-molecules are not known as important contributors to time-of-flight mass spectra. A possibly silicon contamination (silicon is a major component of the vacuum grease) could also be excluded, since the 28 amu feature is not appearing in the mass spectra of carbon projectiles. If the 28 amu feature is present in the mass spectra of aluminium projectiles, it would disappear within the large and broad Al-mass peak at 27 amu. Projectile contamination with aluminium should be excluded, since a PIXE-analysis of the iron sample denied the presence of aluminium contributions.

Regarding the mass spectra of high speed iron projectiles ($v > 20$ km/s), the mass line of iron (56 amu) seemed to be double-peaked. Kuhn (2002a) found that this peak might be the sum of an overlap from atomic iron (56 amu) and doubly ionized rhodium (51.5 amu). This seems reasonable, since iron and rhodium have similar ionization potentials for the second ionization stage ($\approx$ 16 - 18 eV, Table 2.1) and the 51.5 amu feature often appears together with the mass peak at 28 amu. Somewhat problematic is the absolut peak height of the 51.5 amu feature. It can be more than a factor of 100 higher than the 28 amu peak, although iron and rhodium show similar peak heights. Stephan (2002) considered also chromium (Cr, 52 amu) as projectile contamination to explain this mass peak.

A new EDX-analysis[4] of the aluminium and iron samples by Thomas Stephan, Universität Münster, didn't help to answer this question. The preparation with a carbon glue onto an aluminium plate made impossible to figure out aluminium and carbon contaminations of the samples. A new preparation using a gold plate as sample holder would be necessary.

5.4 Comparison with laser-techniques

Another method to generate ions on a target surface is to shot short laser pulses. The first study that compared the laser induced ionization process with hypervelocity microparticle impacts has been done by Kissel and Krüger (1987). In the case of laser induced ionization the projectile is replaced by photons. This implies different ionization processes and complicates the comparison with microparticle impact induced ionization. However, as shown in Table 5.10 with focussed lasers, operating in a pulse mode, similar energy densities than for dust particle impacts can be established (DINGER, 1980; KISSEL, J. and KRÜGER, F.R., 1987). From experiments with laser-shots on a tantalum target Dinger (1980) derived an $\cos^2$-angular-distribution of ions generated at low laser energies and an even better focussing towards the target normal vector for higher laser energies. For the ion velocities he found a Boltzmann-distribution. Ions with kinetic energies up to 300 eV have been observed. The plasma temperature of the electrons is in the range of $5 \cdot 10^4 - 5 \cdot 10^5$ K. The ion temperature is one order of magnitude higher and therefore in the temperature range of the plasma ions, generated by hypervelocity projectile impacts. Recent experiments with laser pulses shot on a carbonaceous target yield time-of-flight mass spectra that show similar carbon cluster features (even at the same mass position) as the experiments with hypervelocity carbon projectiles in this work (MANAGADZE, G.G. et al., 2002). Further experiments on laser ablation of aluminium (WANG, HONGYIEN et al.,

[4]Electron Dispersive X-ray-analysis: a method to determine elemental composition of a sample by their characteristic X-ray-lines in a Bremsstrahlung-spectrum, e.g. K_α-transition.

1991; AMUROSO, S. et al., 1996) describe also the formation and analysis of Al-cluster ions and of multiply ionized aluminium ions. These studies might be useful to determine the probabilities and relative yields for such ion species. However, Wang et al. (1991) reported that the energy distribution of laser induced aluminium ions will not fit with a Maxwell-Boltzmann distribution. The method of holographic interferometry measurements of laser ablation gives hints on the impact plasma development with time (LINDLEY, R.A. et al., 1994). It might be possible to get direct information on the energy and angular distribution of the plasma ions. However, all laser-based experiments suffer to a large disadvantage: ions were only generated from the target material. It is not possible to study the formation of projectile ions and target-projectile cluster ions.

Impactor	Impact energy [J]	Incidence radius [μm] Impact duration [s]	Energy density W/m^2	
Laser-Photons	$10^{-3} - 10^{-1}$	1 - 1000	$10^{-11} - 10^{-8}$	$10^{12} - 5 \cdot 10^{15}$
3000 nm Al-projectile, 2 km/s	3 (- 30)	$2 \cdot 10^{-7}$	$2 \cdot 10^{-8}$	10^{12}
100 nm Al-projectile, 50 km/s	0.1 (- 1)	$2 \cdot 10^{-9}$	$2 \cdot 10^{-11}$	10^{16}

Table 5.10: Comparison between the energy densities of laser pulses and microparticle impacts.

Chapter 6

Summary and Outlook

Summary

The present thesis reports on improvements of laboratory micrometeorite impact simulation. For this, a new dust particle source has been successfully applied to the Heidelberg Dust Accelerator facility. A large variety of projectile materials (aluminium, carbon, iron and latexes), covering a wide range of material properties (e.g. density, chemical constitution, ionization potential), were accelerated to impact speeds between 2 and 70 km/s. For the further experiments these projectiles have been used as analogues for micrometeorites in space. They were used for calibration measurements of the CDA flight spare unit and the CIDA engineering model.

The measured ion yields from hypervelocity microparticle impacts give evidence of different impact ionization regimes depending on the projectile's impact speed. The ion production at low impact speeds ($v < 6$ km/s) is dominated by surface ionization. Ejecta, generated at hypervelocity impacts, cause the ionization of alkali elements with low ionization potentials which cover the target and possibly the projectile as surface contaminants. For high impacts speeds ($v > 18$ km/s) volume ionization is the dominating process. Mainly target and projectile material are ionized. In this work firstly an intermediate impact speed regime could be established where the global charge production shows a reduced increase with the impact speed relative to the low and high speed regimes. A similar behavior was observed for the light flash appearing at hypervelocity impacts (EICHHORN, 1976). The common explanation is that a large fraction of the impact energy is needed for melting and vaporization of the projectile and target material.

The measurement of time-of-flight mass spectra opens the opportunity to observe the chemical plasma composition depending on the impact speed for a certain projectile material. It turned out that for each projectile material the chemical ion composition of the impact plasma is dramatically changing with the impact speed of the projectile. This change is consistent with the change of the impact ionization regimes as described above. The formation of characteristic molecular cluster ions depending on the projectile material can be used for a further type classification of the impacting projectile. An evaluation of single mass lines allowed the derivation of absolute charge yields for specific ion species like contaminants, target material and projectile material. The existing model of the ion yields was improved and extended to contaminant material and molecular target-projectile ions. Additionally, it was possible to calculate the ionization degree of the projectile depending on the material type and impact speed. The shape of projectile and target material related mass lines shows depends on the impact speed and gives a hint of the energy distribution of the plasma ions. The possibly observation of multiply ionized atoms couldn't be finally clarified.

Outlook

The results of this work are encouraging for future measurements. Many aspects still couldn't be investigated with the present projectiles.

It was still not possible to determine the element abundances in projectiles of arbitrary composition. It would be reasonable to calibrate the instrument with two- or three-component projectiles with known abundances of the components.

Isotopes with relative abundances below 10 % couldn't be clearly identified in the mass spectra. Experiments with magnesium coated projectiles would be interesting for statements if CDA is able to resolve the single mass lines and if the relative mass line integrals fit the actual isotope abundances.

The mass spectra of the latex samples showed that projectiles containing organic matter can be distinguished from non-organic projectiles. Further experiments with biologically contaminated projectiles, whether with simple amino acids or whether with bacteria can be characterized by specific mass line features in the time-of-flight mass spectra. The results of such experiments may have large importance for astrobiology.

Appendix A

Application of the new dust source

The data in this work is the first data from accelerating charged projectiles using the newly developed dust source. Therefore this Section is dedicated to give an overview of the advances in hypervelocity micrometeorite impact simulation with the ability of accelerating different projectile types in large impact speed and mass ranges (Section A.1). Section A.2 shows the charging properties of different projectile materials. At last an evaluation of the new dust source is given in Section A.3. It turned out, that different materials can be accelerated in a wide range of impact speeds (1 - 70 km/s) and projectile masses ($10^{-20} - 10^{-12}$ kg). The projectile types cover a wide density range (1100 - 7900 $\mathrm{kg/m^3}$).

A.1 Achievable projectile speed and mass ranges

Since the present work provides the first measurements with the new dust source, in this Subsection are given empirical settings of the voltages (needle potential, focus) and pulse amplitudes, needed for a proper particle extraction and acceleration. The values are summarized in Table A.1. Nevertheless, it was observed that a lot of dust particles get lost during the flight from the dust source to the experiment chamber. Sometimes only a sixth or tenth of all particles reaches the chamber. Present measurements from A. Mocker with a CCD-camera allow a direct observation of the particle beam diameter by the distribution of impact flashes (cf. (EICHHORN, 1976)) and will help to optimize the focus voltage. The final results will be published in a diploma thesis (MOCKER, 2002).

In Table A.2 are given the achievable ranges for projectile speed and mass. For a better comparison, the speed-mass-distributions of all projectile types after several minutes of running the dust source are shown in Figures A.2 to A.4. As already seen in the previous section, the grain size distribution of the the accelerated particles reflects well the photographically measured grain size distribution of the samples, except for aluminium. Table A.2 shows additionally the electric conductivity and the achievable charges. Maximum surface field strengthes are calculated for 1 μm-particles to get an impression how good each material can be charged. The source stability is an empirical value that should help future experimenters to estimate how long a freshly refilled dust source will run at the accelerator. An exchange of the complete dust source will last three working days including two days of vacuum pumping. The dust source exchange itself proceeds quickly in less than one hour, but more time is needed for pumping the protection gas out of the Van-de-Graaff generator and venting the vacuum system.

Projectile material	Needle potential kV	Pulse amplitude %	Focus kV	Stability d
Aluminium	18 -19	80 - 90	11 - 13	2
Carbon	19	80 - 90	11	4 - 7
Carbon + Na	18 -19	80 - 90	11	2
Iron	17	80 - 90	17	2 - 3
0.75 μm PANi-PS-latex	17 - 18	50 - 60	12 - 14	5 - 12
1.6 μm PPY-PS-Latex	16	50 - 60	12	10
0.1 μm PPY-PS-Latex	14 - 16	50 - 60	14	2
0.075 μm PPY-silica	no proper values available			
Iron	17	60	17	11

Table A.1: Overview of the empirical dust source parameters, as used for the measurements. The values for 0.1 μm PPY-PS-Latex and silicon doped μm PPY-silica nanocomposite were kindly provided by S. Kuhn. The stability value gives total runtime in days ($\approx$ 6 h measure time per day), meaning how long the dust source usually works without refilling the reservoir. For comparison, the last row shows the values for iron particles, as extracted from the previous dust source.

Projectile material	Density kg/m^3	Grain sizes μm	Mass range 10^{-18} kg	Charge range 10^{-15} C	Speed range km/s	$E_{max}(1\mu m)$ $10^6 V/m$	El. conductivity $10^3 S/m$	Source stability d
Aluminium	2700	0.1 - 4.1	2 - 95220	0.9 - 220	1.5 - 50.1	1800	37700	2
Carbon	2200	0.2 - 2.4	10 - 16300	4.5 - 25	1.5 - 25.9	540	125	4 - 7
Carbon + Na	2200	0.2 - 1.4	8 - 2920	1.5 - 13	4.2 - 28.9	240	(125)	2
Iron	7900	0.08 - 2.6	2 - 70000	2.0 - 66.0	0.2 - 180	1300	11200	11
0.75 μm PANi-PS-latex	1100	0.61 - 0.83	126 - 327	2.2 - 19	4.2 - 18.8	1000	0.1	5 - 12
		0.2 - 1.4	5 - 1550	0.3 - 19	3.6 - 28.9			
1.6 μm PPY-PS-Latex	1100	1.6 - 1.8	2300 - 3200	2.0 - 40	2.1 - 7.5	580	0.2	10
		0.8 - 1.8	300 - 3200	2.0 - 40	2.1 - 7.5			
0.1 μm Polypyrrole	1500	0.2 - 2.2	4 - 8000	0.8 - 95	5.1 - 30.9	260	0.001	2
0.075 μm PPY-silica	1870	0.2 -2.5	12 - 15000	0.6 - 39	2.7 - 14.9	1650	$10^{-4} - 10^{-5}$	n.m.
Iron	7900	0.02 - 2.4			2 - 100	900	11200	2

Table A.2: Overview of the empirical projectile parameters, as measured in this work. $E_{max}(1\mu m)$ is the value for the maximum achievable electric surface field strength on a 1 μm-sized particle. The values for the latex samples are calculated, assuming $E_{max} \propto \frac{1}{\sqrt{r}}$ (as explained in Section A.2). The values for the 0.1 μm Polypyrrole sample and the 0.075 μm PPY-silica nanocomposite sample were kindly provided by S. Kuhn. For comparison, the last row shows the values for iron particles, extracted from the previous dust source. In Column "Stability" is given the typical runtime of a fresh refilled dust source in days.

A.2 Charging of particles

From regarding the speed-mass-distributions of aluminium and iron projectiles in Figure A.2, an upper and a lower mass limit depending on the impact speed appear. The lower limits are characterized by a minimum observable projectile mass that decreases $\propto v^{-2}$. The upper limits of the projectile mass decrease $\propto v^{-4}$. This behavior has been observed already in earlier studies (FECHTIG, H. et al., 1978). The lower limit can be explained with the minimum detectable charge at the Heidelberg Dust Accelerator facility $q_{min} \approx 2 \cdot 10^{-16}$ C. Then energy conservation in Eq. 2.1 yields a minimum observable projectile mass $\propto v^{-2}$ (Eq. A.1):

$$m_{min} = 2 q_{min} U_{acc.} \cdot v^{-2}. \tag{A.1}$$

The maximum observable mass can be calculated using the Coulomb law in Eq. A.2 and setting a fix maximum electric surface field strength E_{max}, where field ion emission on the particle surface starts. As an empirical value for $E_{max} \approx 3 \cdot 10^{10}$ V/m can be assumed (GERTHSEN, CH. and VOGEL, H., 1993). From energy conservation follows the relation $q \propto v^2$ which is used to get the theoretical maximum projectile mass m_{max} in Eq. A.3.

$$q_{max} = 4\pi\varepsilon_0 E_{max} r^2 \tag{A.2}$$

$$\Rightarrow \quad q_{max} \propto r^2 \propto m^{2/3}$$

$$\Rightarrow \quad m_{max} \propto q_{max}^{1.5}$$

$$\Rightarrow \quad m_{max} \propto v^{-3.0} \tag{A.3}$$

The result in Eq. A.3 contradicts the observed dependence $m_{max} \propto v^{-4}$. This discrepancy can only be explained with a maximum electric surface field strength that is not constant but depends on the grain size and thus on the mass of the particle. Calculating from Eq. A.3 backwards to Eq. A.2 it follows that $E_{max} \propto r^{-0.5}$ to explain $m_{max} \propto v^4$.

The actually measured distribution of the maximum projectile charge depending on the projectile mass for aluminium, carbon and iron can be described by power laws that are summarized in Table A.3. It turns out that the maximum charge is approximately proportional to the square root of the mass (Eq. A.4 with the material specific constant c_ε). For spherical particles as used in this work, Eq. A.5 yields a maximum charge depending on the grain size (Eq. A.6). The corresponding radius-charge-relations for aluminium, carbon and iron are also listed in Table A.3. The maximum electric surface field strength on a particle is described by Eq. A.7. Combined with Eq. A.6, the maximum surface field strength can be described with a power law as in Eq. A.8. This result explains the difference between the theoretical prediction

Material	$q_{max}(m)$ [C]	$q_{max}(r)$ S [S/m]
Aluminium	$4.7 \cdot 10^{-6} \cdot m^{0.54}$	$5.0 \cdot 10^{-4} \cdot r^{1.5}$
Carbon	$1.9 \cdot 10^{-7} \cdot m^{0.47}$	$1.8 \cdot 10^{-5} \cdot r^{1.5}$
Iron	$6.8 \cdot 10^{-7} \cdot m^{0.50}$	$1.2 \cdot 10^{-4} \cdot r^{1.5}$

Table A.3: Power law functions that describe the maximum charge q_{max}, depending on the projectile mass m, respectively the grain radius r. Additionally the electric conductivity S is given.

$$q_{max} = c_\varepsilon \cdot \sqrt{m} \tag{A.4}$$

$$m = \frac{4}{3}\pi r^3 \rho \tag{A.5}$$

$$\Rightarrow \quad q_{max} = \sqrt{\frac{4}{3}\pi c_\varepsilon \rho_\varepsilon} \cdot r^{\frac{3}{2}} \tag{A.6}$$

$$E_{max} = \frac{1}{4\pi\varepsilon_0} \cdot \frac{q_{max}}{r^2} \tag{A.7}$$

$$\Rightarrow \quad E_{max} = \sqrt{\frac{c_\varepsilon^2 \rho_\varepsilon}{12\pi\varepsilon_0^2}} \cdot r^{-\frac{1}{2}} \tag{A.8}$$

A previous work already showed, that the new dust source allows a better particle charging (STÜBIG et al., 2001). The E_{max}-values in Table A.2 also show that the surface charging for the non-latex particles rises with the electric conductivity of the material. From the data of aluminium, carbon and iron the maximum surface field strength E_{max} can be described by the following approximation (Eq. A.9):

$$E_{max}(r = 1\mu\text{m}) = (47 \pm 10) \cdot 10^6 \cdot S^{0.21\pm0.01}\ \text{V/m}, \tag{A.9}$$

where S is the electric conductivity in S/m.

As mentioned above, the maximum charge on a particle depends on the grain size. Figure A.1 shows a comparison between the charging properties of different materials. The assumption of a $r^{-0.5}$-proportionality for the maximum surface field strength (cf. Eq. A.8) adapts only very roughly to the measurements. The slopes range from $r^{-0.5}$ to $r^{-2.5}$ and are not stable. Nevertheless all materials seem to have a maximum absolute value for the surface field strength, which cannot be exceeded. These values are $1.3 \cdot 10^9$ V/m for carbon, $3.0 \cdot 10^9$ V/m for aluminium, and $12 \cdot 10^9$ V/m for iron. The steeper slope for iron particles with radii below 150 nm may be explained by different properties of the Goodfellow particles and the BASF particles (e.g. purity).

Further investigations that compare the maximum surface field strength with the elastic constants or critical tensions of the material yielded no interrelations so far (see also Table A.4).

A.3 Performance of the new dust source

The results described above show, that the new dust particle source was successfully applied to the Heidelberg Dust Accelerator. More material types than ever can now be accelerated at the accelerator facility. It has to be mentioned that further experiments at a test setup had been successful with samples of copper, silver and 2.1 μm latex projectiles (STÜBIG, 1999; STÜBIG et al., 2001). This means an extension in the range of the projectile density up to $\rho = 10500\,\text{kg/m}^3$. Although the acceleration of carbon and aluminium with the old dust source has already been reported in earlier works, the experimenters complained about large difficulties to extract particles (cf. (GÖLLER and GRÜN, 1989; DALMANN et al., 1977; EICHHORN, 1976).

The charging properties show a slight improvement with respect to the old dust source. At the test setup, the dust source has been used with needle potentials up to 30 kV. This leads to an even higher charging of the particles inside the dust reservoir. Unfortunately the electronics of the 2 MV Van-de-Graaff accelerator is not able to provide such high voltage supplies.

Furthermore the technical design of the source allows an easier handling. The lighter weight of the new source will also relieve the high voltage column at the accelerator and prevent ageing effects on the mechanical setup of the dust accelerator (STÜBIG et al., 2001).

Material	σ_{max} [MPa]	σ_B [MPa]	σ_S [MPa]	E [GPa]	G [GPa]	$E_{max}(1\mu\text{m})$ 10^6[V/m]	$E_{abs.max}$ 10^6[V/m]
Aluminium	110	50 - 90	10 - 35	70	25	1800	3000
Carbon	1000			980	21	540	1300
Iron	210	180 - 210	120 - 150	115	45	1300	12000
PANi-PS-latex	70	27				1000	1100

Table A.4: Comparison of elastic constants and the charging properties of different projectile materials: σ_{max}: ultimate strength; σ_B: tensile strength; σ_S: yield stress; E: Young modulus; G: shear modulus; $E_{max}(1\mu\text{m})$: maximum electric surface field strength for a 1μm-sized particle; $E_{abs.max}$: maximum observed field strength.

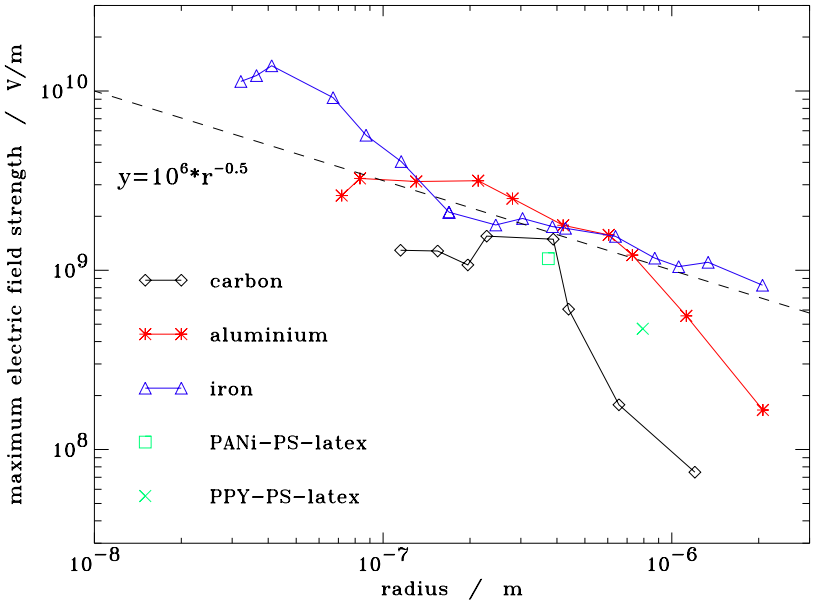

Figure A.1: The achievable maximum surface field strength depending on the grain size of the projectile, and on the projectile material. The dashed line represents a theoretical maximum field strength depending on $r^{-0.5}$.

On the other hand, the new dust source has two main disadvantages: first, the particle extraction is very efficient, leading to a small total runtime of only a few days for the most materials (cf. Table A.2). The old dust source, filled with iron, allowed run times up to four weeks (cf. (SCHÄFER, 2002)). Thus, the old dust source will additionally be used in the future for accelerating iron particles. The second disadvantage are the focussing properties of the new dust source. In her diploma thesis, Mocker (2002) showed, that the optimum beam focus voltage is linearly correlated with the potential of the dust source. Since for extracting particles from the new dust source as described in Section 2.1.1, the whole source housing is pulsed, the focus voltage is only optimized for a short time period. This leads to a widening of the dust particle beam (geometrically limited to 10 mm diameter) with only a faint focus in the center.

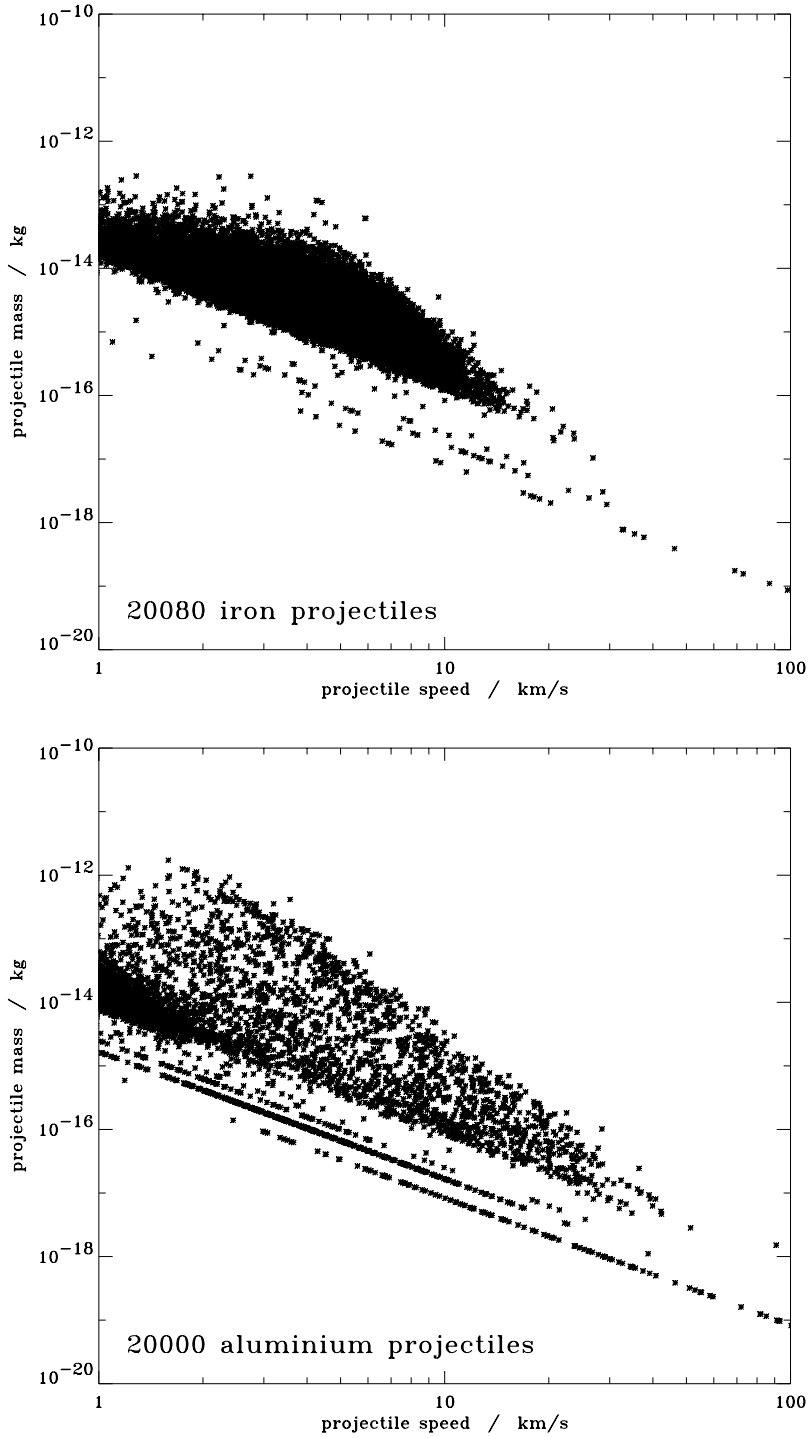

Figure A.2: Speed-mass-distributions of 20080 iron particles (upper figure) and 20000 aluminium particles (lower figure), as provided by the new dust source.

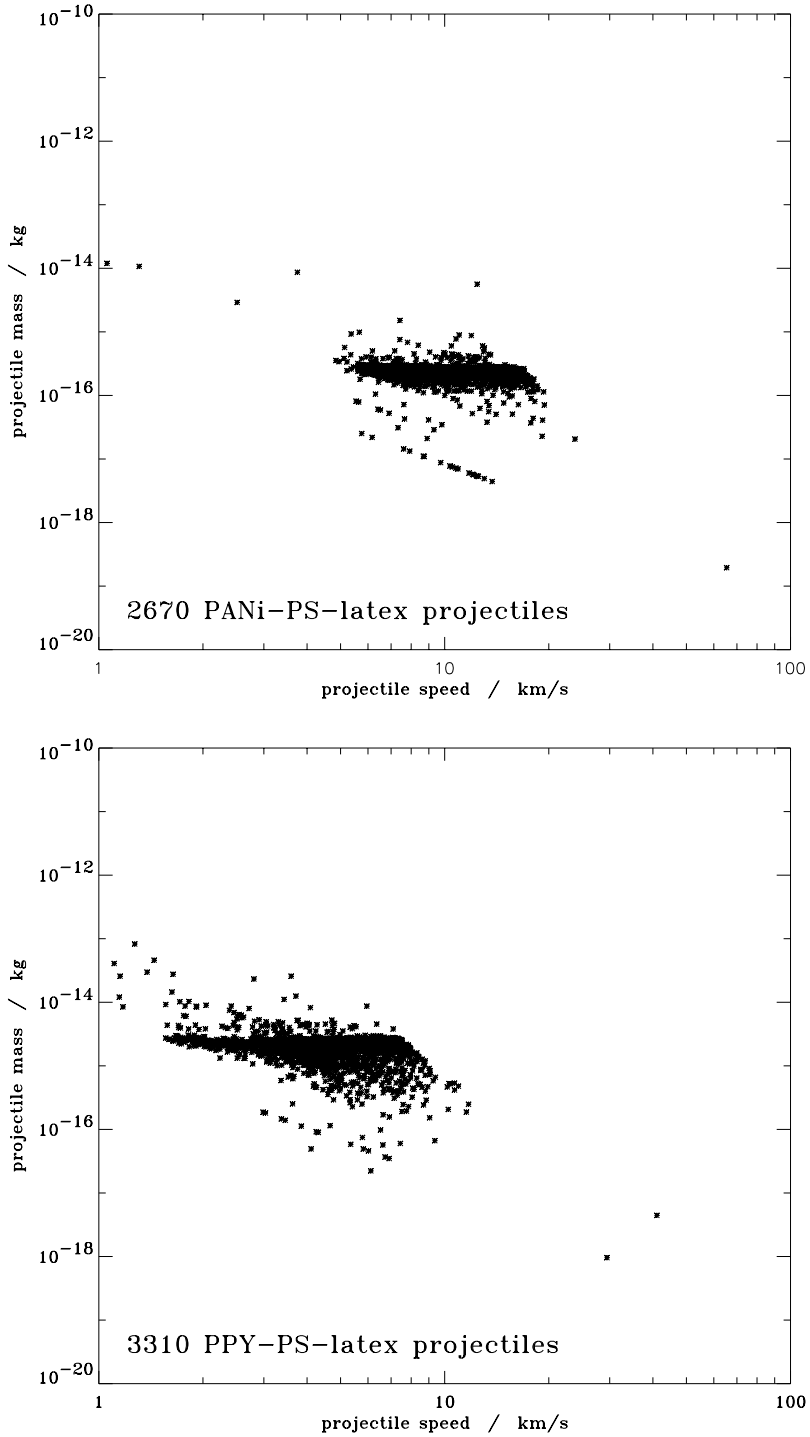

Figure A.3: Speed-mass-distributions of the latex projectiles. The upper figure shows the distribution of 2670 PANi-PS-latex particles, the lower figure shows the distributions 3310 PPY-PS-latex projectiles.

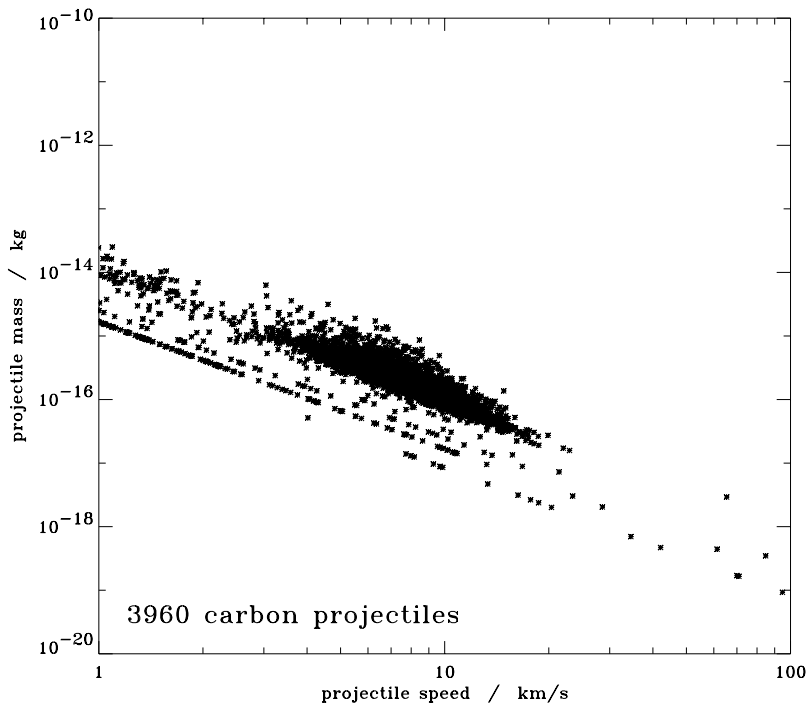

Figure A.4: Speed-mass-distribution of 3960 carbon projectiles from the new dust source.

Appendix B

Setups and data processing

This Appendix gives a more detailed description of the measurement setups and data processing than in Section 3.3. Section B.1 deals with the two different mounts and the exact impact locations. The general settings of the voltages and trigger thresholds are given. Before switching on the high voltages at CDA, a good vacuum is necessary. The following Section B.2 describes how the data from the instrument is derived and stored. The further evaluation of the raw data to the results is explained in Section B.3.

B.1 Setup of CDA

The setup of CIDA has been already explained in Section 3.3. In this section a more detailed description of the CDA setup with different mounts and the various projectile impact sites is given (Sections B.1.1 and B.1.2). Section B.1.3 gives an overview of the general settings. Finally the vacuum pumping process is described (Section B.1.4).

B.1.1 Mount for shots on CAT, IID and WALL

The CDA instrument was set up in two ways. To perform shots on the CAT, the IID and the instrument wall with the same configuration, CDA was put on a inclined desk, so that the projectiles hit the instrument at inclination angles of 0° in z-direction and -20° in y-direction for the CAT. In this frame of reference, the beam itself comes from x-direction. The particle beam hits the instrument 40 mm below the central instrument axis in y-direction. This configuration is shown in Figure B.1 a). The table inside the vacuum chamber allows an external movement of the instrument in y-direction, so that the following target positions can be hit by projectiles: outer CAT (oCAT: -60 mm, -40 mm), central IID (cIID: -150 mm, -40 mm), outer IID (oIID: -180 mm, -40 mm), central WALL (cWALL: -210 mm, -40 mm, in the middle between IID and the innermost grid) and outer WALL (oWALL: -210 mm, -40 mm, 1/3 to the innermost grid, 2/3 to the IID). The (Δx, Δy) mm-values give the offset distance from the CAT center (instrument symmetric axis). Since the IID target has a hemispherical shape, the inclination angle in y-direction changes to 10° for the central IID, to 40° for the outer IID and to 70° for both wall positions. The inclination angle in z-direction remains at 0°. The flight paths of projectiles inside the CDA instrument and the above mentioned impact locations are shown in Figure B.2. The geometry of the beam tube and the narrow widths of the influence tubes along the beam line (Ø = 10 mm) allows the particles to scatter within an area of approximately 1 cm^2 around the nominal target position.

B.1.2 Mount for shots on the central CAT

For shots on the central CAT (cCAT, 0 mm, 0 mm), the instrument was set up on a turntable with a rotational axis parallel to the y-direction. The turntable was tilted, so that the particle beam hit the central CAT with inclination angles of 0° in y direction and -45° in z-direction, as demonstrated in Figure 3.3 b). Once set up, no further movement of the movable table or the rotational axis of the turntable was necessary.

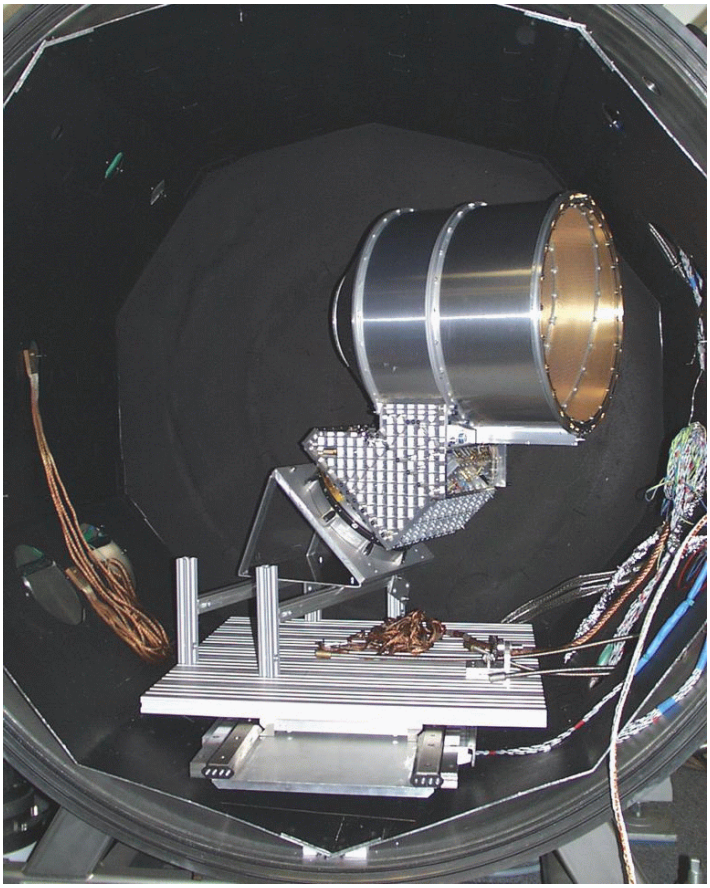

Figure B.1: The CDA flight spare instrument, mounted on a table for shots on the wall, the IID target positions and for shots on the outer CAT. The dust particles enter the instrument from the right side.

B.1.3 General settings of the CDA instrument

The measurements were all performed at the Heidelberg Dust Accelerator with 2 MV acceleration voltage. Only for the 0.75 μm latex sample, the acceleration voltage was reduces to 500 kV to achieve projectile speeds below 6 km/s. The adjustment of the dust source voltages was empirical and is described in Appendix A above. Although iron projectiles will be better charged in the new dust source (STÜBIG et al., 2001), the beam stability for these particles is much better with the previous dust source. Thus, the previous dust source has been used for extracting iron projectiles.

The projectiles have been selected by the particle selection unit (PSU), setting narrow speed ranges. No charge selection has been performed. To check if a selected particle reached the ex-

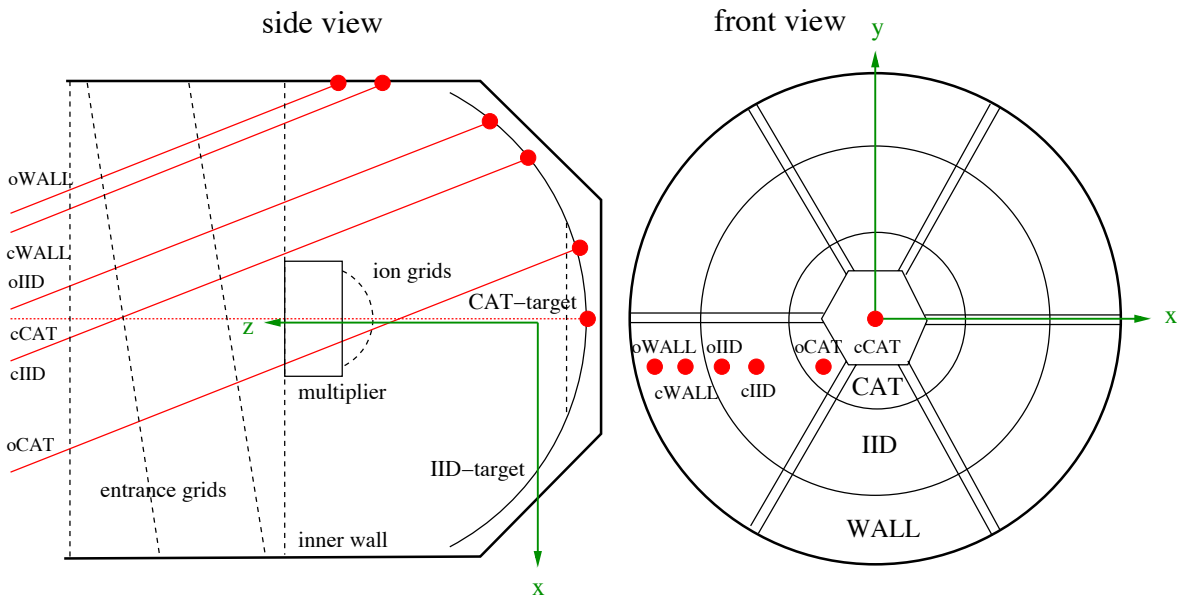

Shoot positions onto the CDA flight spare:

cCAT	central Chemical Analyzer Targert
oCAT	outer Chemical Analyzer Target
cIID	central Impact Ionization Detector
oIID	outer Impact Ionization Detector
cWALL	central instrument Wall
oWALL	outer instrument Wall

Figure B.2: Schematic side view and front view on the CDA instrument. Within the front view, the wall area is projected around the IID. The red dots show the impact locations that were used in the present study, the red lines show the corresponding flight paths through the instrument.

periment chamber and hit the instrument, its flight path was controlled with charge sensitive influence tubes at different places of the beam line tube. 3 m behind the dust source, the PSU measures charge and speed with three 100 mm long detectors. If a particle passes properly through this section, a 280 mm long, double-shielded high sensitive detector follows after a further 2 meters. This detector has two output channels, one for very small absolut charges below 10^{-15} C, the other for charges above this value (HO, 2000). Since the charge measurement of the PSU is not very reliable and often failed, the high sensitive influence tube was also used as reference measure of the particles' charge[1]. A final detector tube is located directly in front of the vacuum chamber (QD) and allows to ensure whether a particle reached the instrument or not.

The CDA instrument settings, that were used for all measurements in this work, are summarized in Table B.1. The threshold values were adapted to the noise environment in the laboratory. Lower values

[1]For the charge measurement with this detector, an empiric charge sensitivity of $1.3^{-12}\frac{C}{V}$ has been taken, obtained from measurements with a calibrated 100 mm influence tube. In her diploma thesis, Ho obtained the same sensitivity value and proofed the detector linearity in the relevant charge range (HO, 2000). Directly at the entrance of the experiment chamber a last detector QD registers if a particle passes. If so, it is assumed that the particle hits the instrument. It is worth annotating that the fraction of particles that reaches the experiment chamber is not only depending on the projectile type, but also on the selected speed range. Typical for the fraction of passing particles are 10 % - 30 %. Further work on beam focussing is presently done by A. Mocker in her diploma thesis (MOCKER, 2002).

Setting	digital value	absolute value
External voltage supply		30 V
HVC (CAT voltage)	178 dn	-350 V
HVI (ion grid voltage)	245 dn	+1021 V
HVM (multiplier voltage)	187 dn	-3140 V
Instrument current	195 - 205 dn	370 - 390 mA
Instrument temperature		290 K
Chamber pressure		$1-2\cdot10^{-4}$ Pa
QT threshold	4 - 5	$5.2-5.7\cdot10^{-14}$ C
QC threshold	5 - 7	$5.3-7.3\cdot10^{-14}$ C
QA* threshold	4 - 5	$4.2-4.5\cdot10^{-13}$ C
QI threshold	4 - 5	$3.5-3.9\cdot10^{-14}$ C
QMA* threshold	2	74 mV
Event definition	QT, QC, QI, QM, QMA (all used)	

Table B.1: General instrument settings for CDA, as used for all measurements in this work. For the absolute values of the trigger thresholds for QA and QMA were taken the values of the flight unit.

will cause frequent or even permanent instrument triggering without projectile impacts. Sometimes bursts with a lot of noise counts up to one count per second appeared. These bursts could only be stopped by setting the QC-threshold to 7 or by taking QC and/or QI out of the event definition scheme. The digital to absolute value conversion is taken from Srama (2000).

B.1.4 Vacuum pumping

Since the secondary electron multiplier of CDA and the microchannel/-sphere plate of CIDA need working voltages of several kilovolts, a good vacuum is required in the experiment chamber to avoid sparkling and instrument damage. After finishing the setup process as described above, the experiment chamber is closed and a pre-vacuum pump is switched on for approximately 20 minutes, until a vacuum of 1 Pa is reached. Now the chamber is vented with pure nitrogen gas to a pressure of 40 kPA (0.4 bar). The chamber is evacuated again with the pre-vacuum pump. The nitrogen venting helps to get rid of humidity in the chamber. If the chamber and/or instrument was not in use for long time, the nitrogen venting process should be repeated. After reaching again a vacuum of 1 Pa, the turbo molecular pump is switched on. Overnight high vacuum pumping follows. The next morning a vacuum of $10^{-2}-10^{-3}$ Pa ($10^{-4}-10^{-5}$ mbar) should be expected. To speed up the degassing process the heating process starts now: The chamber is heated to a temperature of +50°C, for a few hours even +60 °C. After 8 - 10 h of heating, the process is stopped for security reasons (unattended operation). The heating process is repeated at the next day. Then a period of vacuum pumping follows until a final pressure of $1-2\cdot10^{-4}$ Pa is reached. The full vacuum pumping process, including nitrogen venting and heating periods, usually needs one week. Directly before using the high voltages of the respective instrument, the instrument electronics is switched on for a few hours. This allows a warm up and a last degassing of residual gases in the electronic box.

B.2 Data acquisition with CDA and CIDA

The following sections describe how the charge signals that were generated by impact events are acquired from the instrument. The data of the CDA flight spare unit follow a complicate process that simulates the data reception from space (Section B.2.1). The data signals of the CIDA engineering model are directly measured with an oscilloscope (Section B.2.2). I

B.2.1 Data acquisition with CDA

In space, communication with CDA is only possible via the Deep Space Network (DSN) radio antennas (connection Earth - spacecraft) and the Cassini-Huygens main data bus (connection spacecraft - instrument). In the laboratory this is simulated by the so called CDA Ground System Setup, shown in Figure B.3. A RTIU (Remote Terminal Interface Unit, PC in DOS-mode) is directly linked to the CDA flight spare with a 1553 data bus and simulates the communication between instrument and spacecraft as well as the downlink connection to earth. The sending of commands and receiving of data is performed using a BCE (Bench Checkout Equipment, Windows 3.11 PC). The radio transmission from earth to spacecraft is replaced by ethernet connection between BCE and RTIU. The data from space will be stored in a NASA database which can be accessed via a sun workstation in the Science Operations Center (SOPC) at the MPI-K, Heidelberg. Then the data, consisting of housekeeping data (HK, instrument specific data and values like temperatures, voltages, etc., 64+12 byte packages) and science data (SCI, data from impact events, noise and test pulses, like rise times and charge amplitudes, 512+12 byte packages) can be spooled to files for the BCE. Data, that is stored at the BCE can be transferred via ethernet links to computer clusters, where users can analyze and evaluate the data.

B.2.2 Data acquisition with CIDA

To switch and manipulate the target and multiplier voltages, the CIDA engineering model is connected to an external electronic box. The signals of three channels are recorded on a Nicolet Pro 92 digital oscilloscope: target signal, anode signal, multiplier signal. The target signal shows the impact time and, depending on the target voltage polarity, the total amount of electrons/negative ions or the total amount of positive ions, produced by the impact. The anode is the entrance dynode of the micro channel plate and gives an unamplified linear signal of the time-of-flight mass spectrum. The multiplier signal gives the final TOF MS signal after amplification (logarithmic).

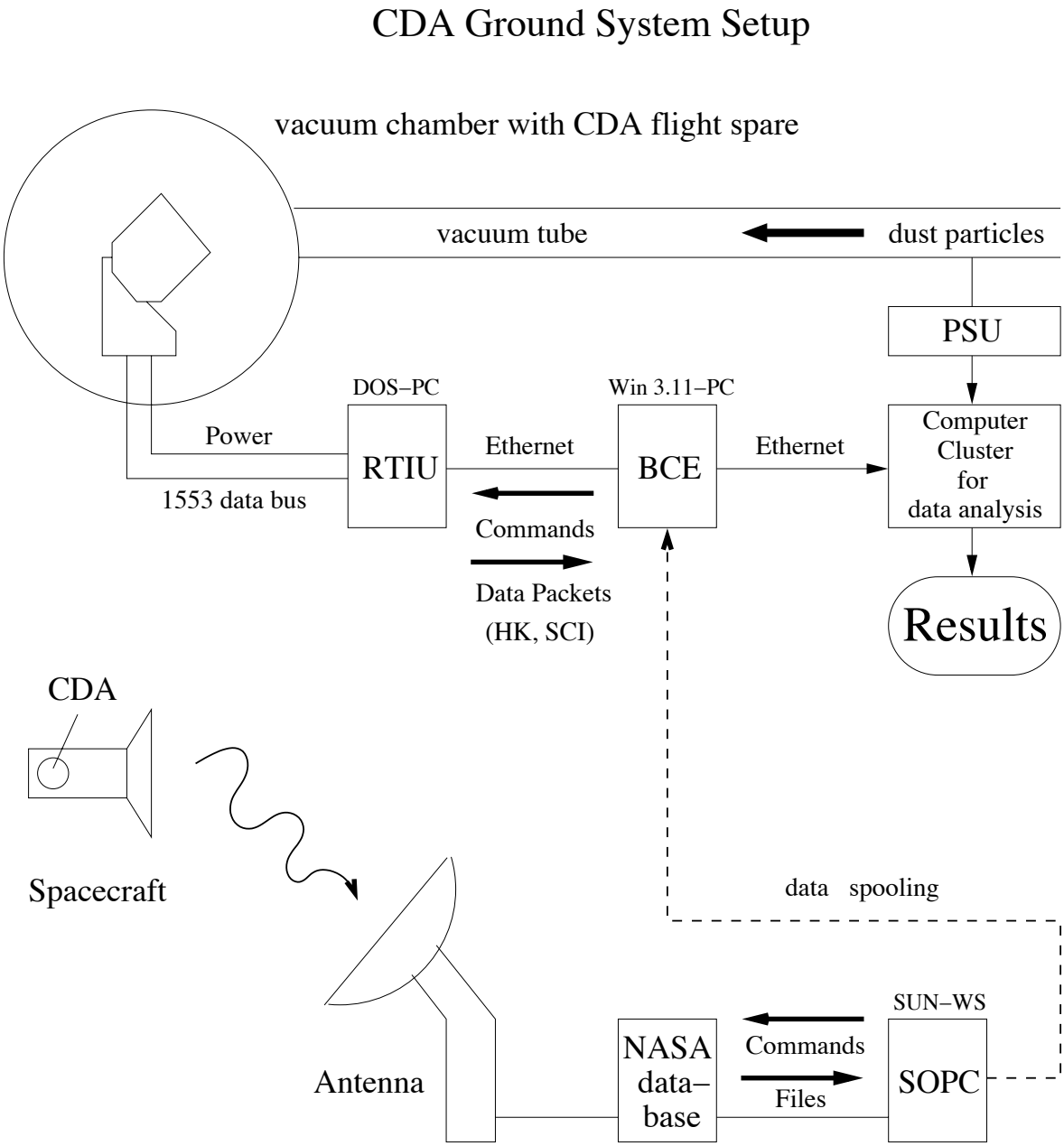

Figure B.3: Schematic overview of the CDA Ground System Setup as it was used for the measurements with the CDA flight spare in this thesis. The abbreviations are explained in the text. The upper system was applied in this work. The lower system with spacecraft and antenna describes the reception of flight data from space and is shown for comparison. In this thesis no flight data has been used.

B.3 Evaluation of CDA and CIDA data

Sections B.3.1 and B.3.2 explain how the data evaluation from raw data to the results proceeds by using different software tools.

B.3.1 CDA data

During the measurements the projectile related data (mass and speed) together with the event time are written in a text file (”messung.txt”). All CDA data is stored from the adapted flight software on the hard disk of the BCE-computer. Since disk space was limited, the data were transferred to the home directory. The data conversion and evaluation proceeds in three steps:

1. First, the flight data packages (maximum size: 1.2 MB) are transferred into *.bin binary files by the software BCE6 or BCE7 (depending on the flight software used). This proceeds mainly automatically.

2. In the next step, the binary files are read and all stored events are sorted by time with the ANALYSE4 program. Now the specific data signals of each channel (e.g. rise times, integrals, charge values) can be evaluated for all events. Several functions and filters allow smoothing of disturbed signals. These data are stored together with the parameters of the impact projectile (speed, mass, ...) into *.dat-files.

3. Finally, the *.dat-files can be read by the EVALUATE4 software. This software package allows to plot physical parameters and values against each other. Also data fitting routines are implemented.

This complete process is also shown in a flow diagram in Figure B.4

B.3.2 CIDA data

The CIDA data has been stored directly on discs with the Nicolet Pro 92 oscilloscope. The data wre converted into float tables with the nicoconv.exe software. A new software tool (CIDASPEC3) has been developed in cooperation with Dr.-Ing. Ralf Srama for the further data evaluation. Since the data evaluation would acquire too much time for this thesis, only sum spectra and mean spectra were taken to get time-of-flight mass spectra with a high mass resolution, and thus to get a better understanding of appearing ions in the spectra. The data processing is shown in flow-diagram Figure B.5.

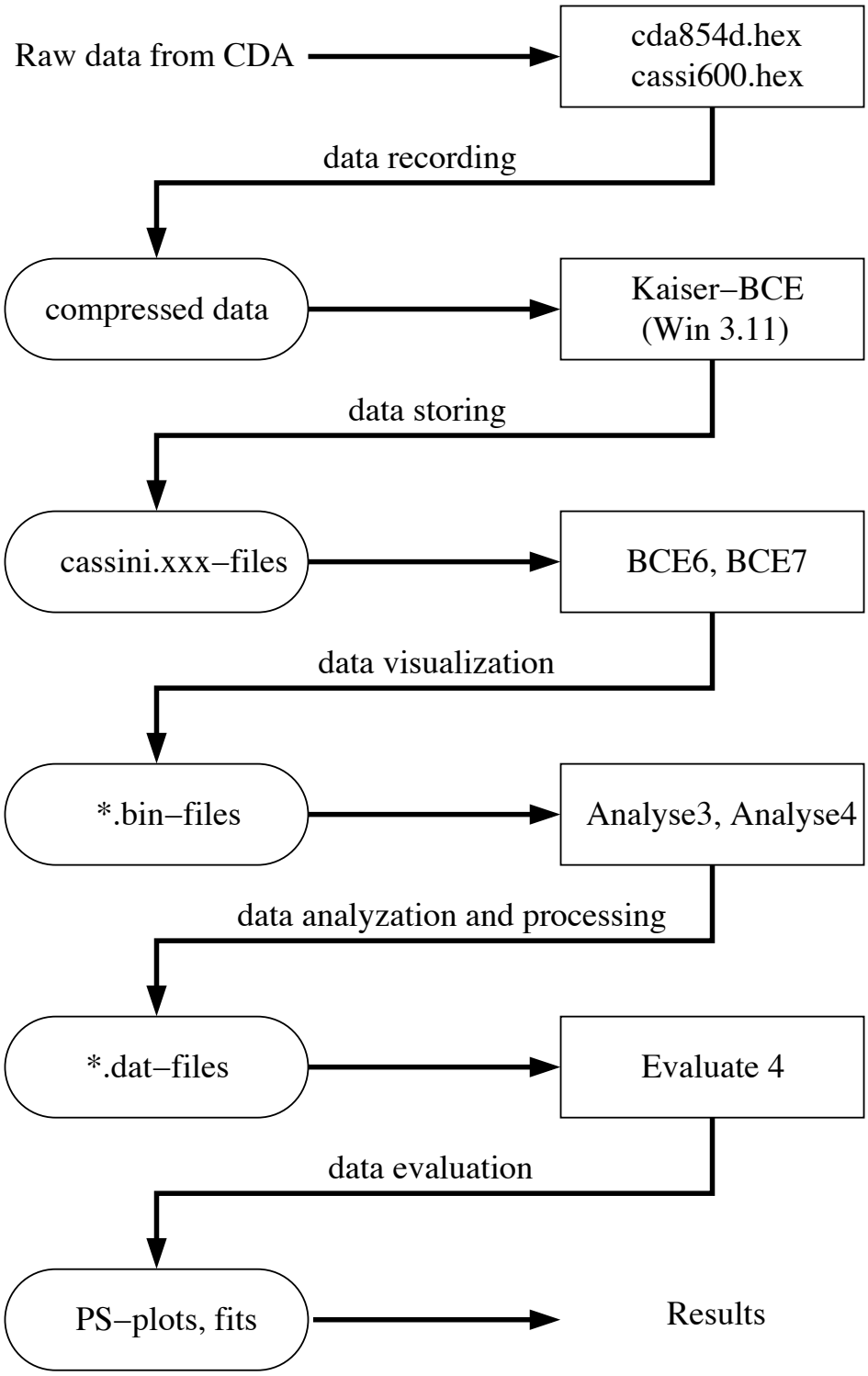

Figure B.4: Flow diagram that shows how the CDA flight spare raw data are processed into data files from which one can obtain diagrams and plots. All software has been developed by Dr.-Ing. Ralf Srama, MPI-K, Heidelberg. The software tools have been permanently improved during data evaluation.

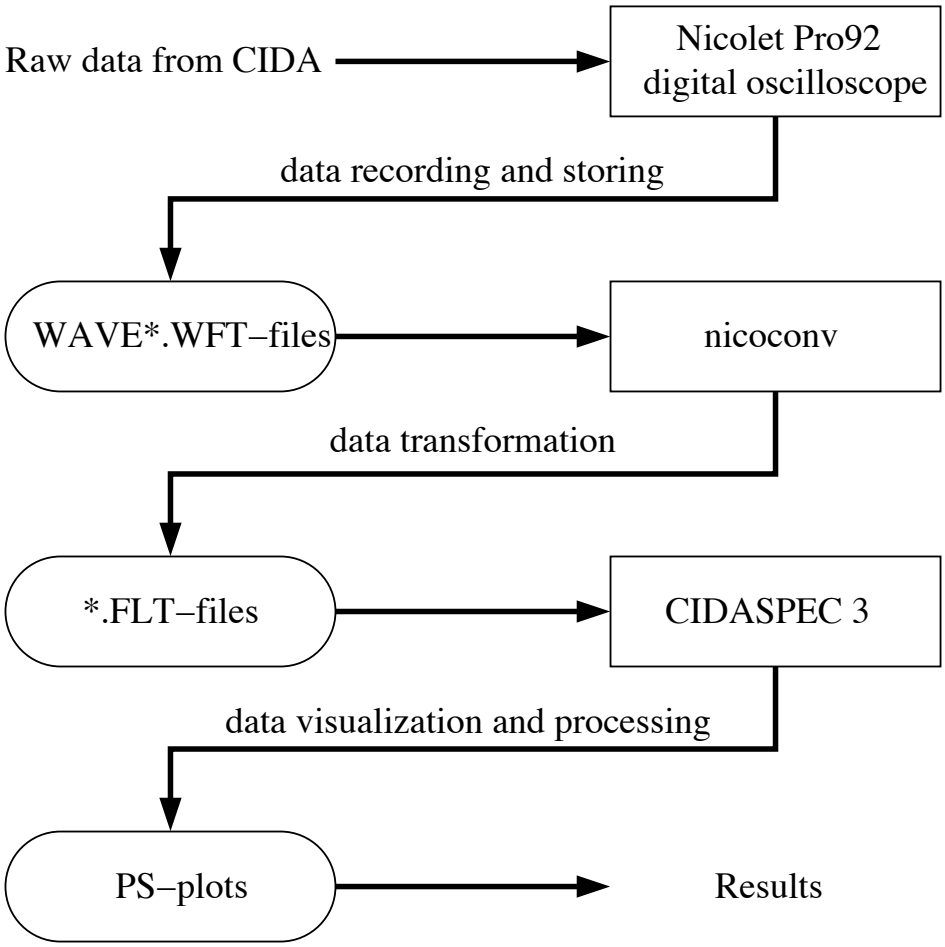

Figure B.5: Flow diagram that shows the processing of the CIDA data.

Appendix C

Summary of the the CDA measurement parameters

This Appendix gives an overview of the measurements that were performed with the CDA instrument. To find the data in the archive (19 ring binders of printed files), a summary of the measurement protocol (messung.txt) is given in Tables C.1 and C.2.

Tables C.3 to C.8 give an overview of the performed measurements with various projectile materials onto the different impact sites. The following values are listed in the tables:

- Total number of shots onto the different impact sites, that definitely passed the last detector QD and hit the instrument.

- Number of impacts, that were registered by the instrument by trigger events.

- Number of time-of-flight mass spectra with at least two mass lines (only for shots onto the CAT).

The target nomenclature is the same as in Section B.1 and can be well seen on Figure B.2. For a better comparison, the tabled data are additionally shown in histogram form in Figures C.1 to C.5. However it is difficult to get a clue on the instrument sensitivity, since higher impact speeds are correlated with smaller particles (cf. Figures A.2 - A.4.

Finally are shown raw signals of shots on the CAT, the IID and the instrument wall, generated by the impact of PANi-PS-Latex projectiles with 16 km/s (Figures C.6 - C.8).

date	projectile material	target Section	impact speed [km/s]
06.09.2000	iron	outer CAT	7 - 15
07.09.2000	iron	outer CAT	3 - 5
08.09.2000	iron	outer CAT	2
11.09.2000	iron	central WALL	6 - 25
12.09.2000	iron	central WALL	2 - 4
		outer WALL	7 - 30
13.09.2000	iron	outer WALL	2 - 6
		central IID	7 - 50
14.09.2000	iron	central IID	2 - 50
15.09.2000	iron	central IID	2
		outer IID	3 - 40
16.09.2000	iron	outer IID	2
		outer CAT	15 - 40
		central WALL	20 - 50
		outer WALL	30 - 70
19.02.2001	PPY-PS-latex	outer CAT	2 - 8
21.02.2001	PPY-PS-latex	outer CAT	2 - 8
		central IID	2 - 8
22.02.2001	PPY-PS-latex	outer IID	2 - 8
		central WALL	8
23.02.2001	PPY-PS-latex	central WALL	2 - 6
		outer WALL	2 - 8
		MP support	8
26.02.2001	PPY-PS-latex	central IID	3 - 8
		outer CAT	3 - 4
		MP support	6 - 10
		central WALL	5 - 10
27.03.2001	PANi-PS-latex	outer CAT	8 - 19
28.03.2001	PANi-PS-latex	outer CAT	4 - 16
		central IID	16 - 19
29.03.2001	PANi-PS-latex	central IID	6 - 14
30.03.2001	PANi-PS-latex	central IID	4
		outer IID	8 - 19
02.04.2001	PANi-PS-latex	outer IID	4 - 8
		central WALL	12 - 19
03.04.2001	PANi-PS-latex	central WALL	6 - 12
05.04.2001	PANi-PS-latex	central WALL	4 - 6
		outer WALL	10 - 19
06.04.2001	PANi-PS-latex	outer WALL	4 - 19

Table C.1: Summary of the measurement protocol. For each day of measurement are given the following values: date, projectile material, target Section and impact speed range v.

date	projectile material	target Section	impact speed [km/s]
14.05.2001	carbon	outer CAT	14 - 30
15.05.2001	carbon	outer CAT	12 - 18
16.05.2001	carbon	outer CAT	2 - 10
17.05.2001	carbon	central IID	4 - 12
21.05.2001	carbon	central IID	4 - 18
		outer CAT	4 - 30
22.05.2001	carbon	outer CAT	2 - 4
		central WALL	8 - 18
23.05.2001	carbon	central WALL	4 - 18
		outer IID	6 - 16
30.05.2001	carbon	central CAT	2 - 16
31.05.2001	carbon	central CAT	2 - 16
06.06.2001	PANi-PS-latex	central CAT	6 - 12
07.06.2001	PANi-PS-latex	central CAT	4 - 20
08.06.2001	PANi-PS-latex	central CAT	18 - 25
13.06.2001	carbon + Na	central CAT	12 - 30
15.06.2001	carbon + Na	central CAT	4 - 16
19.06.2001	aluminium	central CAT	12 - 40
20.06.2001	aluminium	central CAT	12 - 40
22.06.2001	aluminium	central CAT	2 - 16
25.06.2001	aluminium	central CAT	8 - 18
03.12.2001	PPY-latex	central CAT	5 - 30
05.12.2001	PPY-latex	central CAT	20 - 30
06.12.2001	PPY-latex	central CAT	25 - 30
10.12.2001	latex-silica compound	central CAT	2 - 10
13.12.2001	latex-silica compound	central CAT	2 - 20
17.12.2001	aluminium	central CAT	20 - 30
18.12.2001	aluminium	central CAT	20 - 50
19.12.2001	aluminium	central CAT	40 - 55

Table C.2: Summary of the measurement protocol. For each day of measurement are given the following values: date, projectile material, target Section and impact speed range v.

Target		Impact speed / km/s							
		1.5 - 2.5	3.5 - 4.5	5.5 - 6.5	7.5 - 8.5	9.5 - 10.5	11.5 - 12.5	13.5 - 14.5	15.5 - 16.5
cCAT	shots	32	27	26	26	23	37	49	39
	triggered	22	20	21	21	20	30	35	26
	spectra	2	7	11	12	14	24	24	16

Target		Impact speed / km/s								Total
		17.5 - 18.5	19.5 - 20.5	20.5 - 25.5	25.0 - 30.0	30.0 - 35.0	35.0 - 40.0	40.0 - 45.0	> 45	
cCAT	shots	25	5	ca. 175						438
	triggered	19	4	21	9	22	25	22	15	332
	spectra	12	4	12	6	12	18	15	9	198

Table C.3: Overview of the aluminium measurements. The data set includes 87 events, measured by S. Kuhn. ($v > 20$ km/s)

Target		Impact speed / km/s							
		1.5 - 2.5	3.5 - 4.5	5.5 - 6.5	7.5 - 8.5	9.5 - 10.5	11.5 - 12.5	13.5 - 14.5	15.5 - 16.5
cCAT	shots	3	2	30	31	48	35	35	48
	triggered	1	2	15	20	30	30	30	30
	spectra	1	1	8	13	22	22	26	25
oCAT	shots	52	62	43	37	38	55	41	53
	triggered	26	30	13	20	20	30	30	30
	spectra	0	2	1	6	8	21	17	22
cIID	shots	-	21	20	33	36	37	33	35
	triggered	-	1	0	3	6	5	3	5
oIID	shots	-	-	2	34	43	21	20	20
	triggered	-	-	0	4	13	1	0	0
cWALL	shots	-	20	32	36	35	20	21	20
	triggered	-	0	2	6	5	0	1	0

Target		Impact speed / km/s			Total
		17.5 - 18.5	19.5 - 20.5	> 20.5	
cCAT	shots	3	-	-	235
	triggered	0	-	-	158
	spectra	0	-	-	118
oCAT	shots	45	14	17	457
	triggered	30	9	11	246
	spectra	27	5	10	119
cIID	shots	21	-	-	236
	triggered	1	-	-	24
oIID	shots	-	-	-	140
	triggered	-	-	-	18
cWALL	shots	10	-	-	194
	triggered	0	-	-	14

Table C.4: Overview of the Carbon measurements.

Target		Impact speed / km/s							
		1.5 - 2.5	3.5 - 4.5	5.5 - 6.5	7.5 - 8.5	9.5 - 10.5	11.5 - 12.5	13.5 - 14.5	15.5 - 16.5
cCAT	shots	-	12	32	29	30	33	28	3
	triggered	-	8	20	20	20	20	16	3
	spectra	-	2	11	13	13	12	8	2

Target		Impact speed / km/s				Total
		17.5 - 18.5	19.5 - 20.5	20.5 - 25.0	> 25.0	
cCAT	shots	17	13	21	4	222
	triggered	10	10	16	2	135
	spectra	10	6	12	1	90

Table C.5: Overview of the Carbon-Na measurements.

Target		Impact speed / km/s							Total
		2.0 - 2.5	3.0 - 3.5	4.0 - 4.5	5.5 - 6.0	7.0 - 7.5	9.0 - 15.0	$>$ 15.0	
oCAT	shots	n.m.	n.m.	n.m.	n.m.	n.m.	n.m.	14	n.m.
	triggered	20	20	20	20	20	18	12	127
	spectra	1	6	9	1	1	4	6	28
cIID	shots	60	31	25	23	56	93	-	288
	triggered	20	20	20	20	40	32	-	152
oIID	shots	65	29	23	29	28	38	-	212
	triggered	20	20	20	20	20	20	-	120
cWALL	shots	25	42	24	23	24	26	11	175
	triggered	0	20	20	20	20	20	10	110
oWALL	shots	31	49	29	23	24	34	12	202
	triggered	20	20	20	20	20	20	10	130

Table C.6: Overview of the iron measurements.

Target		Impact speed / km/s						
		1.5 - 2.5	3.5 - 4.5	5.5 - 6.5	7.5 - 8.5	9.5 - 10.5	11.5 - 12.5	13.5 - 14.5
cCAT	shots	-	46	34	32	32	61	76
	triggered	-	16	20	20	20	40	49
	spectra	-	0	1	2	2	33	36
oCAT	shots	-	24	32	31	31	34	55
	triggered	-	4	20	20	20	20	40
	spectra	-	0	0	1	0	11	28
cIID	shots	-	20	20	55	28	27	27
	triggered	-	0	0	20	20	20	20
oIID	shots	-	20	20	51	24	26	35
	triggered	-	0	0	20	20	20	20
cWALL	shots	-	20	20	33	64	35	25
	triggered	-	0	0	3	20	20	20
oWALL	shots	-	20	20	35	33	32	22
	triggered	-	0	0	5	20	20	20

Target		Impact speed / km/s				Total
		15.5 - 16.5	17.5 - 18.5	19.5 - 20.5	> 20.5	
cCAT	shots	46	62	14	6	409
	triggered	37	50	12	5	264
	spectra	27	39	5	3	148
oCAT	shots	63		-	-	270
	triggered	50		-	-	174
	spectra	27		-	-	67
cIID	shots	26		-	-	203
	triggered	20		-	-	100
oIID	shots	23		-	-	199
	triggered	20		-	-	100
cWALL	shots	24		-	-	221
	triggered	20		-	-	83
oWALL	shots	25		-	-	187
	triggered	20		-	-	85

Table C.7: Overview of the PANi-PS-latex measurements. These projectiles are characterized by a nearly mono-spherical grain size distribution of $0.75 \pm 0.04 \mu$m with a mean mass of $2.4 \cdot 10^{-16}$ kg.

Target		Impact speed / km/s					Total
		2.0 - 2.5	3.0 - 3.5	4.0 - 4.5	5.5 - 6.0	7.0 - 7.5	
oCAT	shots	35	39	37	29	61	201
	triggered	5	7	20	20	50	102
	spectra	0	0	0	5	10	15
cIID	shots	21	33	33	27	24	138
	triggered	1	3	3	20	20	47
oIID	shots	34	30	36	27	26	153
	triggered	3	0	6	20	20	49
cWALL	shots	21	20	32	44	35	152
	triggered	0	0	2	20	20	42
oWALL	shots	21	20	34	33	29	137
	triggered	0	0	4	20	20	44
MPSUPPORT	shots	-	-	-	-	18	18
	triggered	-	-	-	-	10	10

Table C.8: Overview of the PPY-PS-Latex measurements. Similar to the PANi-PS-latex sample these projectiles have also a nearly mono-spherical grain size of $1.58 \pm 0.13 \mu$m with a mean mass of $2.3 \cdot 10^{-15}$ kg.

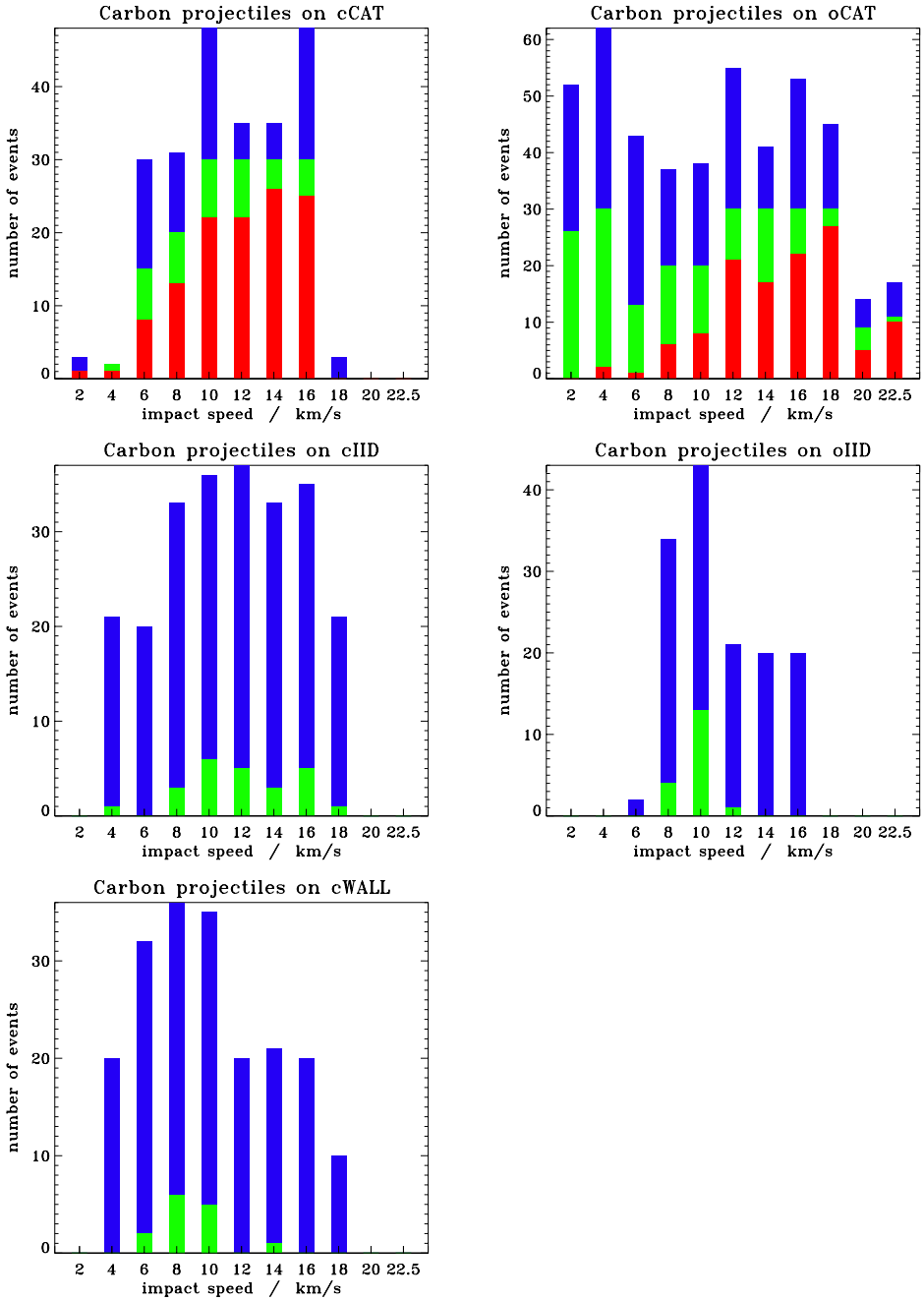

Figure C.1: Histogram comparison of the measurements with carbon. The blue bars show the total number of shots. Additionally the number of trigger events (green bars) and the number of obtained time-of-flight mass spectra (red bars) from all shots are plotted.

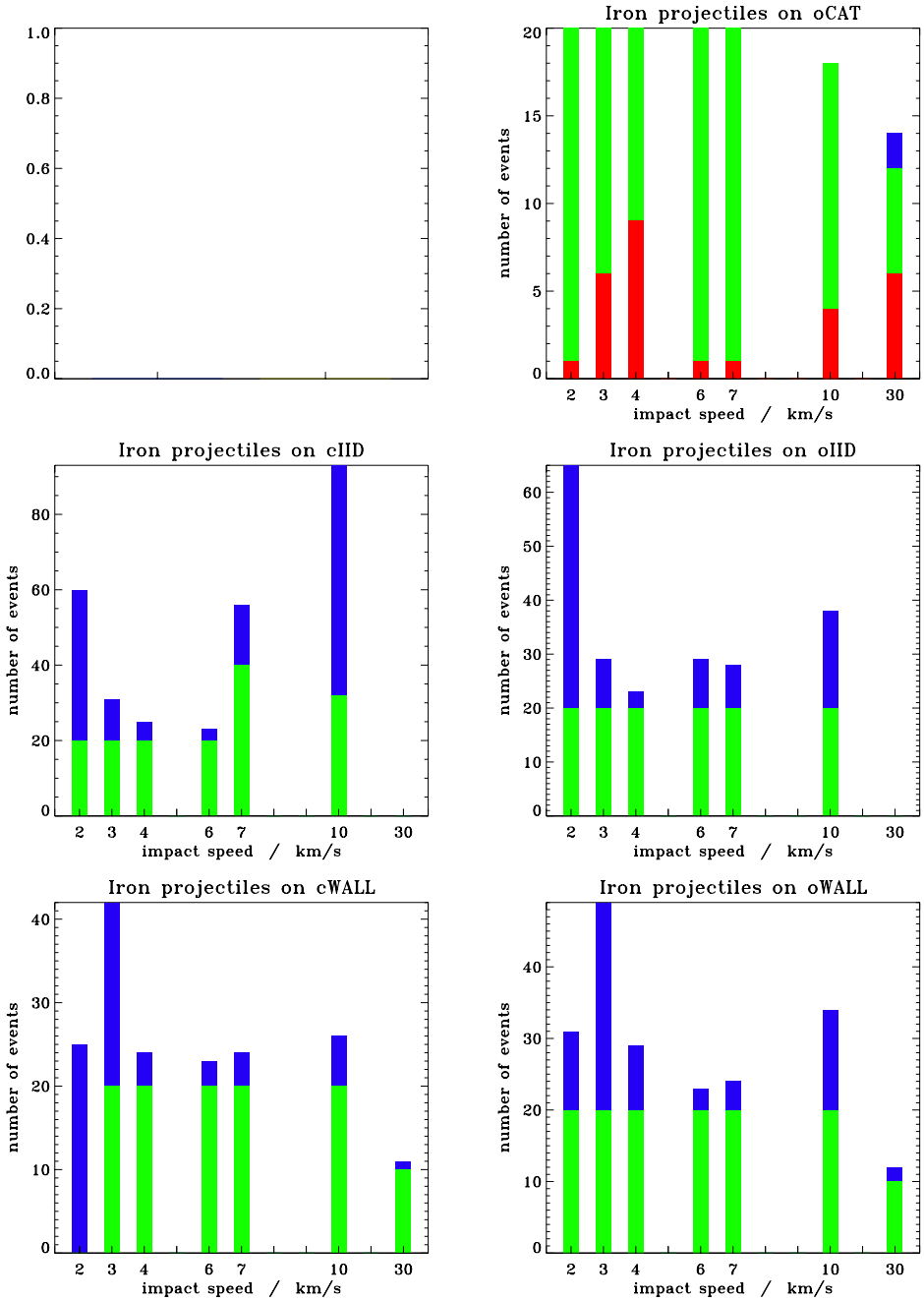

Figure C.2: Histogram comparison of the measurements with iron. The blue bars show the total number of shots. Additionally the number of trigger events (green bars) and the number of obtained time-of-flight mass spectra (red bars) from all shots are plotted.

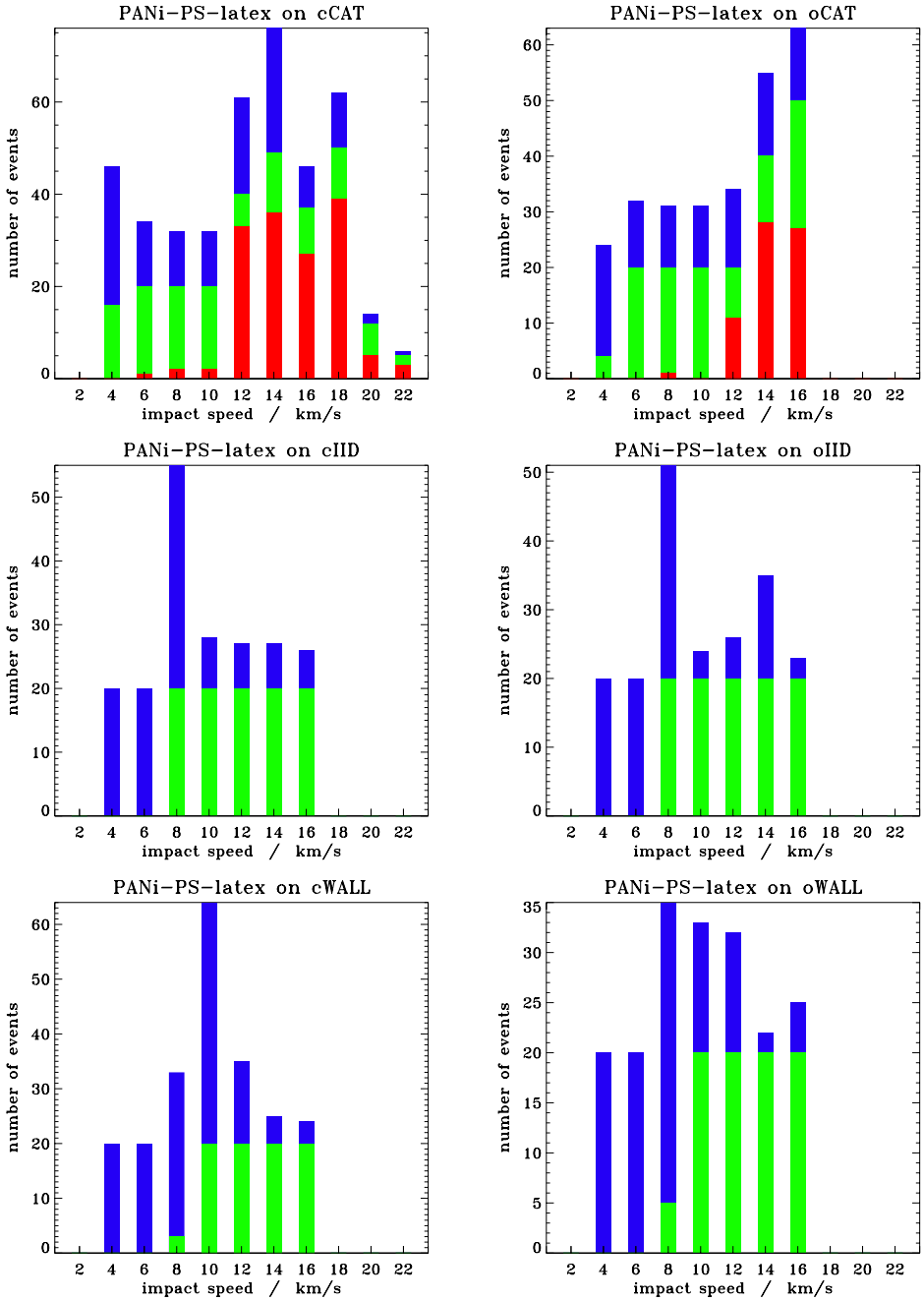

Figure C.3: Histogram comparison of the measurements with PANi-PS-latex. The blue bars show the total number of shots. Additionally are the number of trigger events (green bars) and the number of obtained time-of-flight mass spectra (red bars) from all shots are plotted.

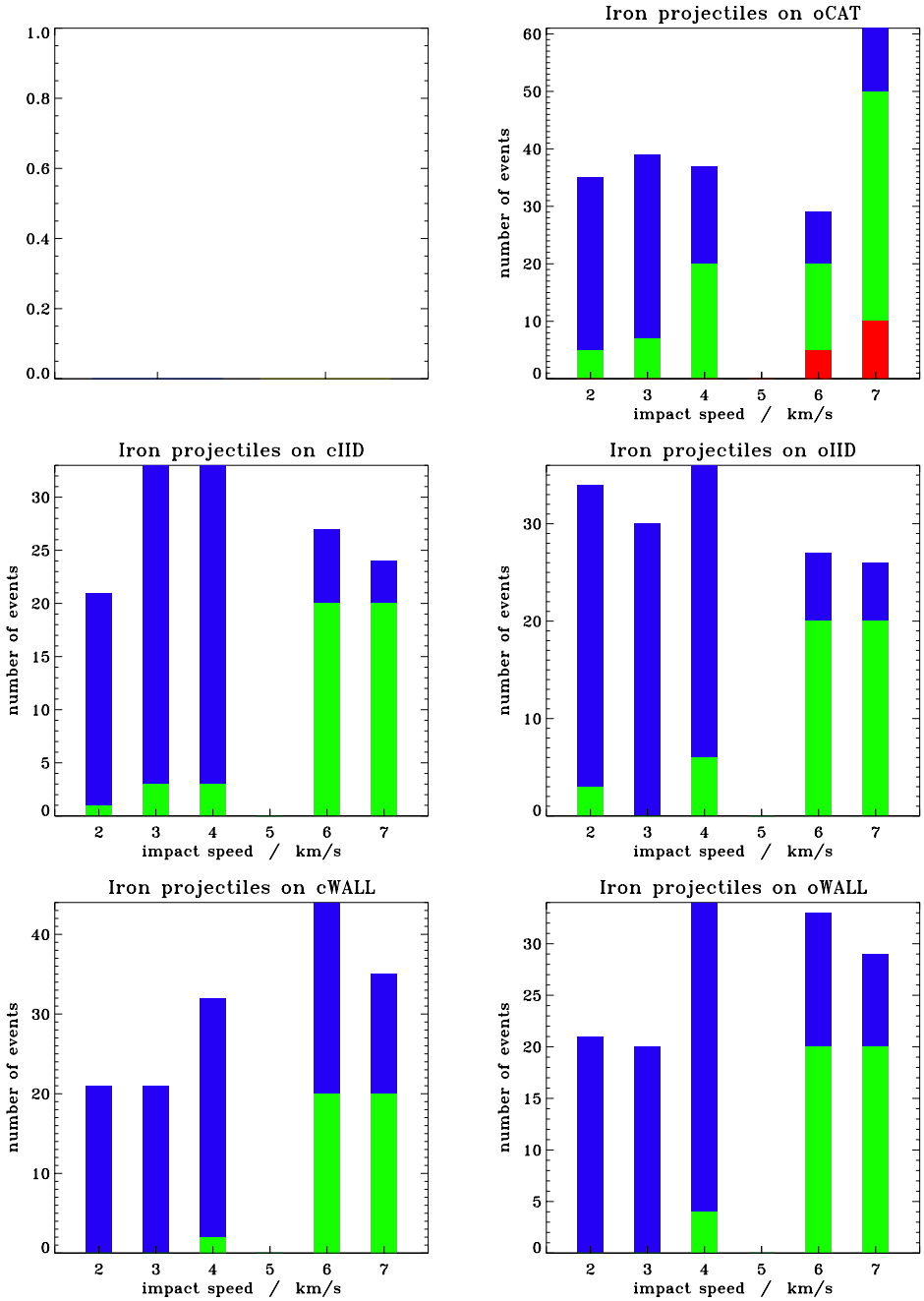

Figure C.4: Histogram comparison of the measurements with PPY-PS-latex. The blue bars show the total number of shots. Additionally are the number of trigger events (green bars) and the number of obtained time-of-flight mass spectra (red bars) from all shots are plotted.

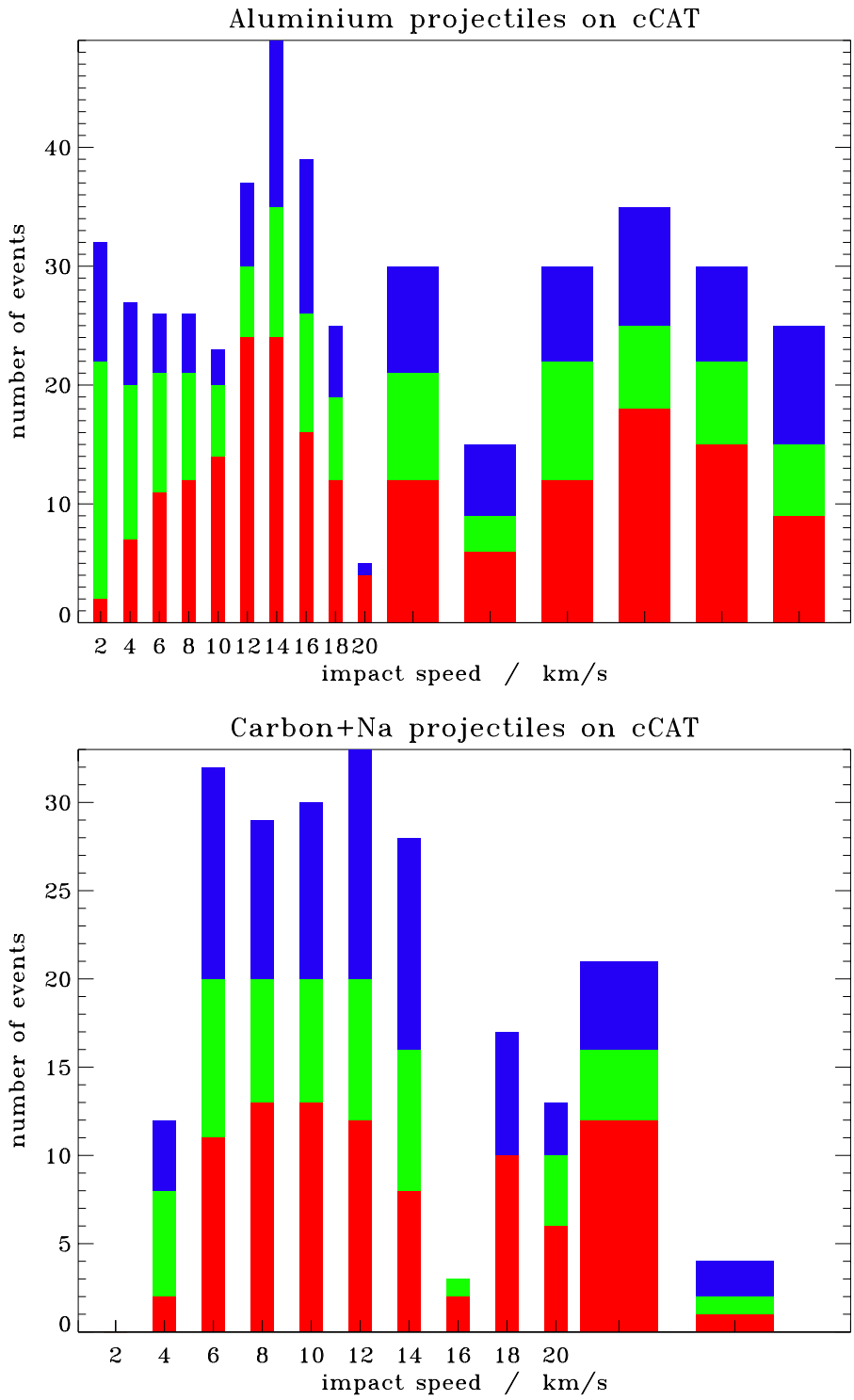

Figure C.5: Histogram comparison of the measurements with aluminium (upper histogram) and carbon + Na (lower histogram), for particles shot on the central CAT region. The blue bars show the total number of shots. Additionally are the number of trigger events (green bars) and the number of obtained time-of-flight mass spectra (red bars) from all shots are plotted.

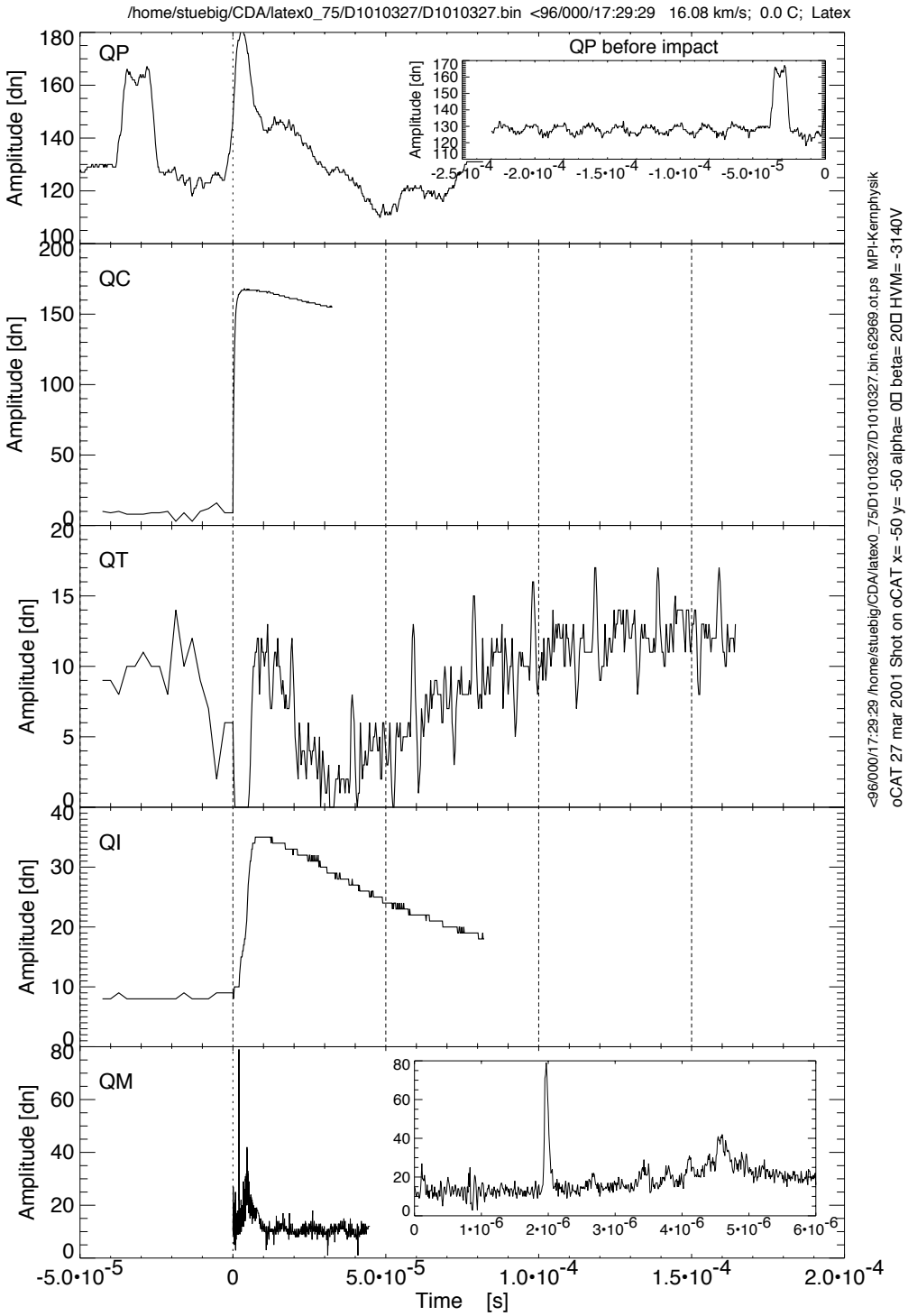

Figure C.6: Raw signal from a shot with an 0.75 μm PANi-PS-latex projectile with 16 km/s on the Chemical Analyzer Target (CAT).

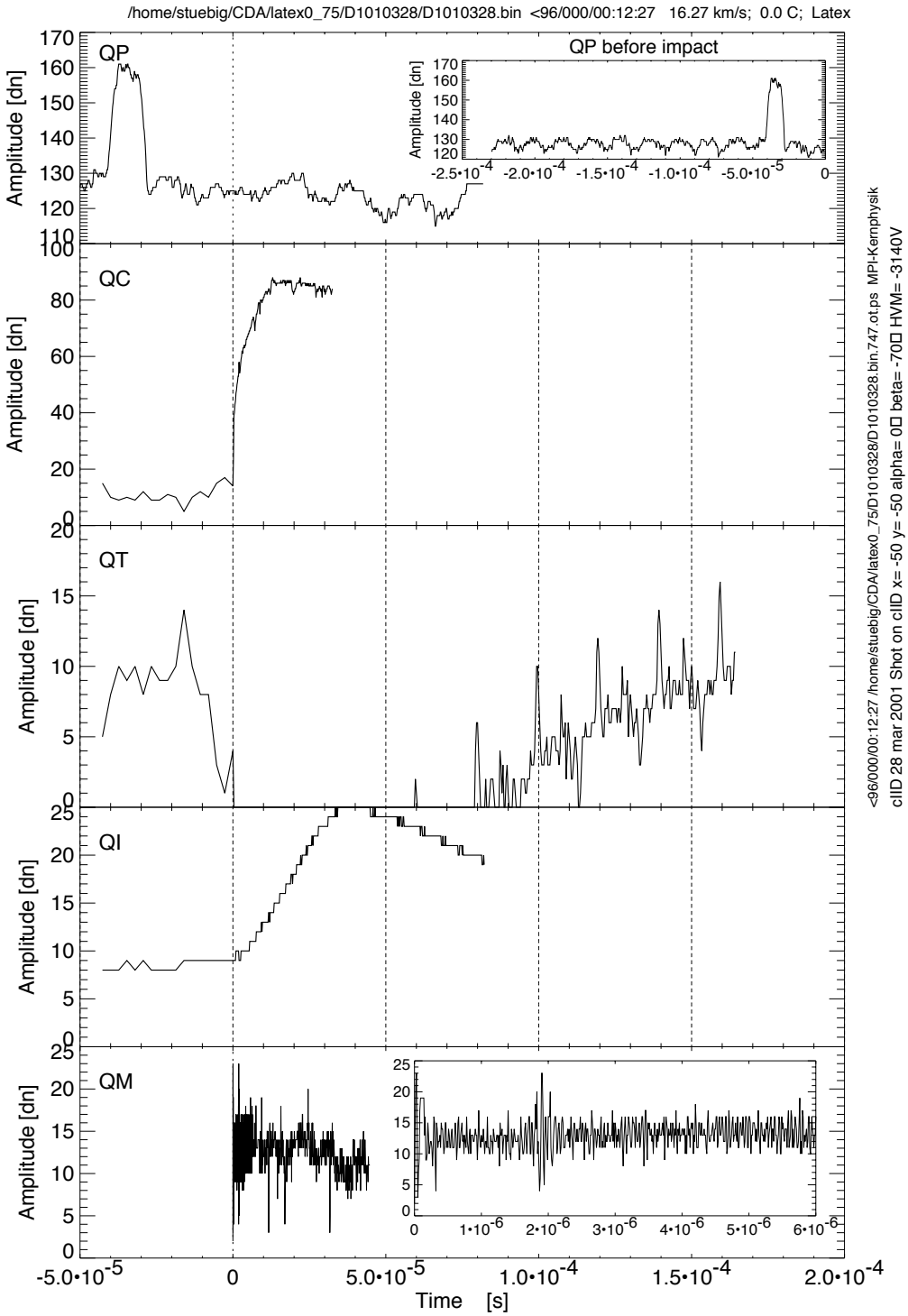

Figure C.7: Raw signal from a shot with an 0.75 μm PANi-PS-latex projectile with 16 km/s on the Impact Ionization Detector (IID).

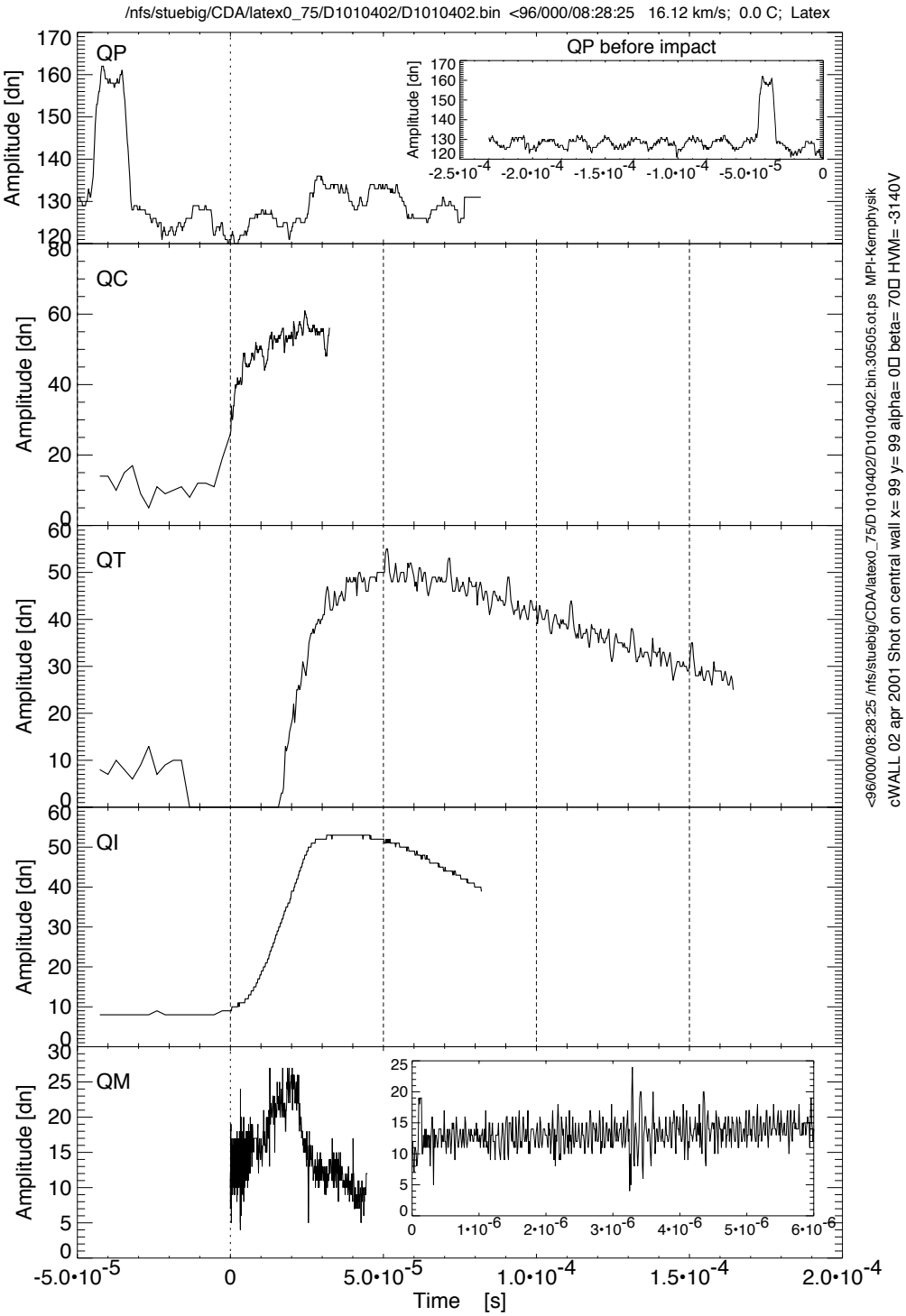

Figure C.8: Raw signal from a shot with an 0.75 μm PANi-PS-latex projectile with 16 km/s on the inner instrument wall (IID).

Appendix D

Calibration results for the CDA flight spare

This chapter contains important results from the calibration of the CDA instrument. The entrance grid system of CDA allows a direct surface charge measurement of the impacting projectile D.1. If the charge is high enough to be detected, the projectile speed and incidence angle can be derived from the signal shape. The following Section D.2 gives a lot of examples of measured impact charge distributions that were described in Section 4.2. Additionally detailed results from shots on the instrument wall are shown. The charge yields measurements of the latex projectiles with constant mass allow a direct measurement of the instrument sensitivity to theses particles depending on the impact speed (Section D.3). The distribution of the ion charge inside the instrument is compared to theoretical simulations. Since the measurements with two different projectile types are consistent, this allows to give absolute sensitivities of the CAT, the IID and even of the instrument wall to arbitrary hypervelocity impacts. Together with an extrapolation of the charge yields to very high impact speeds, the instrument sensitivity for very small and fast projectiles can be modelled (Section D.4). A comparison with recent flight data of Jovian dust stream particles fits well with this model. Section D.5 deals with the signal rise times and time differences between the signals. Unfortunately it was not possible to adapt a reliable impact speed dependency to the rise time data. Combining the rise time data with the charge yield data as done in Section D.6, it is possible to give constraints that allow a reliable determination of the impact site where an unknown projectile hits the instrument. The last section in this appendix gives examples of the mass spectra at various impact speeds for all used projectiles in this work. Additionally is given a verification of the mass sale settings. A weak correlation between the mass scale stretching and the impact speed may help to determine very high impact speeds $v > 100$ km/s via an ion energy depending mass scale stretching. Furthermore are shown calculations of the mass resolution depending on the ion mass and projectile impact speed for the used projectile materials.

D.1 Measurement of projectile charge, speed and incidence angle

The charge sensitive entrance grid system (QP) allows a direct measure of the surface charge, the impact speed and the incidence angle at which the particle enters the CDA detector system relative to the symmetric axis. In Figure D.1 is shown the ratio between the charge that has been measured with the QP-grid system and the actual projectile charge. The ratio is in good agreement with 1.0 which means that the charge measurement of the QP-grids is reliable within the accessible range 10^{-15} – 10^{-13} C. However, the relative error of the charge determination rises with decreasing absolute charge,

manifested by a larger scatter of the data points. Nevertheless the charge ratio shows a minimum of 0.9 at an absolute charge of $2 \cdot 10^{-14}$ C.

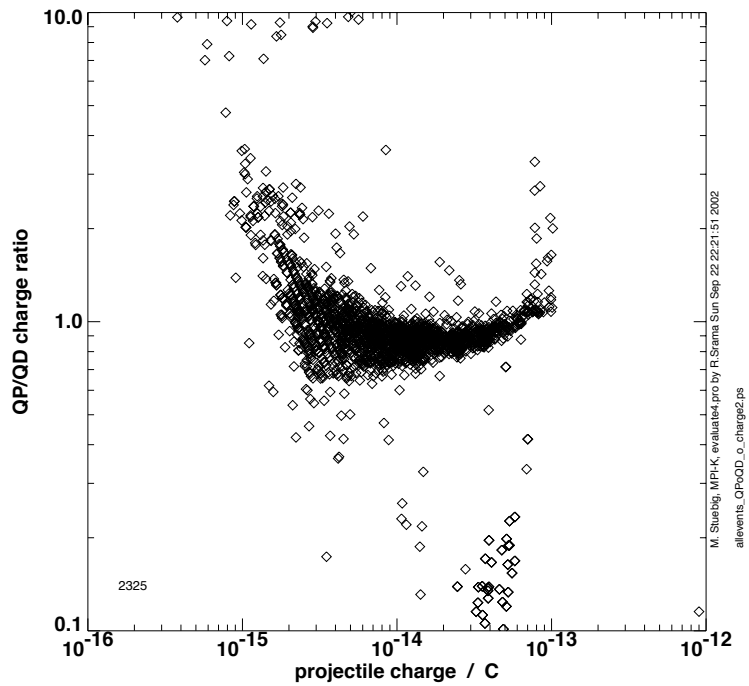

Figure D.1: Ratio between the projectile charge measured with the QP entrance grids and the projectile charge measured with charge sensitive detector by Auer, depending on the actual charge, measured with the charge sensitive detector by Auer.

The impact speed and incidence angle of the projectile can be derived from the shape of the charge signal. A detailed description of this method is given in (SRAMA, 2000). In Figure D.2 shows the impact speed measured with the entrance grid system relative to the actual projectile speed, measured with the Particle Selection Unit of the accelerator facility. It turns out that the measured projectile speed is approximately 90 % of the actual projectile speed. For high impact speeds above 30 km/s the ratio of measured and actual charge is slightly decreasing. The determination of the projectile's incidence angle depending on the surface charge of the projectile is shown in Figure D.3. For low absolute charges, a large scattering between $+60°$ and $-90°$ is obvious. For higher charges, the scatter decreases and converges to a value of $0°$. The actual incidence angle was $20°$ for the shots on the IID, the Wall and the outer CAT. An investigation how the measured impact angle depends on the impact speed (not shown here) yields also a large scattering. Thus, the determination of the incidence angle with the CDA entrance grid system is not reliable.

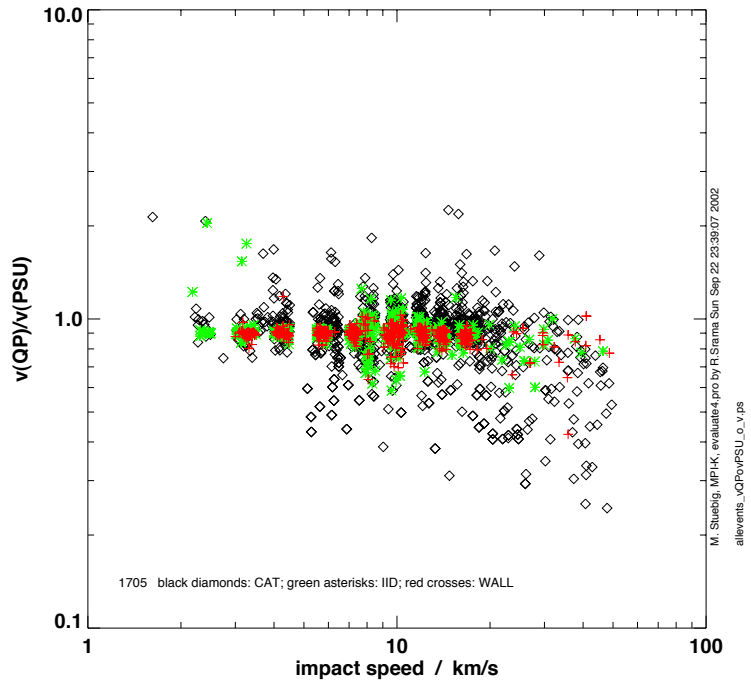

Figure D.2: Ratio between the projectile speed measured with the QP entrance grids and the projectile speed measured with the PSU, depending on the actual speed, measured with the PSU.

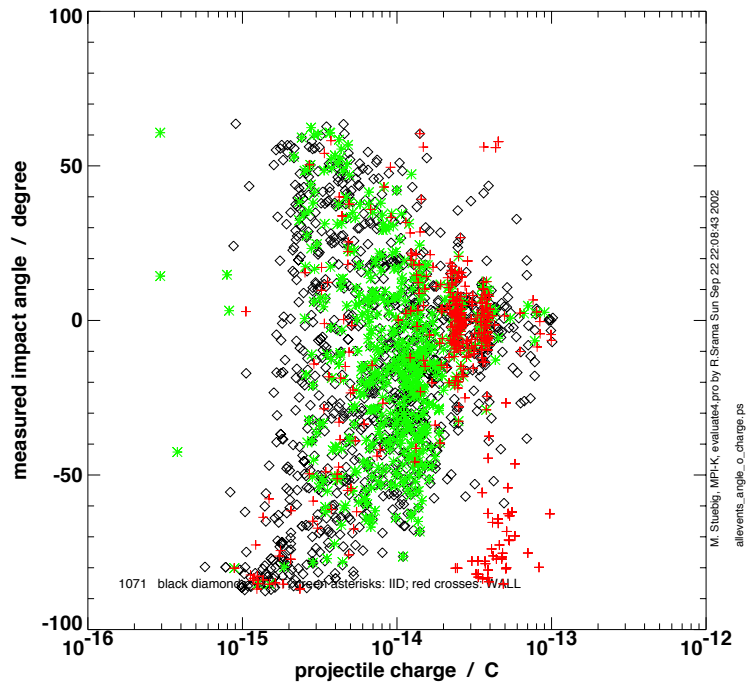

Figure D.3: Measured incidence angle depending on the projectile charge. The actual incidence angle is 20°.

D.2 Charge yield measurements

This section gives an overview of the measurements of the charge yields. The ion charge yields for projectiles that impact on the CAT and IID target are already shown in Section 4.2. The figures in the following Section D.2.1 give additional examples of measured charge yields for impacts onto the CAT and the IID with various projectile materials. Since the instrument geometry allows particles to hit the inner instrument wall, this work includes also shots of various projectiles on this wall region. The results are summarized in Section D.2.2. Finally in Section D.2.3 the distribution of the ion charge on the different targets due to scatter effects is investigated and compared to theoretical simulations by Grün et al. (2002).

D.2.1 Charge yields for shots onto the CAT and IID

Figures D.4 to D.6 show how the total charge yield per mass unit depends on the impact speed. Since the grid in front of the CAT has a transmission of only 68 %, it is expected, that 1/3 of all particles will hit the grid. To avoid falsification of the charge yield values, the data has been divided into impact events that produced time-of-flight mass spectra with at least two mass lines (red crosses in the Figures D.4 to D.6) and those events which produced no TOF mass spectra (black diamonds. Particularly the events with time-of-flight mass spectra should represent ”proper” impacts. The measurements were performed in certain impact speed ranges (cf. Section 4.1). The mean values of these intervals are marked by large blue crosses. Since the data analysis software package needs the setting of single points for using fitting routines, the power law fits (black lines in the figures) were calculated with the mean values.

The charge yields from shots on the IID are shown in Figures D.7 and D.8
.

D.2.2 Charge yields from shots onto the inner instrument wall

The inner instrument wall is represented by the region between the innermost shielding grid from the entrance grid section and the IID target. Like the IID target, the inner wall is gold coated and grounded. Thus, there is also an electric field between the wall and the ion collector grid in the same order as the field for the IID target. The wall is not connected to any charge collector and therefore it cannot measure any impact related charge. Nevertheless, the plasma, that is produced by hypervelocity impacts, will be separated by the electric field in the instrument, and ions may reach also the CAT and IID detectors as well as the ion grid in front of the multiplier. The ion charge and the charge of possible secondary ions from ejecta will be registered at the CAT and the IID. Figures D.9 and D.12 show the characteristic ion charge yield ratios $\frac{QE}{QC}$ and $\frac{QI}{QC}$ as they appear for impacts on the different target sections. These data show particulary how wall impacts (marked with red crosses) can be distinguished from impacts on the CAT and IID. The obtained charge-ratios are summarized in Tables D.1 a) and b).

Significant differences could be found between the QE/QC- and QI/QC-charge ratios for shots on the different target areas and onto the instrument wall for all projectile materials. The ratios are mainly scattering between 0.02 and 10.0 for the QI/QC-ratios, respectively 2.0 - 10.0 for the QE/QC-ratios. The corresponding values for shots on the IID-target show lower ratios, except for the QE/QC-ratios for high impact speeds above 20 km/s. In this case the QE/QC-ratio for IID impacts is higher than for wall impacts. The lowest charge ratios appear at impacts onto the CAT-target. The cause may be the

a)

QI/QC-charge ratio			
Projectile material	CAT	IID	WALL
Carbon	0.02 - 0.2	0.05 - 0.1	0.2 - 2.0
Iron	0.01 - 0.2	0.30 - 2.0	0.3 - 10.0
		(- 10 for $v > 20$ km/s)	
PANi-PS-latex	0.02 - 0.2	0.08 - 1.0	0.3 - 10.0
PPY-PS-latex	0.03 - 0.5	0.50 - 2.0	1.0 - 10.0

b)

QE/QC-charge ratio				(QI)/(QE+QC)
Projectile material	CAT	IID	WALL	WALL
Carbon	0.01 - 0.03	0.06 - 0.2	1.0 - 2.0	0.11 - 0.33
Iron	0.03	2.0 - 3.0	1.0 - 10.0	0.17 - 0.50
		(- 40 for $v > 20$ km/s)		
PANi-PS-latex	0.005 - 0.01	0.01 - 0.5	2.0 - 10.0	$0.01 \cdot v^{1.2}$
PPY-PS-latex	0.01 - 0.04	4.0	10.0	$0.02 \cdot v^{1.4}$

Table D.1: The upper table a) shows the QI/QC-charge ratio for impacts of different projectile materials onto the CAT-target, the IID-target and the inner instrument wall area (WALL). The lower table b) summarizes the QE/QC-charge ratios for the same impact locations and materials. Additionally the QI/(QE+QC)-charge ratio for wall impacts is given.

good charge separation due to the high field at the impact site, leading to the most reliable values for the absolute charge yields. However, large variations of the absolute values of the charge ratios appear depending on the projectile type. No explanation was found for this so far. The acceleration grid transmission will not influence the charge ratios as much, compared to impacts onto the IID-target. Theoretical simulations with the SIMION software by Grün et al. (2002) yield a QI/QC-charge ratio of 0.2 for 300 km/s fast impactors hitting the CAT.

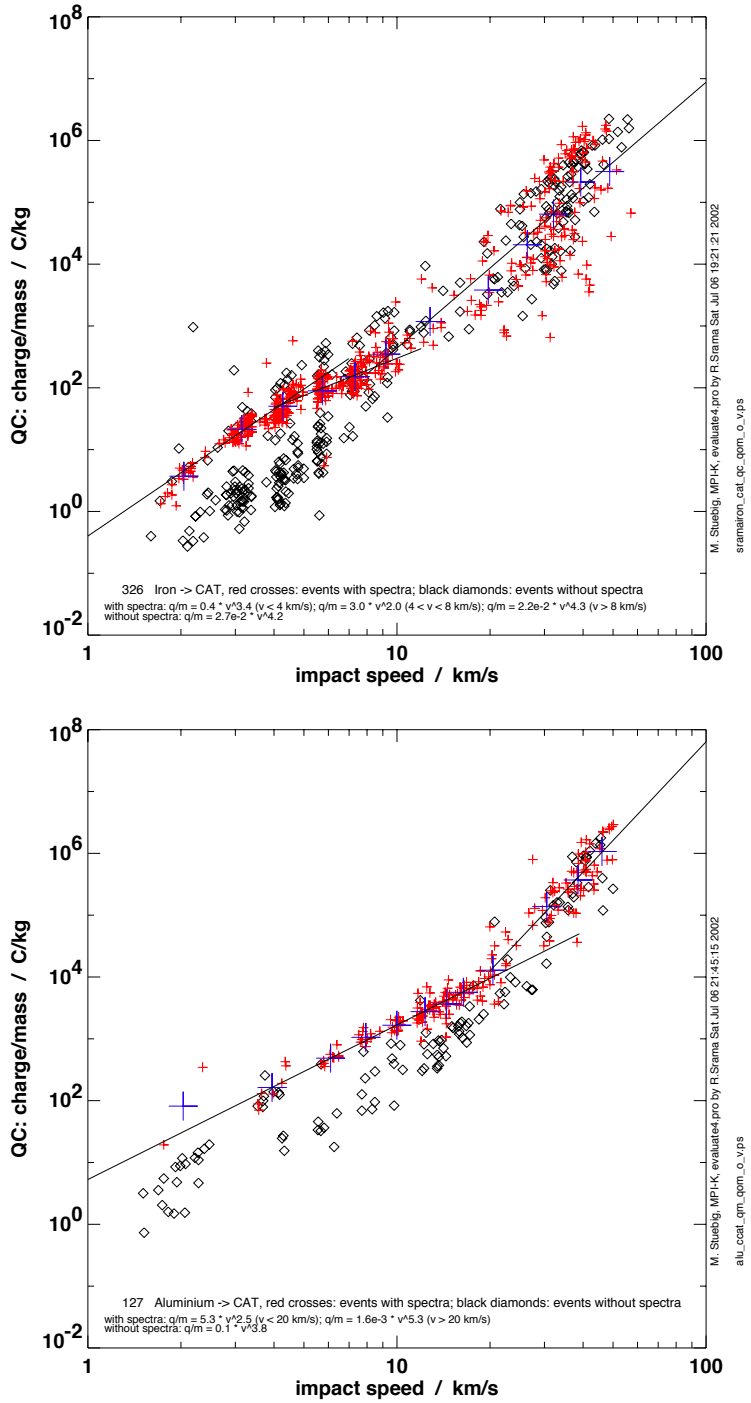

Figure D.4: The ion charge yield per mass unit for shots onto the CAT, depending on the impact speed. Upper figure: iron projectiles, lower figure: aluminium projectiles. Black diamonds show impacts without a TOF mass spectrum, red crosses show impacts with a TOF mass spectrum with at least two mass lines.

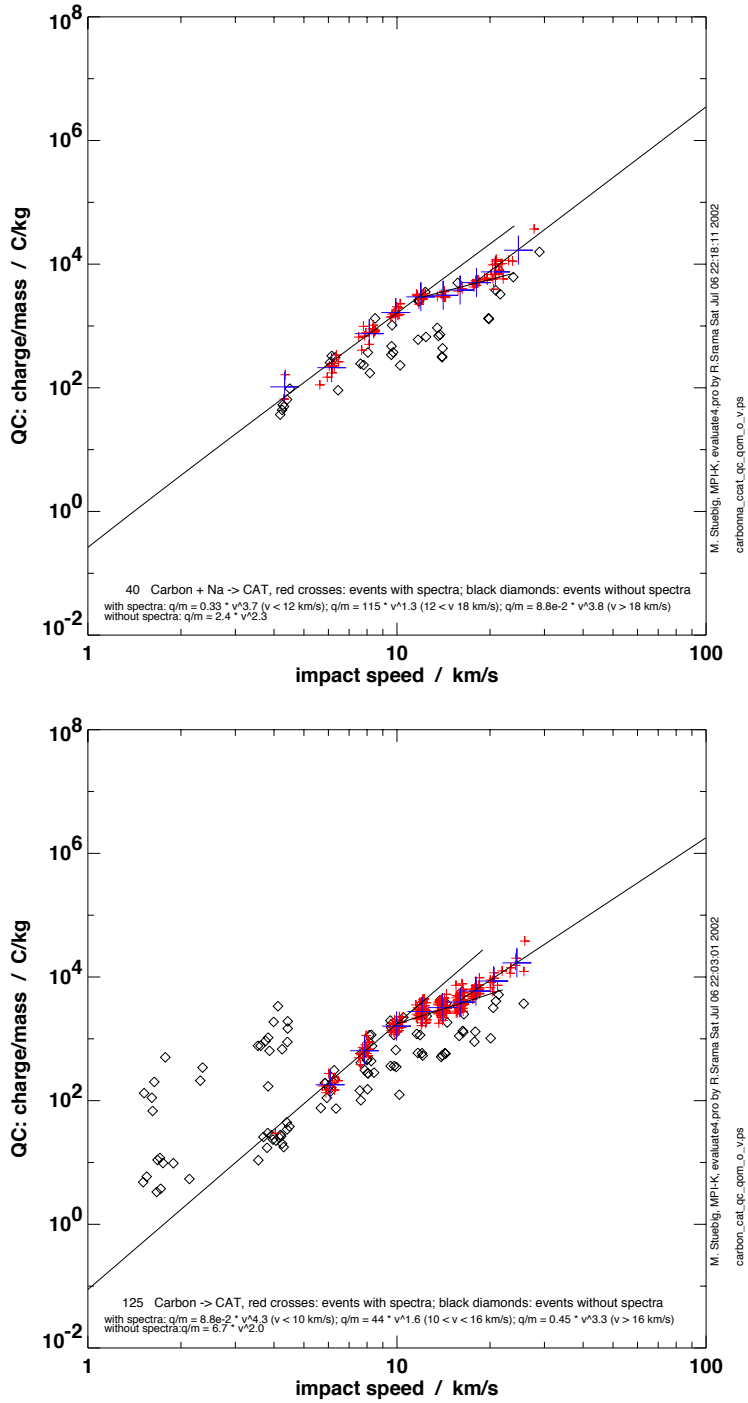

Figure D.5: The ion charge yield per mass unit for shots onto the CAT, depending on the impact speed. Upper figure: sodium contaminated carbon projectiles, lower figure: carbon projectiles. Black diamonds show impacts without a TOF mass spectrum, red crosses show impacts with a TOF mass spectrum with at least two mass lines.

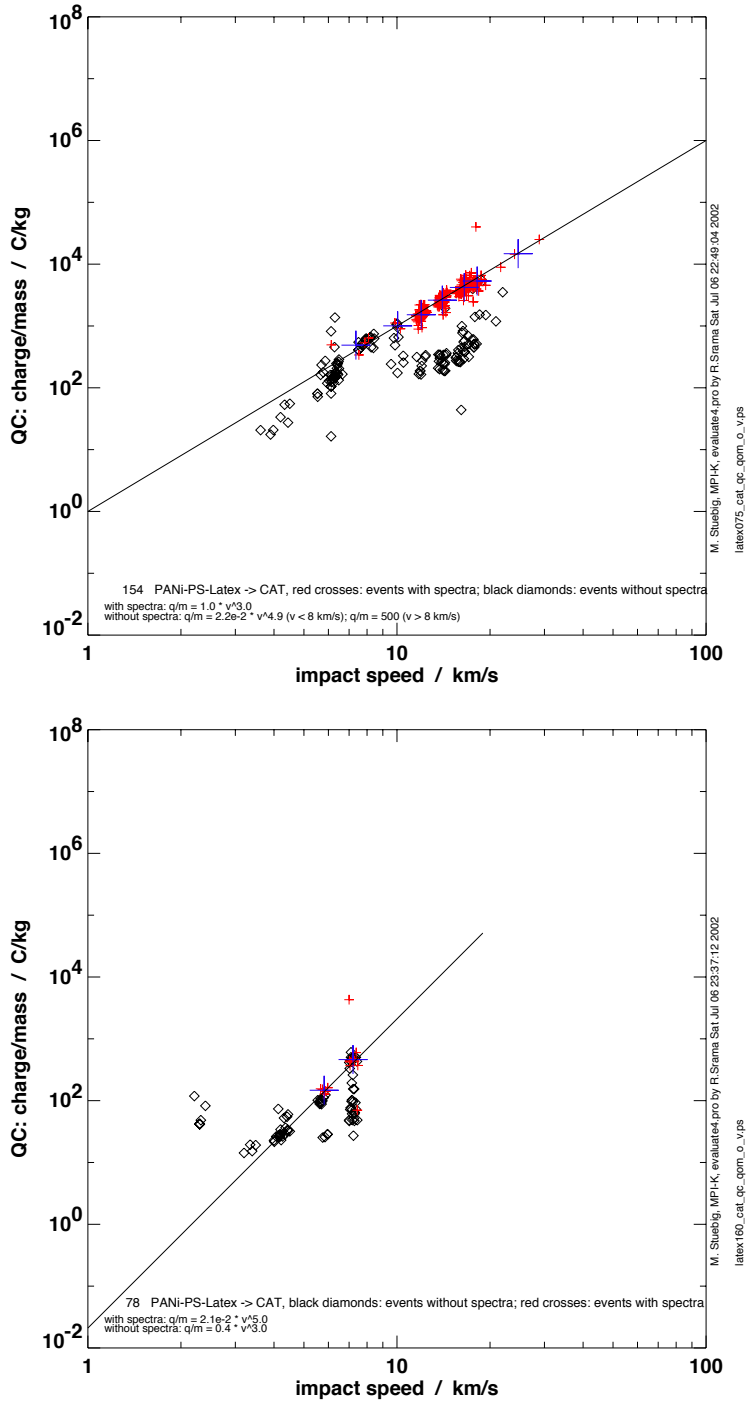

Figure D.6: The ion charge yield per mass unit for shots onto the CAT, depending on the impact speed. Upper figure: polyaniline-coated polystyrene latexes of 0.75 μm grain size, lower figure: polypyrrole-coated polystyrene latexes of 1.60 μm grain size. Black diamonds show impacts without a TOF mass spectrum, red crosses show impacts with a TOF mass spectrum with at least two mass lines.

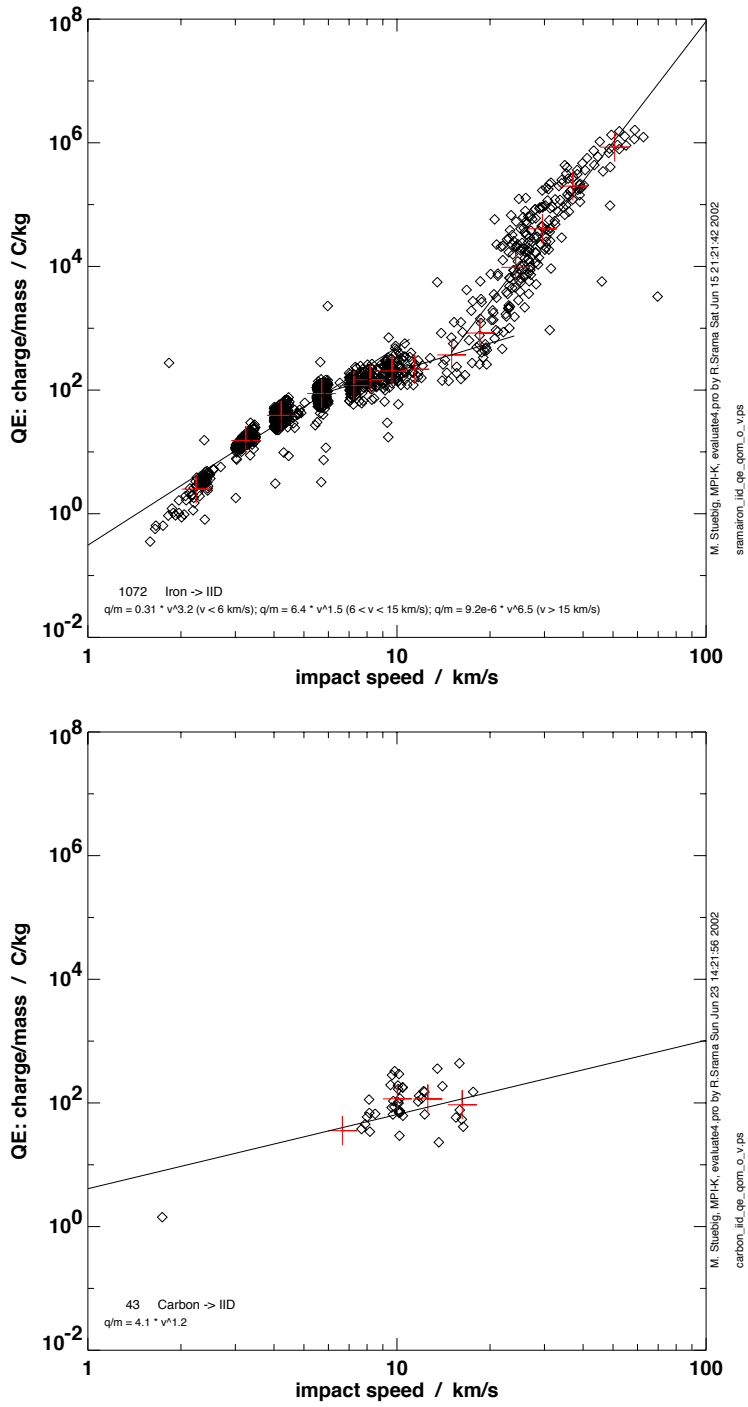

Figure D.7: The ion charge yield per mass unit for shots with iron projectiles (upper diagram) and carbon projectiles (lower diagram) onto the IID depending on the impact speed.

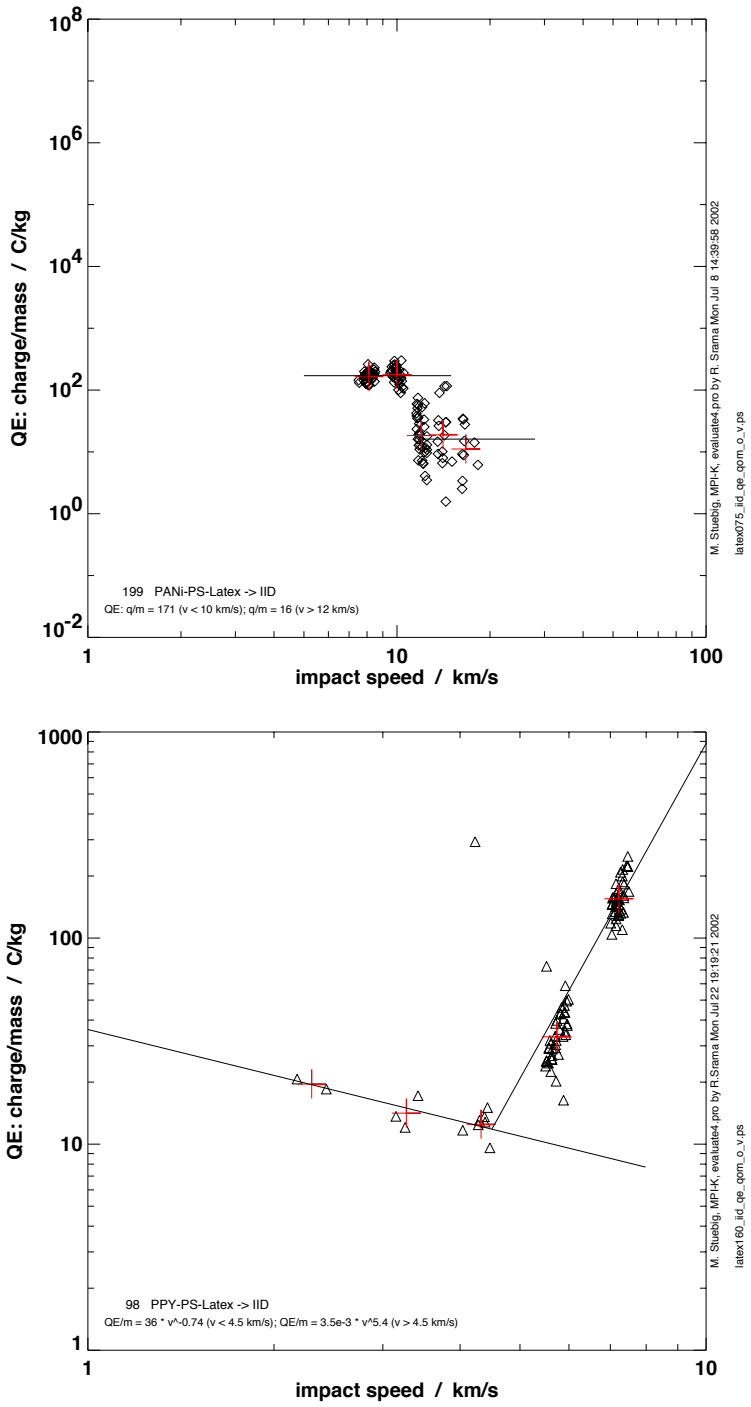

Figure D.8: The ion charge yield per mass unit for shots with PANi-PS-latex projectiles (upper diagram) and PPY-PS-Latex projectiles (lower diagram) onto the IID depending on the impact speed.

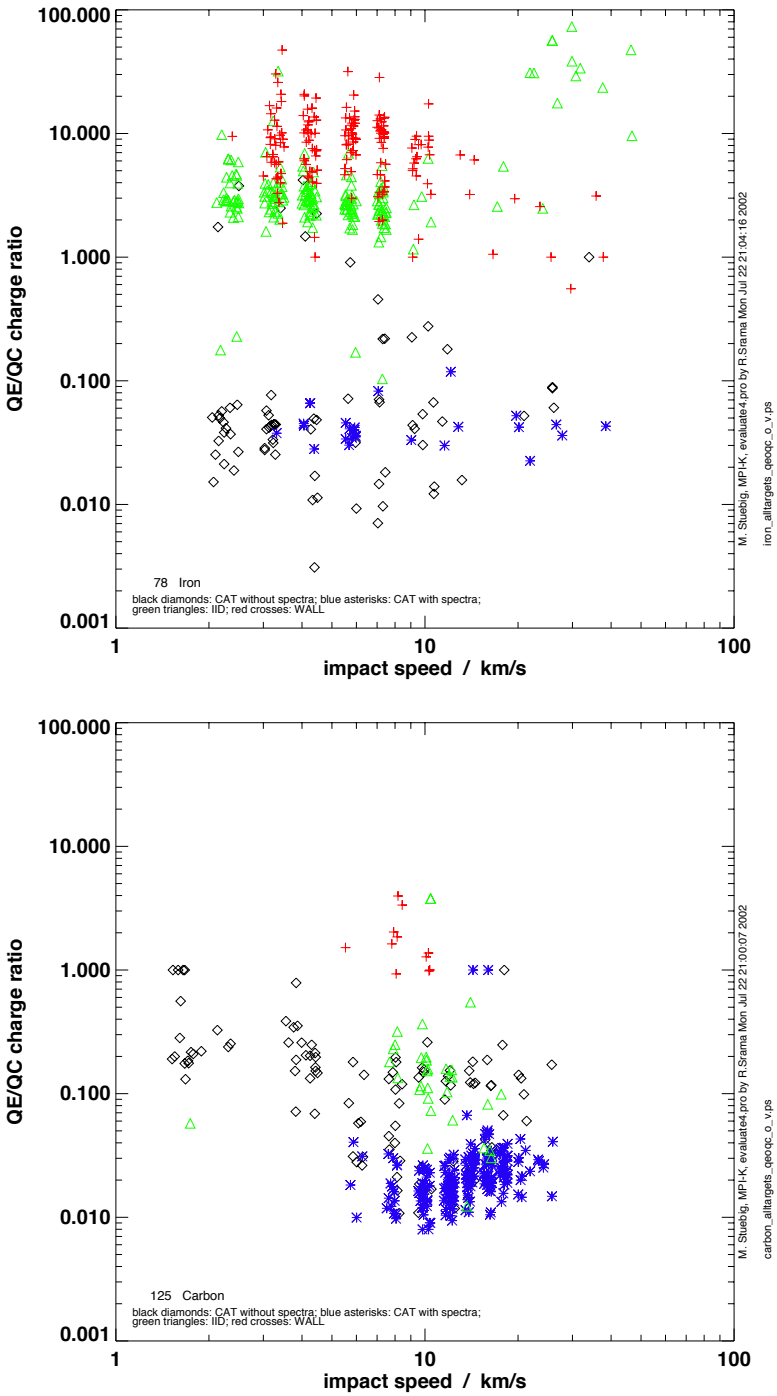

Figure D.9: QE/QC-charge ratio for shots onto the CDA CAT (black diamonds for events without spectra, blue asterisks for events with spectra), IID (green triangles) and WALL (red crosses). The upper figure shows the results for iron projectiles, the lower diagram the results for carbon particles.

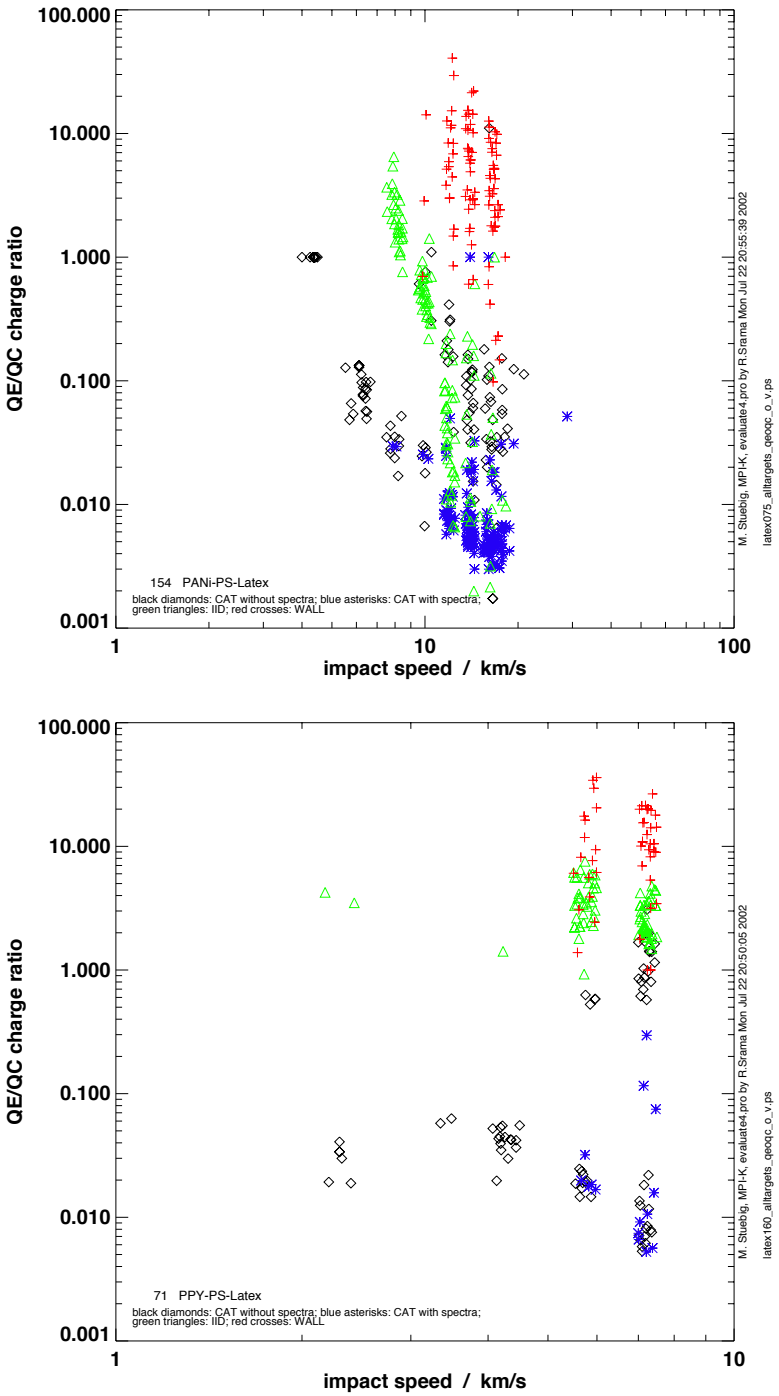

Figure D.10: QE/QC-charge ratio for shots onto the CDA CAT (black diamonds for events without spectra, blue asterisks for events with spectra), IID (green triangles) and WALL (red crosses). The upper figure shows the results for PANi-PS-latex projectiles, the lower diagram the results for PPY-PS-latex particles.

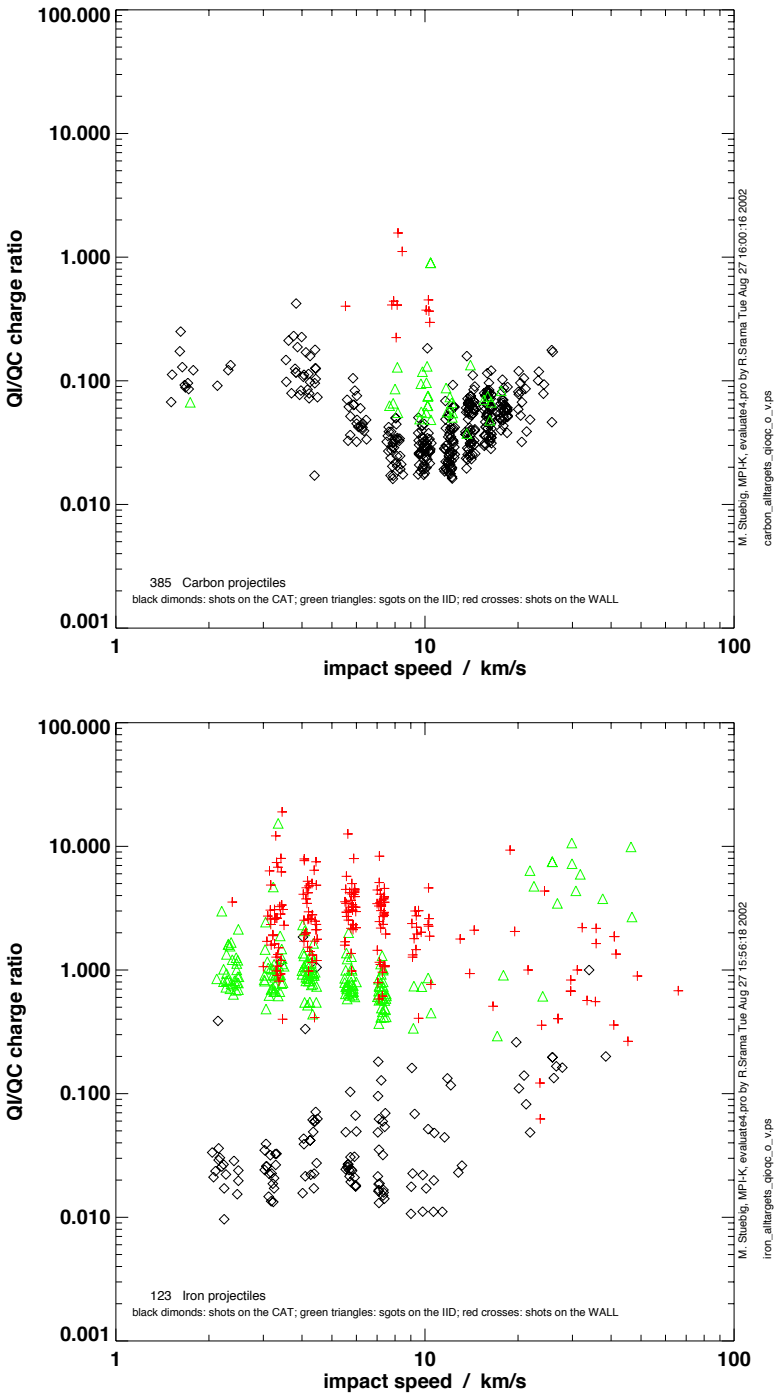

Figure D.11: QI/QC-charge ratio for shots onto the CDA CAT (black diamonds), IID (green triangles) and WALL (red crosses). The upper figure shows the results for carbon projectiles, the lower diagram the results for iron particles.

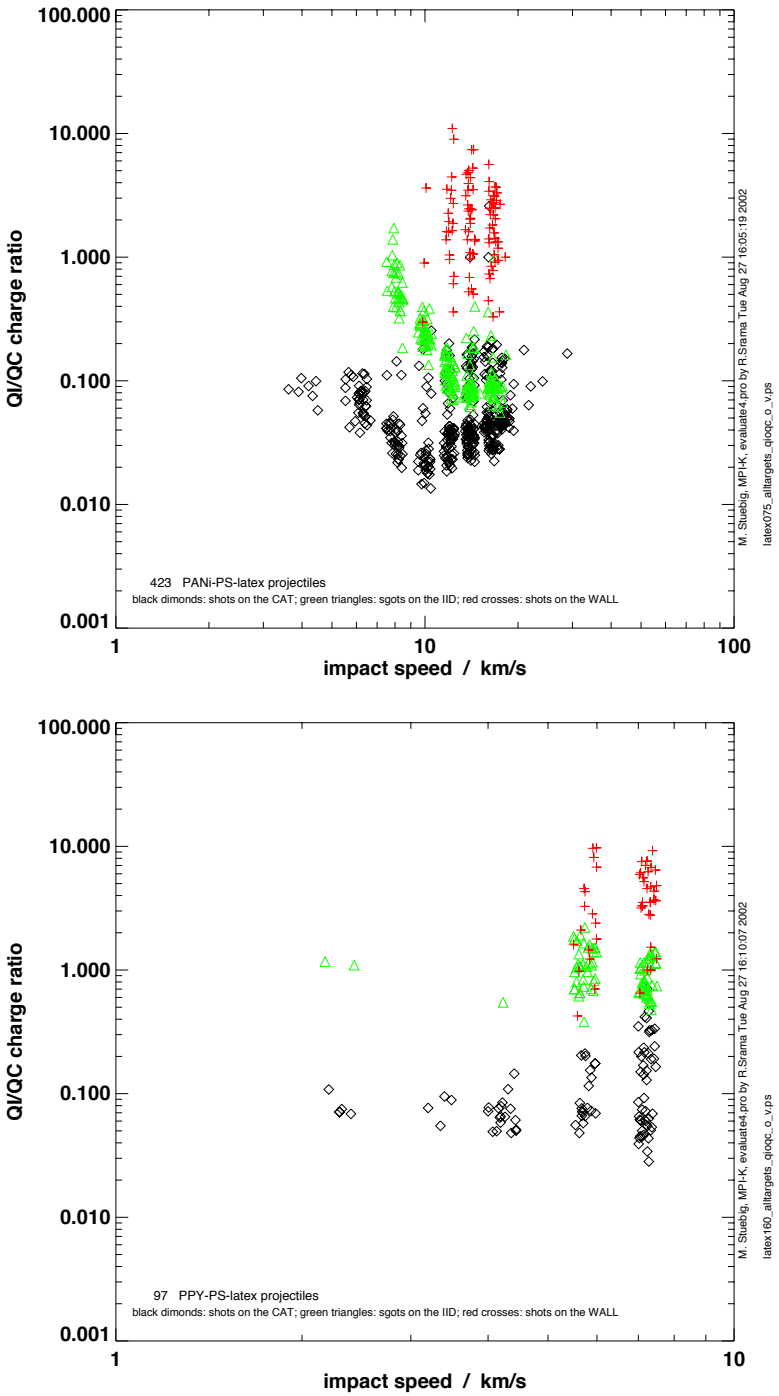

Figure D.12: QI/QC-charge ratio for shots onto the CDA CAT (black diamonds), IID (green triangles) and WALL (red crosses). The upper figure shows the results for PANi-PS-latex projectiles, the lower diagram the results for PPY-PS-latex particles.

D.2.3 Ion focussing

Grün et al. investigated the ion focussing of the ion collector grid QI depending on the kinetic ion energy which is a measure of the impact plasma temperature. The results are given as charge ratios QI/QC for impacts on the CAT respectively QI/QE for impacts on the IID. As expected, the ratios are decreasing for increasing ion energies. It has be mentioned that the plasma temperature and thus also the kinetic ion energy rise with increasing impact speed of the projectile (EICHHORN, 1976). Due to the low transmission of the acceleration grid in front of the CAT, the maximum QI/QC-ratio cannot exceed 0.6 (acc. grid: 0.68 x first ion collector grid: 0.9). However, the QI/QC-ratio for impacts on the CAT decreases more slight than the QI/QE-ratio for impacts on the IID. The forward acceleration of ions generated at the CAT has a stronger focussing effect.

To compare these results with the experimental data, in Table D.3 are summarized the measured QI/QC- respectively QI/QE-charge ratios for projectile impacts on the CAT respectively the IID. Comparing column 2 and column 5 of Table D.3 it appears that the ion focussing for IID-impacts is better than for CAT-impacts. This contradicts the results of Grün et al. (2002). For impacts on the CAT(IID) ratios larger than 0.6(0.9) should not appear. The value of 40 for the QI/QE-ratio for latex projectiles can only be explained by the measure of a reduced charge at the IID-target. The lower electric field strength at the IID ($\approx$ 1 kV/m; CAT: $\approx$ 330 kV/m) might be a general problem for the measurement of absolute charges. As Figure D.13 shows, the experimentally derived absolute charge yields at the IID are equal or slightly lower than the yields at the CAT. Another problem is the comparison between the measured and the theoretically predicted charge ratios. It appears that the measured data corresponds to kinetic ion energies above 150 eV. Such ion energies are only expected for impact speeds of several 10 km/s. Already in Figure 4.1 (upper left diagram) was shown that the QI/QC-charge ratio is rising with increasing impact speed. That this is the case for all projectile materials can be taken from Table 4.3. This result contradicts again the predictions of Grün et al..

Ion energy [eV]	5	10	20	30	50	75	100	150	200
CAT: QI/QC	0.60	0.60	0.60	0.60	0.35	0.30	0.25	0.20	0.20
IID: QI/QE	0.90	0.80	0.45	0.30	0.20	0.15	0.15	0.10	0.10

Table D.2: Theoretically derived QI/QC- and QI/QE-charge ratios for shots on the CAT and IID target by Grün et al. (2002). The data are corrected for the grid transmissions.

	QI/QC-charge ratio		QI/QE-charge ratio	
	CAT	IID	CAT	IID
Aluminium	0.02 - 0.2	no data	0.2 - 100	no data
Carbon	0.02 - 0.2	0.05 - 0.1	0.02 - 0.1	0.04 - 0.1
Iron	0.01 - 0.2	0.3 - 2.0	0.2 - 10	0.2 - 0.4
PANi-PS-latex	0.02 - 0.2	0.08 - 1.0	0.02 - 10	0.2 - 40
PPY-PS-latex	0.03 - 0.5	0.5 - 2.0	0.2 - 10	0.15 - 0.4

Table D.3: Experimentally derived QI/QC- and QI/QE-charge ratios for shots on the CAT and IID target.

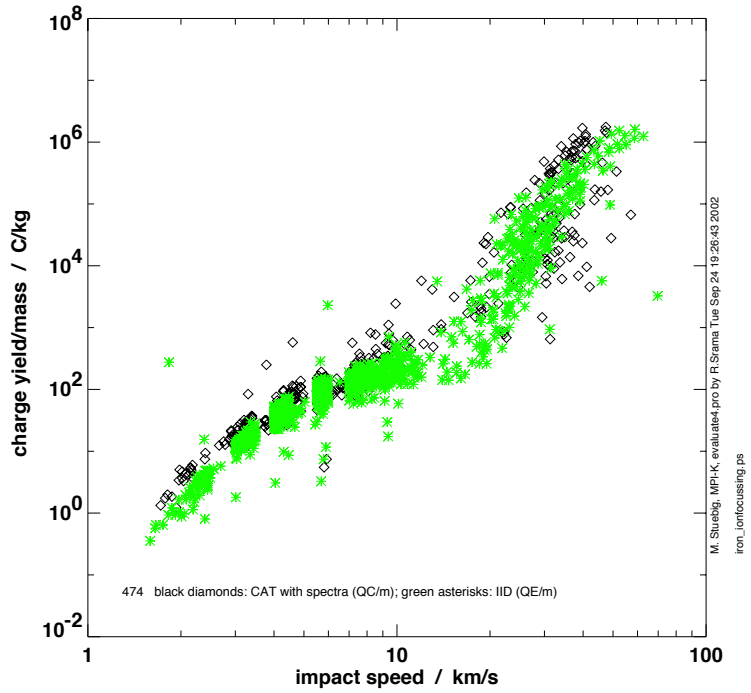

Figure D.13: Comparison of the absolute charge yields depending on the impact speed for iron projectiles impacting on the CAT (QC/m-charge yield, black diamonds) and on the IID (QE/m-charge yield, green asterisks).

D.3 Instrument sensitivity

Apart from transmission coefficients of the entrance grids, the ratio of the registered impacts to the total number of shots is a measure for the instrument sensitivity. The evaluation of the sensitivity for projectile mass and speed is somewhat complicated, since the most dust powders in this work show a broad mass distribution within three orders of magnitude for aluminium, carbon and iron particles, and the present projectile mass depends strongly on the selected impact speed (cf. Appendix A). The use of samples with nearly mono-sized grain size distributions, like the latex samples in this work, will allow a better clue on the instrument sensitivity. The results allow a real impact speed depending sensitivity, since the projectile mass is nearly constant for all selected impact speeds. As an example in Figure D.14 the sensitivities depending on the impact speed for the central regions of the CAT-target, the IID target and the instrument wall are shown. The complete data are shown in Figures D.16 - D.21 at the end of this section. All detection probability functions follow a similar scheme: a more or less steep increase of the detection probability from $p = 0$ to $p = 0.8$, followed by a stable probability value of $p = 0.8$ for even higher impact speeds. This corresponds to the total transmission of the four entrance grids. The increase of the detection probability function for IID impacts develops steeper than for WALL impacts. It is to note that the detection probability for CAT impacts first rises up to $p = 0.6$, remains for a certain impact speed range at 0.6 and will rise to $p = 0.8$ only for much higher speeds. To reach the $p = 0.8$-level, the larger PPY-PS-latex particles need much lower impact speeds than the smaller PANi-PS-latex projectiles. Table D.4 gives an overview of the minimum impact speeds that are necessary for an impact detection with the probability p. For example a value of 9 km/s for $p = 0.6$ in the cIID-row for the PANi-PS-latex sample means that a $2.4 \cdot 10^{-16}$ kg projectile, that hits the central IID-section with a speed of 9 km/s will be detected with a probability of 60 %. It is obvious that similar target regions (e.g. central IID and outer IID) show a very similar behavior of the detection probability function.

For particles that hit the CAT region with similar impact speeds, the probability for obtaining a time-of-flight mass spectrum with at least two mass lines (red lines in Figures D.16 and D.19) is much lower than for a general event detection. The probability for a time-of-flight mass spectrum from hitting the outer CAT region is even lower than from hitting the central CAT region with similar impact speeds. However, the probability-values at high impact speeds scatter between $p = 0.4$ and $p = 0.6$ but won't exceed the upper value. It has also to be noted that the sensitivity of the outer wall region is a little bit higher than the sensitivity of the central wall region.

A comparison with the impact charge distribution from the projectiles (cf. Table 4.2) gives only rough hints, that the fraction of particles, that produce enough charge ($q >$ trigger threshold) is correlated to the detection probability. Since the impact charge distribution is well-balanced, it is appropriate to use the a mean charge, as given by the charge yield functions, to calculate the absolute sensitivity of the instrument.

The sensitivity for aluminium, carbon and iron projectile couldn't be investigated here, since the projectiles, provided by the dust source, show a large scatter in their mass for a fixed velocity.

Target region	0.75μm PANi-PS-latex				1.58μm PPY-PS-Latex			
	$p = 0.1$	$p = 0.4$	$p = 0.6$	$p = 0.8$	$p = 0.1$	$p = 0.4$	$p = 0.6$	$p = 0.8$
cCAT	< 4	5	7	16	n.m.	n.m.	n.m.	n.m.
oCAT	< 4	5	6	16	2	3.75	5	7
cIID	7	8	9	10	3	5.0	5.5	7
oIID	7	8	9	10	3	4.75	5.5	6
cWALL	8	10.5	12	14	5	5.5	7	[$\approx$ 10]
oWALL	8	9	10	14	4.5	5.0	6	[$\approx$ 10]

Table D.4: Lower impact speed limits in km/s for various detection probabilities p and different impact sites. (n.m. = not measured, values in []-brackets are extrapolated from the detection probability function.)

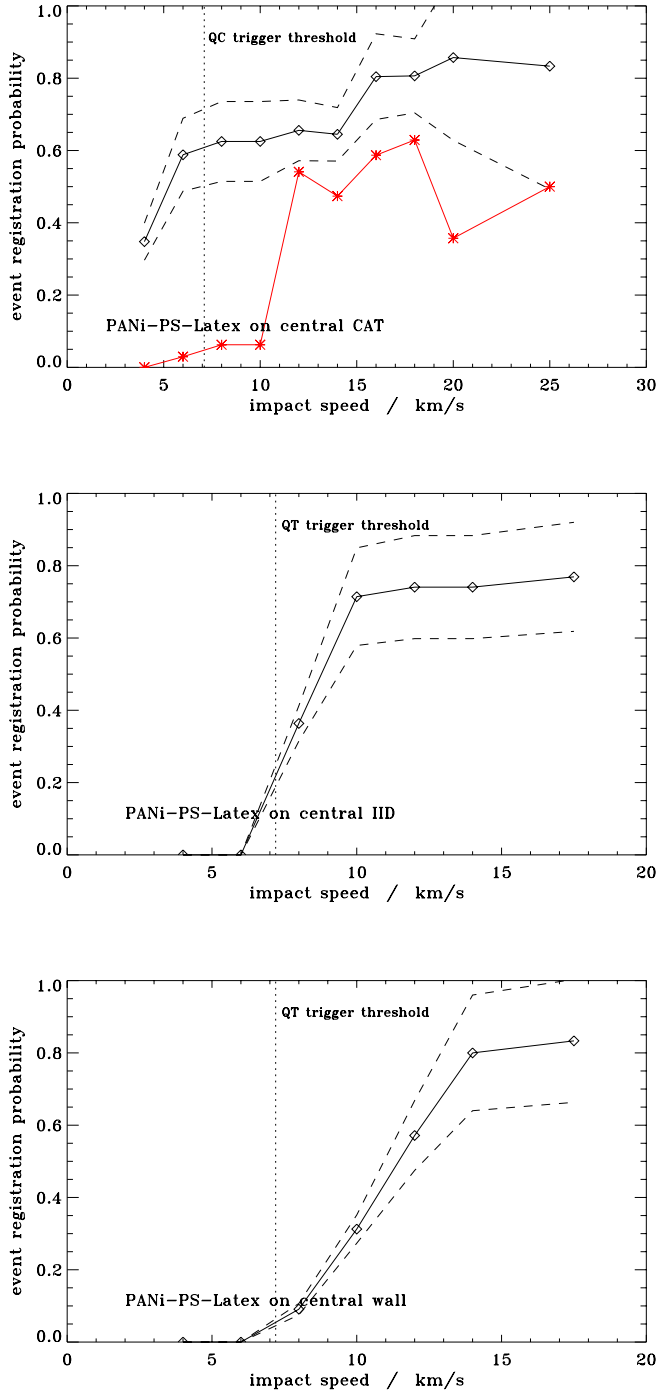

Figure D.14: The CDA instrument sensitivity depending on the impact speed for 0.75 μm PANi-PS-latex projectiles with a nominal mass of $2.4 \cdot 10^{-16}$ kg. Upper diagram: sensitivity of the central CAT region; middle diagram: sensitivity of the central IID target; lower diagram: sensitivity of the central wall region. The red curve in the upper diagram reflects the probability for obtaining a TOF mass spectrum.

D.3.1 Absolute instrument sensitivity

CDA provides five charge sensitive channels (QC, QT, QA, QI and QMA). Their sensitivity can be changed by setting different thresholds or even by making them insensitive to any impact events. The threshold levels for the measurements in this work have been chosen as low as possible to obtain signals from small and/or slow projectiles but not to disturb the measurements with permanent instrument triggering from noise. Two main noise sources are present: the first is instrument related "internal" noise from electronic disturbances and from sparking between the high voltage dynodes of the multiplier due to bad vacuum. The second source, "external noise", comes from the laboratory itself: vibrations from the vacuum pumps, electromagnetic disturbance from the Van-de-Graaff generator and the high-voltage switching of the particle selection unit. The trigger thresholds that have been used during the measurements with the latex samples are summarized in Table D.5. The higher QC-threshold for the PPY-PS-latex sample was necessary to avoid noise.

	thresholds for PANi-PS-latex		thresholds for PPY-PS-latex	
channel	dn	Coulomb	dn	Coulomb
QT	4	$5.2 \cdot 10^{-14}$	4	$5.2 \cdot 10^{-14}$
QC	5	$5.3 \cdot 10^{-14}$	7	$7.3 \cdot 10^{-14}$
QA*	5	$4.6 \cdot 10^{-13}$	5	$4.6 \cdot 10^{-13}$
QI	5	$3.9 \cdot 10^{-14}$	5	$3.9 \cdot 10^{-14}$
QMA*	2	(74 mV)	2	(74 mV)

Table D.5: Trigger thresholds for the experiments with the latex samples. The thresholds are given in digital numbers (dn). The corresponding absolute charge values are taken from Srama (2000). For the QA and QMA channel were used the flight unit calibration data.

The threshold values have to be compared with the actual charge q that is produced by a projectile of mass m at an impact speed v. The charge q can be calculated from the charge yields that were derived from the measurements in Section 4.2. Since the measured charge yields at the IID target are still not understood (influence of ion recombination and cluster formation for latex), they might be somewhat misleading. It is assumed that the charge production at the IID and the WALL are similar to that at the CAT. For the absolute charge production at the impact site are used the following relations:

$$\begin{array}{lcccccc} & & & m\ [\mathrm{kg}] & & \frac{q}{m}\ [\mathrm{C/kg}] & & \mathrm{C} \\ \text{PANi-PS-latex} & : & q(v) = & 2.4 \cdot 10^{-16} & \cdot & 1.0 \cdot v^{3.0} & = & 2.4 \cdot 10^{-16} \cdot v^3 \\ \text{PPY-PS-latex} & : & q(v) = & 2.3 \cdot 10^{-15} & \cdot & 0.4 \cdot v^{3.0} & = & 9.2 \cdot 10^{-16} \cdot v^3 \end{array}$$

These charge yields allow to recalculate the measured detection probabilities depending on the impact speed as given in Table D.4 into detection probabilities depending on the absolute impact charge. The results are summarized in Table D.6. Although the calculated values are rough assessments, both latex samples show a similar charge sensitivity for all target regions and detection probabilities p. The majority of the corresponding data is equal within a factor of 2. All targets show no big difference between the sensitivity of their central or their outer region. The observed upper limit of the detection probability $p = 0.8$ corresponds well with the total transmission of the four entrance grids: $t_{EG} = 0.95 \Rightarrow t_{EG}^4 = 0.81$. The detection limit of $p = 0.6$, that occurs in the shots onto the CAT can be explained with hits on the acceleration grid in front of the target. With a grid transmission

of $t_{AG} = 0.68$, the total transmission for projectiles to hit the CAT is $t_{total} = t_{EG}^4 \cdot t_{AG} = 0.55$. Only impacts with higher speeds will produce enough charge that might be scattered inside the instrument and than trigger other channels than QC. The reduced transmission $t_{total} = 0.55$ explains also, why the probability to achieve a proper time-of-flight spectrum scatters between 40 % and 60 %. Except for shots on the CAT all calculated impact charge limits, even for a detection probability of $p = 0.1$, exceed the trigger threshold settings. The investigation of the charge yield distribution for projectiles with constant mass and impact speed showed that the absolute charge scatters by chance within a factor of 3 around the mean value (cf. Section 4.2.1). Considering a theoretical maximum of $p = 0.8$, the detection probability should be 0.4 when the mean charge production equals the trigger threshold. This is proven for impacts on the CAT as shown in Figure D.15. It is not clear, if the impact charge at the IID has to be much larger although the trigger thresholds of the CAT and the IID are similar (cf. Table D.5). Carbon and latex projectiles of a certain mass and impact speed that hit the IID produce much less absolute charge than similar particles that hit the CAT, while the charge production on both targets is not so different for iron projectiles. It is necessary to proof the instrument sensitivity with iron and aluminium projectiles of constant mass over a large impact speed range. The even higher impact charge that is necessary to trigger the instruments with wall impacts can be explained with the point, that the wall itself has no charge sensitive detector. The parts of the charge that scatter inside the instrument has to be large enough to trigger any charge sensitive unit of the CDA.

Target	0.75μm PANi-PS-latex				1.58μm PPY-PS-Latex			
region	$p = 0.1$	$p = 0.4$	$p = 0.6$	$p = 0.8$	$p = 0.1$	$p = 0.4$	$p = 0.6$	$p = 0.8$
cCAT	< 15	30	82	980	n.m.	n.m.	n.m.	n.m.
oCAT	< 15	30	52	980	7	50	110	320
cIID	82	120	170	240	24	115	150	320
oIID	82	120	170	240	24	100	150	200
cWALL	120	280	410	660	110	150	320	920
oWALL	120	175	240	660	84	120	200	920

Table D.6: Absolute impact charge limits in fC (10^{-15} C) for various detection probabilities p and different impact sites. (n.m. = not measured)

The reproducible behavior of the measured charge limits allows to set absolute charge limits for the different target regions and for various detection probabilities. Therefore have been calculated mean values of corresponding data in Table D.6. The results are summarized in Table D.7 and plotted in Figure D.15. The sensitivity functions are rough estimations from the shown data. The dashed lines for the CAT and the WALL data are extrapolated, since for both a detection sensitivity of $p = 0.8$ is only reached for impact charges of about $8 \cdot 10^{-13}$ C. The data can be approximated with linear charge limit functions of the form $q_{min} = \gamma \cdot p + \delta$ as given in Table D.8.

Target region	$p = 0.1$	$p = 0.4$	$p = 0.6$	$p = 0.8$
CAT	10 ± 3	40 ± 10	80 ± 30	760 ± 380
IID	50 ± 30	110 ± 10	160 ± 10	350 ± 50
WALL	110 ± 20	180 ± 70	290 ± 90	790 ± 150

Table D.7: Mean impact charge limits in fC (10^{-15} C) for various detection probabilities p and different impact sites.

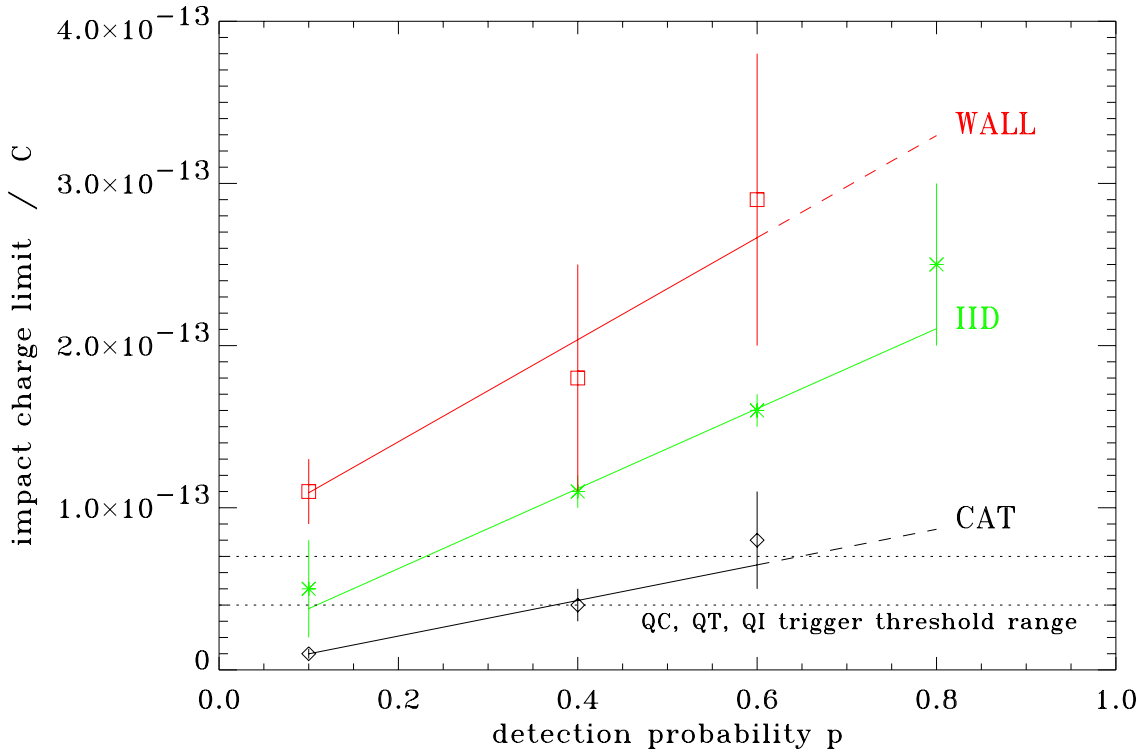

Figure D.15: Lower impact charge limits for various detection probabilities p and different impact sites.

Setting the charge limit functions equal to charge yield functions $\frac{q}{m}(\varepsilon, v)$ (ε: projectile type, v: impact speed) as evaluated in Section 4.2, one obtains detection probabilities depending on the projectile mass and impact speed.

$$\begin{aligned} \frac{q}{m}(\varepsilon, v) \cdot m &= \gamma \cdot p + \delta \\ \Rightarrow p(\varepsilon, v) &= \frac{m \cdot \frac{q}{m}(\varepsilon, v) - \delta}{\gamma} \end{aligned} \tag{D.1}$$

Target	Charge [C]	=	γ	$\cdot p$	+	δ
CAT	q_{min}	=	$1.1 \cdot 10^{-13}$	$\cdot p$	−	$1.1 \cdot 10^{-15}$
IID	q_{min}	=	$2.5 \cdot 10^{-13}$	$\cdot p$	+	$1.3 \cdot 10^{-14}$
WALL	q_{min}	=	$3.1 \cdot 10^{-13}$	$\cdot p$	+	$7.8 \cdot 10^{-14}$

Table D.8: Charge limit functions to calculate the minimum impact charge that is necessary to trigger any channel of the CDA instrument with the probability $0 < p < 0.8$ for projectiles that hit the CAT-, the IID-target or the inner instrument wall.

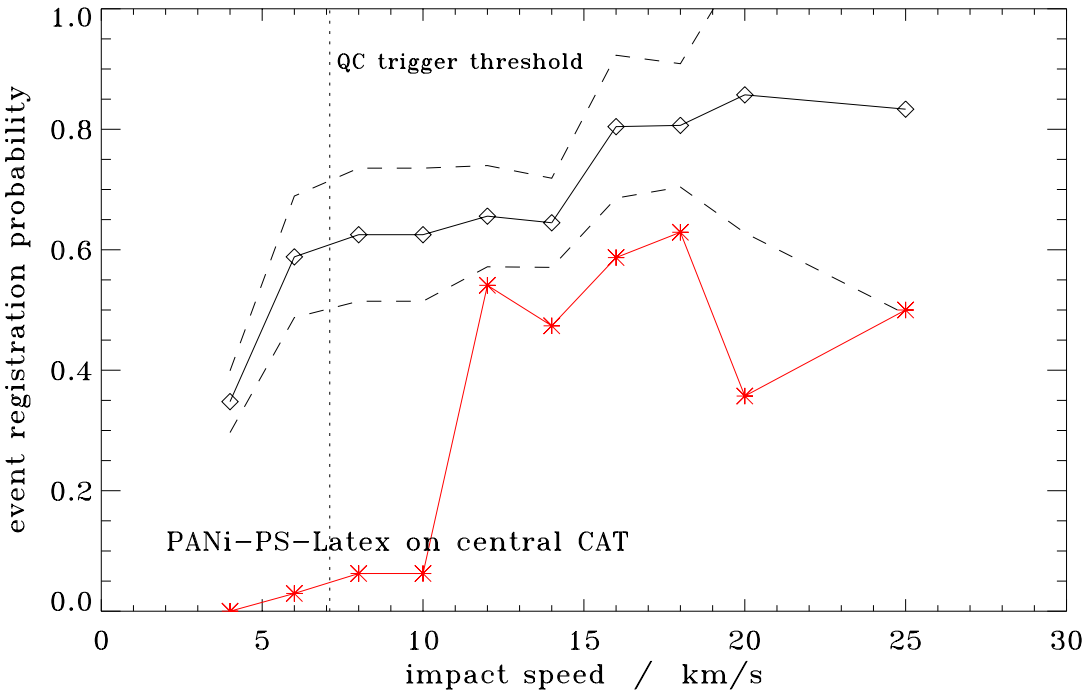

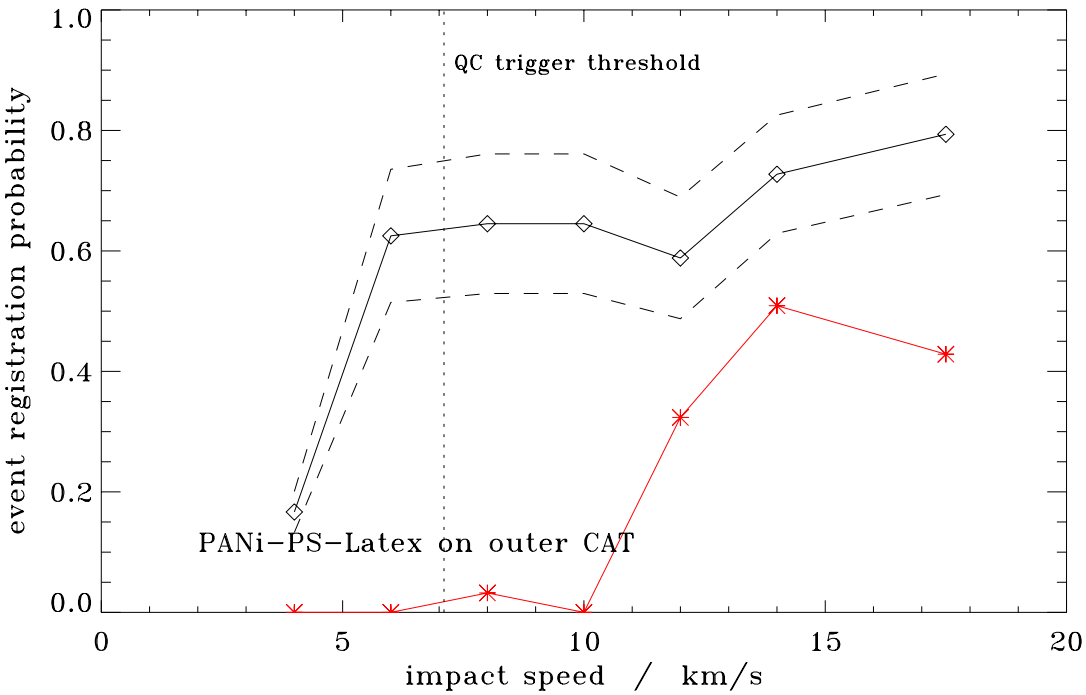

Figure D.16: Impact speed depending CDA instrument sensitivity for 0.75 μm PANi-PS-latex projectiles with a nominal mass of $2.4 \cdot 10^{-16}$ kg. Upper diagram: sensitivity of the central CAT region; lower diagram: sensitivity of the outer CAT region. The red curves reflect the probabilities for obtaining TOF mass spectra.

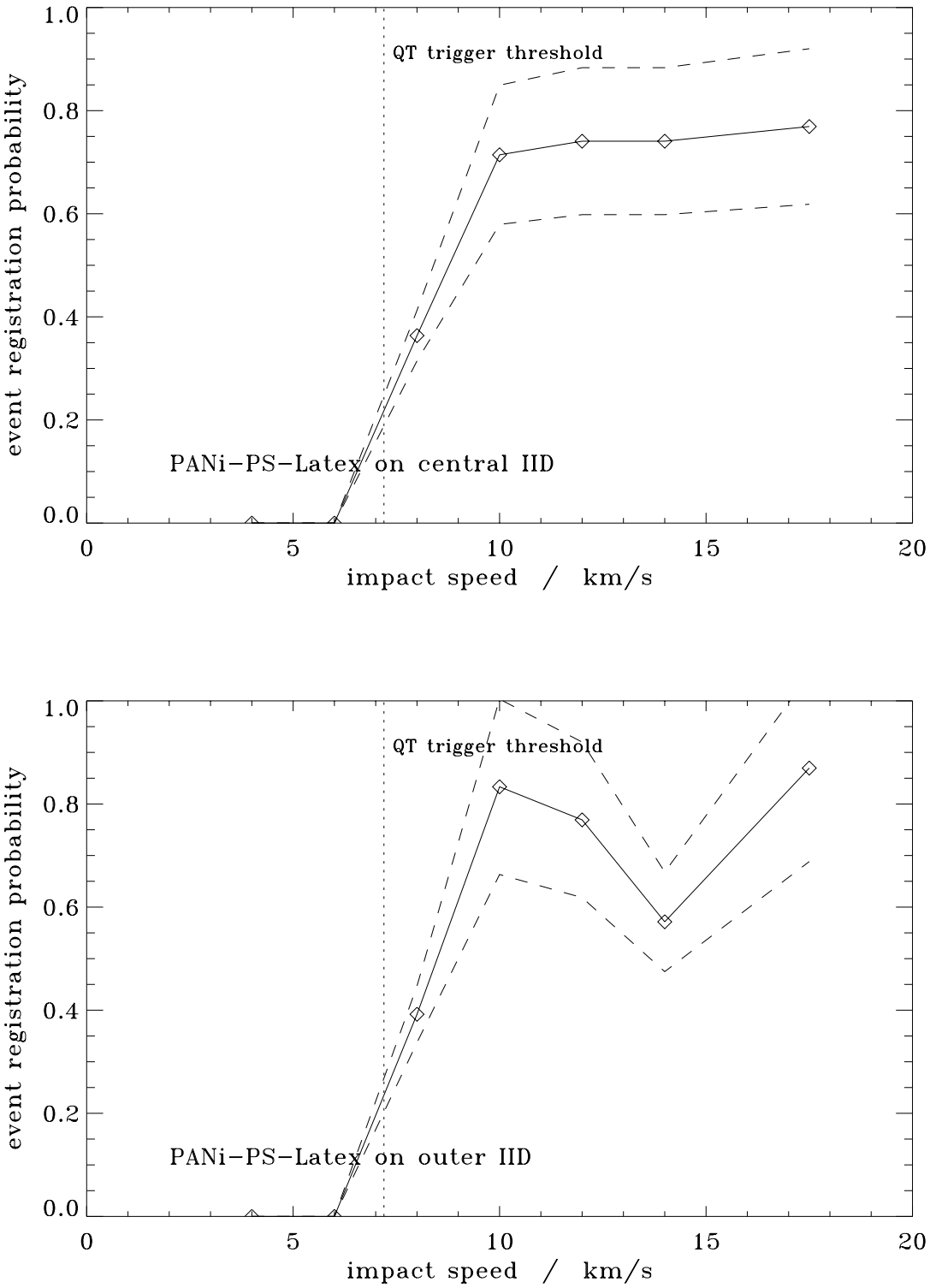

Figure D.17: Impact speed depending CDA instrument sensitivity for 0.75 μm PANi-PS-latex projectiles with a nominal mass of $2.4 \cdot 10^{-16}$ kg. Upper diagram: sensitivity of the central IID region; lower diagram: sensitivity of the outer IID region.

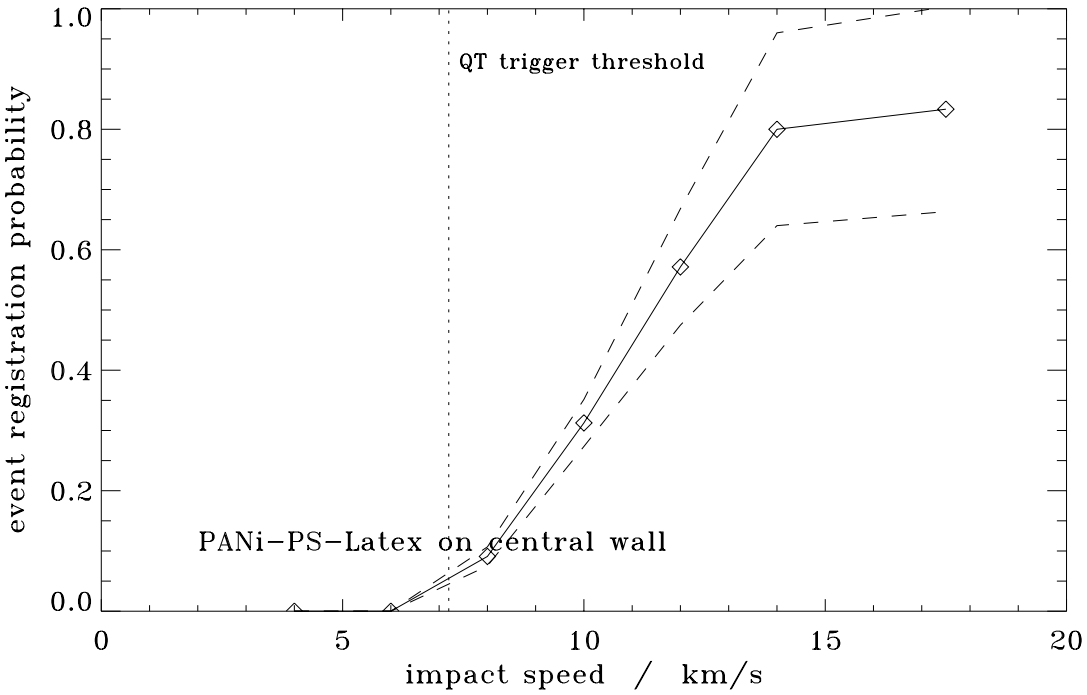

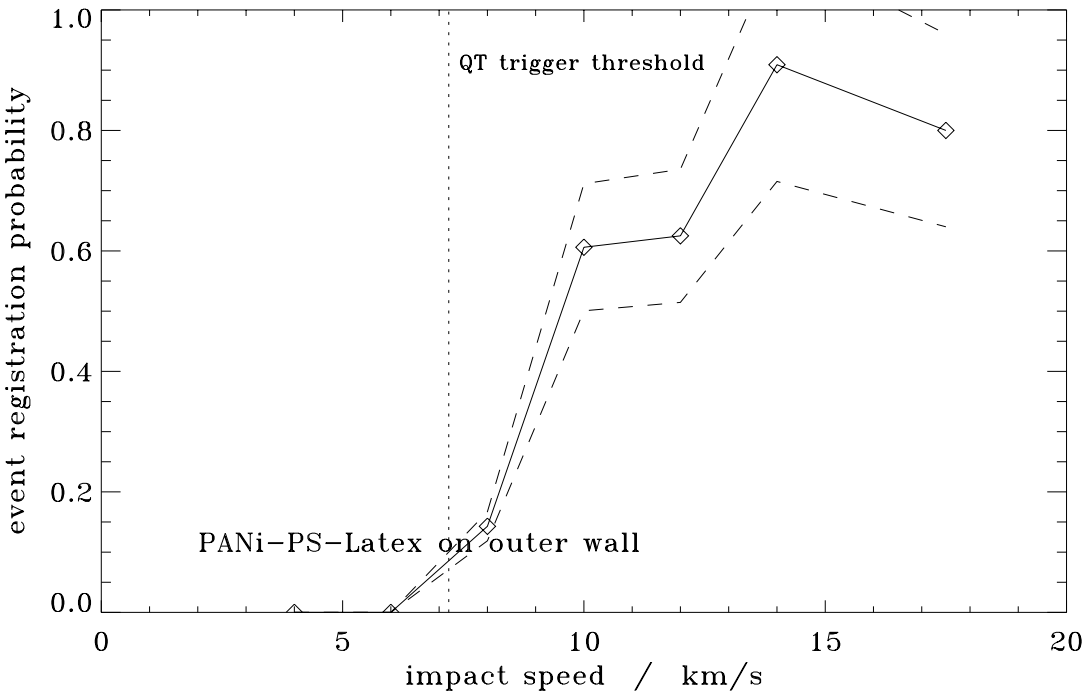

Figure D.18: Impact speed depending CDA instrument sensitivity for 0.75 μm PANi-PS-latex projectiles with a nominal mass of $2.4 \cdot 10^{-16}$ kg. Upper diagram: sensitivity of the central wall region; lower diagram: sensitivity of the outer wall region.

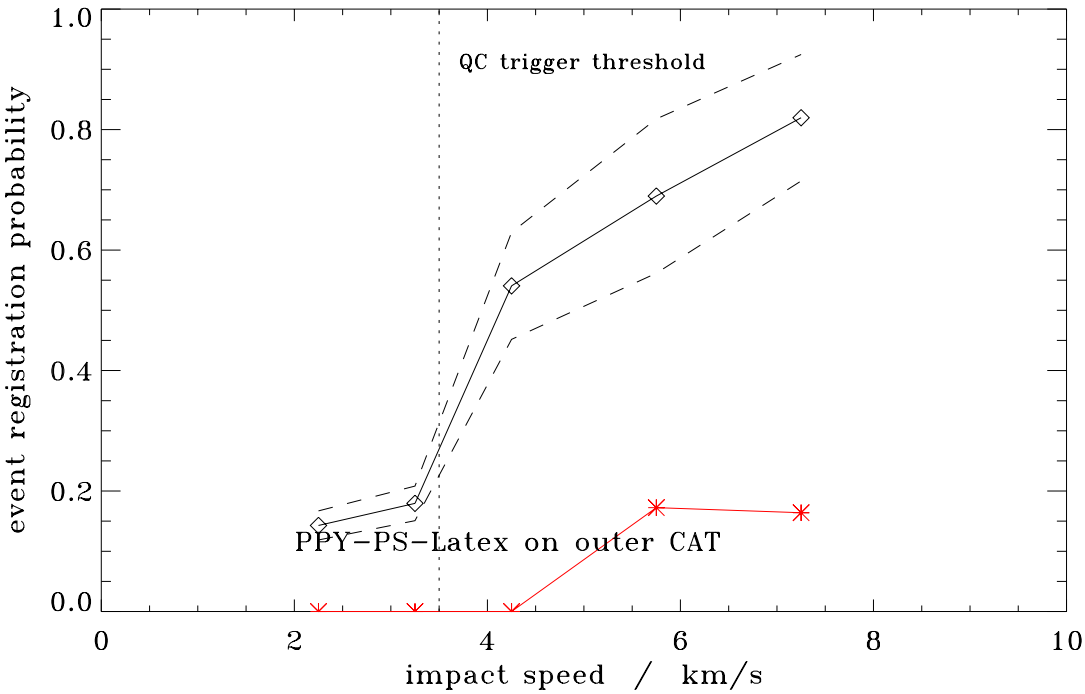

Figure D.19: Impact speed depending CDA instrument sensitivity for 1.58 μm PANi-PS-latex projectiles with a nominal mass of $2.3 \cdot 10^{-15}$ kg. Here: sensitivity of the outer CAT region. The red curve reflects the probability for obtaining TOF mass spectra.

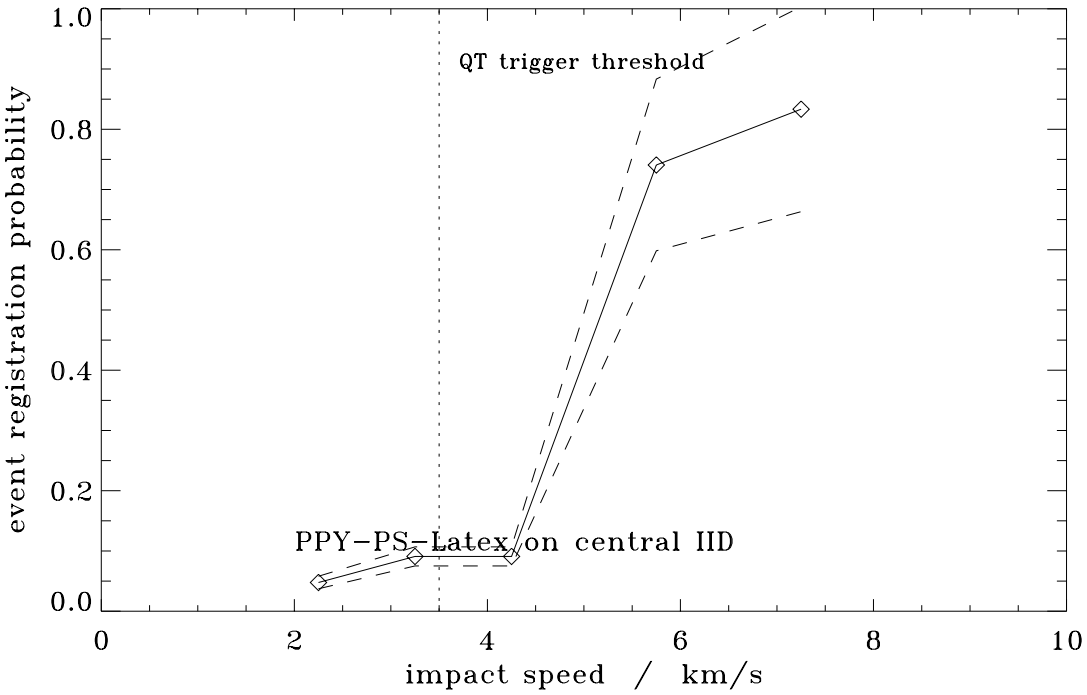

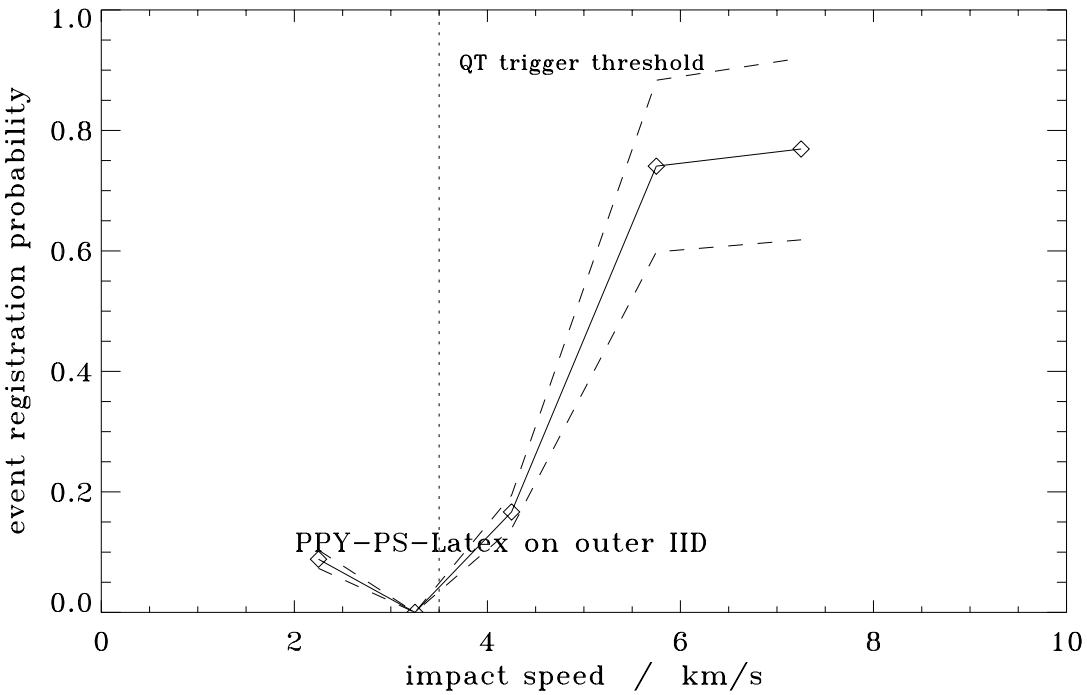

Figure D.20: Impact speed depending CDA instrument sensitivity for 1.58 μm PANi-PS-latex projectiles with a nominal mass of $2.3 \cdot 10^{-15}$ kg. Upper diagram: sensitivity of the central IID region; lower diagram: sensitivity of the outer IID region.

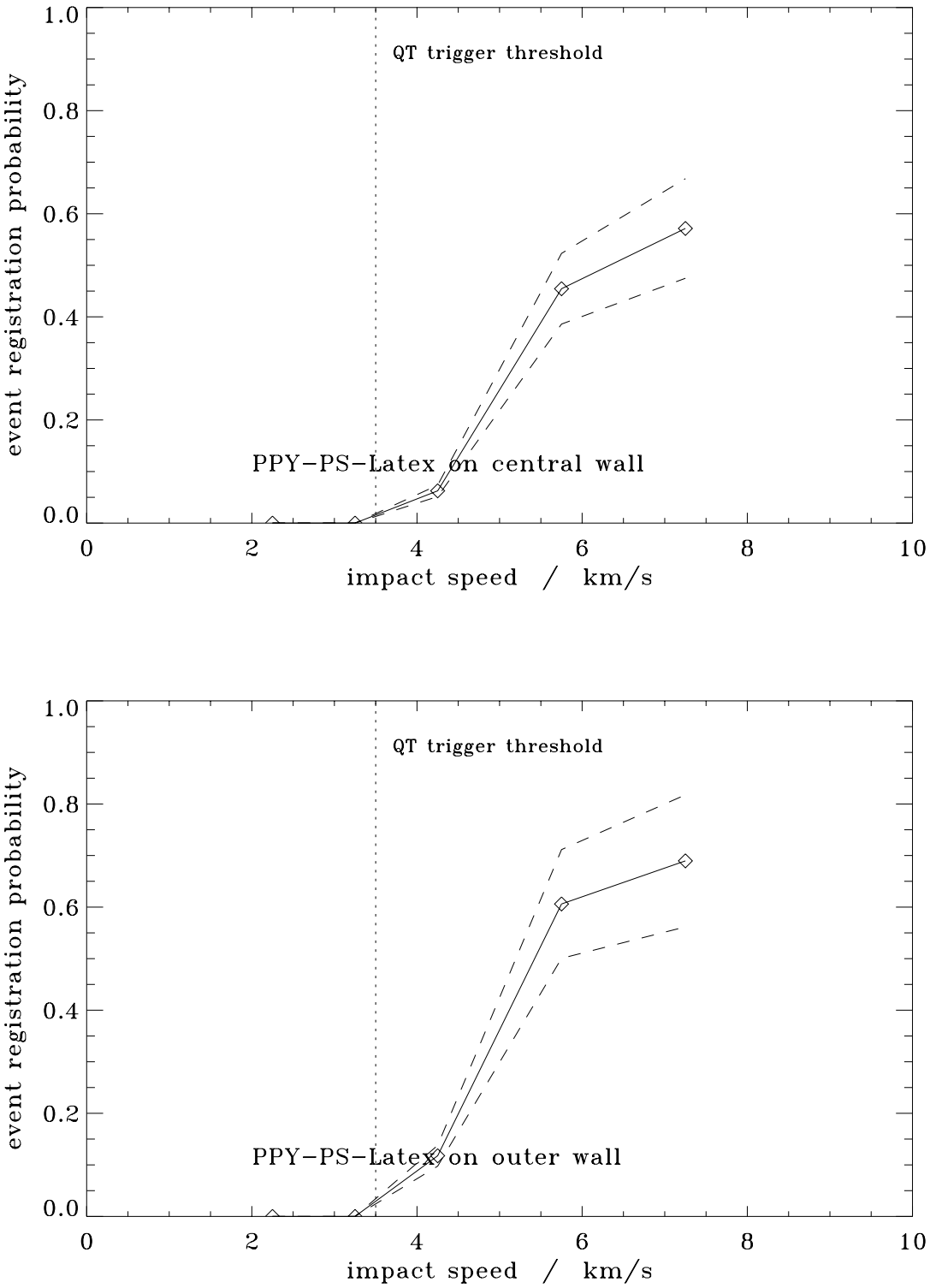

Figure D.21: Impact speed depending CDA instrument sensitivity for 1.58 μm PANi-PS-latex projectiles with a nominal mass of $2.3 \cdot 10^{-15}$ kg. Upper diagram: sensitivity of the central wall region; lower diagram: sensitivity of the outer wall region.

D.4 Detection of small and fast particles

Since charged dust particles in space can be accelerated by magnetic fields, much higher impact speeds than accessible in the laboratory, are possible. As example should be mentioned the Jovian dust stream particles, which can achieve velocities up to 450 km/s (ZOOK, H.A. et al., 1996). In the following section an extrapolation of the charge yield to high impact speeds is given. This leads to an improved estimation of the instrument sensitivity to very small and fast projectiles expressed by detection probabilities (Section D.4.2). In Section D.4.3 the results are compared to flight data that show time-of-flight mass spectra of Jovian dust stream particles.

D.4.1 Extrapolation of the charge yields to very high impact speeds

In Section 5.2.3 was shown that above a certain impact speed v_{CI} the complete projectile is fully ionized. For even higher impact speeds, only target material and surface contamination elements can be ionized. Additionally ions with higher ionization stages will be generated. Regarding Figures 4.8 - 4.10 in Section 4.3.3 and from the charge yields in Table 4.4 on page 30, it turns out that the production of contamination ions like Na and K can be neglected for high impact speeds.

Somewhat unclear is the role of hydrogen in this case. For the highest observed impact speeds of 50 km/s, H-ions give an important contribution of approximately 10 % - 20 % of all ions to the time of flight mass spectra. This ratio seemed to be stable if one regards the ion composition of the TOF mass spectra for aluminium and iron. It is assumed that hydrogen is present in the spectra since protons may be diffused into the atomic metal-grid structure of the Rhodium target. Then it would be expected, that for high impact speeds, where the different ionization potentials for Rh and H are small against the mean plasma energy, both elements will be produced with similar power laws depending on the impact speed. Regarding Table 4.4 it appears that this is not the case for high impact speeds above 30 km/s, as measured with aluminium and iron projectiles. The Rh-charge yield shows a steeper increase than the H-charge yield.

This leads to the final assumption that for highest impact speeds, above v_{CI}, the charge yield function is dominated by the production rate of Rh-ions from the target. The power laws of the Rh-charge yields rise with the impact speed to the power of 5 to 7. Since the projectile's kinetic energy is rising only with v^2, for very high impact speeds the charge production should be limited by the kinetic energy, meanining a charge production $\propto v^2$. The value of v_{EL}, which marks the bend in the charge yield function from v^{5-7} to v^2 can easily be calculated from setting Eq. 5.32 equal to 1.0. The charge yield functions and ionization potential for rhodium can be found in Tables 2.1 (p. 14) and 4.4 (p. 30). The values for v_{EL}, where the bend appears in the charge yield function, have been calculated for all projectile materials and are summarized in Table D.9. Additionally the charge yield functions for impact speeds $v > v_{EL}$ have been calculated, assuming only the production of rhodium ions from the target. All listed impact speeds v_{EL} are far beyond the achievable impact speeds in the laboratory.

Above the impact speed limit v_{EL}, the absolute charge yield function $(\frac{q}{m})_{EL}$ for Rh^+-ions is limited by the kinetic energy of the projectile. The charge yield function $(\frac{q}{m})_{EL}$ can be easily calculated using energy conservation, assuming that all kinetic energy from the projectile is used for the ionization of rhodium. This assumption is acceptable, since for such high impact speeds all other ionization processes including multiple ionization and other energy dissipating processes (melting, vaporizing) can be neglected. The resulting charge yield $(\frac{q}{m})_{EL}$ is given by Eq. D.2, n_{Rh} is the absolute number of

Material	v_{EL} [km/s]
Aluminium	203 ± 11
Carbon	$> c$
Carbon + Na	400 ± 76
Iron	485 ± 36
PANi-PS-latex	724 ± 124

Table D.9: Calculated impact speeds v_{EL} where the ion charge yield functions are changing to $\propto v^2$-power laws due to kinetic energy limitation.

Material	Charge yields [C/kg]			v_{CI}	v_{EL}
	$v < v_{CI}$	$v_{CI} < v < v_{EL}$	$v > v_{EL}$		
Aluminium	$0.0016 \cdot v^{5.3}$	$2.3 \cdot 10^{-8} \cdot v^{7.4}$	$\frac{5.0 \cdot 10^5 v^2}{\chi_{Rh}}$	73	200
Carbon	$0.45 \cdot v^{3.3}$	$1.0 \cdot 10^{-3} \cdot v^{5.0}$	$\frac{5.0 \cdot 10^5 v^2}{\chi_{Rh}}$	52	400
Iron	$0.022 \cdot v^{4.3}$	$1.7 \cdot 10^{-4} \cdot v^{5.2}$	$\frac{5.0 \cdot 10^5 v^2}{\chi_{Rh}}$	233	500
PANi-PS-latex	$1.0 \cdot v^{3.0}$	$6.6 \cdot 10^{-4} \cdot v^{4.8}$	$\frac{5.0 \cdot 10^5 v^2}{\chi_{Rh}}$	30	700
Mean function	$0.015 \cdot v^{4.41}$		$\frac{5.0 \cdot 10^5 v^2}{\chi_{Rh}}$	-	500

Table D.10: Charge yield functions depending on the impact speed with respect to the limits v_{CI} for complete projectile ionization and v_{EL} for the available kinetic impact energy

rhodium ions, χ_{Rh} the ionization potential of rhodium in eV.

$$\begin{aligned} 0.5 \cdot 10^6 m v^2 &= \chi_{Rh} e \cdot n_{Rh} \\ n_{Rh} &= \frac{5 \cdot 10^5 m v^2}{\chi_{Rh} e} \\ q_{Rh} &= n_{Rh} \cdot e = \frac{5 \cdot 10^5 m v^2}{\chi_{Rh}} \\ \Rightarrow \qquad \left(\frac{q}{m}\right)_{EL} &= \frac{5 \cdot 10^5 v^2}{\chi_{Rh}} \qquad (v > v_{EL}) \end{aligned} \tag{D.2}$$

The full set of charge yield functions in all impact speed regimes and the corresponding limits v_{CI} and v_{EL} are summarized in Table D.10. The related functions are plotted in Figure D.22. The charge yields depend on the projectile material and can vary up to three orders of magnitude for certain impact speeds.

These extrapolations have to be regarded with care, since it is not known if there exist further bents in the charge yield functions for impact speeds higher than 70 km/s. Another problem is, that the calibration for the highest impact speeds was performed with projectiles which have masses that are 3 to 4 orders of magnitude lower than the projectile masses at the lowest speeds. The effect of the grain size on the charge yield is not clear. Hornung and Drapatz (1981) pointed out that the ionization degree of the projectile at a constant impact speed decreases strongly with increasing projectile mass. This would have big impact on the speed v_{CI}, where complete ionization occurs.

The ions in time-of-flight mass spectra have thermal energies of several ten eV (e.g. (REBER, 1997)). Since theses energies can be observed already at impact speeds above 30 km/s, thermal heating

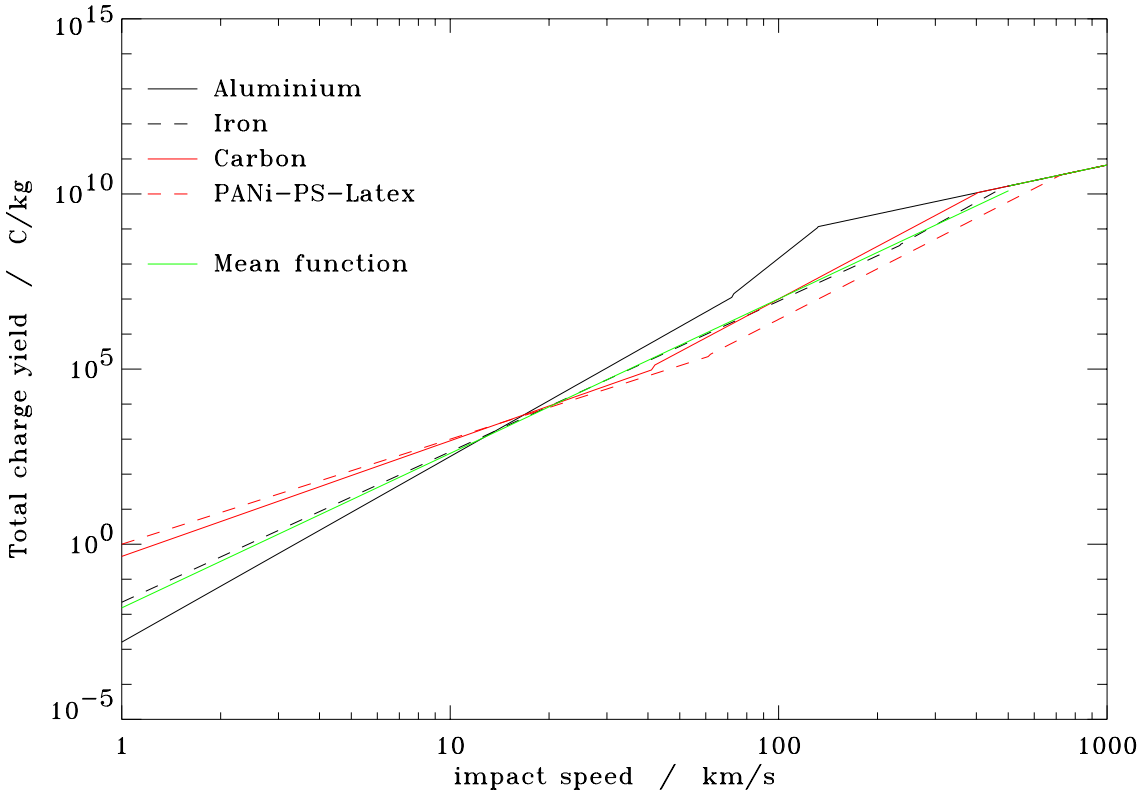

Figure D.22: Comparison of the extrapolated absolute charge yields for hypervelocity impacts on a rhodium target. All values are given in C/kg. Additionally a mean function which shows no v_{CI} limit is given.

processes should be neglected at impact speeds above 100 km/s and therefore have no influence on the charge yield at such speeds.

D.4.2 Instrument sensitivity for small and fast projectiles

As mentioned above, in space very small particles (< 10 nm) with high impact speeds have been observed (ZOOK, H.A. et al., 1996). Since these projectile parameters are out of range for laboratory investigations, the in Section D.4.1 obtained charge yield extrapolations for very high impact speeds should be applied to the instrument sensitivity functions (cf. Section D.3). For an unknown projectile type ε in space, a very rough, material independent charge yield should be sufficient. For the present estimation of the sensitivity a mean function of the impact charge yields for all materials, that is extended to very high impact speeds as shown in Figure D.22 will be taken. Without taking care for details, from Table D.10 and Eq. D.2 one gets the global charge yield functions shown in equations D.3 and D.4.

$$\frac{q}{m}(v) = 0.015 \cdot v^{4.4} \qquad (v \leq 500\text{km/s}) \tag{D.3}$$

Target	detection probability	
CAT	$p(m,v) = 5.5 \cdot 10^{11} \rho r^3 v^{4.4} + 0.01$	$v \leq 500\mathrm{km/s}$
	$2.5 \cdot 10^{18} \rho r^3 v^{2.0} + 0.01$	$v > 500\mathrm{km/s}$
IID	$p(m,v) = 2.4 \cdot 10^{11} \rho r^3 v^{4.4} - 0.05$	$v \leq 500\mathrm{km/s}$
	$1.1 \cdot 10^{18} \rho r^3 v^{2.0} - 0.05$	$v > 500\mathrm{km/s}$
WALL	$p(m,v) = 1.9 \cdot 10^{11} \rho r^3 v^{4.4} - 0.25$	$v \leq 500\mathrm{km/s}$
	$0.9 \cdot 10^{18} \rho r^3 v^{2.0} - 0.25$	$v > 500\mathrm{km/s}$

Table D.11: Summary of the absolute sensitivities of the different target sections of CDA.

$$= \frac{5.0 \cdot 10^5 v^2}{\chi_{\mathrm{Rh}}} \qquad (v > 500\mathrm{km/s}) \tag{D.4}$$

A combination of the instrument sensitivity function Eq. D.1 with the globale charge yield Eq. D.3 for impact speeds below 500 km/s respectively Eq. D.4 for impact speeds above 500 km/s results into a global instrument sensitivity formula D.5 respectively D.6 that is independent of the projectile material.

$$p(m,v) = \frac{0.015 m v^{4.4} - \delta}{\gamma} \qquad (v \leq 500\mathrm{km/s}) \tag{D.5}$$

$$= \frac{5.0 \cdot 10^5 m v^2}{\chi_{\mathrm{Rh}} - \delta} \gamma \qquad (v > 500\mathrm{km/s}) \tag{D.6}$$

$$p(m,v) = \frac{0.06 \cdot r^3 \rho v^{4.4} - \delta}{\gamma} \qquad (\text{for spherical particles }, v \leq 500\mathrm{km/s}) \tag{D.7}$$

$$= \frac{2.8 \cdot 10^5 r^3 \rho v^2 - \delta}{\gamma} \qquad (\text{for spherical particles }, v > 500\mathrm{km/s}) \tag{D.8}$$

Using the γ- and δ-values from Table D.8 (p. 165), one obtains instrument sensitivity functions for all target regions shown in Table D.11 extrapolated to very high impact speeds. These functions can be used to calculate the detection probability of an arbitrary projectile with the grain radius r and the density ρ that hits any region of the CDA instrument with an impact speed v. Such a calculation has been done for projectiles with a density of 2000 $\mathrm{kg/m^3}$ and with grain diameters between 10 nm and 10 μm. The calculated results for the detection probablity of such projectiles, hitting CDA at the CAT, IID and instrument wall at various impact speeds, are shown in Figure D.23.

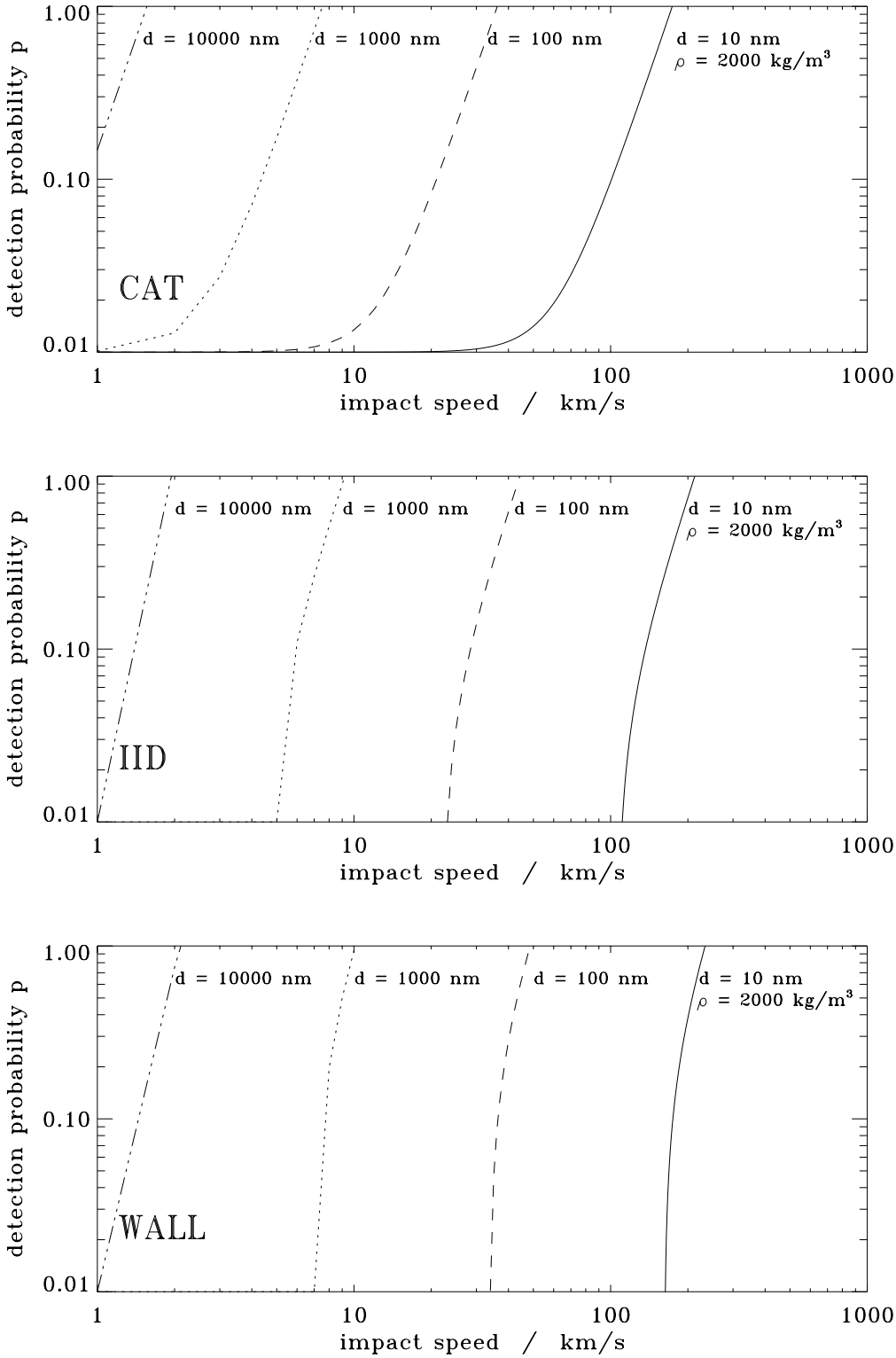

Figure D.23: Sensitivity of the CDA detector targets CDA and IID and the inner instrument wall depending on the impact speed. The sensitivity functions are shown for projectiles with grain size between 10 nm and 10 μm and a density of 2000 kg/m^3.

D.4.3 Comparison with flight data

Impact speeds above 70 km/s are not accessible in the laboratory. The considerations of the charge yields and the instrument sensitivity for very high impact speeds above 100 km/s can only be checked with dust particles in space. A good opportunity was the gravity assist maneuver at Jupiter 2000/2001. The CDA instrument was able to detect hundreds of the Jovian dust stream particles (SRAMA, R. et al., 2002). These particles have grain sizes of 10 nm and absolute velocities of 400 $\pm$ 100 km/s (ZOOK, H.A. et al., 1996; GRAPS et al., 2000). Nearly 200 time-of-flight mass spectra could be obtained. Examples are shown in Figure D.24 (KEMPF, 2002). These spectra are characterized by dominant mass peaks at 12 and 103 amu (carbon and rhodium). Both peaks appear broadened towards smaller flight times ($\equiv$ smaller masses). In some spectra appear other mass lines that might be identified with sodium and potassium. The mass lines can all be assigned to the CAT-target. This would be in agreement with the model that small projectiles of such high impact speeds are completely ionized and ions from the target material are the dominating species. The broadened peaks indicate a strong energy distribution of the ions. Grün et al. (2002) approximated energy distribution with mean energies up to 50 eV ($T_{plasma} \approx 6 \cdot 10^5$ K) to the rhodium mass line. No evidence of multiply ionized atoms was found so far.

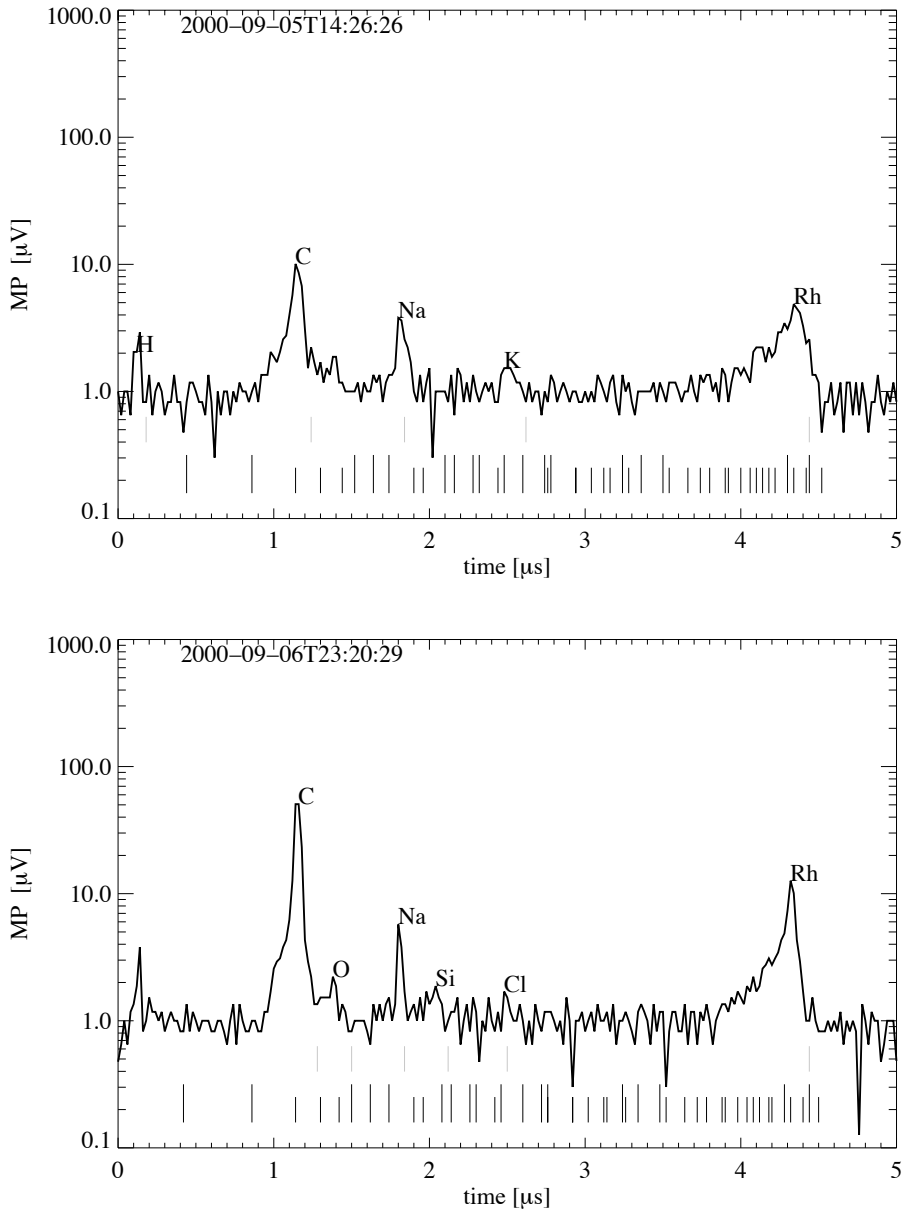

Figure D.24: Time-of-flight mass spectra of Jovian dust stream particles.

D.5 Rise times and time differences

This Section deals with the signal rise times from the different sensitive signal channels of the CDA instrument. The first part (Section D.5.1) describes the rise times of the charge signals. In a second part (Section D.5.2) are considered the time differences between certain signals depending on the impact location.

D.5.1 Signal rise times

The rise time is defined as the time span in which the signal of any channel rises from 10 % to 90 % of the signals' maximum value. For example, Figure D.25 shows the QI-channel rise time depending on the impact speed from impacting iron projectiles. Each symbol and its colour represent one impact region. The complete data set with the rise time of all four channels, measured with iron projectiles, can be found Figures D.26 and D.27. Similar data sets were obtained for all other projectile materials. The wide scattering of the data points as seen in the figures, prevents a reliable data fitting rise times depending on the impact speed. Nevertheless a comparison of the rise times obtained with iron projectiles from Srama (2000) with the values obtained from own measurements show a good agreement within an estimated error of 20 % for the impact speed exponent. All rise times from all signal channels and projectile types are summarized in Table D.12.
Regarding Figure D.25 it appears that the data show a large scatter. This causes the large variation of the derived impact speed dependencies. Comparing the rise time data for iron projectiles derived by Srama (2000) with the results for iron in this work, it appears the they are badly reproducible. Often only a constant value for the accessible impact speed range can be assumed. Since the scatter is too large, it is not possible to give reliable statements how the rise times may depend on the projectile material. However, the results can be summarized as follows:

Shots on the CAT: The signal rise times of the QC- and the QI-channel follow roughly a v^{-1}-law. The rise time is decreasing with an increasing impact speed. This effect is even more obvious at the QE-channel, where the signal rise time is decreasing with a v^{-2}-law. This might express the impact energy of ejecta that produce secondary ions at the IID-target. The rise time of the QP-channel is also decreasing with an increasing impact speed. But the power law fits show a large scattering of the impact speed exponent between -0.6 and -2.0, depending on the material.

Shots on the IID: The rise time of the relevant QE-channel decreases with a $v^{-0.7\pm-0.5}$-law. The signal rise time of the QC- and QI-channel are decreasing with increasing impact speed. But they show a larger scattering of the rise time functions $\propto v^{-0.2} - v^{-1.8}$. Both channels are not as well correlated as for CAT impacts. For the QP channel no explicit statements are possible.

Shots on the WALL: The QC channel shows a decreasing signal rise time with an increasing impact speed of the form $\propto v^{-0.6\pm-0.1}$. The impact speed dependencies of the QI- and QE-channel are not as large: $\propto v^{-0.3\pm-0.1}$. Only carbon projectiles show a similar impact speed dependence. Although there seems to be little difference between the results for IID-impacts and WALL-impacts a final decision would not be reliable. Regarding the Figures D.26 and D.27, it turns out that both impact types show a similar behavior for all channels. The large scattering in the data leads to a large uncertainty of the actual impact speed dependence.

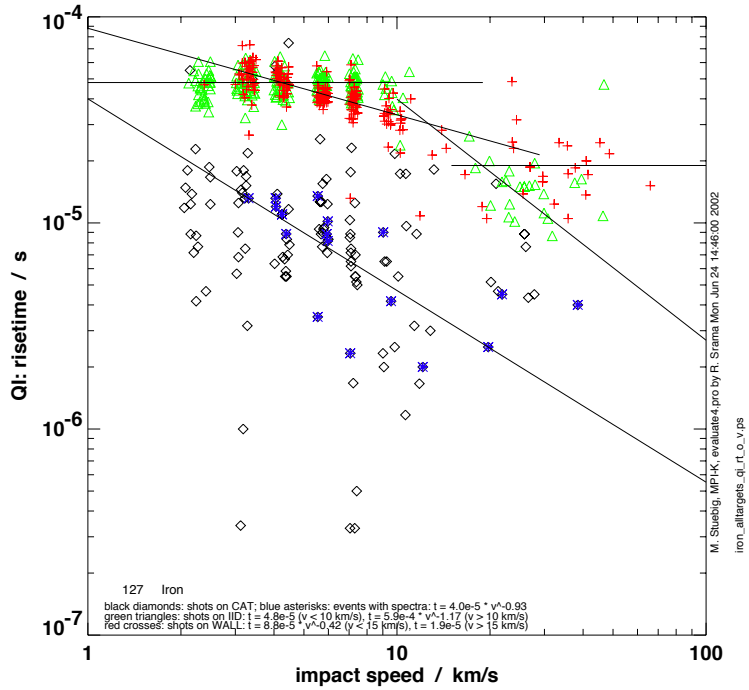

Figure D.25: Signal rise times of the QI-channel from impacting iron projectiles. The projectiles are shot onto the CAT (black diamonds for events without spectra, blue asterisks for events with spectra), the IID (green triangles) and the WALL (red crosses).

Limits of rise time measurements

The time resolution of the signal channels can be limited in two ways. The first factor is, that the measured signal rise time cannot be smaller than the sample rate of the corresponding channel. The other limiting factor is the rise time of the charge sensitive amplifiers. In Table D.13 the sample rates of all channels (except QM) and the corresponding time resolutions are summarized. Additionally the amplifier rise times, taken from Srama (2000), are given. The 5th and 6th column represent the measured minimum rise times and the corresponding impact speeds of the projectiles for shots with iron on the CAT- and the IID-target. The table shows, that the limiting factor in all cases is the amplifier rise time.

It is obvious that the rise times for impacts on the IID-target are much larger than for impacts on the CAT. This could be expected because the ions produced at CAT impacts are accelerated by the 1000 V potential between the target and the acceleration grid. Therefore they will reach the other charge sensitive channels much faster than the ions that are generated at the IID-target or instrument wall. The rise times at the highest observed impact speeds are still larger than the theoretical time resolution given by the sample rate of the corresponding channel. The minimum signal rise times at the QC channel are already reached at impact speeds of 40 km/s and don't change for higher speeds.

Impact speed determination from the signal rise time

Already Göller and Grün (1989) observed that the signal rise time of the electron pulse signal of the Galileo/Ulysses dust detector system depends only on the projectile's impact speed. The charge signal is a superimposed signal of plasma charge that is directly produced by the impact and plasma charge produced by impacts of ejecta. The superposition of both ion generating processes yield the total rise time of the charge signal (RATCLIFF, P.R. et al., 1996). The here measured rise times for shots on the CAT with impact speeds at about 50 km/s are roughly two to ten times larger than the instrumental limit of about 300 ns (Table D.13). Assuming a rough rise time power law $t \propto v^{-1}$ (cf. Table D.12), the signal rise times should allow a rough impact speed determination for projectiles with impact speeds between 100 and 500 km/s. Since the rise times for impacts on the IID are even higher, the impact speeds of even faster projectiles should be determinable. Unfortunately this impact speed range is out of range for laboratory measurements at present.

As can be seen in Table D.12 the impact speed dependence on the signal rise times shows a large scattering for all signal channels. This won't allow to set up formulae that describe reliable correlations between the impact speed and the signal rise time.

Target	rise time / s			
	QC	QI	QE	QP
Aluminium				
CAT ($4 < v < 50$ km/s)	$6.8 \cdot 10^{-5} \cdot v^{-1.4}$	$4.8 \cdot 10^{-5} \cdot v^{-0.9}$	$1.1 \cdot 10^{-3} \cdot v^{-1.6}$	$9.3 \cdot 10^{-4} \cdot v^{-2.0}$
Carbon				
CAT ($6 < v < 25$ km/s)	$6.6 \cdot 10^{-6} \cdot v^{-0.6}$	$5.0 \cdot 10^{-6}$	$1.1 \cdot 10^{-4} \cdot v^{-0.5}$	$1.5 \cdot 10^{-4} \cdot v^{-0.9}$
IID ($6 < v < 20$ km/s)	$3.4 \cdot 10^{-5} \cdot v^{-0.2}$	$5.7 \cdot 10^{-5} \cdot v^{-0.2}$	$1.2 \cdot 10^{-4} \cdot v^{-0.5}$	$2.0 \cdot 10^{-5}$
WALL ($6 < v < 20$ km/s)	$8.3 \cdot 10^{-5} \cdot v^{-0.7}$	$5.8 \cdot 10^{-5} \cdot v^{-0.2}$	$4.7 \cdot 10^{-5} \cdot v^{-0.2}$	$2.0 \cdot 10^{-5}$
Carbon + Na				
CAT ($4 < v < 15$ km/s)	$1.0 \cdot 10^{-5} \cdot v^{-0.8}$	$2.8 \cdot 10^{-7} \cdot v^{1.3}$	$2.6 \cdot 10^{-3} \cdot v^{-2.1}$	$1.2 \cdot 10^{-4} \cdot v^{-0.8}$
CAT ($15 < v < 25$ km/s)	$1.3 \cdot 10^{-6}$	$2.4 \cdot 10^{-5} \cdot v^{-0.6}$	$2.6 \cdot 10^{-3} \cdot v^{-2.1}$	$1.2 \cdot 10^{-4} \cdot v^{-0.8}$
Iron (Stübig)				
CAT ($2 < v < 50$ km/s)	$4.1 \cdot 10^{-5} \cdot v^{-1.4}$	$4.0 \cdot 10^{-5} \cdot v^{-0.9}$	$5.0 \cdot 10^{-5} - 3.0 \cdot 10^{-6}$	$3.0 \cdot 10^{-5} - 3.0 \cdot 10^{-6}$
IID ($2 < v < 50$ km/s)	$4.3 \cdot 10^{-5} \cdot v^{-0.3}$	$5.9 \cdot 10^{-4} \cdot v^{-1.2}$	$4.5 \cdot 10^{-5} - 1.3 \cdot 10^{-5}$	$3.0 \cdot 10^{-5} \cdot v^{-0.2}$
WALL ($2 < v < 10$ km/s)	$5.5 \cdot 10^{-5} \cdot v^{-0.5}$	$8.8 \cdot 10^{-5} \cdot v^{-0.4}$	$7.5 \cdot 10^{-5} \cdot v^{-0.3}$	$3.9 \cdot 10^{-5} \cdot v^{-0.2}$
WALL ($10 < v < 50$ km/s)			$1.5 \cdot 10^{-3} \cdot v^{-1.6}$	
Iron (Srama)				
CAT ($2 < v < 10$ km/s)	$4.1 \cdot 10^{-5} \cdot v^{-1.5}$	$2.9 \cdot 10^{-5} \cdot v^{-0.8}$	$1.5 \cdot 10^{-4} \cdot v^{-1.1}$	$3.1 \cdot 10^{-5}$
CAT ($10 < v < 35$ km/s)	$5.7 \cdot 10^{-6} \cdot v^{-0.6}$	$4.0 \cdot 10^{-6}$	$1.5 \cdot 10^{-4} \cdot v^{-1.1}$	$2.2 \cdot 10^{-4} \cdot v^{-1.3}$
CAT ($35 < v < 60$ km/s)	$7.0 \cdot 10^{-7}$	$4.0 \cdot 10^{-6}$	$1.5 \cdot 10^{-4} \cdot v^{-1.1}$	$2.5 \cdot 10^{-6}$
IID ($2 < v < 6$ km/s)	$5.0 \cdot 10^{-5} \cdot v^{-0.5}$	$5.4 \cdot 10^{-5}$	$6.0 \cdot 10^{-5}$	$3.1 \cdot 10^{-5}$
IID ($6 < v < 15$ km/s)	$5.0 \cdot 10^{-5} \cdot v^{-0.5}$	$4.0 \cdot 10^{-4} \cdot v^{-1.0}$	$3.0 \cdot 10^{-4} \cdot v^{-1.0}$	$1.2 \cdot 10^{-4} \cdot v^{-0.9}$
IID ($15 < v < 60$ km/s)	$7.0 \cdot 10^{-6}$	$4.0 \cdot 10^{-4} \cdot v^{-1.0}$	$3.0 \cdot 10^{-4} \cdot v^{-1.0}$	$1.0 \cdot 10^{-5}$
PANi-PS-latex				
CAT ($6 < v < 18$ km/s)	$2.0 \cdot 10^{-5} \cdot v^{-1.0}$	$5.5 \cdot 10^{-5} \cdot v^{-0.9}$	$2.9 \cdot 10^{-5}$	$2.7 \cdot 10^{-5} \cdot v^{-0.6}$
IID ($6 < v < 12$ km/s)	$1.0 \cdot 10^{-3} \cdot v^{-1.8}$	$2.8 \cdot 10^{-5}$	$1.3 \cdot 10^{-5} \cdot v^{0.4}$	-
WALL ($10 < v < 18$ km/s)	$8.3 \cdot 10^{-5} \cdot v^{-0.5}$	$2.0 \cdot 10^{-5}$	$6.5 \cdot 10^{-5} \cdot v^{-0.4}$	$2.0 \cdot 10^{-5}$
PPY-PS-Latex				
- The impact speed range is too small and the data scattering to high for a reliable fitting procedure. -				

Table D.12: Least square power law fits of the signal rise times from projectiles impacting on the CAT, the IID and the WALL for specific speed ranges.

Channel	sample rate [MHz]	time resolution [ns]	ampl. rise time [ns]	observed minimum rise time [ns]	$v_{min(rt)}$ [km/s]
QC	0.375, 6.0	2700, 170	320	600 (CAT)	> 40
				5500 (IID)	> 40
QI	0.375, 6.0	2700, 170	320	1000 (CAT)	50
				10000 (IID)	50
QE	0.375, 3.0	2700, 330	450	2000 (CAT)	50
				5000 (IID)	60
QP	6.0	170	250	2500 (CAT)	50
				10000 (IID)	60

Table D.13: Comparison of the nominal time resolution of the charge sensitive amplifiers by their sampling frequencies and by their rise times, and the practical observed minimum rise times for impacts on the CAT and IID.

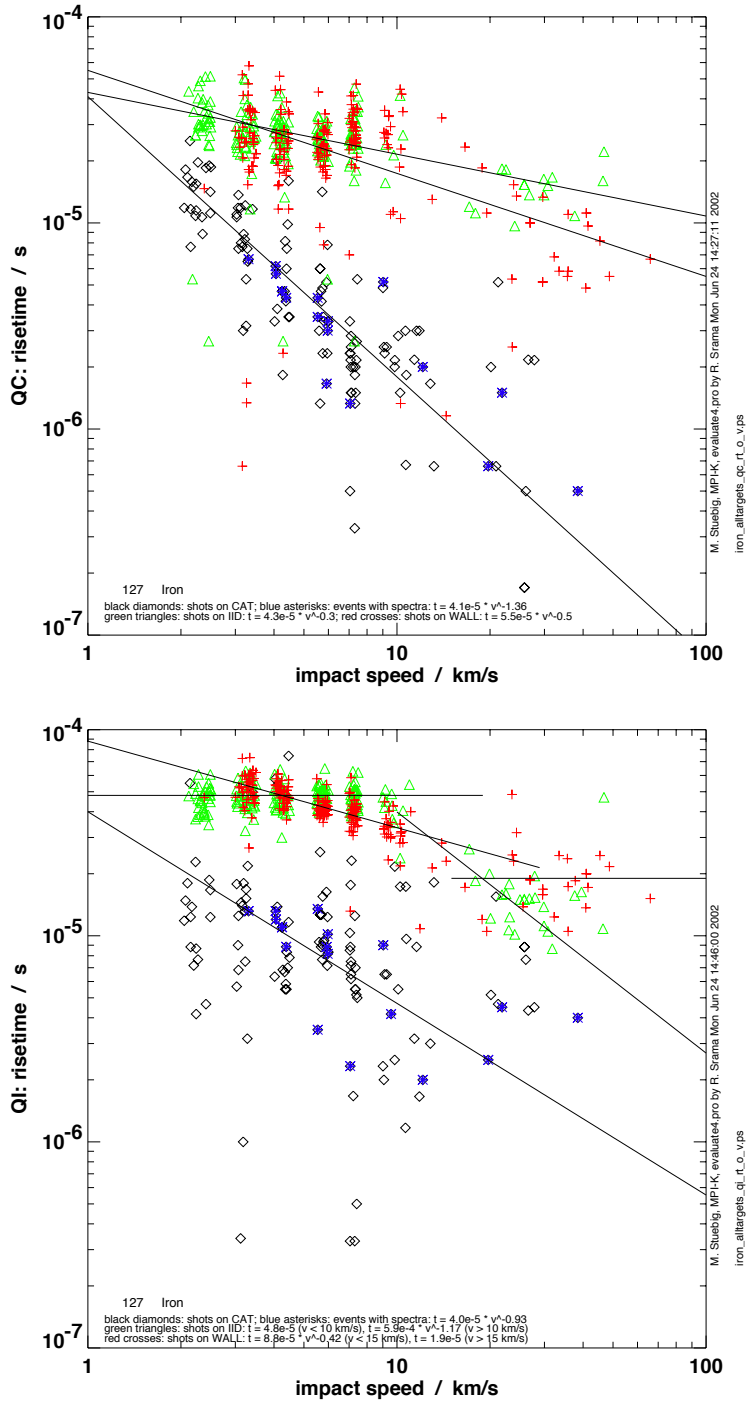

Figure D.26: Signal rise times of the QC-channel (upper diagram) and the QI-channel (lower diagram) from impacting iron projectiles. Projectiles are shot on the CAT (black diamonds for events without spectra, blue asterisks for events with spectra), the IID (green triangles) and on the WALL (red crosses).

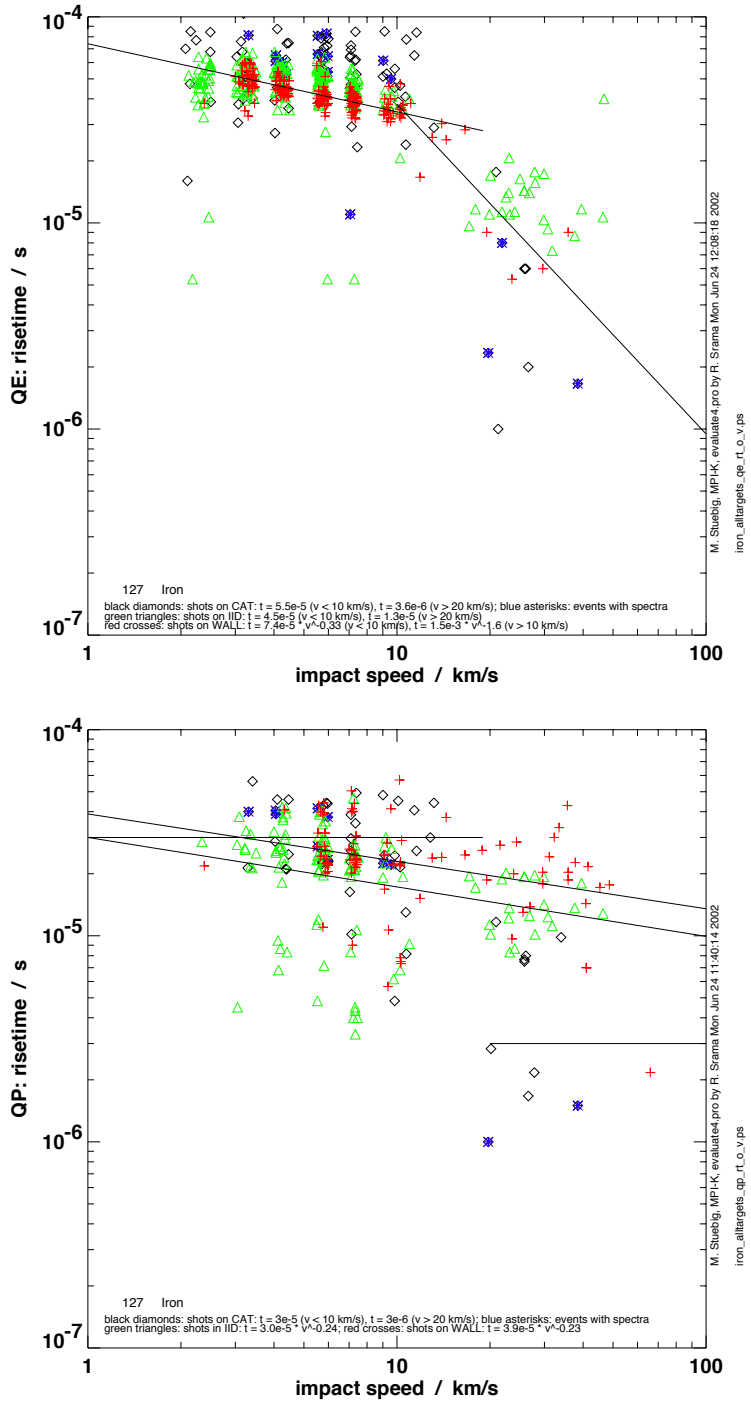

Figure D.27: Signal rise times of the QE-channel (upper diagram) and the QP-channel (lower diagram) from impacting iron projectiles. Projectiles are shot on the CAT (black diamonds for events without spectra, blue asterisks for events with spectra), the IID (green triangles) and on the WALL (red crosses).

time difference	CAT without spectrum	CAT with spectrum
QE - QC	> +50	> +100
QI - QE	< -60	< -100
QP - QE	< -70	< -100
QP - QI	> +20	> +50

Table D.14: Characteristic time differences for 90 % maximum values between two signals. The characteristics are exclusively valid for impacts on the CAT. All times are given in μs. These criteria are only valid for impact speeds below 12 km/s.

D.5.2 Time differences between signals

Since carbon, iron and latex projectiles were shot on different targets of the instrument (CAT, IID, WALL), the time differences between the maxima of the signals have been investigated. The goal here is a determination of the impact location by characteristic time differences between the signals. For this investigation, the time difference between the 90 %-values of the signal maxima of two channels are evaluated and plotted against the impact speed. This has to be done for shots on all target regions of CDA and for all signal pairs as shown in Figures D.29 to D.31. The diagrams for the other projectile materials show similar results. It turns out that shots on the CAT can be distinguished from shots on the IID-target and the instrument wall, while there are no significant differences between the time differences from shots on the wall and on the IID-target. The absolute time differences between the signals are in the order of 50 μs, while impacts on the CAT may cause even time differences of 150 μs. Since the time differences scatter and are sometimes larger 0 although they should be smaller 0 and vice versa, it is not possible to distinguish noise events from proper signals by time difference criteria. The best criteria for impacts on the CAT are summarized in Table D.14. Typical time difference values for impacts on all target regions are summarized in Table D.16. It has to be noted, that the criteria are only valid for impact speeds below 12 km/s. For higher impact speeds, the time differences are too low to distinguish even impacts on the CAT from impacts on the IID or wall. Criteria for the other target regions and higher impact speeds cannot be given since other time differences than given in Table D.14 can be obtained with impacts on all target regions, including the CAT.

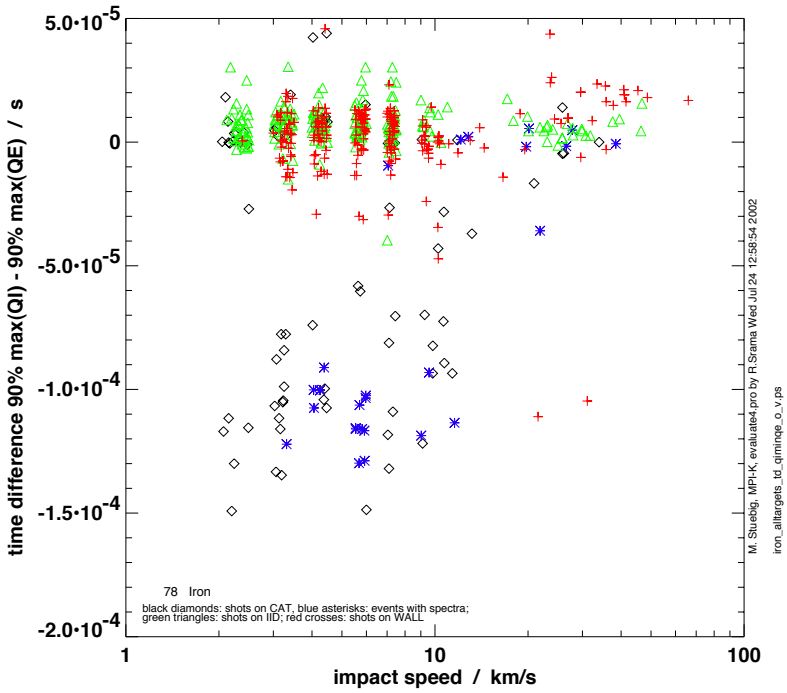

Figure D.28: Time differences between the 90 %-values of QI- and QE-signal. The projectiles were shot on the CAT (black diamonds for events without spectra, blue asterisks for events with spectra), the IID (green triangles) and on the WALL (red crosses).

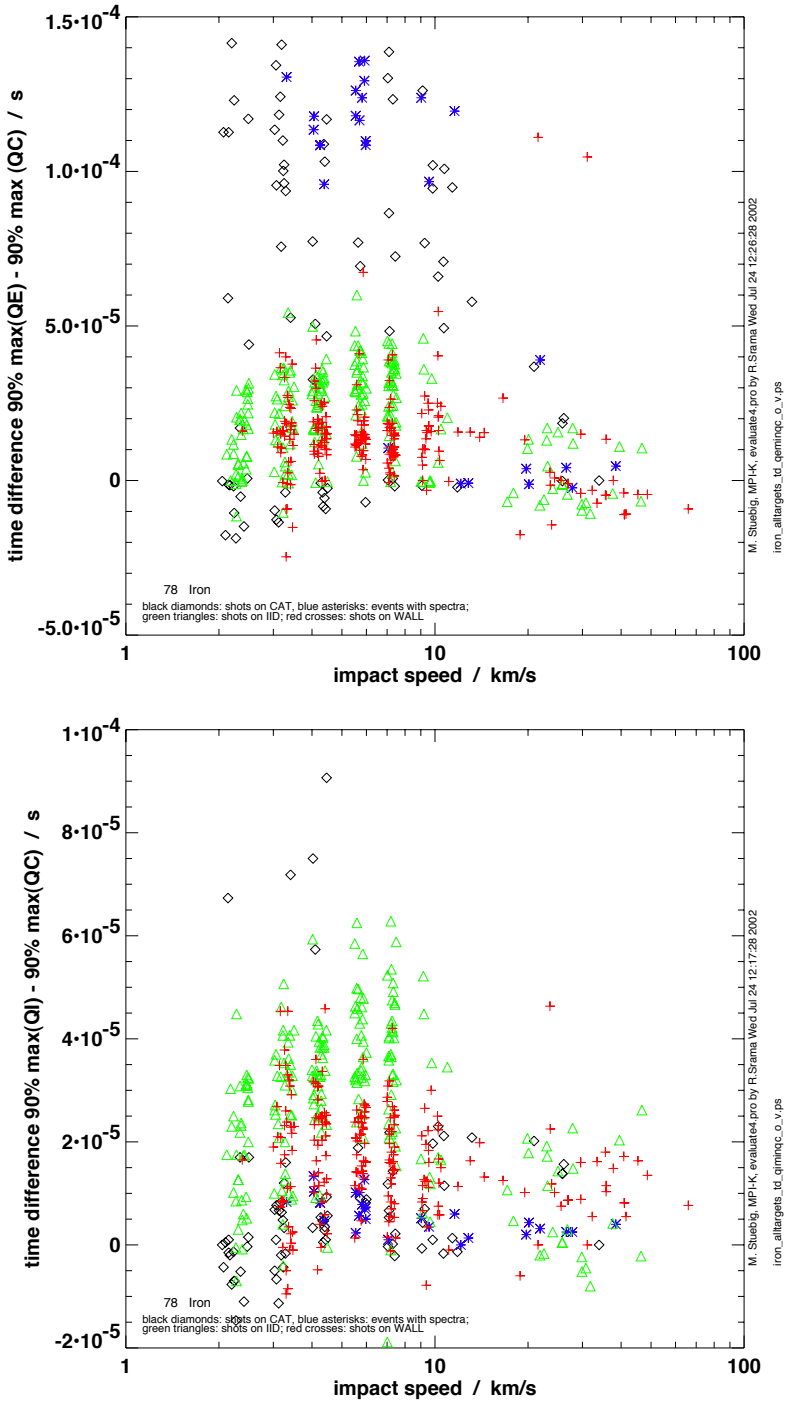

Figure D.29: Time differences between QE- and QC-signal (upper diagram) and the QI- and QC-signal (lower diagram). Projectiles are shot on the CAT (black diamonds for events without spectra, blue asterisks for events with spectra), the IID (green triangles) and on the WALL (red crosses).

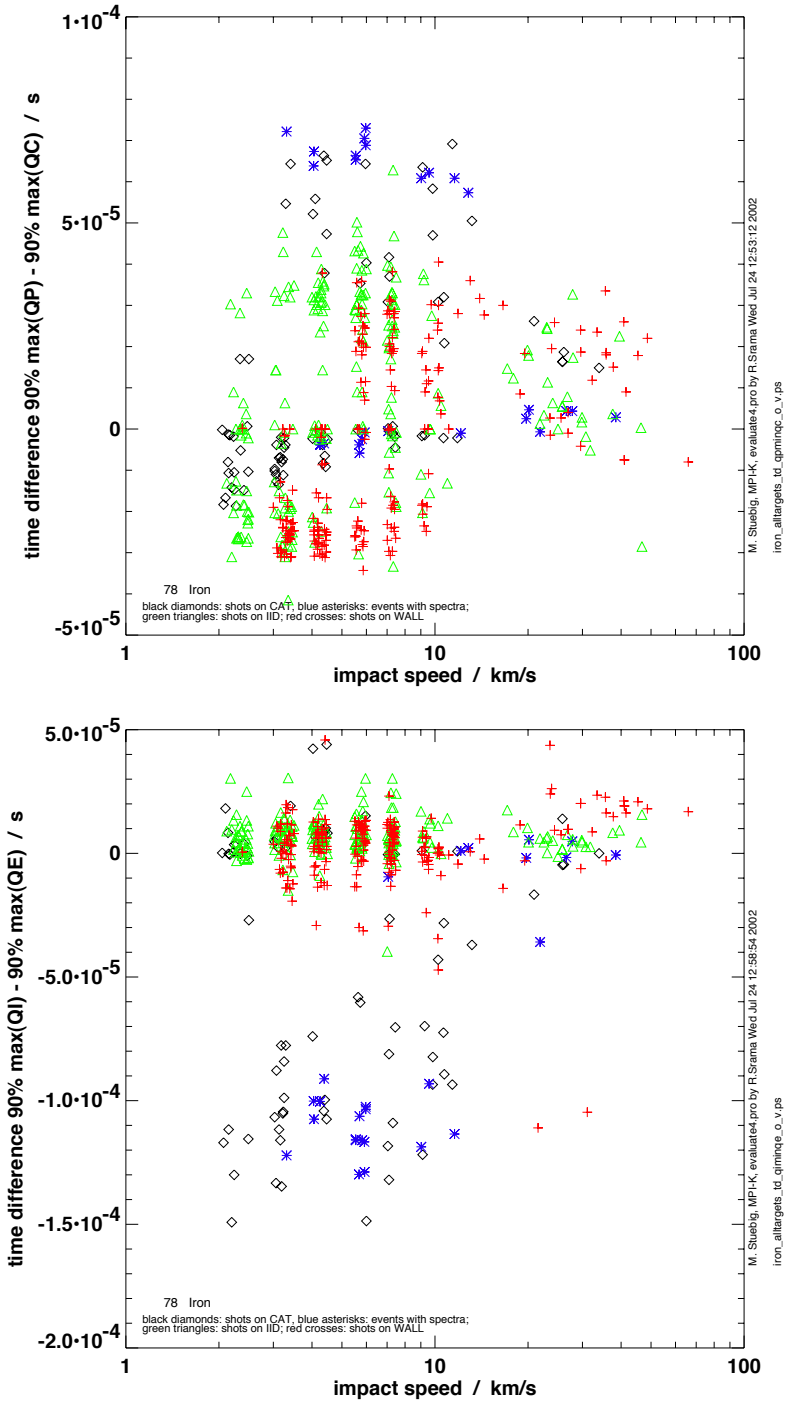

Figure D.30: Time differences between QP- and QC-signal (upper diagram) and the QI- and QE-signal (lower diagram). Projectiles are shot on the CAT (black diamonds for events without spectra, blue asterisks for events with spectra), the IID (green triangles) and on the WALL (red crosses).

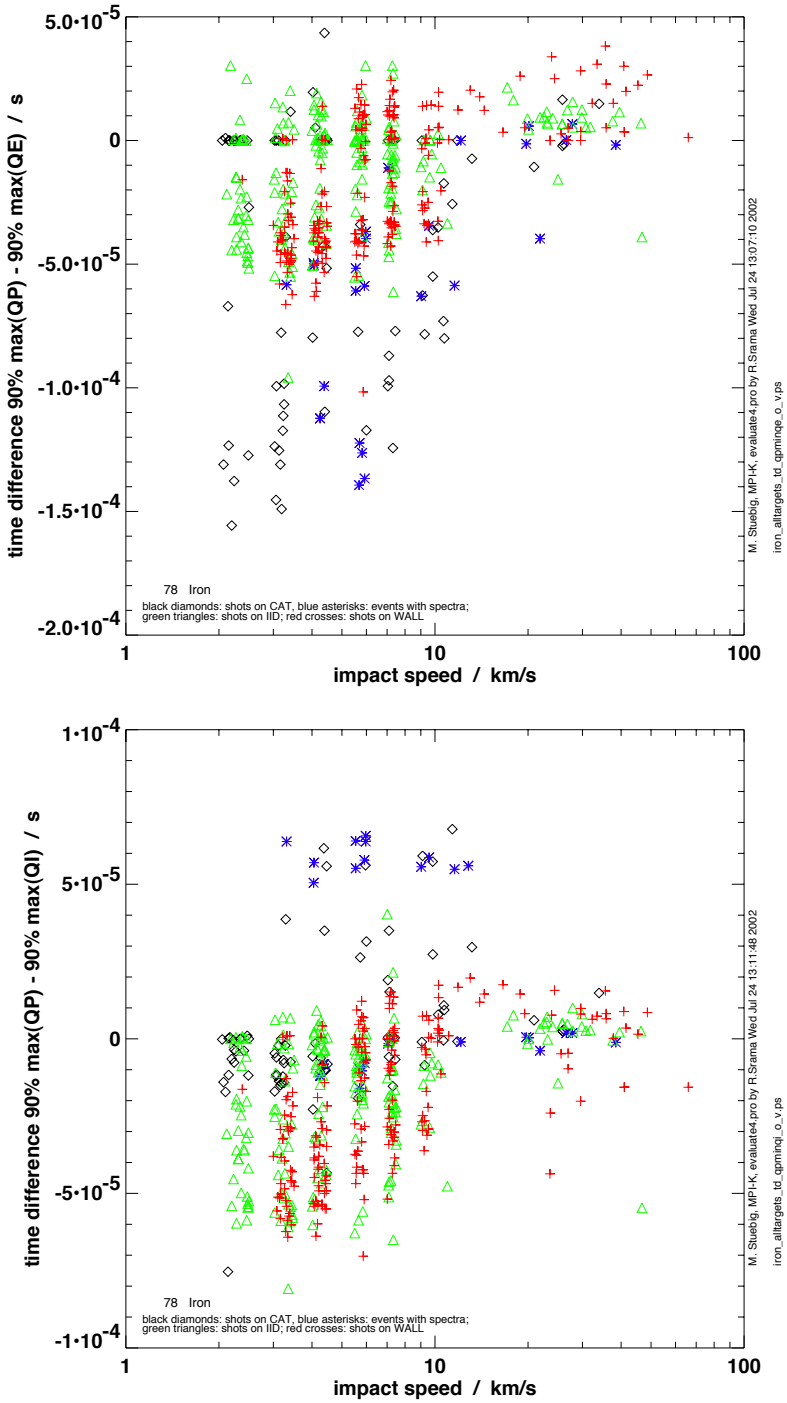

Figure D.31: Time differences between QP- and QE-signal (upper diagram) and the QP- and QI-signal (lower diagram). Projectiles are shot on the CAT (black diamonds for events without spectra, blue asterisks for events with spectra), the IID (green triangles) and on the WALL (red crosses).

D.6 Determination of the impact location

In space it is unknown at which target Section the projectile hits the CDA instrument. The values of impact charges, charge ratios and rise times from the calibration work described above may be used as criteria for the determination of the impact location. A similar evaluation has been done before by Srama (2000), but this work also considers impacts on the inner instrument wall and various projectile materials. A comparison of characteristic values is done in Table D.16. As can bee seen from the table, a really clear determination of the impact location is not possible by regarding only one criterion. A comparison of several criteria will a allow a more reliable classification. If one or more of the criteria in Table D.15 will be matched by the evaluated parameters, a determination of the impact location should be possible.

Criteria for impact site determination $v < 20$ km/s	Impact location
$\frac{QE}{QC} < 0.04$, $\frac{QI}{QC} < 0.05$, $\frac{QP}{QC} < 0.1$, $\frac{QI}{QE} > 1.0$, $\frac{QP}{QE} > 0.1$, $\frac{QE}{QC} < 0.04$, $\frac{QP}{QI} > 0.1$ td (QE-QC) $> 50\mu$s, td (QI-QE) $< -60\mu$s, td (QP-QE) $< -70\mu$s $\frac{rt(QE)}{rt(QC)} > 10$, $\frac{rt(QI)}{rt(QC)} > 40$, $\frac{rt(QP)}{rt(QC)} > 10$, $\frac{rt(QI)}{rt(QE)} < 0.1$	$\Rightarrow$ CAT
$0.04 < \frac{QE}{QC} < 1.0, 0.05 < \frac{QI}{QC} < 2.0$	$\Rightarrow$ IID
$\frac{QE}{QC} > 4.0$, $\frac{QI}{QC} > 2.0$ td (QI-QE) $> 25\mu$s, td (QP-QE) $> 50\mu$s	$\Rightarrow$ WALL

Table D.15: Criteria that allow a reliable determination of the impact location for impact speeds $v < 20$ km/s. The given values are exclusive values for the corresponding impact site. Values that are out of the given constraints might be achieved by impacts on even all three impact locations. The used signal channels are the following: Chemical Analyzer Target (QC), Impact Ionization Detektor (QE), ion grids (QI) and entrance grids (QP). ”rt” means rise time of the corresponding channel (10 % - 90 % signal amplitude), ”td” the time difference between reaching the 90 % signal amplitude level of different channels. All values are rough mean values from the calibration work with aluminium, carbon, iron and PANi-PS-latex. The values are only reliable for impact speeds below 20 km/s (time differences: $v < 12$ km/s).

Criterion	Impact location CAT	IID	WALL
$\frac{QE}{QC}$-charge ratio	0.005 - 0.04	0.05 - 4.0 (40.0)	1.0 - 10.0
$\frac{QI}{QC}$-charge ratio	0.01 - 0.5	0.05 - 2.0	0.2 - 10
$\frac{QP}{QC}$-charge ratio	< 0.1	(> 0.1)	> 0.1
$\frac{QI}{QE}$-charge ratio	0.2 - 10	0.1 - 0.4	0.1 - 0.6
$\frac{QP}{QE}$-charge ratio	> 0.1	< 0.1	< 0.1
$\frac{QP}{QI}$-charge ratio	0.08 - 1.0	0.02 - 0.2	0.01 - 0.1
$\frac{QC+QE}{QI}$-charge ratio	4 - 50	6 - 10 (30)	2 - 10
absolute charge yields $\frac{q}{m}$	not useful for unknown projectile type and impact speed		
rt(QC) [μs]	$2 \cdot 10^{-5} v^{-1.0}$	$4 \cdot 10^{-5} v^{-0.4}$	$6 \cdot 10^{-5} v^{-0.5}$
rt(QI) [μs]	$4 \cdot 10^{-5} v^{-1.0}$	$4 \cdot 10^{-4} v^{-1.0}$	$7 \cdot 10^{-5} v^{-0.3}$
rt(QE) [μs]	$1 \cdot 10^{-4} v^{-1.5}$	$2 \cdot 10^{-4} v^{-0.7}$	$6 \cdot 10^{-5} v^{-0.3}$
rt(QP) [μs]	$1 \cdot 10^{-4} v^{-1.0}$	$3 \cdot 10^{-5} v^{-0.2}$	$2 \cdot 10^{-5}$
$\frac{rt(QE)}{rt(QC)}$-rise time ratio	0.2 - 100	0.4 - 8 (50)	0.4 - 6 (30)
$\frac{rt(QI)}{rt(QC)}$-rise time ratio	0.02 - 100	0.2 - 5 (30)	0.3 - 5 (40)
$\frac{rt(QP)}{rt(QC)}$-rise time ratio	0.1 - 100	0.1 - 7 (20)	0.2 - 6
$\frac{rt(QI)}{rt(QE)}$-rise time ratio	0.02 - 14	0.4 - 10	0.3 - 2
$\frac{rt(QP)}{rt(QE)}$-rise time ratio	0.01 - 8	0.07 - 10	0.2 - 3
$\frac{rt(QP)}{rt(QI)}$-rise time ratio	0.1 - 10	0.03 - 10	0.3 - 2.5
td (QP-QC) [μs]	-20 - 50	-30 - 40	-30 - 40
td (QI-QC) [μs]	-10 - 10	> 0	-10 - 30
td (QE-QC) [μs]	> 50	< 50	< 30
td (QI-QE) [μs]	$<$ -60	-5 - 25	-10 - 50
td (QP-QE) [μs]	$<$ -70	$>$ -50	-30 - 30
td (QP-QI) [μs]	$>$ -20	< 10	< 10

Table D.16: Characteristic charge ratios, rise times, rise time ratios and time differences between signals for projectiles that hit the CAT, the IID and the WALL, independent of the projectile material. The used signal channels are the following: Chemical Analyzer Target (QC), Impact Ionization Detektor (QE), ion grids (QI) and entrance grids (QP). ”rt” means rise time of the corresponding channel (10 % - 90 % signal amplitude), ”td” the time difference between reaching the 90 % signal amplitude level of different channels. All values are rough mean values from the calibration work with aluminium, carbon, iron and PANi-PS-latex. The values are only reliable for impact speeds below 20 km/s (time differences: $v < 12$ km/s). Values in brackets appear very seldom or are valid for higher impact speeds.

D.7 Mass spectra of different projectile materials

The mass spectra of various projectile materials have been already investigated within a wide impact speed range in Section 4.3. Here is given an additional verification of the mass scale setting (Section D.7.1). It turns out that the mass scale is stretched for high impact speeds. The stretching parameter a of the mass scale might be used for a rough estimation of high impact speeds (Section D.7.2). In Section D.7.3 are finally shown examples of mass spectra depending on the impact speed for all used projectiles in this work. Additionally are tabled empirical mass resolutions depending on the ion mass and projectile impact speed for all projectile materials except PPY-PS-latex. Figures D.39 and D.40 compare the absolute ion yields of rhodium, hydrogen, sodium and potassium ions.

D.7.1 Verification of mass scale setting

Since the acceleration voltages (HVC, HVI) have been constant for all measurements, the factor a in Eq. 4.3 is expected to be constant for all projectile materials and impact speeds. The time offset b depends on the trigger thresholds and the ion charge yield from the impact. Since the variations of the trigger thresholds are only very slight, but the produced impact charge changes strongly with the projectiles' impact speed (cf. Section 4.2), b should change significantly with the impact speed. The empirical a and b values from the time-of-flight mass spectra of different projectile materials and various impact speed ranges are listed in Table D.17. It appears that the a-values are independent of the impact speed and of the projectile material. They all fit within their error bars. Whereas the b-values show a large scattering between values of +500 and - 2500 ns depending on the impact speed. The scatter range is at the highest for low impact speed ($v < 10$ km/s) and decreases with higher impact speeds. These results fit well with experimental results and theoretical calculations of the parameters a and b from the CDA flight unit obtained by Lavila (2002a), although he found different absolute values due to different voltages and trigger thresholds. Lavila also showed that the parameter b correlates with the charge signal QI at the ion grids. In cases of very low charges, he found, that the high rate sampling of the multiplier signal will be triggered by the charge signal of the hydrogen mass line. These results can be confirmed by the measurements in this work. It has to be mentioned that the reference masses that are used for the mass scale setting change with the impact speed. For low impact speeds, sodium and potassium appear firstly in the spectra and are used as reference masses (23 amu, 39 amu). At higher impact speeds appear projectile and target related mass lines which can also be used for mass scale setting. If possible, the hydrogen and rhodium mass lines were used as reference masses (1 amu, 103 amu). Since these mass lines cover a large mass range the error of a should be decreased. For standard SIMS-technology the change of the references masses might be critical, but the mass resolution of CDA is by a factor of 100 lower than for SIMS and thus too low for different mass scales depending on the reference material (contaminants, projectile, target). A more detailed analysis of a, using the aluminium data set and the large iron data set of Srama show a very slight increase of a with rising impact speed (upper diagrams in Figure D.32). This is consistent with the proposition by Lavila (2002b) that the intrinsic ion energy in the impact plasma may influence the absolute value of a. However the observed correlation is poor. The lower diagrams in Figure D.32 show, how the trigger time parameter b is related to the charge amplitude at the ion grid QI. The lower the absolute charge at the grid, the later the trigger time (negative values). Values of about -490 ns for b correspond with a triggering on the hydrogen mass line at 1 amu. Some of the low impact speed mass spectra in this work show such a late triggering that even the sodium mass line at 23 amu ($b \approx -2300$ ns) is cut off. In this case, sodium ions, that pass the ion grids, may trigger the high rate sampling of the multiplier.

a - values				
Impact speed [km/s]	Aluminium	Carbon	Iron	PANi-PS-latex
0 - 10	487 ± 9	487 ± 4	485 ± 8	484 ± 3
10 - 20	484 ± 10	485 ± 3	494 ± 8	483 ± 3
20 - 30	490 ± 11	484 ± 2	487 ± 3	488 ± 8
30 - 40	488 ± 7			493 ± 11
40 - 50	489 ± 5			501 ± 3
50 - 70				492 ± 14
mean	487 ± 3	485 ± 3	490 ± 5	490 ± 7

b - values				
Impact speed [km/s]	Aluminium	Carbon	Iron	PANi-PS-latex
0 - 10	-2500 - +500	-2500 - -500	-1500 - -300	-1500 - -200
10 - 20	-600 - +400	-1500 - -500	-1000 - -200	-1200 - -200
20 - 30	-400 - 0	-600 - -300	-400 - -300	-600 - -200
30 - 40	-300 - 0			-600 - -200
40 - 50	-200 - 0			-600 - -200
50 - 70				-600 - -200

Table D.17: Empirical values for *a* and *b* in the ion flight time formula. All values are given in 10^{-9} s.

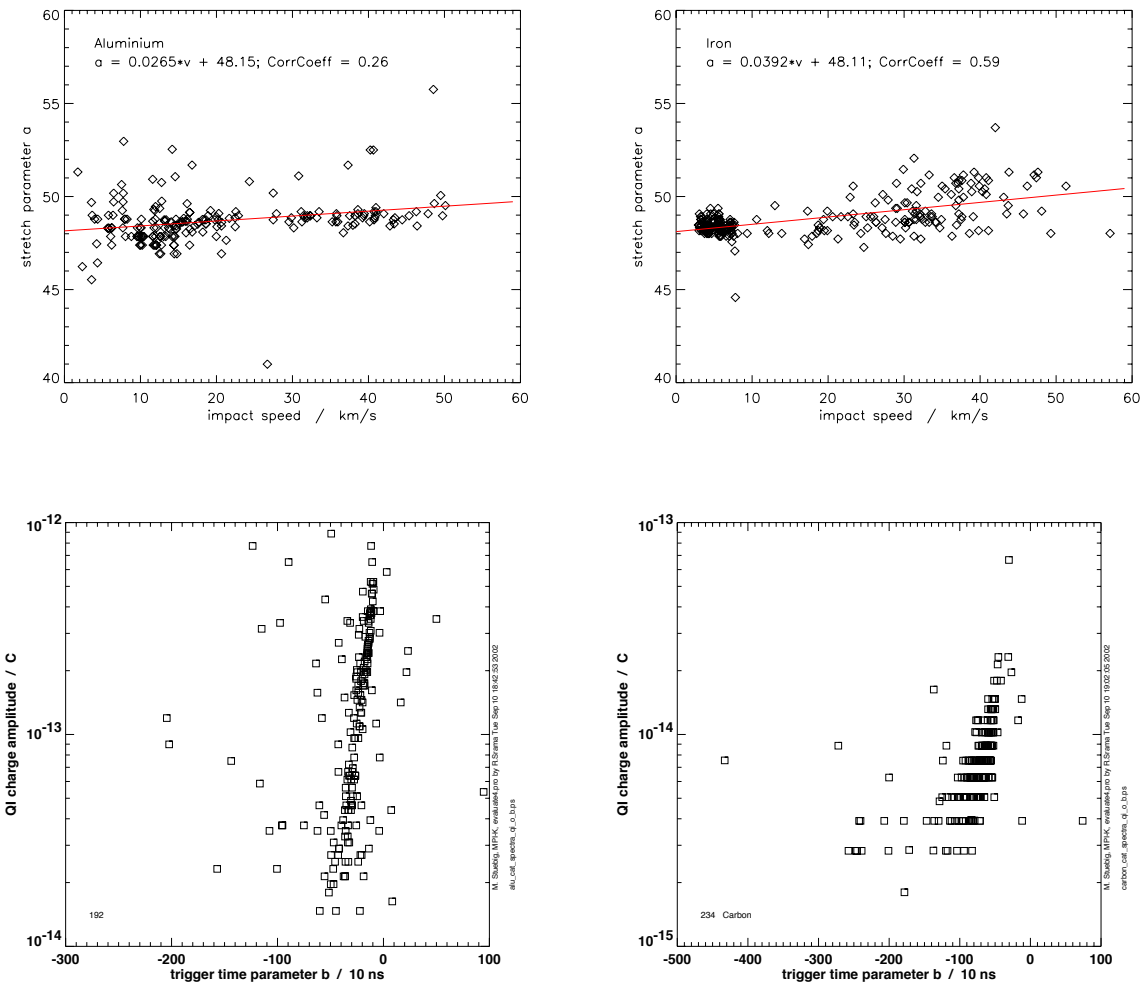

Figure D.32: Upper diagrams: the stretch parameter a for the mass scale depends on the impact speed v; left diagram: aluminium projectiles, right diagram: iron projectiles. Lower diagrams: the trigger time parameter b depends on the charge amplitude q at the ion grid QI; left diagram: aluminium projectiles, right diagram: iron projectiles.

v_{impact} [km/s]	$\frac{\Delta s}{\Delta t}$ [m/s]	$v_{\mathrm{H-Ion}}$ [km/s]	$\Delta v_{\mathrm{H-Ion}}$ [km/s]
2	$\frac{0.23}{480 \cdot 10^{-9}}$	479	
60	$\frac{0.23}{(480-180) \cdot 10^{-9}}$	767	+ 287

Table D.18: Calculation of the initial ion speed at high projectile impact speeds. A H^+-ion in the impact plasma of a 60 km/s fast projectile has an initial speed of 287 km/s relative to hydrogen ions released in the impact plasma of a 2 km/s fast projectile.

D.7.2 Correlation between impact speed and mass scale stretching

Although the correlation between a and v is poor, the absolute values change from 480 ns to 500 ns between 2 and 60 km/s. Thus the flight time difference between H (1 amu) and Rh (103) increases from 4390 ns at 2 km/s to 4570 ns at 60 km/s. The time scale stretching of 180 ns is 18 times larger than the time resolution of the multiplier. An explanation of this behavior can be the impact plasma temperature T. As mentioned before, the plasma temperature rises with increasing impact speeds of the projectiles. Assuming that all ions have a similar plasma temperature, they will also have a similar kinetic energy (Eq. 5.6). Due to their higher masses, heavy ions have smaller initial speeds than light ions, and therefore they will reach the multiplier relatively later.

In the following considerations, the effect of mass scale stretching with increasing impact speeds should be used to get a clue on the plasma temperature at the impact site and to get information on the impact speed for very high speeds above 100 km/s as expected for Jovian dust stream particles in space (ZOOK, H.A. et al., 1996). In Table D.18 is shown that hydrogen ions, released at impact speeds of 60 km/s, get an additional speed of 287 km/s relative to hydrogen ions, released at impact speeds of 2 km/s. Using this value in Eq. 5.6 follows for the impact plasma a temperature of $T \approx 5 \cdot 10^6$ K (Eq. D.9). This is in very good agreement with plasma temperature estimations using light flash observations (EICHHORN, 1978a) and the energy distribution of Rh-ions at high impact speeds (LAVILA, 2002a; LAVILA, 2002b).

$$T_{Plasma} = \frac{m_{\mathrm{H-Ion}} \cdot \Delta v^2}{2k_B} \tag{D.9}$$

Taking the mean values of the correlations between the stretch parameter a and the projectile impact speed v that could be measured for aluminium and iron projectiles (Eq. D.11), a rough estimation of the impact speed from the stretching of the mass scale should be possible (Eq. D.12). The results confirm the proposition by Lavila (2002b) that the stretching parameter "a" depends on the kinetic impact energy per mass unit of the projectile D.10.

$$a = a_0 + f(E_{kin}/m) \tag{D.10}$$

$$= 481 \cdot 10^{-9} + 0.3 \cdot 10^{-9} \cdot v \tag{D.11}$$

$$v = \frac{a - 481 \cdot 10^{-9}}{0.3 \cdot 10^{-9}} \tag{D.12}$$

D.7.3 Example spectra

Figures D.33 to D.38 show examples of time-of-flight mass spectra from all projectile materials, that have been used in this work. For each materials except PPY-PS-latex typical spectra at three different

impact speeds are given.

In Table D.19 are compared the mass resolutions of different projectiles materials for various impact speeds and ion masses. All materials show a similar behavior: the mass resolution is rising with increasing ion mass from about 20 at 1 amu to 40 at 100 amu. Furthermore the mass resolution remains stable or is even getting worse with increasing impact speed. This can be seen especially for aluminium and latex projectiles where the mass resolution drops to values of about 10 for low ion masses. The sodium contaminated carbon sample shows a relatively high mass resolution for very low impact speeds below 10 km/s. This might be due to a strong sodium peak in the time-of-flight-spectra.

Figures D.39 and D.40 give a comparison of the absolute yields of specific ion types (projectile material ions, H, Na, K), depending on the projectile material.

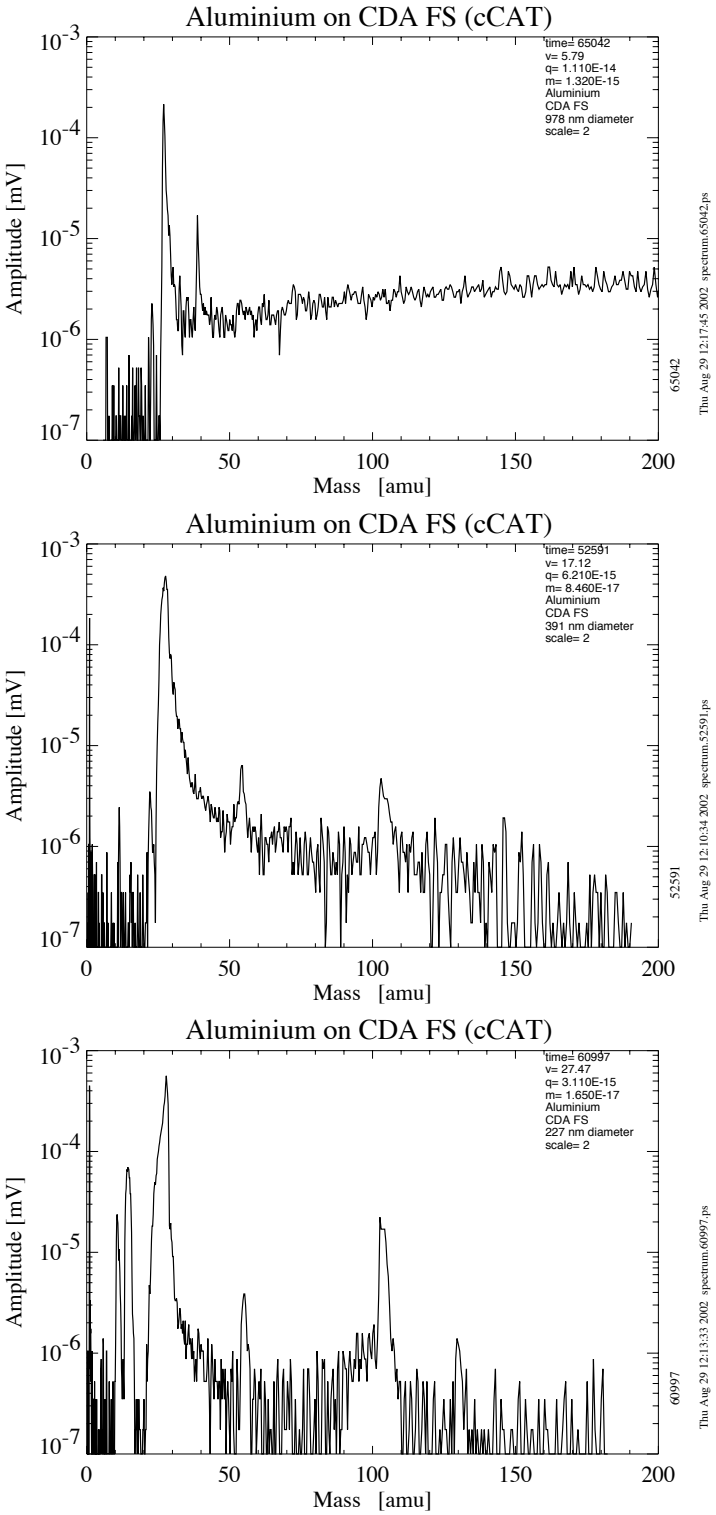

Figure D.33: Time-of-flight mass spectra from aluminium projectiles shot on the CAT. The impact speeds were, from top to bottom, 6, 17 and 27 km/s.

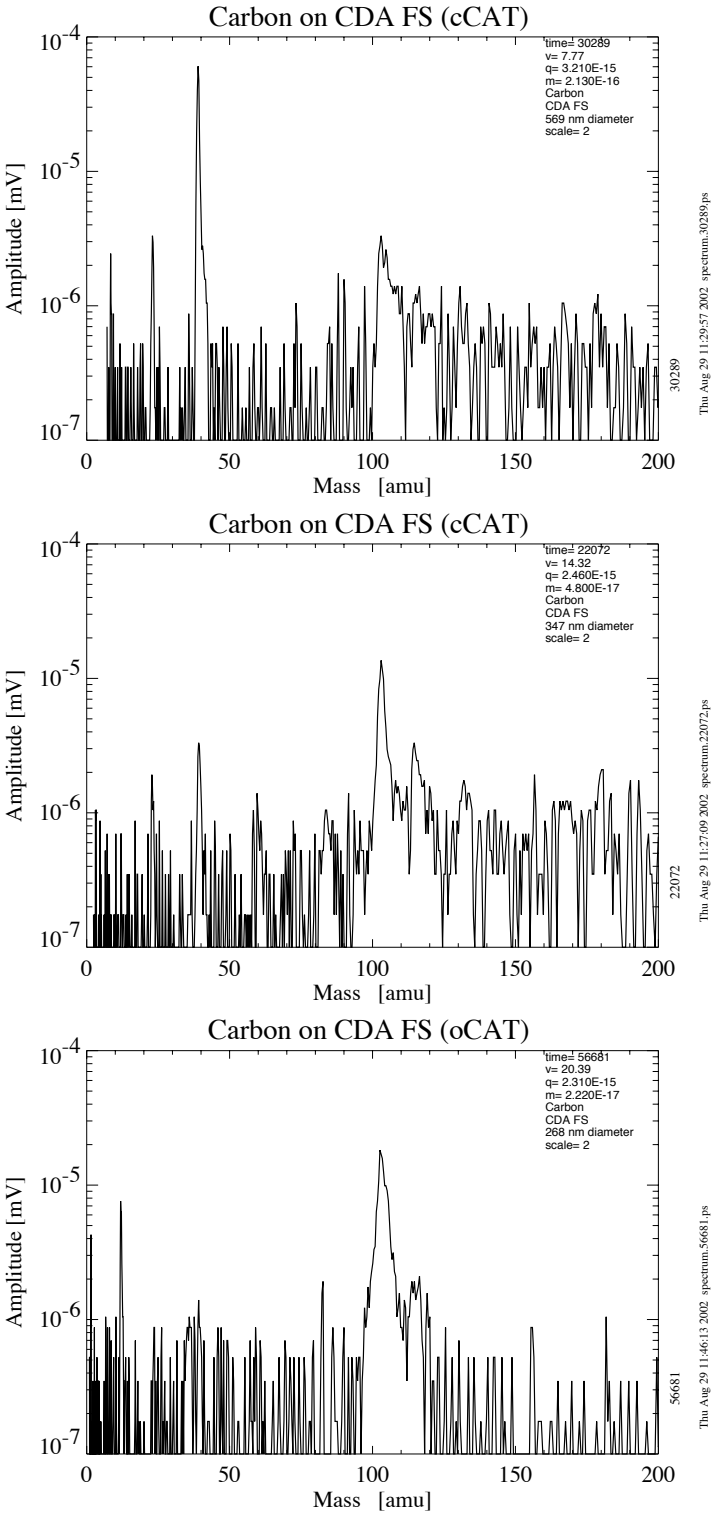

Figure D.34: Time-of-flight mass spectra from carbon projectiles shot on the CAT. The impact speeds were, from top to bottom, 8, 14 and 20 km/s.

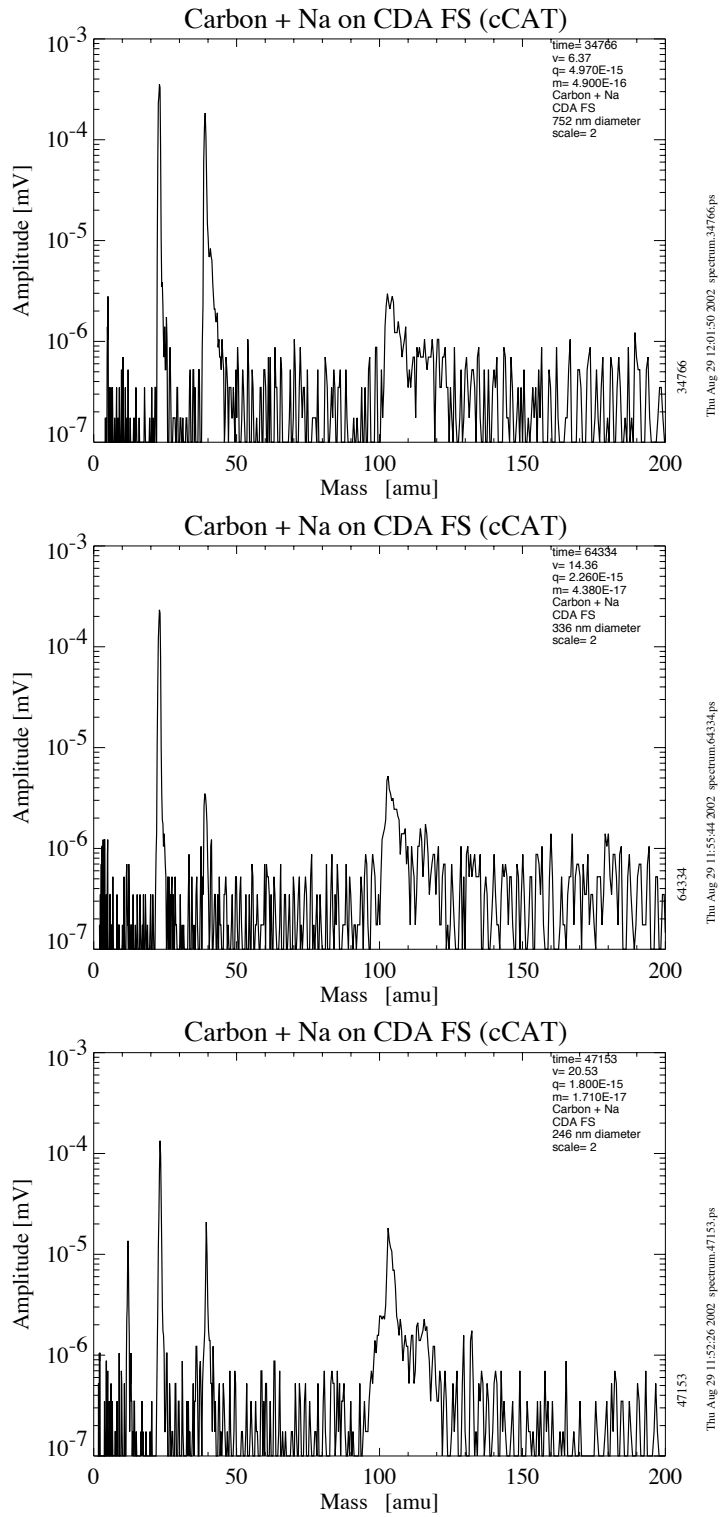

Figure D.35: Time-of-flight mass spectra from sodium contaminated carbon projectiles shot on the CAT. The impact speeds were, from top to bottom, 6, 14 and 21 km/s.

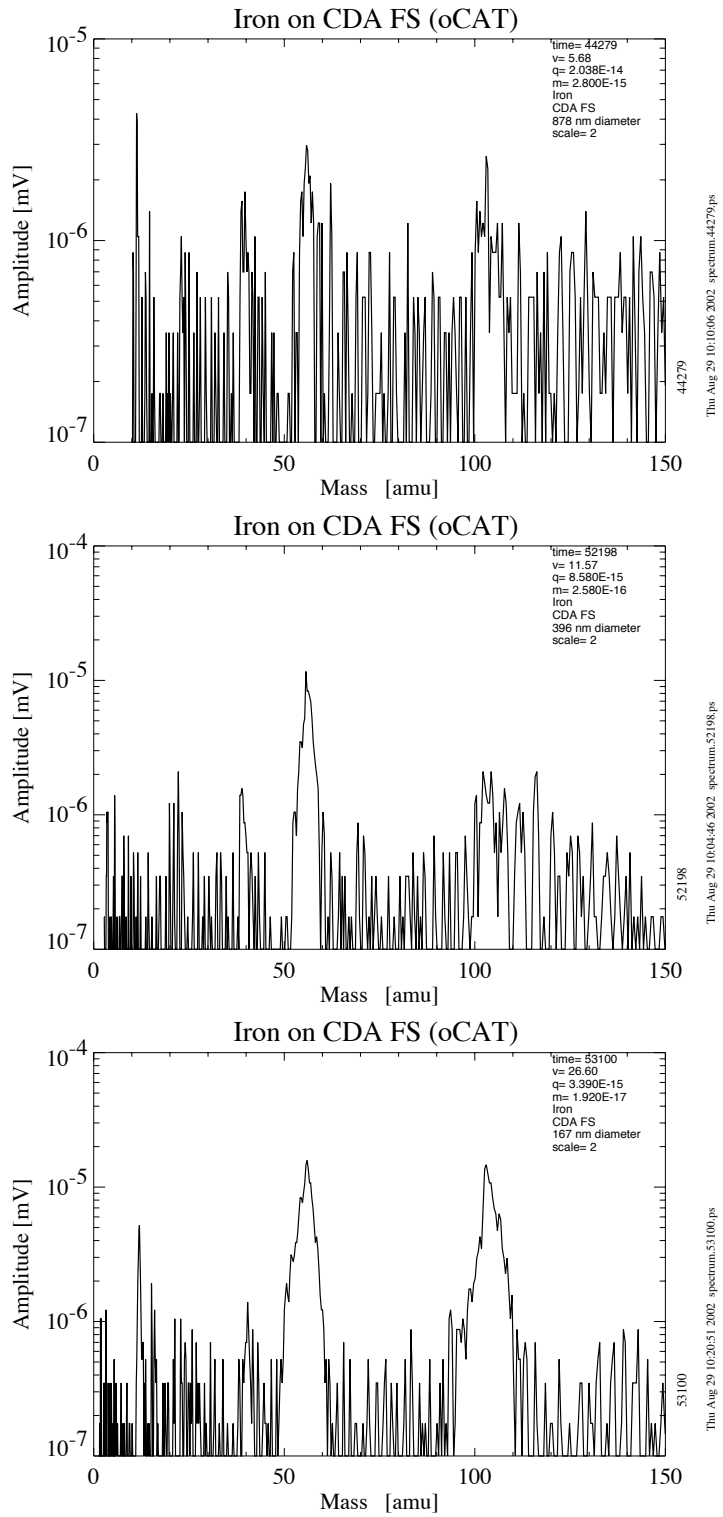

Figure D.36: Time-of-flight mass spectra from iron projectiles shot on the CAT. The impact speeds were, from top to bottom, 6, 12 and 27 km/s.

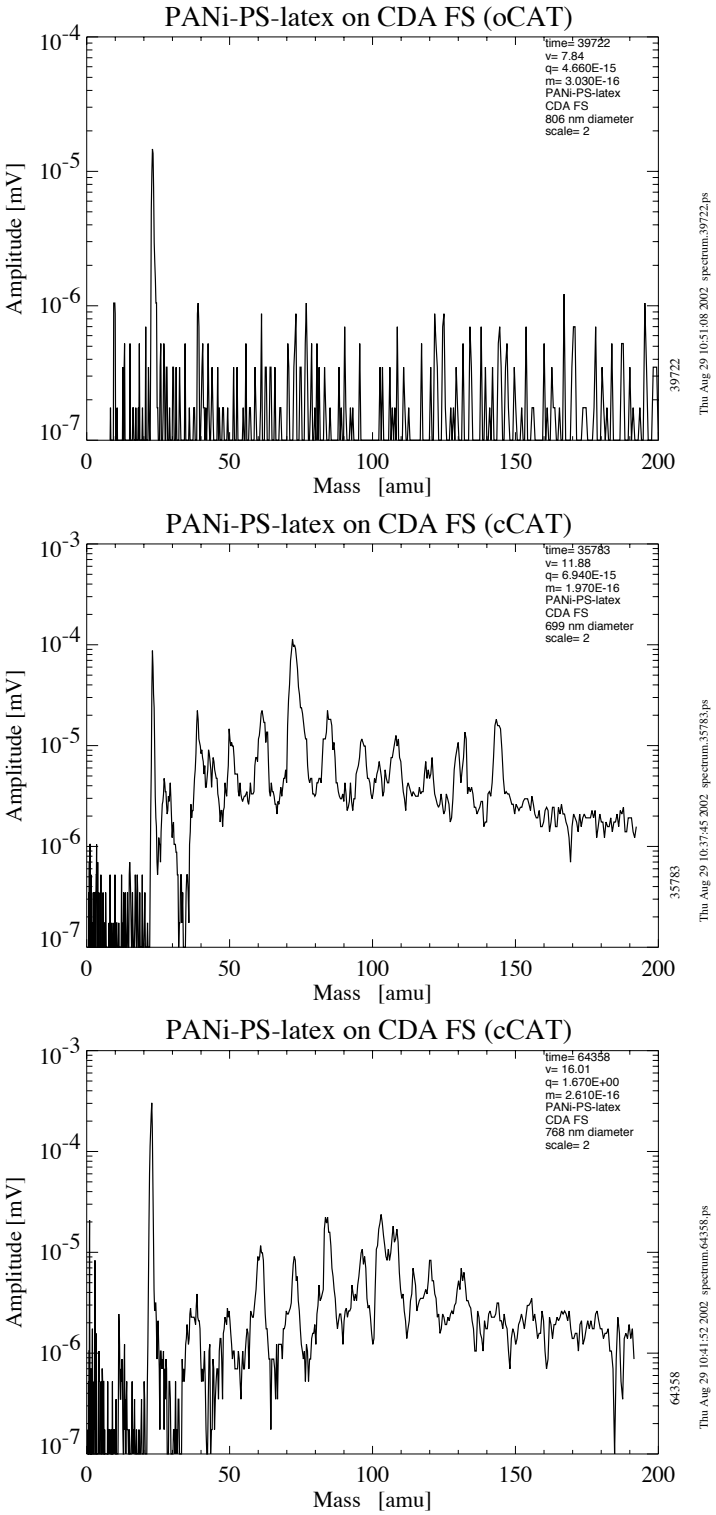

Figure D.37: Time-of-flight mass spectra from PANi-PS-latex projectiles shot on the CAT. The impact speeds were, from top to bottom, 8, 12 and 16 km/s.

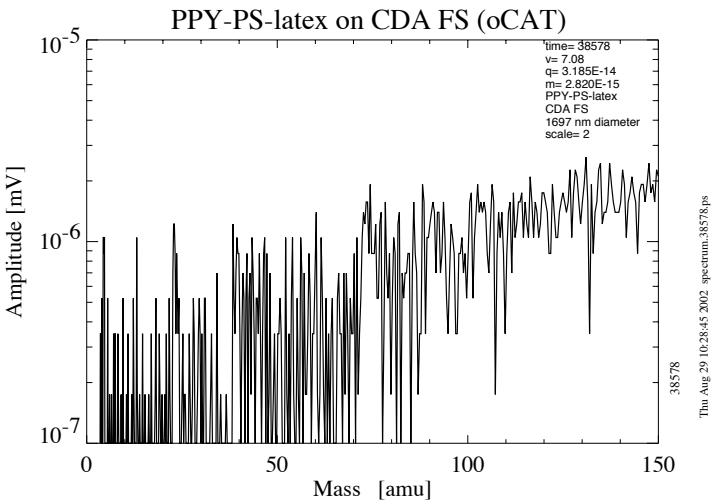

Figure D.38: Time-of-flight mass spectrum from a PPY-PS-latex projectile shot on the CAT. The impact speed was 7 km/s.

m	$\frac{m}{\Delta m}$		
	5 km/s	20 km/s	40 km/s
1	18	15	11
10	21	18	14
50	35	33	26
100	52	52	42

Aluminium

m	$\frac{m}{\Delta m}$		
	5 km/s	20 km/s	40 km/s
1	24	25	19
10	24	26	21
50	30	31	30
100	28	37	41

Iron

m	$\frac{m}{\Delta m}$		
	5 km/s	15 km/s	25 km/s
1	19	16	18
10	21	18	20
50	28	26	30
100	36	37	42

Carbon

m	$\frac{m}{\Delta m}$		
	5 km/s	15 km/s	25 km/s
1	29	19	18
10	31	20	20
50	36	29	30
100	43	39	43

Carbon + Na

m	$\frac{m}{\Delta m}$		
	5 km/s	15 km/s	25 km/s
1	17	17	11
10	18	18	13
50	21	27	25
100	26	37	40

PANi-PS-latex

Table D.19: Overview of the mass resolution of time-of-flight mass spectra, depending on the ion mass and the impact speed. Each table corresponds to one projectile material

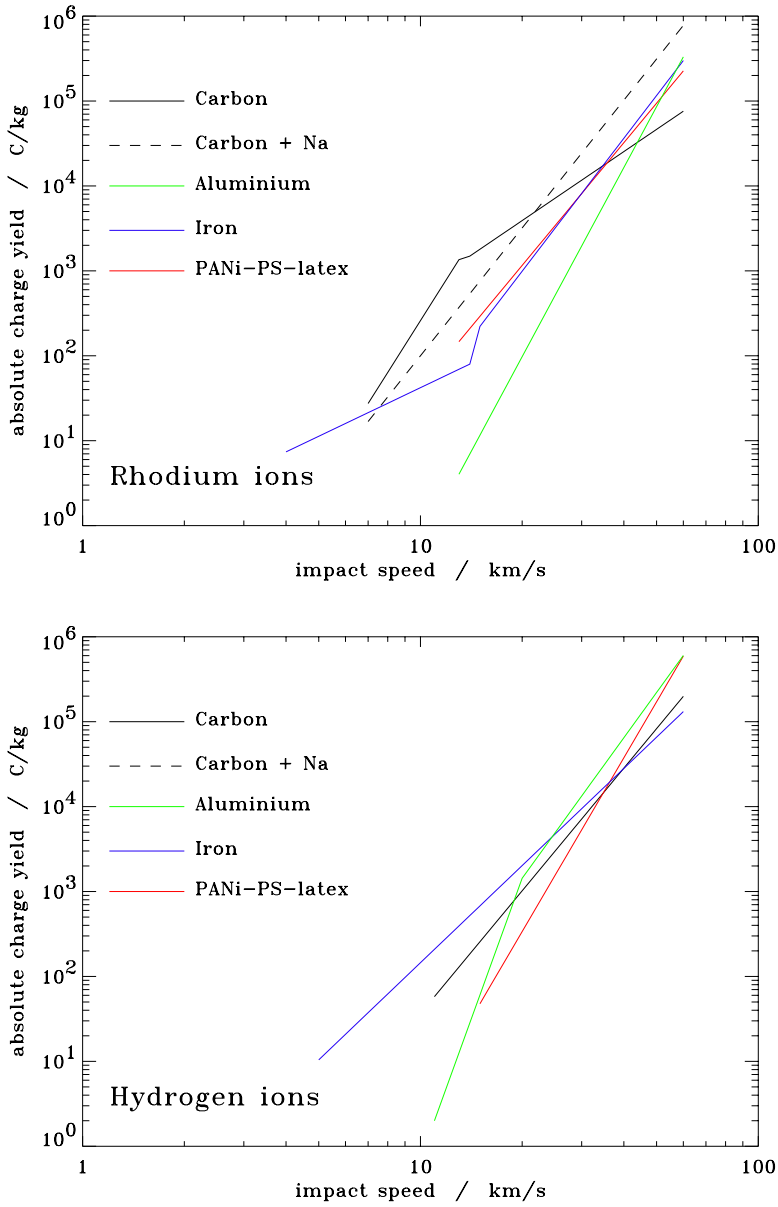

Figure D.39: Absolute ion charge yields of rhodium ions (upper figure), and of hydrogen ions (lower figure).

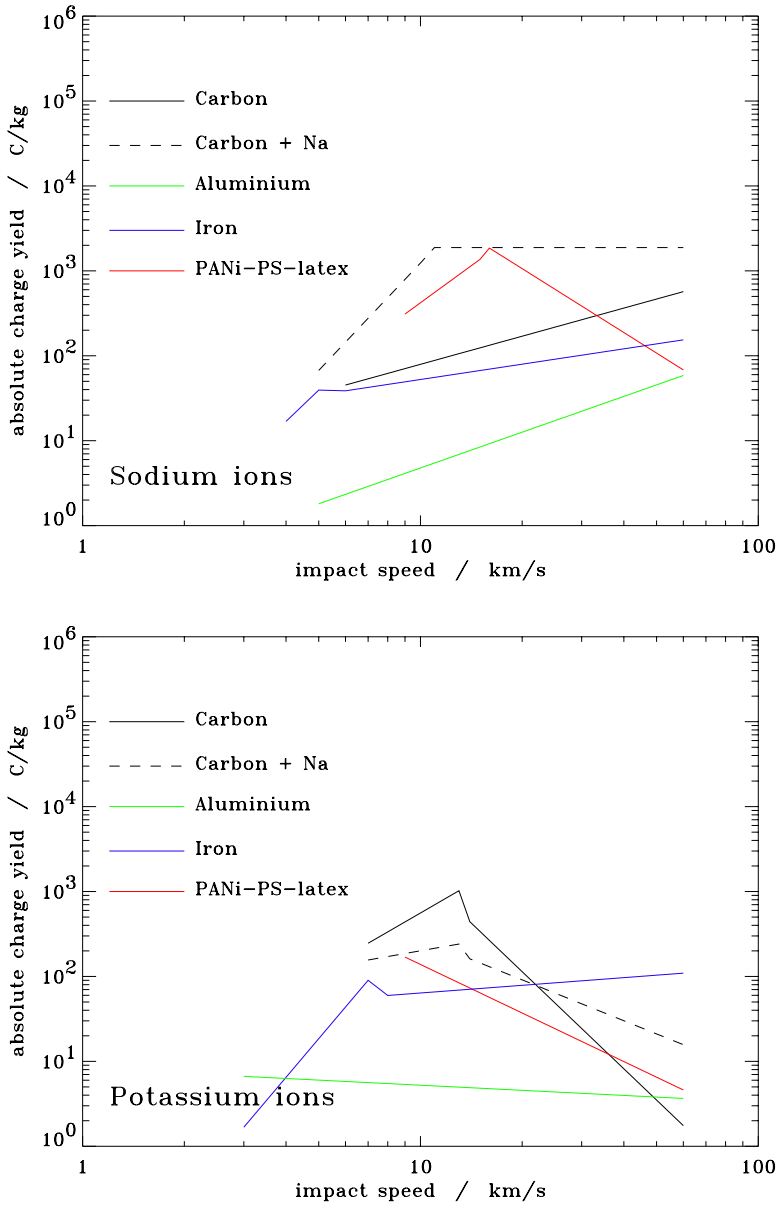

Figure D.40: Absolute ion charge yields sodium ions (upper figure), and of potassium ions (lower figure).

Appendix E

Physical constants

Here are listed frequently used physical constants.

ε_0	:	$8.854 \cdot 10^{-12}$ As $V^{-1}m^{-1}$	electric field constant
e	:	$1.602 \cdot 10^{-19}$ C	elementary charge
m_e	:	$9.109 \cdot 10^{-31}$ kg	electron mass
h	:	$6.626 \cdot 10^{-34}$ Js	Planck constant
k_B	:	$1.381 \cdot 10^{-23}$ J K^{-1}	Boltzmann constant
N_A	:	$6.022 \cdot 10^{23}$	Avogadro number
u	:	$1.661 \cdot 10^{-27}$ kg	atomic mass unit (amu)

All measurement dimensions in this thesis are given in SI-units[1] or multiples of them, using standard prefixes like e.g. MV (Megavolt) for 10^6 V or μm (micrometer) for 10^{-6} m. Exceptions are the measures of the vacuum pressure. These values are often given in mbar. The conversion into SI-units is as follows:

$$\begin{aligned} 1\,\mathrm{Pa} &= 10^{-5}\,\mathrm{bar} = 0.01\,\mathrm{mbar}, \\ 1\,\mathrm{mbar} &= 100\,\mathrm{Pa}. \end{aligned}$$

[1] SI-units are international standard dimensions of the *S*ystème International d' Unités (cf. Stöcker (1994), S 815).

Acknowledgements

The successful completion of this thesis would not be possible with the help and support of many persons whom I like to thank at this place.

First of all I like to thank Prof. Eberhard Grün to have confidence in my work as PHD-student at the Max-Planck-Institut für Kernphysik.

Many thanks also to Dr.-Ing. Ralf Srama for entrusting me the CDA flight spare unit for measurements in the laboratory. The later data evaluation would have been impossible without providing the software tools and his great support with the further software development.

Very special thanks to Mr. Gerhard Schäfer, the technician of the laboratory, who makes impossible things possible. His readiness to solve even the most complicate problems that appear with experimental setups (Murphy's law) is one key for a successful work.

I also like to thank Cand.-Phys. Anna Mocker-Ahlreep and Dipl.-Phys. Sebastian Kuhn for their support, the stimulating discussions, funny lunch breaks and coffee.

Not mentioned by name but not forgotten are the other members of the Cosmic Dust Group at the MPI-K for their support and productive contributions and discussions. All team members produced a fantastic and motivating working atmosphere.

The facilities of the Max-Planck-Institut für Kernphysik provided a straightforward and mostly trouble-free working. Thanks to all employees who contributed in any way to my thesis.

A lot of thanks to Dr. Jochen Kissel, Max-Planck-Institut für Extraterrestrische Physik, Garching, for providing me the CIDA engineering model to perform the measurements with the PANi-PS-latex particles and for interesting discussions on time-of-flight mass spectroscopy and the impact ionization process.

Last but not at least, I like to thank Dr. Thomas Stephan, Institut für Planetology der Universität Münster, for the discussion on the time-of-flight mass spectra and for the analysis of dust samples.

Bibliography

Amuroso, S., Berardi, V., Bruzzese, R., Capobianco, R., Velotta, R., and Armenante, M.: 1996, *High fluence laser ablation of aluminium targets: Time-of-flight mass analysis of plasmas produced at wavelengths 532 and 355 nm*, *Applied Physics A* 533–541

Anders, E. and Grevesse, N.: 1989, *Abundances of the elements: Meteoritic and solar*, *Geochimica et Cosmochimica Acta* **53**, 197

Artmann, J.: 1966, *Rankine-Hugoniot-Berechnungen für Nichtgleichgewichts-Plasmen*, *Zeitschrift f. Naturforschung* **21 a**, 1969

Barthet, Chr., Armes, S.P., Chehimi, M.M., Bilem, C., and Omastova, M.: 1998a, *Synthesis and Characterization of Micrometer-Sized, Polyaniline-Coated Polystyrene Latexes*, *Langmuir* **14**, 2023

Barthet, Chr., Armes, S.P., Lascelles, S.F., Luk, S.Y., and Stanley, H.M.E.: 1998b, *Surface Characterization of Polyaniline-Coated Polystyrene Latexes*, *Langmuir* **14**, 5032

Beatty, J.K., Collins Petersen, C., and Chaikin, A. (eds.): 1999a, *The new Solar System*, Chapt. 26. Meteorites (H.Y. McSween Jr.), pp 175 – 192, Cambridge University Press, Cambridge, New York, Melbourne, 4. edition

Beatty, J.K., Collins Petersen, C., and Chaikin, A. (eds.): 1999b, *The new Solar System*, Chapt. 5. Cometary reservoirs (J.K. Weissman), pp 175 – 192, Cambridge University Press, Cambridge, New York, Melbourne, 4. edition

Beatty, J.K., Collins Petersen, C., and Chaikin, A. (eds.): 1999c, *The new Solar System*, Chapt. 13. Atmospheres of the terrestrial planets (B.M. Jakosky), pp 175 – 192, Cambridge University Press, Cambridge, New York, Melbourne, 4. edition

Beckwith, S.V.W., Sargent, A.I., Chini, R.S., and Güsten: 1990, *A Survey for Circumstellar Disks around Young Stellar Objects*, *The Astronimical Journal* **99(3)**, 924

Benninghoven, A., Rüdenauer, F.G., and Werner, H.W.: 1987, *Secondary Ion Mass Spectrometry - Basic concepts, instrumental aspects, applications and trends*, John Wiley & Sons, New York

Berg, O. and Richardson, F.: 1968, *The Pioneer 8 cosmic dust experiment*, *The Review of Scientific Instruments* **40**, 1333

Brownlee, D.: 1985, *Cosmic Dust: Collection and Research*, *Annual Reviews in Earth and Planetary Sciences* **13**, 147

Brownlee, D. E., Tsou, P., Burnett, D., Clark, B., Hanner, M. S., Horz, F., Kissel, J., McDonnell, J. A. M., Newburn, R. L., Sandford, S., Sekanina, Z., Tuzzolino, A. J., and Zolensky, M.: 1997, *The STARDUST Mission: Returning Comet Samples to Earth*, *Meteoritics & Planetary Science* **32**, 22+

Brownlee, D. E., Tsou, P., Clark, B., Hanner, M. S., Hörz, F., Kissel, J., McDonnell, J. A. M., Newburn, R. L., Sandford, S., Sekanina, Z., Tuzzolino, A. J., and Zolensky, M.: 2000, *Stardust: A Comet Sample Return Mission*, *Meteoritics & Planetary Science, Supplement* **35**, 35+

Burchell, M.J., Cole, M.J., Lascelles, S.F., Khan, M.A., Barthet, C., Wilson, S.A., Cairns, D.B., and

Armes, S.P.: 1999, *Acceleration of Conducting Polymer-Coated Latex Particles as Projectiles in Hypervelocity Impact Experiments*, *Journal of Physics D: Applied Physics* **32**, 1719

Choi, B.-G., Huss, G.R., Wasserburg, G.J., and Gallino, R.: 1998, *Presolar Corundum and Spinel in Ordinary Chondrites: Origins from AGB Stars and a Supernova*, *Science* **282**, 1284

Dalmann, B.-K., Grün, E., Kissel, J., and Dietzel, H.: 1977, *The ion-composition of the plasma produced by impacts of fast dust particles*, *Planetary and Space Science* **25**, 135

Descartes, R.: 1637, *Discours de la méthode*, Jan Maire, Leyden

Dietzel, H., Eichhorn, G., Fechtig, H., Grun, E., Hoffmann, H.-J., and Kissel, J.: 1973, *The HEOS 2 and HELIOS micrometeoroid experiments*, *Journal of Physics E Scientific Instruments* **6**, 209

Dinger, R.: 1980, Energie- und winkelverteilung lasererzeugter plasmaionen, *Diploma/Master's thesis*, Technische Universität Kaiserslautern, Kaiserslautern

Draine, B.T. and Salpeter, E.E.: 1979, *On the Physics of Dust Grains in Hot Gas*, *The Astrophysical Journal* **231**, 77

Drapatz, S. and Michel, K.W.: 1974, *Theory of Shock-Wave Ionization upon High-Velocity Impact of Micrometeorites*, *Zeitschrift für Naturforschung* **29 a**, 870

Drawin, H.-W. and Felenbok, P.: 1965, *Data for Plasmas in Locat Thermodynamic Equilibrium*, Gauthier-Villars, Paris

Eichhorn, G.: 1972, Untersuchung der lichtemission beim einschlag energiereicher mikroteilchen, *Diploma/Master's thesis*, Max-Planck-Institut für Kernphysik, Heidelberg

Eichhorn, G.: 1976, *Analysis of the hypervelocity impact process from impact flash measurements*, *Planetary and Space Science* **24**, 771

Eichhorn, G.: 1978a, *Heating and Vaporization during Hypervelocity Particle Impact*, *Planetary and Space Science* **26**, 463

Eichhorn, G.: 1978b, *Primary velocity dependence of impact ejecta parameters*, *Planetary and Space Science* **26**, 469

Fahr, H.J. and Willerding, E.A.: 1998, *Die Entstehung von Sonnensystemen*, Spektrum Akademischer Verlag, Heidelberg, Berlin

Falk, W.: 1983, *Untersuchungen über die Ionenerzeugung beim Einschlag schneller Staubteilchen mit Massen bis* 10^{-7} *g auf Metalloberflächen*, *Doctoral/Ph.D. thesis*, Max-Planck-Institut für Kernphysik, Heidelberg

Fechtig, H., Grün, E., and Kissel, J.: 1978, *Cosmic Dust*, Chapt. 9: Laboratory Simulation, John Wiley and Sons, Chichester, New York, Brisbane, Toronto

Fegley, B. and Zolotov, M. Y.: 2000, *Carbon Chemistry of Volcanic Gases on Io*, *Meteoritics and Planetary Science, vol. 35, Supplement, p.A52* **35**, 52+

Frenklach, M., Carmer, C. S., and Feigelson, E. D.: 1989, *Silicon carbide and the origin of interstellar carbon grains*, *Nature* **339**, 196

Friichtenicht, J.: 1962, *Two-Million-Volt Electrostatic Accelerator for Hypervelocity Research*, *The Review of Scientific Instruments* **33(2)**, 209

Gerthsen, Ch. and Vogel, H.: 1993, *Physik*, Springer-Verlag, Berlin, 17. edition

Gmelin-Institut für anorganische Chemie (ed.): 1965, *Gmelins Handbuch der anorganischen Chemie - Natrium (System-Nummer 21)*, Ergänzungsband, Lieferung 2, Verlag Chemie GmbH, Weinheim/Bergstr., 8. edition

Goldsworthy, B.J., Burchell, M.J., Cole, M.J., Green, S.F., Leese, M.R., McBride, N., McDonnell, J.A.M., Müller, M., Grün, E., Srama, R., Armes, S.P., and Khan, M.A.: 2002, *Laboratory calibration of the Cassini Cosmic Dust Analyzer (CDA) using new, low density projectiles*, *Advances in Space Research* **29(8)**, 1139

Göller, J. and Grün, E.: 1989, *Calibration of the GALILEO/ULYSSES Dust Detectors with different*

projectile materials and at varying impact angles, *Planetary and Space Science* **37(10)**, 1197

Götting, G.: 1977, *Das Impactleuchten: Ein Indikator für Vorgänge bei Hochgeschwindigkeitskollisionen*, *Doctoral/Ph.D. thesis*, Technische Universität München, München

Graps, A. L., Grün, E., Svedhem, H., Krüger, H., Horányi, M., Heck, A., and Lammers, S.: 2000, *Io as a source of the jovian dust streams*, *Nature* **405**, 48

Greenberg, J. M. and Hong, S.-S.: 1974, The chemical composition and distribution of interstellar grains, in *IAU Symp. 60: Galactic Radio Astronomy*, Vol. 60, pp 155–177

Grün, E.: 2002, *Discussion on the Energy distribution*, private communication

Grün, E., Gustafson, B.Å.S., Dermott, S., and Fechtig, H. (eds.): 2001, *Interplanetary Dust*, Springer, Heidelberg

Grün, E., Baguhl, M., Hamilton, D.P., Riemann, R., Zook, H.A.and Dermott, S., Fechtig, H., Gustafson, B.A., Hanner, M.S., Horányi, M., Khurana, K.K., Kissel, J., Kivelson, M., Lindblad, B.A., Linkert, D., Linkert, G., Mann, I., McDonnell, J.A.M., Morfill, G.E., Polanskey, C., Schwehm, G., and Srama, R.: 1996, *Constraints from Galileo observations on the origin of jovian dust streams*, *Nature* **381**, 395

Grün, E., Gustafson, B., Mann, I., Baguhl, M., Morfill, G.E., Staubach, P., Taylor, A., and Zook, H.A.: 1994, *Interstellar dust in the Heliosphere*, *Astronomy and Astrophysics* **286**, 915

Grün, E., Kempf, S., Srama, R., Moragas-Klostermeyer, G., and Altobelli, N.: 2002, *Analysis of impact ionization from 300 km/s fast projectiles*, contribution to the EUROJOVE conference: Jupiter after Galileo and Cassini, Lisbon, 17. - 21.06.2002

Grün, E., Krüger, H., Dermott, S., Fechtig, H., Graps, A.L., Zook, H.A., Gustafson, B.A., Hamilton, D.P., Hanner, M.S., Heck, A., Horányi, M., Kissel, J., Lindblad, B.A., Linkert, D., Linkert, G., Mann, I., McDonnell, J.A.M., Morfill, G.E., Polanskey, C., Schwehm, G., and Srama, R.: 1997, *Dust measurements in the Jovian magnetosphere*, *Geophysical Research Letters* **24(17)**, 2171

Gürtler, J. and Dorschner, J.: 1993, *Das Sonnensystem*, Johann Ambrosius Barth, Leipzig, Berlin, Heidelberg

Hansen, D.: 1968, *Mass analysis of ions produced by hypervelocity impact*, *Applied Physics Letters* **13(3)**, 89

Ho, T.-M.: 2000, Messungen mit einem hochempfindlichen staubdetektor zum nachweis kleiner und schneller teilchen, *Diploma/Master's thesis*, Max-Planck-Institut für Kernphysik, Heidelberg

Hoffman, N.: 1999, Carbonatite Volcanism on Mars, in *The Fifth International Conference on Mars, July 19-24, 1999, Pasadena, California, abstract no. 6083*, pp 6083+

Hornung, K. and Drapatz, S.: 1981, Residual ionization after impact of large dust particles, in *The Comet Halley Probe - Plasma Environment*, pp 23–38, European Space Agency, Paris, ESA SP-155

Hornung, K. and Kissel, J.: 1994, *On shock wave impact ionization of dust particles*, *Astronomy and Astrophysics* **291**, 324

Hornung, K., Malama, Yu.G., and Thoma, K.: 1996, *Modeling of the Very High Velocity Impact Process with respect to In-Situ Ionization Measurements*, *Advanced Space Research* **17(12)**, (12)77

Hornung, K. and Michel, K.W.: 1972, *Equation-of-State Data of Solidds from Shock Vaporization*, *The Journal of Chemical Physics* **56(5)**, 2072

Humes, D.: 1980, *Results of Pioneer 10 and 11 meteoroid experiments: Interplanetary and near-Saturn*, *Journal of Geophysical Research* **85**, 5841

Jäger, C., Mutschke, H., Begeman, B., Dorschner, J., and Henning, Th.: 1994, *Steps toward interstellar silicate mineralogy, I. Laboratory results of a silicate glass of mean cosmic composition*, *Astronomy and Astrophysics* **292**, 641

Kant, I.: 1755, *Allgemeine Naturgeschichte und Theorie des Himmels*, J. F. Petersen, Königsberg,

Leipzig

Kempf, S.: 2002, *Discussion on mass spectra of Jovian dust stream particles*, private communication

Kissel, J., Brownlee, D. E., Buchler, K., Clark, B. C., Fechtig, H., Grun, E., Hornung, K., Igenbergs, E. B., Jessberger, E. K., Krüger, F. R., Kuczera, H., McDonnell, J. A. M., Morfill, G. M., Rahe, J., Schwehm, G. H., Sekanina, Z., Utterback, N. G., Volk, H. J., and Zook, H. A.: 1986a, *Composition of comet Halley dust particles from Giotto observations*, *Nature* **321**, 336+

Kissel, J. and Krüger, F. R.: 1987, *The Organic Component in Dust from Comet Halley as Measured by the PUMA Mass Spectrometer on Board VEGA 1*, *Nature* **326**, 755

Kissel, J., Sagdeev, R. Z., Bertaux, J. L., Angarov, V. N., Audouze, J., Blamont, J. E., Buchler, K., Evlanov, E. N., Fechtig, H., Fomenkova, M. N., von Hoerner, H., Inogamov, N. A., Khromov, V. N., Knabe, W., Krüger, F. R., Langevin, Y., Leonasv, B., Levasseur-Regourd, A. C., Managadze, G. G., Podkolzin, S. N., Shapiro, V. D., Tabaldyev, S. R., and Zubkov, B. V.: 1986b, *Composition of comet Halley dust particles from VEGA observations*, *Nature* **321**, 280

Kissel, J. and Krüger, F.R.: 1987, *Ion Formation by Impact of Fast Dust Particles and Comparison with Related Techniques*, *Applied Physics A - Solids and Surfaces* **42**, 69

Kissel, J. and Krüger, F.R.: 2001, *Time-of-flight mass spectrometric analysis of ion formation in hypervelocity impact of organic polymer microspheres: comparison with secondary ion mass spectrometry, 252Cf mass spectrometry and laser mass spectrometry*, *Rapid Communications in Mass Spectrometry* **15**, 1713

Knabe, W.: 1980, Untersuchungen am einschlags-ionisationsdetektor für die galileo- und isp-mission, *Diploma/Master's thesis*, Max-Planck-Institut für Kernphysik, Heidelberg

Knabe, W.: 1983, *Massenspektroskopische Untersuchungen der Ionenbildung beim Einschlag schneller Staubteilchen*, *Doctoral/Ph.D. thesis*, Universität Heidelberg, Heidelberg

Knabe, W. and Krüger, F.R.: 1982, *Ion Formation from Alkali Iodide Solids by Swift Dust Particle Impact*, *Zeitschrift für Naturforschung* **37 a**, 1335

Krüger, H., Srama, R., Kempf, S., Graps, A., Horányi, M., and Grün, E.: 2001, *Simultaneous observations of a Jovian dust stream with Galileo and Cassini*, *AAS/Division for Planetary Sciences Meeting*

Krüger, F.: 1982, *Thermodynamics of ion formation by fast dissipation of energy at solid surfaces*, *Zeitschrift für Naturforschung* **38 a**, 385

Krüger, F.: 1996, *Ion formation by high- and medium-velocities dust impacts from laboratory measurements and Halley results*, *Advances in Space Research* **17(12)**, 71

Krüger, F.R. and Kissel, J.: 1984, *Experimental investigations on ion emission with dust impacts on solid surfaces*, *Proceedings of the Giotto PEWG Meeting, ESA SP-224* pp 43–48

Krüger, F.R. and Kissel, J.: 1987, *The Chemical Composition of the Dust of Comet P/Halley as Measured by PUMA on Board VEGA-1*, *Naturwissenschaften* **74**, 312

Kuhn, S.: 2002a, *Discussion on multiply ionized atoms*, private communications

Kuhn, S.: 2002b, Hochgeschwindigkeitsmessungen am staubbeschleuniger mit der cda flugersatzeinheit, *Diploma/Master's thesis*, Max-Planck-Institut für Kernphysik, Heidelberg

Laplace, S.: 1796, *Exposition du système du monde*, Courcier, Paris, 5. edition

Lascelles, S.F and Armes, S.P.: 1997, *Synthesis and characterization of micrometer-Sized, polypyrrole-coated polystyrene latexes*, *Journal of Material Chemistry* **7(8)**, 1339

Lascelles, S.F, Armes, S.P., Zhdan, P.A., Greaves, S.J., Brown, A.M., Watts, J.F., Leadley, S.R., and Luk, S.Y.: 1997, *Synthesis and characterization of micrometer-Sized, polypyrrole-coated polystyrene latexes: verification of a 'core-shell' morphology*, *Journal of Material Chemistry* **7(8)**, 1349

Lavila, P.: 2002a, *Analyzing Time-of-Flight Spectra of CDA*, Technical report, Max-Planck-Institut

für Kernphysik, Heidelberg

Lavila, P.: 2002b, *Discussion on ion energy distribution*, private communication

Lindley, R.A., Gilgenbach, R.M., Ching, C.H., Lash, J.S., and Doll, G.L.: 1994, *Resonant holographic interferometry measurements of laser ablation plumes in vacuum, gas, and plasma environments*, *Journal of Applied Physics* **76(9)**, 5457

Managadze, G.G., Brinckerhoff, W.B., and Chumikov, A.E.: 2002, *Molecular synthesis in hypervelocity impact plasmas on the primitive Earth and in interstellar clouds*, *submitted to Nature*

Matthes, S.: 1996, *Mineralogie*, Springer-Verlag, 5. edition

Mattmüller, C.: 1994, *Ries und Steinheimer Becken*, Ferdinand Enke Verlag, Stuttgart

Mocker, A.: 2002, Optimierung der strahlfokussierung am heidelberger staubbeschleuniger (extreme beam focussing), *Diploma/Master's thesis*, Max-Planck-Institut für Kernphysik, Heidelberg

Neukum, G.: 1971, *Untersuchungen über Einschlagskrater auf dem Mond*, *Doctoral/Ph.D. thesis*, Max-Planck-Institut für Kernphysik, Heidelberg

Norton, G. E. and Pinkerton, H.: 1992, The Physical Properties of Carbonatite Lavas: Implications for Planetary Volcanism, in *Lunar and Planetary Institute Conference*, Vol. 23, pp 1001+

Øren, J. I.: 2000, *First order dust impact ionisation mass spectrometer - Intitial energy and angular distributions of ions generated at hyper velocity impacts*, Young graduate trainee report, ESTEC, Noordwijk, Netherlands

Posner, A.: 1995, Untersuchungen von flugzeit-massenspektren im rahmen der kalibrierung des cosmic dust analyzer detektors für die cassini-mission, *Diploma/Master's thesis*, Max-Planck-Institut für Kernphysik, Heidelberg

Ratcliff, P.R., Burchell, M.J., Cole, M.J., Murphy, T.W., and Allahdadi, F.: 1997, *Experimental measurements of hypervelocity impact plasma yield and energetics*, *International Journal of Impact Engineering* **20**, 663

Ratcliff, P.R., Gogu, F., Grün, E., and Srama, R.: 1996, *Plasma production by secondary impacts: implications for velocity measurements by* in-situ *dust detectors*, *Advances in Space Research* **17(12)**, 111

Reber, O.: 1997, *Bestimmung der Energie- und Winkelverteilung von Primärionen beim Einschlag von Hochgeschwindigkeits-Mikrometerpartikeln auf Oberflächen und deren Anwendung auf Einschlagsensoren an Bord interplanetarer Raummissionen*, *Doctoral/Ph.D. thesis*, Max-Planck-Institut für Kernphysik, Heidelberg

Rudolph, V.: 1966, *Massen-Geschwindigkeitsfilter für künstlich beschleunigten Staub*, *Zeitschrift f. Naturforschung* **21 a**, 1993

Schäfer, G.: 1968 - 2002, *Measurement protocols of the Heidelberg dust accelerator*, laboratory protocols

Shelton, H., Hendricks, C.D., and Wuerker, R.F.: 1960, *Electrostatic Acceleration of Microparticles to Hypervelocities*, *Journal of Applied Physics* **31(1)**, 1243

Shimizu, N.: 1978, *Analysis of the zoned plagioclase of different magmatic environments: a preliminary ion-microprobe study*, *Earth and Planetary Science Letters* **39**, 398

Showalter, Mark R., Cuzzi, Jeff N., and Larson, Stephen M.: 1991, *Structure and particle properties of Saturn's E ring*, *Icarus* **94**, 451

Silverstein, R.M., Bassler, G.C., and Morill, T.C.: 1981, *Spectrometric identification of organic compounds*, John Wiley & Sons, New York, fourth edition

Srama, R.: 2000, *Kombination von Meßsystemen zur simultanen Messung der Eigenschaften von kosmischen Staub*, *Doctoral/Ph.D. thesis*, Technische Universität München, Garching

Srama, R., Ahrens, T., Altobelli, N., Auer, S., Bradley, J., Burton, M., Dikarev, V., Fechtig, H., Görlich, M., Grande, M., Graps, A., Grün, E., Havnes, O., Helfert, S., Horanyi, M., Igenbergs,

E., Jessberger, E., Johnson, T., Kempf, S., Krivov, A., Krüger, H., Moragas-Klostermeyer, G., Lamy, P., Landgraf, M., D., L., Linkert, G., Lura, F., McDonnell, J., Möhlmann, D., Morfill, G., Müller, M., Schäfer, G., Schlozthauer, G., Schwehm, G., Spahn, F., Stübig, M., Svestka, J., Tschernjawski, V., Tuzzolino, A., Wäsch, R., and Zook, H.: 2002, *The Cassini Cosmic Dust Analyzer*, *Space Science Review* **???**, ???

Srama, R. and Grün, E.: 1997, *The dust sensor for CASSINI*, *Advances in Space Research* **20**, 1467

Srama, R., Altobelli, N., Dikarev, V., Graps, A., Grün, E., Kempf, S., Krüger, H., Moragas-Klostermeyer, G., and Stübig, M.: 2002, The cosmic dust analyzer onboard cassini-huygens: An overview of cruise science results, in *Geophysical Research Abstracts, 27th General Assembly of the EGS*, Vol. 4

Stephan, T.: 2001, *TOF-SIMS in chosmochemistry*, *Planetary and Space Science* **49**, 859

Stephan, T.: 2002, *Discussion on time-of-flight mass spectra*, private communication

Stöcker, H.: 1994, *Taschenbuch der Physik*, Verlag Harry Deutsch, Thun und Frankfurt am Main, 2. edition

Stübig, M.: 1999, Aufbereitung von mineralen und neukonstruktion einer staubquelle für den einsatz am heidelberger staubbeschleuniger, *Diploma/Master's thesis*, Max-Planck-Institut für Kernphysik, Heidelberg

Stübig, M., Schäfer, G., Ho, T.-M., Srama, R., and Grün, E.: 2001, *Laboratory simulation improvements for hypervelocity micrometeorite impacts with a new dust particle source*, *Planetary and Space Science* **49**, 853

Trafton, L., Parkinson, T., and Macy, W.: 1974, *The Spatial Extent of Sodium Emission around Io*, *The Astrophysical Journal* **190**, L85+

Unsöld, A. and Baschek, B.: 1991, *Der neue Kosmos*, Springer-Verlag, Berlin, Heidelberg, 5. edition

Wang, Hongyien, Salzberg, A.P., and Weiner, B.R.: 1991, *Laser ablation of aluminium at 193, 248, and 351 nm*, *Applied Physical Letters* **59(8)**, 935

Weinberg, J.L. and Sparrow, J.G.: 1978, *Cosmic Dust*, Chapt. 2: Zodiacal Light as an Indicator of Interplanetary Dust, John Wiley and Sons, Chichester, New York, Brisbane, Toronto

Whipple, F.: 1978, *Cosmic Dust*, Chapt. 1: Comets, John Wiley and Sons, Chichester, New York, Brisbane, Toronto

Wondraschek, R.: 1997, Untersuchungen über Energie- und Winkel-Verteilungen der bei Hochgeschwindigkeitskollisionen entstehenden Primärionen, *Diploma/Master's thesis*, Max-Planck-Institut für Kernphysik, Heidelberg

Zook, H.A., Grün, E., Baguhl, M., Hamilton, D.P., Linkert, G., Liou, J.-C., Forsyth, R., and Phillips, J.L.: 1996, *Solar Wind Magnetic Field Bending of Jovian Dust Trajectories*, *Science* **274**, 1501

Declaration

This thesis has been written in LaTeX 2_ε and was produced by using software tools that belong to the work group. I assure that I wrote this thesis independently and that I didn't used other than the given resources.

Erklärung

Diese Arbeit wurde unter Zuhilfenahme der gruppeninternen Software erstellt und in LaTeX 2_ε gesetzt. Ich versichere, daß ich diese Arbeit selbständig verfasst und keine anderen als sie angegebenen Hilfsmittel benutzt habe.

Heidelberg, den